

2D sparse array optimization and operating strategy for real-time 3D ultrasound imaging

Emmanuel Roux

▶ **To cite this version:**

Emmanuel Roux. 2D sparse array optimization and operating strategy for real-time 3D ultrasound imaging. Acoustics [physics.class-ph]. Université de Lyon; Università degli Studi di Firenze, 2016. English. ⟨NNT : 2016LYSE1255⟩. ⟨tel-01451208⟩

HAL Id: tel-01451208

https://theses.hal.science/tel-01451208v1

Submitted on 31 Jan 2017

HAL is a multi-disciplinary open access archive for the deposit and dissemination of scientific research documents, whether they are published or not. The documents may come from teaching and research institutions in France or abroad, or from public or private research centers.

L'archive ouverte pluridisciplinaire **HAL**, est destinée au dépôt et à la diffusion de documents scientifiques de niveau recherche, publiés ou non, émanant des établissements d'enseignement et de recherche français ou étrangers, des laboratoires publics ou privés.



HAL Authorization

N°d'ordre NNT : 2016LYSE1255

THESE de DOCTORAT DE L'UNIVERSITE DE LYON

opérée au sein de
l'Université Claude Bernard Lyon 1
en cotutelle avec
l'Università degli Studi di Firenze

Ecole Doctorale N° 162
MÉCANIQUE, ÉNERGÉTIQUE, GÉNIE CIVIL, ACOUSTIQUE

Spécialité de doctorat :
Acoustique et Ingénierie de l'Information

Soutenue publiquement le 29/11/2016, par :
Emmanuel Roux
Ingénieur INSA Lyon 2013

2D sparse array optimization and operating strategy for real-time 3D ultrasound imaging

---

Devant le jury composé de :

Bridal, S. Lori	DR	UPMC Sorbonne Université	Examinatrice
Matrone, Giulia	CR.	Università degli Studi di Pavia	Examinatrice
Richard, Cédric	PU	Université Nice Sophia-Antipolis	Rapporteur
Savoia, Alessandro S.	CR. (HDR)	Università Roma TRE	Rapporteur
Liebgott, Hervé	PU	Université de Lyon	Directeur de thèse
Tortoli, Piero	PU	Università degli studi di Firenze	Directeur de thèse
Cachard, Christian	PU	Université de Lyon	Dir. de thèse (Invité)
Diarra, Bakary	MCU.	BIUST, Palapye, Botswana	Invité

This work is licensed under a Creative Commons Attribution-NonCommercial-ShareAlike 3.0 France License.

UNIVERSITE CLAUDE BERNARD - LYON 1

Président de l'Université	**M. le Professeur Frédéric FLEURY**
Président du Conseil Académique	M. le Professeur Hamda BEN HADID
Vice-président du Conseil d'Administration	M. le Professeur Didier REVEL
Vice-président du Conseil Formation et Vie Universitaire	M. le Professeur Philippe CHEVALIER
Vice-président de la Commission Recherche	M. Fabrice VALLÉE
Directeur Général des Services	M. Alain HELLEU

COMPOSANTES SANTE

Faculté de Médecine Lyon Est – Claude Bernard	Directeur : M. le Professeur J. ETIENNE
Faculté de Médecine et de Maïeutique Lyon Sud – Charles Mérieux	Directeur : Mme la Professeure C. BURILLON
Faculté d'Odontologie	Directeur : M. le Professeur D. BOURGEOIS
Institut des Sciences Pharmaceutiques et Biologiques	Directeur : Mme la Professeure C. VINCIGUERRA
Institut des Sciences et Techniques de la Réadaptation	Directeur : M. X. PERROT
Département de formation et Centre de Recherche en Biologie Humaine	Directeur : Mme la Professeure A-M. SCHOTT

COMPOSANTES ET DEPARTEMENTS DE SCIENCES ET TECHNOLOGIE

Faculté des Sciences et Technologies	Directeur : M. F. DE MARCHI
Département Biologie	Directeur : M. le Professeur F. THEVENARD
Département Chimie Biochimie	Directeur : Mme C. FELIX
Département GEP	Directeur : M. Hassan HAMMOURI
Département Informatique	Directeur : M. le Professeur S. AKKOUCHE
Département Mathématiques	Directeur : M. le Professeur G. TOMANOV
Département Mécanique	Directeur : M. le Professeur H. BEN HADID
Département Physique	Directeur : M. le Professeur J-C PLENET
UFR Sciences et Techniques des Activités Physiques et Sportives	Directeur : M. Y.VANPOULLE
Observatoire des Sciences de l'Univers de Lyon	Directeur : M. B. GUIDERDONI
Polytech Lyon	Directeur : M. le Professeur E.PERRIN
Ecole Supérieure de Chimie Physique Electronique	Directeur : M. G. PIGNAULT
Institut Universitaire de Technologie de Lyon 1	Directeur : M. le Professeur C. VITON
Ecole Supérieure du Professorat et de l'Education	Directeur : M. le Professeur A. MOUGNIOTTE
Institut de Science Financière et d'Assurances	Directeur : M. N. LEBOISNE

Acknowledgements

First of all I would like to thank the jury members for their enthusiast cooperation in evaluating the present work, their patience to formulate very relevant remarks to refine the report and their kindness to all come to Lyon for the oral examination. Thanks to my super supervisors, Christian, Hervé and Piero for their brilliant international cooperation and their wonderful management skills inspiring the work. A special thanks to Marc Robini for the time he dedicated in explaining me a small part of his exceptional knowledge in stochastic optimization with a rigorous sensibility. Many thanks to Alessandro Ramalli for his marvelous efficiency during our cooperation in Florence, and to all the members of the MSD Lab (dream team!) I was lucky to work with during 10 months. Thanks to the PhD students, Master students, post-docs, permanent scientific and administrative staff members of CREATIS for making every day a lively day in the laboratory! I would like to thank all the people I have been lucky to work with and share scientifically and humanly during these three years.

Remerciements

Je tiens à remercier en tout premier lieu les membres du jury qui ont accepté d'évaluer mon travail de thèse et à mes directeurs pour leur confiance, leurs conseils avisés, et leur encadrement exemplaire. Remerciements sincères à tous les doctorants, étudiants de master, post-docs, permanents et membres de l'équipe administrative de CREATIS avec qui j'ai partagé une ambiance de travail plus qu'agréable. J'aimerais également remercier tous mes amis qui de près ou de loin m'ont su porter dans la joie et la bonne humeur. Merci à ma mamie pour son incroyable optimisme et sa générosité sans limite qui rayonne sur tous ceux qui l'entourent. Un remerciement à mes parents qui m'inspirent sans relâche par leur souffle créatif exceptionnel et la justesse avec laquelle ils savent faire respirer le temps entre les pas qu'esquisse la danse de la vie. Merci à Christine pour sa volonté et son engagement exemplaire, sa patience et son dévouement aux générations futures à qui elle apporte avec une conviction précieuse, la fabuleuse faculté de lire. Remerciements affectueux à Inés qui m'accompagne au quotidien et qui m'a apporté un soutien sans faille tout au long de ce travail, attention d'autant plus remarquable qu'elle-même travaille pour son doctorat dans le même temps. Remerciements à Lisa et Nicolas pour leur accueil chaleureux dans la Pomme et le partage de leur regard scientifique d'excellence. Enfin, remerciements à Côme pour la vitalité qu'il propage par sa présence sans cesse en devenir.

À Côme,

Résumé

Optimisation et pilotage de sondes parcimonieuses 2D pour l'imagerie ultrasonore 3D temps-réel

Aujourd'hui l'utilisation de l'échographie 3D en cardiologie est limitée car l'imagerie de la totalité du myocarde sur un cycle cardiaque, sans apnée, reste un défi technologique. Une solution consiste à réduire le nombre de capteurs dans les sondes échographiques matricielles afin d'alléger le procédé d'acquisition: ces sondes sont dites parcimonieuses. Le but de cette thèse est de proposer les meilleures dispositions d'un nombre réduit de capteurs piézo-électriques répartis sur la surface active de la sonde afin d'optimiser leur capacité à produire des images homogènes en termes de contraste et résolution dans tout le volume d'intérêt. Ce travail présente l'intégration de simulations acoustiques réalistes élaborées au sein d'un processus d'optimisation stochastique (algorithme de recuit simulé). La structure proposée pour le design des sondes parcimonieuse est suffisamment générale pour être appliquée aux sondes régulières (éléments actifs disposés selon une grille) et non-régulières (positionnement arbitraire des éléments actifs). L'introduction d'une fonction d'énergie innovante permet de sculpter en 3D le diagramme optimal de rayonnement de la sonde. Les résultats de sondes optimisées obtenues possèdent 128, 192 ou 256 éléments pour favoriser leur compatibilité avec les échographes commercialisés à ce jour, ce qui permettrait de déployer l'échographie 3D à moindre coût et à très large échelle.

Abstract

2D sparse array design optimization and operating strategy for real-time 3D ultrasound imaging

Today, the use of 3D ultrasound imaging in cardiology is limited because imaging the entire myocardium on a single heartbeat, without apnea, remains a technological challenge. A solution consists in reducing the number of active elements in the 2D ultrasound probes to lighten the acquisition process: this approach leads to sparse arrays. The aim of this thesis is to propose the best configuration of a given number of active elements distributed on the probe active surface in order to maximize their ability to produce images with homogeneous contrast and resolution over the entire volume of interest. This work presents the integration of realistic acoustic simulations performed in a stochastic optimization process (simulated annealing algorithm). The proposed sparse array design framework is general enough to be applied on both on-grid (active elements located on a regular grid) and non-grid (arbitrary positioning of the active elements) arrays. The introduction of an innovative energy function sculpts the optimal 3D beam pattern radiated by the array. The obtained optimized results have 128, 192 or 256 active elements to help their compatibility with currently commercialized ultrasound scanners, potentially allowing a large scale development of 3D ultrasound imaging with low cost systems.

Sommario

Ottimizzazione e pilotagio di sonde sparse 2D per l'ecografia 3D tempo reale

L'uso dell'ultrasonografia 3D in cardiologia è oggi limitato, perché scandire l'intero volume miocardico per un solo ciclo cardiaco, senza apnea, rimane una sfida tecnologica. Una soluzione consiste nel ridurre il numero di sensori nelle sonde ecografiche matriciali per facilitare il processo di acquisizione: questo approccio porta allo sviluppo dei cosiddetti *"sparse arrays"* (o sonde *sparse).* Lo scopo di questa tesi è di individuare la migliore configurazione possibile di un numero assegnato di elementi ultrasonici distribuiti sulla superficie attiva della sonde, per massimizzare la loro capacità di produrre immagine omogenee in termini di contrasto e di risoluzione in tutto il volume osservato. Questo lavoro presenta l'integrazione di simulazioni acustiche "realistiche", elaborate all'interno di un processo di ottimizzazione stocastico (*simulated annealing*). La struttura proposta per la progettazione di sonde sparse è sufficientemente generale per essere applicata alle sonde 2D con elementi "*on-grid*" (distribuiti in una griglia) e "*non-grid*" (distribuzione con posizioni del tutto arbitrarie). L'introduzione di una nuova funzione di energia permette di "scolpire" in 3D il diagramma di radiazione ottimale della sonda. I risultati ottenuti di sonde ottimizzate hanno 128, 192 o 256 elementi attivi per massimizzare la loro compatibilità con gli scanner ad ultrasuoni oggi commercializzati, permettendo potenzialmente di diffondere l'ecografia 3D su larga scala e a basso costo.

Glossary

2D	Two Dimensional
3D	Three Dimensional
A/D	Analog-to-digital (converters)
ADC	Analog to Digital Conversions
ASIC	Application Specific Integrated Circuits
BP	Beam Pattern
CNR	Contrast to Noise Ratio
CPU	Central Processing Unit
CW	Continuous Wave
DAS	Delay and Sum
DOF	Depth Of Field
FDA	Food and drug administration
FOV	Field of View
FWHM	Full Width Half Maximum
Gb	Giga bit
GLL	Grating Lobe Level
GPU	Graphic Processing Unit
GUI	Graphical User Interface
HIFU	High Intensity Focused Ultrasounds
HRTF	Head Related Transfer Function
HS	Hemisphere
MAC	Multiply-and-accumulate
OOP	Object Oriented Programing
PF	Pressure Field
PMP	Pressure Measurement Points
PSF	Point Spread Function
RF	Radio frequency (signals)
RX	Reception
SA	Simulated Annealing
SC	Stochastic Continuation
SIR	Spatial Impulse Response
SLL	Side Lobe Level
SMER	Side-to-main-lobe Ratio
TB	Tera Bytes
TGC	Time Gain Compensation
TX	Transmission
US	Ultrasound
WFS	Wave Field Synthesis
WSS	Wideband and Shape Sensitive

List of symbols

Geometry

$\boldsymbol{r}$	Position vector	
x, y, z	Cartesian coordinates	$\boldsymbol{r} = x\hat{\mathbf{x}} + y\hat{\mathbf{y}} + z\hat{\mathbf{z}}$ (unit vectors $\hat{\mathbf{x}}, \hat{\mathbf{y}}, \hat{\mathbf{z}}$)
R, θ, ϕ	Spherical coordinates	$\boldsymbol{r} = R\hat{\boldsymbol{r}}$ (unit vector $\hat{\boldsymbol{r}}$)
t	Time	

Acoustic waves

$\Upsilon_{\text{reflect}}$	Reflection coefficient
$\Upsilon_{\text{transmit}}$	Transmission coefficient
$\alpha_{\text{i}}, \alpha_{\text{t}}, \alpha_{\text{r}}$	Incident, transmission and reflection angles
c	Propagation velocity (speed of sound)
F_{s}	Sampling frequency
f_{c}	Central frequency of the transducer
h	Transducer element thickness
u	Transducer membrane displacement
v	Particle velocity vector
Z	Acoustic impedance of the medium
λ	Wavelength
ρ	Density of the medium
φ	The wave phase
ψ	Velocity potential
ω	Angular velocity

Transducers

A_k	Spatial region occupied by $\mathbf{e}_k$
d	Pitch (distance between consecutive elements centers)
$\mathbf{e}_k$	k-th element of the array
E_k	Set of properties of $\mathbf{e}_k$
θ_k, ϕ_k	Orientation of the normal vector to the element surface
τ_k	Delay
a_k, b_k	Element size on x direction (a_k) and y direction (b_k)
Exc_k	Excitation signal
Imp_k	Impulse response
w_k	Weighting coefficient
x_k, y_k, z_k	Position of the element center

G	Cartesian grid
$\mathrm{h}(\boldsymbol{r}, t)$	Spatial Impulse Response
N_{e}	Number of active elements
N_x	Number of elements along x direction (2D gridded array)
N_y	Number of elements along y direction (2D gridded array)
r_{p}	Aperture radius

$\boldsymbol{P_i}$	Transducer polarization along direction $\boldsymbol{i}$
$\boldsymbol{T_j}$	Transducer stress tensor applied along direction $\boldsymbol{j}$
d_{ij}	Transducer strain constants ($\boldsymbol{i} \rightarrow \boldsymbol{j}$)

Imaging strategies

$\delta_{\mathrm{l}}, \delta_{\mathrm{a}}$	Lateral and axial sizes of the focal spot
$\theta_{\mathrm{steer}}, \phi_{\mathrm{steer}}$	Steering angles
D	Aperture size (in case of a disk $D = 2r_{\mathrm{p}}$)
F	Focal depth (= z_{f})
N_{s}	Number of scatterers
$p_0(t)$	Initial pressure about the transducer surface
$p(\boldsymbol{r}, t)$	pulse-echo signal received from a set of scatterers
$\mathrm{RF}_{\mathrm{post}}(t)$	post-beamforming RF signals
$\mathrm{RF}_k(t)$	pre-beamforming Radio-Frequency (RF) signals (raw data)
$\boldsymbol{r}_{\mathrm{f}}$	Focal point position vector
$\boldsymbol{r}_{\mathrm{s}}$	Virtual source position (diverging waves transmission)
$\mathrm{s}(\boldsymbol{r}, t)$	Scatterer in the medium
$x_{\mathrm{f}}, y_{\mathrm{f}}, z_{\mathrm{f}}$	Focal point Cartesian coordinates

Simulated Annealing

$(\beta_n)_{n\in\mathbb{N}}$	Cooling sequence (inverse temperature)
β_n	Inverse of the temperature at iteration n
K	Number of iteration of the constant-temperature stages
N_{iter}	Number of iterations
n	iteration index
$\mathrm{P}(S_{n+1}\|S_n)$	Transition matrix
$(S_n)_{n\in\mathbb{N}}$	Simulated Annealing Markov Chain
S_0	Initial solution
S_n	Solution at iteration n
$\tilde{S}_n$	New proposition from a perturbation of S_n
S_{opti}	Best solution encountered during the optimization process $(S_n)_{n\in\mathbb{N}}$
Θ	Communication mechanism
Ω	State space of solutions
$\mathcal{G}(S)$	Neighborhood of solution S
σ	Number of constant-temperature stages

Energy function

$\theta_{\mathrm{ML}}(R)$	Main lobe region limit angle (at depth R)
$\rho_1, \dots, \rho_{N_{\mathrm{H}}}$	Weight associated to $U_{R_1}(S) \dots U_{R_{N_{\mathrm{H}}}}(S)$
$\mathrm{BP}_S(R, \theta, \phi)$	Normalized (one-way) beam pattern radiated by S at depth R
$L(R)$	Main lobe region at depth R
$\mathrm{MASK}\ (R, \theta, \phi)$	The sculpting mask at depth R
$\mathrm{C}(R)$	Cut value of MASK (R, θ, ϕ)
q_{mask}	Quantization step of MASK (R, θ, ϕ)
$M_+(R)$	Maximum positive pressure difference with MASK (R, θ, ϕ)
$M(R)$	Maximum of pressure above MASK (R, θ, ϕ)
N_{H}	Number of hemispheres
N_{PMP}	Number of Pressure Measurement Points (PMP)
$\mathrm{PF}_S(R, \theta, \phi, t)$	Pressure Field radiated by S at depth R
$R_1, \dots, R_{N_{\mathrm{H}}}$	Radius of the PMP hemispheres
$U^{N_{\mathrm{H}}}(S)$	Multi-depth (N_{H} depths) energy function associated to solution S
$U_R(S)$	Energy function associated to solution S computed at depth R

Content

RÉSUMÉ VI

ABSTRACT VIII

SOMMARIO X

GLOSSARY XII

LIST OF SYMBOLS XIII

CONTENT XVI

GENERAL INTRODUCTION: JOINING WIDEBAND ACOUSTIC SIMULATIONS AND SIMULATED ANNEALING OPTIMIZATION FOR ULTRASOUND 2D SPARSE ARRAYS INDIVIDUATION 1

I CHAPTER I CONTEXT OF 3D ULTRASOUND IMAGING 3

I.A ACOUSTICS IN ULTRASOUND IMAGING: FROM MATTER TO WAVES 3
I.A.1 DOUBLE ROLE OF PIEZOELECTRIC SENSORS: DIRECT ("MICROPHONES") AND REVERSE ("SPEAKERS") EFFECTS. 3
I.A.2 MATERIAL ENGINEERING TO CUSTOMIZE THE ULTRASOUND TRANSDUCER. 5
I.A.3 GENERATING ULTRASOUND WAVES 7
I.A.4 ULTRASOUND WAVES USED IN MEDICAL ENVIRONMENT 9
I.B BEAMFORMING: FROM WAVES TO IMAGES 12
I.B.1 PRESSURE FIELD COMPUTATION FOR ANY TRANSDUCER CONFIGURATION 12
I.B.2 TRANSMISSION STRATEGIES 14
I.B.3 BEAM PATTERNS 18
I.B.4 IMAGE RECONSTRUCTION 20
I.C INTEREST AND CURRENT LIMITS OF 3D+T (4D) ULTRASOUND IMAGING 22
I.C.1 EXISTING APPLICATIONS OF 3D+T (4D) ULTRASOUND IMAGING 22
I.C.2 ARRAYS DESIGN EVOLUTION 22
I.C.3 A TECHNICAL CHALLENGE FOR 3D+T ULTRASOUND IMAGING 23
I.C.4 EXISTING PROBE DESIGNS FOR 3D IMAGING 24
I.D 2D SPARSE ARRAY OPTIMIZATION METHODS 26
I.D.1 STATE-OF-THE-ART AND LIMITATIONS 26

II CHAPTER II REALISTIC ACOUSTIC SIMULATIONS IN A GENERAL 2D SPARSE ARRAY OPTIMIZATION FRAMEWORK 31

II.A INTRODUCTION: MOTIVATIONS AND LIMITATIONS 31
II.B SPEED-UP OF THE REALISTIC ACOUSTIC SIMULATIONS 31

II.B.1 PRESSURE MEASUREMENT POINTS (PMP) REDUCTION TECHNIQUE 31
II.B.2 ERGONOMIC DATA MANAGEMENT 34
II.B.3 BENEFITS 36
II.C GENERAL 2D SPARSE ARRAY OPTIMIZATION FRAMEWORK 40
II.C.1 GENERAL STATE SPACE 40
II.C.2 COMMUNICATION MECHANISM 41
II.C.3 ENERGY FUNCTION 42
II.D SIMULATED ANNEALING WORKFLOW 43
II.E DISCUSSION 44
II.F CONCLUSION 44

III CHAPTER III MULTI-DEPTH RADIATION OPTIMIZATION OF NON-GRID 2D ULTRASOUND SPARSE ARRAYS 45

III.A INTRODUCTION 45
III.B METHODS 46
III.B.1 NON-GRID 2D SPARSE ARRAY OPTIMIZATION 46
III.B.2 STATE SPACE OF NON-GRID 2D SPARSE ARRAYS 46
III.B.3 COMMUNICATION MECHANISM 47
III.B.4 ENERGY FUNCTION 48
III.B.5 OPTIMIZATION SETUP 50
III.B.6 POST-OPTIMIZATION EVALUATION: 3D BEAM PATTERN PERFORMANCE METRICS 52
III.C OPTIMIZED NON-GRID 2D SPARSE ARRAYS AND SPIRAL ARRAY COMPARISON 52
III.C.1 NUMBER OF ITERATIONS 52
III.C.2 NUMBER OF PRESSURE MEASUREMENT POINTS 53
III.C.3 NUMBER OF HEMISPHERES 53
III.C.4 ENERGY FUNCTION 54
III.D DISCUSSION 58
III.D.1 LAYOUT CHARACTERISTICS 58
III.D.2 DEGREES OF FREEDOM AND CONSTRAINTS 59
III.D.3 MULTI-DEPTH ENERGY FUNCTION 59
III.D.4 OPTIMIZATION SETUP 60
III.E CONCLUSION 60

IV CHAPTER IV WIDEBAND ON-GRID 2D ARRAY DESIGN OPTIMIZATION WITH FABRICATION CONSTRAINTS FOR 3D US IMAGING 63

IV.A INTRODUCTION 63
IV.B FINDING THE BEST CONFIGURATION OF Ne ACTIVE ELEMENTS IN A $NxNy$ 2D ARRAY 64
IV.B.1 STATE SPACE AND DESIGN CONSTRAINTS 64
IV.B.2 COMMUNICATION MECHANISM 65
IV.B.3 ENERGY FUNCTION 66
IV.B.4 OPTIMIZATION SETUP AND RANDOM DESIGN COMPARISON 68
IV.B.5 PERFORMANCE ANALYSIS 69

IV.C RESULTS **71**
IV.C.1 LAYOUTS AND ENERGY FUNCTION VALUES 71
IV.C.2 COMPARISON OF THE MULTI-DEPTH BEAM PATTERNS 72
IV.C.3 3D BEAM PATTERNS ANALYSIS OVER 81 STEERING ANGLES 75
IV.C.4 IMAGE SIMULATIONS 78
IV.C.5 DESIGN ROBUSTNESS 78
IV.D DISCUSSION **80**
IV.D.1 GENERALITIES 80
IV.D.2 THE MULTI-DEPTH ENERGY FUNCTION AND THE LAYOUTS 80
IV.D.3 THE 3D BEAM PATTERN SIMULATIONS 81
IV.D.4 THE 3D VOLUME IMAGES 82
IV.D.5 THE DESIGN ROBUSTNESS 83
IV.D.6 TENSION AND METASTABILITY 83
IV.E CONCLUSION **84**

V GENERAL DISCUSSION: LIMITS AND PERSPECTIVES **87**

V.A LACK OF EXPERIMENTAL 3D IMAGES AND PROTOTYPING **87**
V.B THE STATE SPACE AND ACOUSTIC SIMULATIONS **87**
V.C THE ENERGY FUNCTION **88**
V.D THE COMMUNICATION MECHANISM **88**
V.E THE COMPUTATION TIME **89**
V.F STOCHASTIC CONTINUATION AND CONTINUOUS MODULATION **90**
V.G MULTI ORDERS INDIVIDUATION OF ULTRASOUND 2D SPARSE ARRAYS **91**
V.H OTHER FIELDS OF APPLICATIONS **92**

GENERAL CONCLUSION **95**

PERSONAL PUBLICATIONS **99**

REFERENCES **101**

APPENDIX CONTENT **107**

APPENDIX I: OPTIMIZATION AND ANALYSIS PIPELINE **109**
APPENDIX II: ONLINE VIDEO DESCRIPTION **115**
APPENDIX III: DISSEMINATION ACTIVITIES **117**
APPENDIX IV: RESUME SUBSTANTIEL EN FRANÇAIS **119**

General introduction: Joining wideband acoustic simulations and simulated annealing optimization for ultrasound 2D sparse arrays individuation

The sense of hearing is shared over any living species on Earth, hence sensing the acoustical environment is essential for life. But viewing is also the predominant sense exploited in our human organized-society. In between, the production of images from sound is a fascinating process which is allowed thanks to the propagation of acoustic waves. In medicine, ultrasound scanners listen to the echoes of transmitted acoustic waves in the patient's body and the operation of converting these back-propagating sounds into diagnostic images is designated as echography. Three-dimensional ultrasound (3D US) imaging is the 3D extension of the traditional 2D US imaging which is daily used for medical exams. In general, ultrasound waves are transmitted and received from the ultrasound probe which is the device that the clinician holds in his hand during an ultrasound exam.

How can acoustic waves be generated? At this scale, the electro-mechanical transduction is a fundamental property presented by some materials or artificially mimicked with technological artifacts. It consists in converting the electrical energy into mechanical energy and vice versa. A piece of material capable of such a conversion is called a transducer and in ultrasound imaging they are used as both acoustic transmitters (to transmit waves) and acoustic sensors (to receive echoes). Several individual transducers (say active elements) are located in the probe head and they are connected to the ultrasound scanner through a cable. The transduction property emanates from the crystallographic structure[1] of specific materials, which itself results from the annealing process of the material.

At a larger scale, the design of 2D array probes is a higher order issue. Designing a 2D array for 3D US is the operation[2] of organizing a group of individual active elements to form a "3D acoustic information extraction" structure. In other words, it consists in searching for a combination of individual points of view to grasp all the facets of the observed 3D reality. When scanning is performed by steering electronically the acoustic beam, the transmitting and sensing capability of the ultrasound probe depends on the spatial distribution of the active elements. This is valid for both 2D US and 3D US imaging. However, in traditional 2D US imaging the active elements are placed along a line so that they can image a plane parallel to this line; whereas in 3D US imaging they are

[1] « A crystal which, from a very small unit cell, grows and spreads toward all directions in its mother-water gives the simplest image of the transductive operation: each already constituted molecular layer serves as the structuring base of the layer being formed; the result is an amplifying reticular structure. » (Simondon 2005), p. 33, personal translation.

« The amplification phenomenon is then automatic and undefined, all successive layers of the crystal being able to structure the surrounding amorphous medium; as long as this medium stays metastable; in this way, a crystal may have its amplification stopped, but never achieved, and it can always continue to grow if put back in a metastable medium. », *Ibidem*, p. 86, personal translation.

[2] The allagmatic is defined as the theory of operations, complementary to the theory of structures (Corry 1992): « The *allagmatic theory is the study of the individual being*. It organizes and defines the relations between the theory of operations (applied cybernetic) and the theory of structures (deterministic and analytical science). », *Ibidem*, p. 565, personal translation.

distributed over the 2D surface of the active aperture so that a full volume can be scanned. The element distribution in 2D arrays may lead to “fully populated arrays” (when they cover the entire surface) or to “sparse arrays” (when only a limited number is used to partially cover the available surface). In the latter case, the quality of the imaging capabilities depends on the shape of the array radiated beam pattern (BP), which in turn can be modulated to fit with the targeted application imaging requirements by adjusting the relative positions of the active elements. Two main approaches can be identified to broach the 2D array design issue. The first one is based on deterministic designs where immediate rational designs emerge from theory. The second approach based on stochastic optimization is often relatively slower because exploring a huge amount of solutions can be quite time consuming. The intention here is to present the advantages and drawbacks when adopting each point of view, and the aim is to show the benefits of joining practical design aspects (thanks to realistic acoustic simulations where time dimension is considered) with a *transductive* optimization operation[3]. Indeed, the simulated annealing optimization algorithm that was used in the present work is directly inspired by the annealing process that produced, at a smaller order/scale, each individual vibrating crystal. The same *transductive* principle operates at a microscopic level for the organization of the crystal particles and at a macroscopic scale for the organization of the individual active elements to form the transducer array. In accordance with the definition of *transduction*[4] defended in the doctoral thesis (Simondon 2005) of Gilbert Simondon, the optimization of transducer arrays using the simulated annealing algorithm is analog to a *transductive individuation* process.

The issue of 2D array design for 3D US imaging has been addressed at CREATIS for six years starting with the work of Bakary Diarra who studied the non-grid optimization of 2D sparse arrays. Yet, considering that gridded arrays are encountered more often in practice and that they are easier manufactured than non-grid arrays, the present thesis could not have been restricted to the extension of non-grid sparse array designs. As a consequence, it is intended to join both on-grid and non-grid designs within a general 2D array optimization framework.

[3] Paradoxically the realistic acoustic simulations are grounded in the theoretical acoustic radiation model while, on the contrary, the optimization process is grounded in material crystallization.

[4] « By transduction we mean a physical, biological, mental, social operation by which an activity propagates step by step inside a domain, founding this propagation on the structuration of the domain operated from place to place: each region of constituted structure serves as the constitution principle for the next region, so that a modification progressively spreads along with the structuring operation », (Simondon 2005), p. 32, personal translation. « The transduction […] is that by which a structure appears in a domain of issues as bringing the resolution of the arisen problems. But […] the transduction does not search elsewhere for a principle resolving the problem in a domain: it extracts the resolving structure from the domain tensions themselves as the supersaturated solution crystallizes thanks to its own potentials and the chemical species it contains, not by bringing any outsider form. », *Ibidem*, p. 34, personal translation.

I Chapter I Context of 3D ultrasound imaging

I.A Acoustics in ultrasound imaging: from matter to waves

I.A.1 Double role of piezoelectric sensors: direct ("microphones") and reverse ("speakers") effects.



Figure 1 Jacques (left) and Pierre (right) Curie discovered the phenomenon of piezoelectricity in 1880. (image source: http://www.aps.org/publications/apsnews/201403/physicshistory.cfm)

The ultrasound probes are sometimes designated as ultrasound transducers because they are made of a collection of individual transducers (also known as active elements) that can convert a form of energy to another (which is the technical definition of a transduction process). To be more precise, the active elements are electroacoustic transducers because the conversion is performed between electric energy (*electro-*) and acoustic energy. Historically, the electroacoustic transduction has been based on the piezoelectricity phenomenon. A reversible pressure-electricity effect can be noted in certain crystals: the direct piezoelectric effect was discovered by the French physicists Jacques (1856 - 1941) and Pierre (1859 - 1906) Curie in 1880 (Curie and Curie 1880): a piezoelectric solid crystal is polarized under a mechanical stress. The prefix *piezo-* comes from the greek "piezein" (πιέζειν) which means to press or squeeze. One year later, the reverse effect (Curie and Curie 1881) was predicted theoretically by Gabriel Lippmann[5] (1845 – 1921), and immediately verified experimentally by the Curie brothers: a piezoelectric solid crystal is strained under the application of an electric field. In a nutshell, in ultrasound imaging the *direct effect* is used (as in a microphone) to *receive* (*listen*) acoustic energy and the reverse effect is used (as in a loudspeaker) to transmit acoustic energy.

[5] Gabriel Lippmann supervised Pierre Curie for his Ph.D. dissertation (Pierre Curie 1985) at Université de Paris and École Supérieure de Physique et de Chimie Industrielles (1895). It can be noticed that Pierre Curie (along with Joseph John Thomson and Gabriel Lippmann) supervised Paul Langevin for his Ph.D. dissertation at Université de Paris (1902).

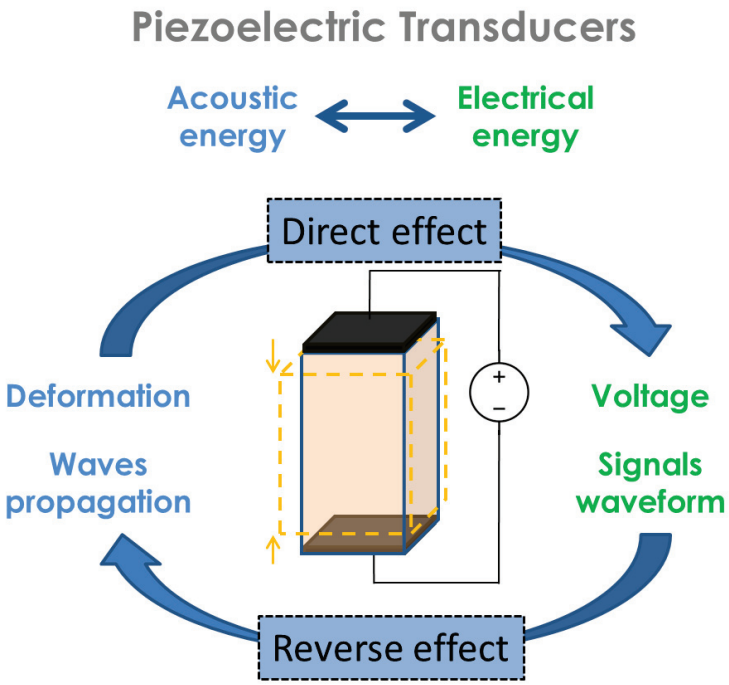


Figure 2 Illustration of the piezoelectric effect: the direct effect (from acoustic energy to electrical energy) is used in reception while the indirect (from electrical energy to acoustic energy) is used in transmission.

The previous description of piezoelectricity is a macroscopic effect of a specific structuration of the crystal at microscopic scale. 32 crystal classes have been defined based on the symmetry properties of the unit cell, i.e. the smallest repeating pattern of particles in the crystal. The appearance of electric charges on certain faces of the crystal, i.e. the crystal polarization, is due to the uneven rearrangement of the charge distribution within each unit cell. There are 20 out of the 32 crystal classes which present this piezoelectric property. It is necessary (but not sufficient[6]) for a piezoelectric crystals to be non-centrosymmetric which means that no inversion center exist in the unit cell: for any point (x,y,z) inside the unit cell, the points (x,y,z) and (-x,-y,-z) are distinguishable. Because of the non-centrosymmetric property the application of a stress separates the centers of positive and negative charges and produces an electric polarization $\boldsymbol{P_i}$ (direct effect) where i designates one of the orthogonal coordinate directions x,y,z. Piezoelectricity is a linear phenomenon which means that the polarization $\boldsymbol{P_i}$ and the stress tensor $\boldsymbol{T_j}$ quantities are linearly related by

$$\boldsymbol{P_i} = d_{ij}\boldsymbol{T_j} \tag{1}$$

where d_{ij} are the piezoelectric strain constants (in $\mathrm{C.N^{-1}}$). The crystal class determines the non-zero elements of the piezoelectric strain constants matrix. A rigorous mathematical formalism that links the stress tensor with the electric polarization can be found in (Beyer and Letcher 1969).

Among the 20 piezoelectric crystals that exist, 10 of them are *pyroelectrics*: they show a *spontaneous* polarization (even without the application of a mechanical strain) that varies with the

[6] The exception is the cubic class 432 which is non-centrosymmetric but where the charges cancel each other.

temperature. If the spontaneous polarization can be reversed by the application of a (high enough) electric field, the crystals are called *ferroelectrics*. Some natural minerals possess the *piezoelectric/ferroelectric* property by default: for instance the Perovskite mineral ($CaTiO_3$) is a *ferroelectric* crystal that was discovered in the Ural Mountains in 1839 by the German mineralogist Gustave Rose (1798-1873) and maned after Lev Perovski (1792-1856) a Russian mineralogist. But it is also possible to synthesize crystals presenting such physical behavior: this is the case for the widely used PZT (Lead Zirconium Titanate or $Pb[Zr_XTi_{1-X}]O_3$) is a synthetic *ferroelectric* crystal that has the so called perovskite unit cell structure (Figure 3) which is the same structure as in the Perovskite mineral (Figure 3): A lead ion (Pb^{2+}) is located in each of the 8 corners of the unit cell, an oxygen ion (O^{2-}) occupies each of the 6 faces center. Slightly off-centered, an ion Zr^{4+} or $Ti^{4+}$is found, with respective probability X and $1-X$, a little above (or below) the unit cell center which gives the orientation of the effective electric dipole formed by the unit cell. It is noteworthy that above the Curie temperature T_c (also called the Curie point) the substance shows a paraelectric phase in which the spontaneous polarization disappears, because of the disorder of the unit cell dipoles, but where the latter can potentially be aligned in a new polarization direction if an external electric field is applied.

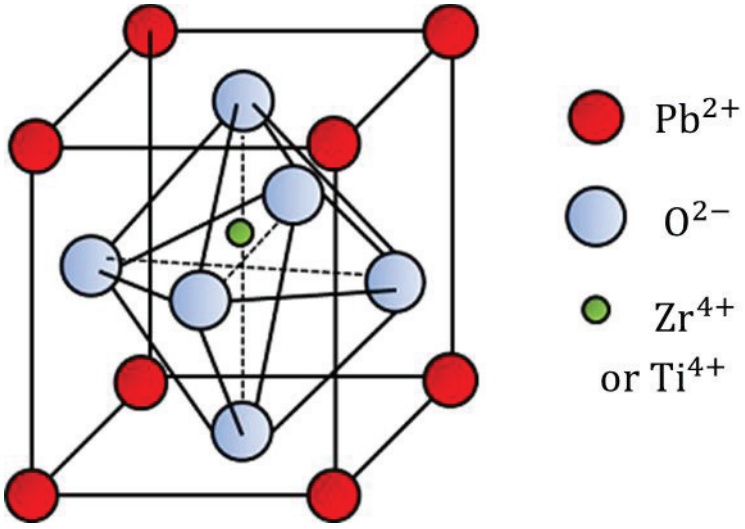


Figure 3 The perovskite unit cell structure of Lead (Pb) Zirconate (Zr) Titanate (Ti) (PZT). The ions Zr^{4+} or Ti^{4+} are not centered which is the origin of the piezoelectric properties of the PZT crystal. (original image on www.comsol.com)

I.A.2 Material engineering to customize the ultrasound transducer.

Manufacturing a *piezoelectric/ferroelectric* substance requires complex material engineering processes (doping, mixing, dry pressing, grinding, laminating, dicing, sintering, metalizing…). Interestingly, at the beginning of the manufacturing process a heat treatment (annealing) is applied to the material to remove internal stresses in three steps known as recovery, recrystallization and grain coarsening (Smallman and Bishop 1999; Doherty et al. 1997; Verhoeven 1975). During recovery the material microstructure is deformed. The changes in the dislocations distribution allow reducing the stored energy in the lattice. The recrystallization is when a new grain structure grows from sub-cells present in the deformed microstructure. The grain coarsening happens once the growing crystal has consumed the entire strained material: a further decrease of the internal energy is achieved by reducing the surface tension of the grain boundaries. One of the last engineering steps consists of

applying an electric field of several $\mathrm{kV.mm^{-1}}$ to polarize the crystal. This action of aligning the electric dipoles on the same orientation is called the *poling* process. Remaining microscopic defects in the crystalline structure prevent most dipoles to return back to their original orientation, this is called the *pinning* effect. The direction of the polarization has a direct impact on the way the transducer responds by increasing of the electroacoustic coupling coefficient in that direction.

Moreover, a very fine tuning of electroacoustic performance can be achieved by combining a piezoelectric phase with a polymeric phase (e.g. epoxy) to make a piezocomposite material. The most famous geometrical structures connecting the piezoelectric phase and the polymeric phase are known as the 1-3 connectivity and the 2-2 connectivity. By convention the first digit refers to the piezoelectric phase while the second digit refers to the polymeric phase. They indicate the connectivity of each phase, i.e., the number of dimensions through which the material is continuous. The transduction efficiency (piezoelectric coupling coefficient), the electric impedance (dielectric constant), the acoustic impedance and the central frequency (speed of sound in the material) depend on the proportion of each phase in the piezocomposite. The geometrical structure of the piezocomposite arrangement (shape, connectivity, and dimension) influences the way the transducers (i.e. the active elements of the ultrasound array) will vibrate. When several transducers are used together to scan a volume using electronic steering (as in phased array imaging, I.B.2.b) it is particularly important to reduce the cross-talk (electro-mechanic coupling) between neighboring elements. This has made the 1-3 connectivity relatively successful thanks to the lateral vibration reduction compared to the longitudinal one which improves the inter-elements isolation.

The transducer can be characterized by its impulse response (i.e. the transducer output when the excitation is a Dirac) which depends on the material itself (its composition with another polymeric phase in case of a piezocomposite structure) and its dimension. In particular the central frequency f_c $[\mathrm{Hz}]$ of the transducer is its resonance frequency which depends on the element thickness h $[\mathrm{m}]$ and the longitudinal perturbation velocity c $[\mathrm{m.s^{-1}}]$ in the crystal:

$$f_\mathrm{c} = \frac{c}{2h} \quad \text{or} \quad h = \frac{\lambda_\mathrm{c}}{2} \tag{2}$$

with $\lambda_\mathrm{c} = c/f_\mathrm{c}$, the central wavelength $[\mathrm{m}]$ associated to the transducer.

The transducer - 6 dB-bandwidth is the range of frequencies where the normalized and log compressed Fourier transform of the impulse response is above - 6 dB. In transmission mode the displacement $u(t)$ (in m) of a transducer membrane is the convolution ($*$) between the excitation signal $\mathrm{Exc}(t)$ and the impulse response of the transducer $\mathrm{Imp}(t)$

$$u(t) = \mathrm{Exc}(t) * \mathrm{Imp}(t) \tag{3}$$

The transducer behaves as a filter: the wider the bandwidth the higher the fidelity of the transducer membrane displacement $u(t)$ to the excitation signal $\mathrm{Exc}(t)$. By linearity of the piezoelectric transduction, the same happens in reception when the reverse effect generates a measurable electric signal which corresponds to the convolution of the received acoustic energy on the transducer surface and the impulse response of the transducer.

The recent development of Capacitive Micromachined Ultrasonic Transducers (CMUT) technology (Caronti et al. 2006; Caliano et al. 2005; Oralkan et al. 2002) has allowed the design of transducers (Savoia, Caliano, and Pappalardo 2012) with a larger bandwidth compared to ceramics. Another very interesting aspect is that they can be shaped and located with more flexibility compared with other transducer technologies.

I.A.3 Generating ultrasound waves

The velocity $\mathrm{v}(t) = \frac{\partial u(t)}{\partial t}$ (in $\mathrm{m}.s^{-1}$) of a transducer surface (considered uniform over the surface of the element[7]) is transmitted to the interacting field (medium) in which an acoustic wave is generated. A wave is defined as the propagation of a perturbation and it can be expressed as the solution of the wave equation

$$\nabla^2\psi = \frac{1}{c^2}\frac{\partial^2\psi}{\partial t^2} \tag{4}$$

with c $[\mathrm{m}.\mathrm{s}^{-1}]$ the propagation speed (speed of sound) and ψ the velocity potential which is related to the particle velocity vector $\mathbf{v}(t)$ (in $\mathrm{m}.\mathrm{s}^{-1}$) by $\mathbf{v} = \nabla\psi$. (bold characters designate vectors.)

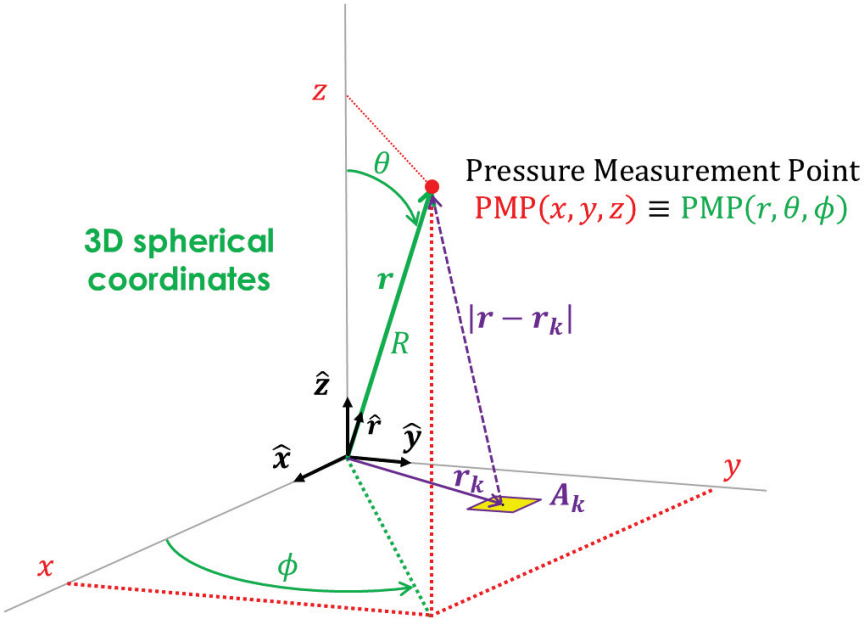


Figure 4 Adopted convention for 3D spherical coordinates (ISO-80000-2) and distance between an active surface A_k and pressure measurement point in $\boldsymbol{r}$.

The spherical coordinate convention is presented in Figure 4 (ISO 80000-2). The conversion formulas with Cartesian coordinates are

[7] "The edges are more or less clamped, so that we may expect $[v(t)]$ to be smaller in these regions. The crystal itself may vibrate more strongly on certain portions of its surface". (Beyer and Letcher 1969) p.14

$$\begin{cases} x = R\sin\theta\cos\phi \\ y = R\sin\theta\sin\phi \\ z = R\cos\theta \end{cases} \leftrightarrow \begin{cases} R = \sqrt{x^2+y^2+z^2} \\ \theta = \arccos(z/R) \\ \phi = \arctan(y/x) \end{cases} \tag{5}$$

So for any point located in (R, θ, ϕ), a position vector $\boldsymbol{r}$ can be defined:

$$\boldsymbol{r} = R\hat{\boldsymbol{r}} = x\hat{\boldsymbol{x}} + y\hat{\boldsymbol{y}} + z\hat{\boldsymbol{z}} \tag{6}$$

where $\hat{\boldsymbol{r}}$ is the unit vector pointing at (x, y, z), the associated Cartesian coordinates as mentioned in (5).

The wave equation (4) can be written in spherical coordinates:

$$\frac{1}{R^2}\frac{\partial}{\partial R}\left(R^2\,\frac{\partial\psi}{\partial R}\right) + \frac{1}{R^2\sin(\theta)}\frac{\partial}{\partial\theta}\left[\sin(\theta)\frac{\partial\psi}{\partial\theta}\right] + \frac{1}{R^2\sin^2(\theta)}\frac{\partial^2\psi}{\partial\phi^2} = \frac{1}{c^2}\frac{\partial^2\psi}{\partial t^2}. \tag{7}$$

and assuming the case of spherical waves (with source located at space origin), ψ does not depend on θ and ϕ so (7) can be simplified in

$$\frac{\partial^2(R\mathbf{v})}{\partial R^2} = \frac{1}{c^2}\frac{\partial^2(R\mathbf{v})}{\partial t^2} \tag{8}$$

which has solutions of the form

$$\mathbf{v} = \frac{1}{R}\boldsymbol{F}(R \pm ct), \tag{9}$$

where $\boldsymbol{F}$ can be interpreted as an outgoing wave $\boldsymbol{F}(R - ct)$ or as an incoming wave $\boldsymbol{F}(R + ct)$ to the space origin.

An individual monochromatic (oscillating at f_c) punctual source located in $\boldsymbol{r_k}$ radiates, in any point $\boldsymbol{r}$ of space, a spherical wave of the form

$$\mathbf{v}(\boldsymbol{r}, t) = \frac{\rho}{2\pi|\boldsymbol{r} - \boldsymbol{r_k}|}\,w_k\,e^{j\left(\frac{2\pi}{\lambda}|\boldsymbol{r}-\boldsymbol{r_k}|-\omega t\right)} \tag{10}$$

where $\omega = 2\pi f_c$ $[\mathrm{rad}.s^{-1}]$ is the angular velocity, w_k the amplitude of the source, and ρ $[\mathrm{kg}.\mathrm{m}^{-3}]$ the density of the medium. The wave phase φ $[\mathrm{rad}]$ is defined as the argument of $\mathbf{v}(\boldsymbol{r}, t)$.

The punctual monochromatic source is not a realistic model to represent the acoustic radiation of the active elements used in ultrasound imaging. A first contribution of this thesis was the integration of a more realistic acoustic model (wideband and shape sensitive) into the optimization process (Chapter II). However, compared to reality, many other approximations are assumed in the present work as detailed in the next paragraph.

I.A.4 Ultrasound waves used in medical environment

I.A.4.a Longitudinal waves and shear waves

In general, the displacement of the perturbation is not purely parallel (longitudinal waves) or perpendicular (shear waves) to the direction of propagation. Pure mode waves can be propagated only in certain crystalline directions (Beyer and Letcher 1969). Shear waves are particularly useful for elastography methods (Berg et al. 2012) and a recent investigation has addressed the issue in 4D (Gennisson et al. 2015). However, in practice the waves that are used in traditional ultrasound imaging are longitudinal waves. In the following, the only considered direction of the perturbation, i.e. the direction of particle velocity vector $\mathbf{v}(t)$, is the one parallel to the direction of propagation.

I.A.4.b Speed of sound and non-linearity

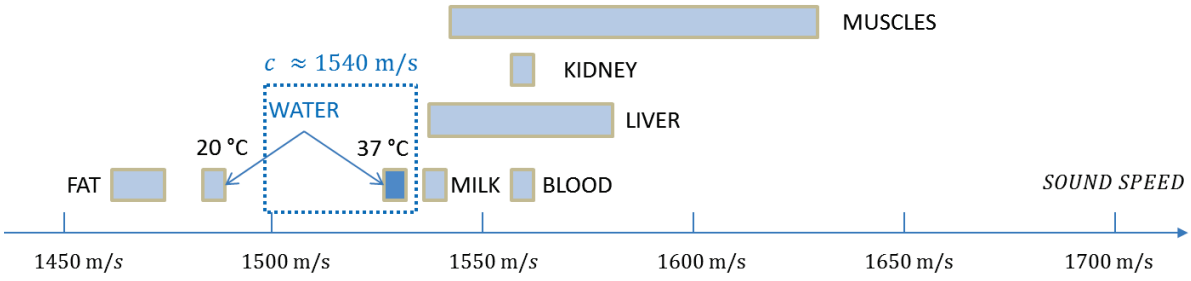


Figure 5 Speed of sound in different biological liquids and soft tissues. Personal figure based on (Vray et al. 2014) data source.

As presented in Figure 5 the speed of sounds depends on the medium in which it propagates and in the human body several kind of tissues do not present the same speed of sound (Vray et al. 2014). Moreover, the sound velocity $c(t)$ $[\mathrm{m.s^{-1}}]$ is non-linearly related to the particle velocity $v(t)$:

$$c(t) = c_0 + \left(1 + \frac{B}{2A}\right) v(t) \tag{11}$$

In tissues, the non-linear parameter B/A ranges from 5 to 11 but it can be increased up to 50 by the use of contrast agent (F. Varray et al. 2011; Wu and Tong 1998). It results that high pressure perturbations propagate faster than low pressure perturbations which distorts the waveform and generates harmonics. This property is useful for harmonic imaging but in practice, for standard imaging, the speed of sound in the human body is approximated by the constant $c = 1540$ m/s, which is the speed of sound in water at 37 °C.

I.A.4.c Range of frequencies and attenuation

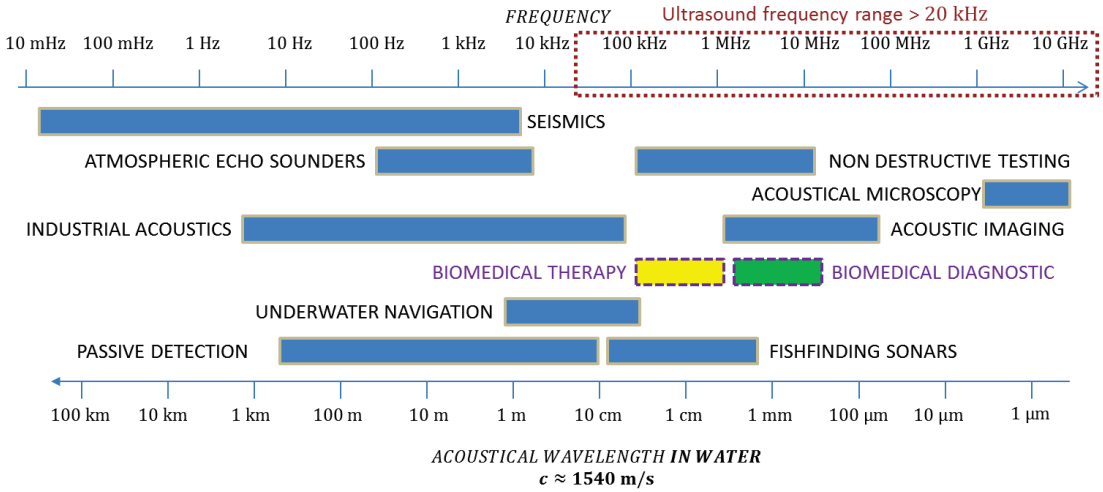


Figure 6 Fields of applications in function of the acoustical frequency (the wavelengths are in water medium).
The range of frequencies used in biomedical therapy is from ~100 kHz to few MHz.
The range of frequencies used in biomedical diagnostic is from few MHz to ~50 MHz.

As illustrated by Figure 6, a very large field of applications uses the acoustic waves (Vray et al. 2014). The frequency range of ultrasound starts above 20 kHz. The central frequency f_c of a given array is generally adjusted taking into account the required resolution (the size of the smallest details that will be distinguishable): the higher the central frequency f_c, the finest the resolution. Knowing the central frequency f_c [Hz] and the wave velocity c [m.s^{-1}], it is possible to define its wavelength $= f_c/c$ [m]. The range of frequencies that is used in diagnostic ultrasound imaging is between approximately 2.5 MHz (lower resolution) and 50 MHz (higher resolution). For therapy the range is from approximately 100 kHz to few MHz.

Another important parameter is the depth of exploration which brings a tradeoff because of the attenuation of the acoustic energy in depth. In fact, the attenuation increases linearly with the frequency and in biological tissues the "two-way" rate is of approximately 1 dB.cm^{-1}.MHz^{-1}. This limits the penetration depth if the central frequency is relatively high (approximately 50 dB loss at 5 cm with a 10 MHz transducer). The Time Gain Compensation (TGC) compensates the attenuation effect by enhancing the signals with a gain stronger for signals arriving from deep locations. The amplitude could be increased but there is a certain limit, not to break down the crystal, and to avoid damage in the patient's body. For instance for cardiac applications, the Food and Drug Administration (FDA) limits the spatial peak temporal average (Vray et al. 2014; Nelson et al. 2009) to 430 mW.cm^{-2}. In the following the attenuation effect is not considered, in other words the waves are supposed to propagate in medium without loss.

I.A.4.d Medium specific acoustic impedance: the origin of echoes

The medium in which the wave propagates is characterized by its specific acoustic impedance Z [kg.s^{-1}.m^{-2}] or in [Rayleigh], named by John William Strutt, Lord Rayleigh (1842–1919). In its general

form the acoustic impedance Z is a complex number defined as the ratio between the acoustic pressure[8] $\mathrm{PF}(\boldsymbol{r},t)$ and the oscillating particle velocity $\mathbf{v}(\boldsymbol{r},t)$ as expressed in the equation (12)

$$Z = \frac{\mathrm{PF}(\boldsymbol{r},t)}{\mathbf{v}(\boldsymbol{r},t)}, \tag{12}$$

In the specific case of monochromatic plane waves it remains only the real part as expressed in (13)

$$Z_{\mathrm{real}} = \rho c. \tag{13}$$

It is of particular interest highlighting that the origins of the *echoes* that are used in *echo*graphy is the acoustic impedance discontinuities that waves encounter during propagation. An echo is the reflection of a wave on an obstacle (presenting a difference of acoustic impedance compared to the propagation medium) so that it propagates back to the ultrasound probe.

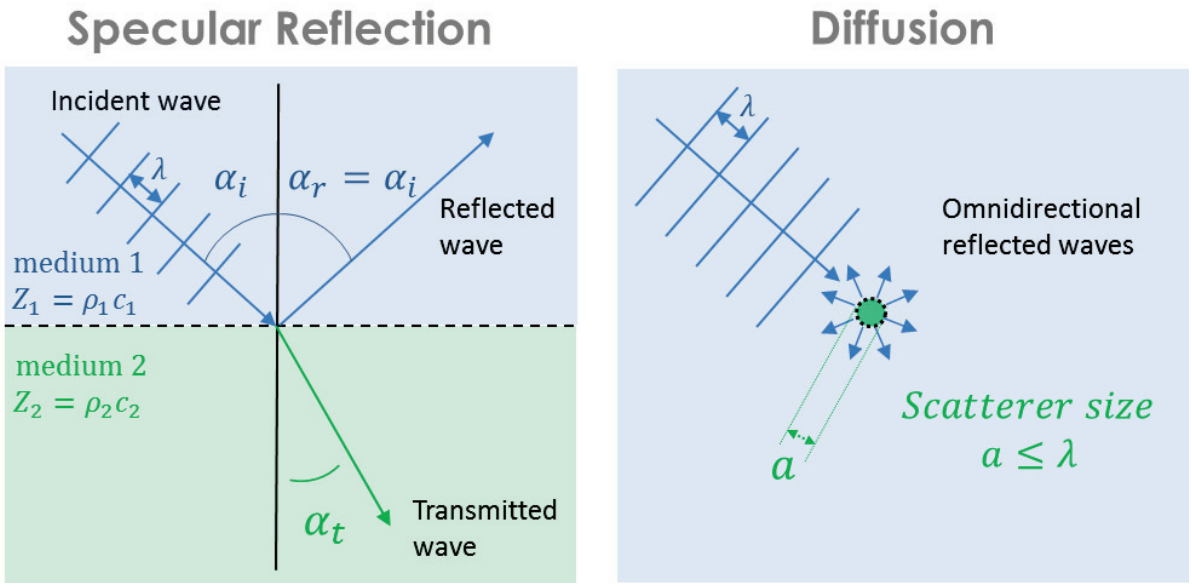


Figure 7 Specular reflection and transmission (left) of waves at the interface of two medium with different acoustic impedance. The incident wave is diffused (right) when the size of the encountered structure is smaller than the wavelength.

The type of reflection depends on the size of the structure encountered by the incident wave. A specular reflection occurs when the interface is wider than the wavelength λ (Figure 7 left). Otherwise, when the size of the scatterer is smaller than λ an omnidirectional reflection (diffusion) occurs (Figure 7 right).

In the case of specular reflection, an incident plane wave arrives with angle α_i (Figure 7) and the acoustic energy splits in two. One part of the wave energy is transmitted to the second medium (the transmitted wave) while the rest of the energy is reflected in the first medium (the reflected wave). In terms of energy, the transmission coefficients $\Upsilon_{\mathrm{transmit}}$ and the reflection coefficient $\Upsilon_{\mathrm{reflect}}$ are defined by:

[8] The acoustic pressure $\mathrm{PF}(\boldsymbol{r},t)$ is defined in I.B.1, equation (16)

$$\Upsilon_{\text{transmit}} = \frac{4\,Z_1 Z_2 \cos\alpha_i \cos\alpha_t}{(Z_2 \cos\alpha_i + Z_1 \cos\alpha_t)^2} \tag{14}$$

$$\Upsilon_{\text{reflect}} = \frac{(Z_2 \cos\alpha_i - Z_1 \cos\alpha_t)^2}{(Z_2 \cos\alpha_i + Z_1 \cos\alpha_t)^2} \tag{15}$$

with $\alpha_t = \arcsin\left(\frac{c_2}{c_1}\sin\alpha_i\right)$ (Snell-Descartes) and $\alpha_r (= \alpha_i)$ the transmission and reflection angles respectively (illustrated on Figure 7). In practice the vibration that takes place at the surface of the active elements would be strongly reflected by the air ($\Upsilon_{\text{reflect}} \approx 99\ \%$) so the combination of a quarter-wave impedance transformer[9] (matching layer located in the probe face) and the use of a specific gel (acoustic coupling between the ultrasound probe and the patient body) allows matching the acoustic impedances and facilitates the transmission of the acoustic energy.

I.B Beamforming: from waves to images

In passive imaging the ultrasound array only receives acoustic energy from the observed medium (the so-called "listening mode") which is amplified and converted into electrical signals (analog amplifiers and analog-to-digital A/D converters) and beamformed into an image. This passive imaging mode is used in both photo-acoustic imaging (Ningning 2014) and seismology (Gazdag and Sguazzero 1984). More often the transducers are used to both transmit and receive acoustic energy. The transmission is designated by TX (but no confusion should be made with previous section I.A.4.d) while the reception (RX) aims at recording the echoes from the potential obstacles present in the insonified medium.

I.B.1 Pressure field computation for any transducer configuration

During TX, the waves generated by all the transducers are propagating and the distribution of the pressure in the medium is called the Pressure Field (PF). Let the pressure field $\mathrm{PF}(R,\theta,\phi,t)$ $[\mathrm{kg.m^{-1}.s^{-2}}]$ or in $[\mathrm{Pa}] = [\mathrm{Pascal}]$ (named by Blaise Pascal (1623-1662)) be the difference of pressure evolution with the equilibrium pressure $\mathrm{PF}_0(R,\theta,\phi,t)$ in any pressure measurement point (PMP) located in (R,θ,ϕ), i.e. at position vector $\boldsymbol{r}$.

Evaluating experimentally the PF radiated by thousands of transducer array configurations would be very time consuming and too expensive (building a new array each time is impracticable). Numerical simulations are welcomed to evaluate the pressure field relatively quickly. The evaluation of the pressure field radiated by an array of transducers can be more or less realistic depending on the chosen acoustic radiation model. The more realistic the greedier in computation load. So usually a spherical wave radiating model, as expressed in (10), is adopted which means an active element is

[9] In practice multiple intermediate matching layers are placed in the probe face (Mills and Smith 2002; Seyed-Bolorforosh et al. 1997) to gradually change from the high impedance of the element (approximately 20-35 × 106 kg.s^{-1}.m^{-2}) to the low acoustic impedance of the human skin (approximately 2 × 106 kg. s^{-1}.m^{-2}) and water (approximately 1.5 × 106 kg. s^{-1}.m^{-2}) (Azhari 2010; L. S. Smith and Brisken 1980).

approximated to be a punctual omnidirectional source (located in the element center) transmitting at a single frequency. More complex model can take into account the spatial impulse response (SIR) of the elements (which depends on their size and shape) and the wideband characteristic of the transmitted wave (the signal has a certain bandwidth). Several programs (ultrasound simulators) have been developed: FIELD II at *Danmarks Tekniske Universitet* (Jensen and Svendsen 1992; Jensen 1996), FOCUS at *Michigan State University* (Kelly and McGough 2006), Ultrasim at *Universitetet i Oslo* (Sverre Holm 2001), Abersim© at *Norges teknisk-naturvitenskapelige universitet* (Varslot and Taraldsen 2005), DREAM at *Uppsala Universitet* (Piwakowski and Sbai 1999), CREANUIS at *Université de Lyon* (François Varray et al. 2013). All are available on the World Wide Web[10]. The first one available to the general public (hence the most famous) is FIELD II: it allows simulating the entire imaging system (including artificial phantoms) and it works in the temporal domain (wideband). However it does not take into account nonlinear propagation effects conversely to CREANUIS, FOCUS and Abersim©. FIELD II and DREAM are based on (Stepanishen 1971) where, using the Huygens-Fresnel's principle (named by Christiaan Huygens (1629-1695) and Augustin-Jean Fresnel (1788-1827)), the pressure field (PF) generated by an active surface A is computed as the integration of spherical wave contributions transmitted from each infinitesimal radiating surface dA located in $\boldsymbol{r_{dA}}$:

$$\mathrm{PF}(R,\theta,\phi,t) = \mathrm{PF}(\boldsymbol{r},t) = \rho \int_A \frac{1}{2\pi|\boldsymbol{r}-\boldsymbol{r_{dA}}|} \frac{\partial v_n(t-|\boldsymbol{r}-\boldsymbol{r_{dA}}|/c)}{\partial t}\, dA \tag{16}$$

where ρ is the density of the medium $[\mathrm{kg.m^{-3}}]$ and v_n the normal velocity $[\mathrm{m.s^{-1}}]$ of the elementary radiating surface dA.

Let us consider a group of N_e transducers with $k = 1..N_\mathrm{e}$. A weighting coefficient w_k and an individual delay τ_k (in $[\mathrm{s}]$) can be associated to each element and considering that the velocity is homogeneous over each active element surface A_k, the pressure field (PF) can be computed using the concept of spatial impulse response (Matrone, Quaglia, and Magenes 2010; Piwakowski and Sbai 1999; Stepanishen 1971):

$$\mathrm{PF}(R,\theta,\phi,t) = \rho \frac{\partial v_n(t)}{\partial t} * \mathrm{h}(\boldsymbol{r},t) \tag{17}$$

with $\mathrm{h}(\boldsymbol{r},t)$ is the spatial impulse response of the group of N_e active elements

$$\mathrm{h}(\boldsymbol{r},t) = \sum_{k=1}^{N_\mathrm{e}} w_k \frac{\delta(t-|\boldsymbol{r}-\boldsymbol{r_k}|/c-\tau_k)}{2\pi|\boldsymbol{r}-\boldsymbol{r_k}|} A_k \tag{18}$$

[10] FIELD II: http://field-ii.dk/
FOCUS: http://www.egr.msu.edu/~fultras-web/
Abersim©: http://www.ntnu.edu/isb/ultrasound/abersim/download
Ultrasim: http://www.mn.uio.no/ifi/english/research/groups/dsb/resources/software/ultrasim/
DREAM: http://www.signal.uu.se/Toolbox/dream/
CREANUIS: https://www.creatis.insa-lyon.fr/site/fr/CREANUIS.html

Summing the N_e individual contributions implies that interferences appear in the generated PF. It means that in some locations of the space the acoustic perturbation will be stronger than any individual wave because the majority of the transported energy is in phase, i.e., their contributions are added together; while in other places the perturbation will be cancelled because locally the summation is done on waves which are out of phase. The transmission strategies used in ultrasound imaging are based on the phenomenon of interferences which is managed by adjusting individually the moment when each element starts to transmit.

I.B.2 Transmission strategies

In phased array imaging the active aperture is made of several active elements that are joined together (an array) to produce an electronically controllable (by steering) acoustic beam. Various transmission strategies can shape the constant-phase wave front generated by a group of active elements by adjusting the individual weighting coefficients w_k and delays τ_k (Figure 8). The constant-phase wave front is delimited by the points of space where the perturbation is in phase. In particular, a high flexibility is achieved using the synthetic aperture strategy where each element is excited individually. More details about synthetic aperture can be found in (B.Y.S. Yiu, Tsang, and Yu 2011; Daher and Yen 2006; Lockwood, Talman, and Brunke 1998). Here only the main transmission strategies (focused, diverging and plane waves) along with beam steering and apodization concepts are presented. The complete review by (Szabo 2004) on transmission strategies (and much more on ultrasound imaging) can be recommended. More specifically, concepts and applications of diverging and plane waves can be found in (Kruizinga et al. 2012; Montaldo et al. 2009).

I.B.2.a Focused waves

When transmitting focused waves, the aim is to create a high acoustic energy concentration at focal point located in $\boldsymbol{r_f}$ by compensating the time of flight for each wave**.** To make all waves converge in phase at focal point $\boldsymbol{r_f}$, the individual delays τ_k are computed as follows:

$$\tau_k = \max_k(\tilde{\tau}_k) - \tilde{\tau}_k \tag{19}$$

with

$$\tilde{\tau}_k = \left|\boldsymbol{r_k} - \boldsymbol{r_f}\right|/c \tag{20}$$

where c $[\mathrm{m.s^{-1}}]$ is the propagation speed of the waves in the medium.

The lateral size δ_l (orthogonal to $\boldsymbol{r_f}$) and the axial size δ_a (parallel to $\boldsymbol{r_f}$) of the focal spot (defined as the – 6dB region) depend on the wavelength, the aperture size D (the dimension of the active surface) and the focal depth F (the distance to the focal point):

$$\delta_l = \frac{\lambda F}{D} \tag{21}$$

$$\delta_a = 7\lambda\left(\frac{F}{D}\right)^2 \tag{22}$$

It is possible to improve the image resolution by dynamically changing F throughout the desired field of view. Hence multi-foci are defined for a single image but this dynamic focusing technique requires as many transmissions as the number of focal points. In order to maintain the same resolution at each depth when dynamic focusing is performed, the F-number (F#), which is defined by the ratio F/D, must be kept constant (by activating more or less side elements when the depth changes). This is implemented by gradually deactivating lateral elements, i.e. reducing the aperture size, when the focal point gets closer to the transducer. Note that if the full width of the aperture is used all the time the resolution will get coarser with depth.

Since the aim is to create a source of intense acoustic energy at focal point $\boldsymbol{r_f}$, the act of focusing can be seen as the time-reversal process (Fink 1992) of the acoustic energy received from a source that would be located at $\boldsymbol{r_f}$. It is noteworthy to mention that, compared to the reception step (where dynamic focalization is possible), in transmission the delays τ_k must be updated and a new transmission is required each time the focal point is moved. A fully focused imaging approach can be very time consuming which can reduce the frame rate to a few Hz, while other transmission strategies such as diverging waves or plane waves enable ultrafast imaging (hundreds and even thousands of frames per second).

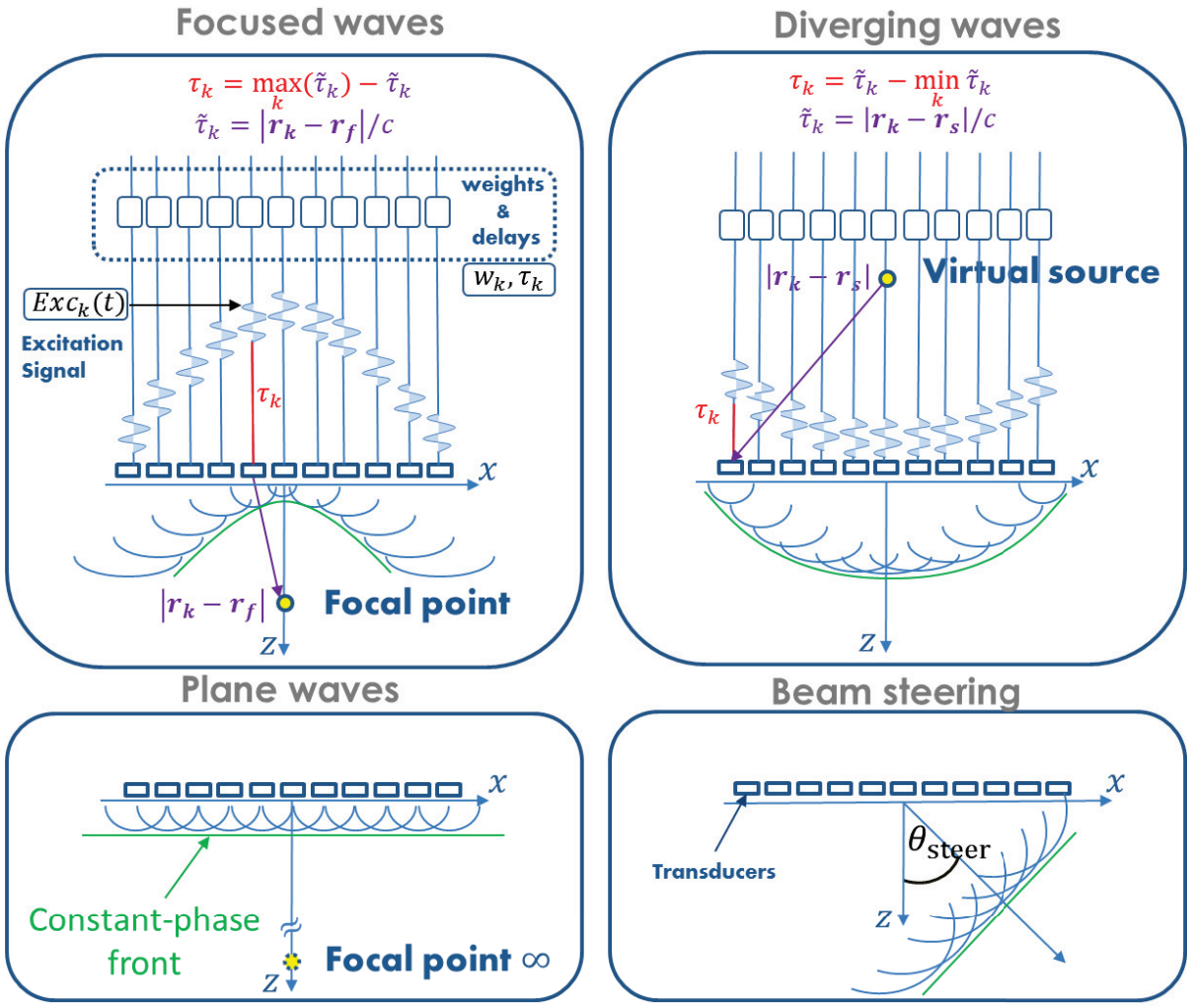


Figure 8 Illustration of the main transmission strategies. Focused waves (top-left) converging to the focal point. Diverging waves (top-right) are propagating the wave front created by a virtual source loacted behind the transducer. A plane constant-phase front is obtained by setting the same delay for all the transducers (bottom-left.) Plane waves are obtained by setting the focal point at infinite distance. The beam steering (bottom-right) corresponds to the wave front orientation by adjusting the indivudual delays τ_k.

I.B.2.b Beam steering

Steering in transmission consists in changing the wave front direction by adjusting the individual delays τ_k so that the wave front propagates toward the steering direction (given by angle θ_{steer} on Figure 8 and Figure 9). This technique is usually combined with the focused wave transmission in order to scan the medium sequentially with the transmitted beam. Usually the delays are applied so that the focal point is located at focal depth F on the steering direction given by the steering angle θ_{steer} (Figure 9).

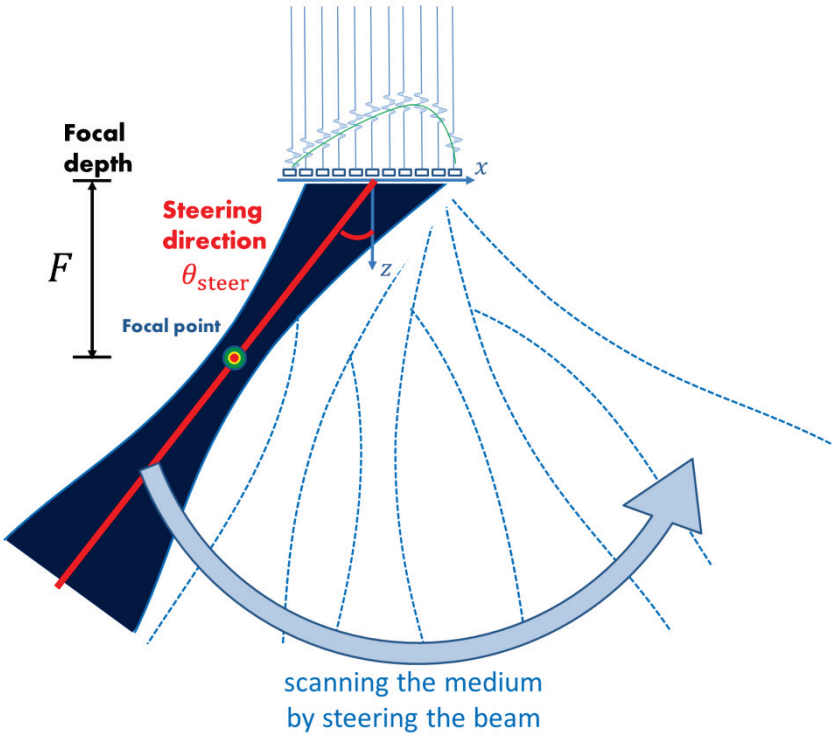


Figure 9 Illustration of how a medium is scanned by steering the acoustic beam when used focused waves transmission strategy.

As described in I.A.4.d, the incident angle of the wave changes the reflection coefficient. The beam steering allows scanning the field-of-view with different wave front orientation which is exploited to compound information given by waves with different incident angles (I.B.2.e).

I.B.2.c Diverging waves

When transmitting diverging waves a virtual source is located in $\boldsymbol{r_s}$ behind ($z < 0$) the transducer and the delays τ_k are computed as

$$\tau_k = \tilde{\tau}_k - \min_k(\tilde{\tau}_k) \tag{23}$$

with

$$\tilde{\tau}_k = |\boldsymbol{r_k} - \boldsymbol{r_s}|/c \tag{24}$$

The individual transducers transmit when they would be reached by the wave front created by a virtual source transmitting a spherical wave in $\boldsymbol{r_s}$. The advantage of this transmission technique is that a large entire field-of-view is insonified at each transmission. However, because the acoustic

energy is spread over the entire field-of-view, little energy reaches each region and the intensity of the echoes is drastically reduced. Compounding techniques allows compensating for this effect by repeating several transmissions (I.B.2.e). Note that the virtual source can also be situated in front of the transducer. Delays must then be adapted.

I.B.2.d Plane waves

The plane wave can be seen as an extreme case of focused waves (and diverging waves) by setting the focal point (virtual source) at infinite distance from the transducers.

With infinite distance to focal point (focused waves)

$$\lim_{|\boldsymbol{r_f}|\to\infty} \tilde{\tau}_k = \infty \tag{25}$$

which gives

$$\tau_k = \max_k(\tilde{\tau}_k) - \tilde{\tau}_k \to 0 \tag{26}$$

The same limit is obtained considering the virtual source (diverging waves) at infinite distance behind the transducer array.

A plane constant-phase front is obtained by setting the same delay for all the transducers and in practice the delay is set to zero for all the elements (no superfluous delay is desired in high-frame rate imaging). Plane wave and divergin wave transmission strategies both enable very high frame rates (thousands of frames per second) thanks to a full insonification of the medium at each ultrasound transmission.

I.B.2.e Compounding waves

Compounding techniques allows enhancing the resolution and contrast in the images (very low for a single transmission of diverging or plane wave) by repeating several transmissions (muli-angle techniques use different steering angles for each transmission) and combining them together. Compounding technique is both used for plane waves (Montaldo et al. 2009; Tanter et al. 2002; Jespersen, Wilhjelm, and Sillesen 1998) and diverging waves (Jean Provost et al. 2014; Papadacci et al. 2014; Hasegawa and Kanai 2011).

I.B.2.f Individual weights for apodization windows

Apodization designates the weighting of the active surface of the array with a specific window (a Blackman or a Hanning window for instance). The impact of the weighting/apodization windows is usually illustrated considering the transmission of focused waves: it is used in order to control the size and shape of the focal spot and to reduce the undesired acoustic energy out of the focal spot. The apodization window shapes the Beam Pattern (BP) of the active elements array on which the radiating performance can be evaluated as described in the following section.

I.B.3 Beam patterns

The quality of the acoustic radiation by a group of transducers is evaluated on the radiated Beam Pattern (BP). It represents the spatial distribution of the acoustic energy broadcasted (in transmission mode) by the active aperture. The procedure to plot a Beam Pattern (BP) is illustrated on Figure 10: the Pressure Field (PF) evolution is measured above the array by surrounding Pressure Measurement Points (PMP); the maximum (along time) of each PF signal is normalized, log-compressed and finally plotted against the θ —angle of the associated PMP.

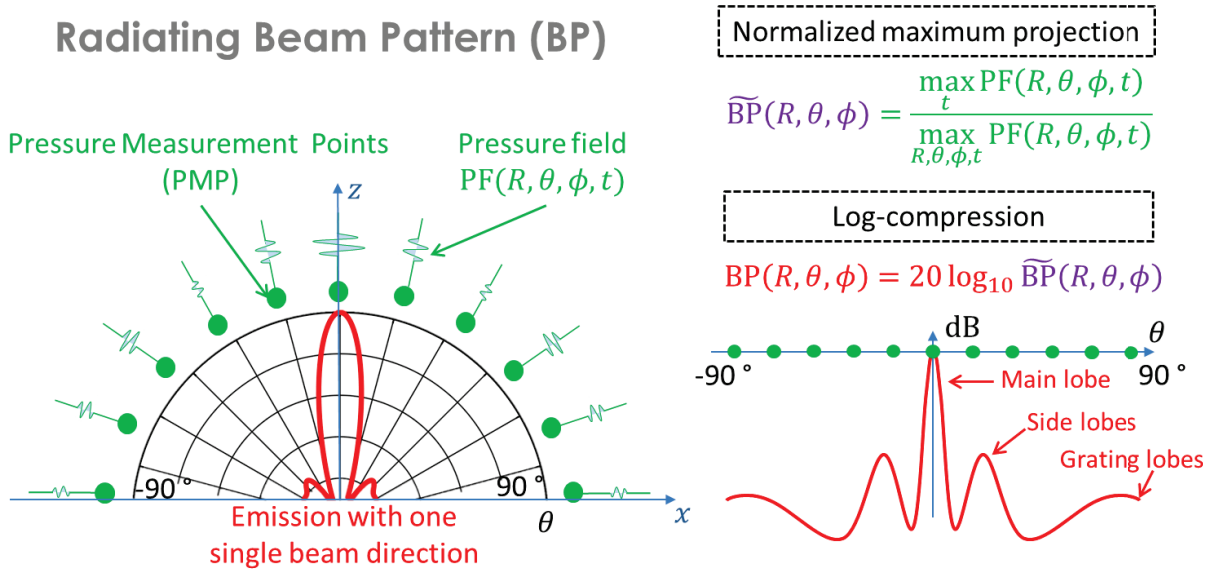


Figure 10 The radiating Beam Pattern (BP) is computed from the Pressure Field evaluation in several Pressure Measurement Points (PMP). The maximum (along time) of each pressure signal is normalized, log-compressed and finally projected against the PMP θ-angle.

The dual analysis in listening mode (transmitting with a source sequentially located at the positions of the PMP and measuring the received energy with the array for each position of the source) corresponds to the spatial sensitivity of the array. The reciprocity theorem[11] implies that, considering the same array in transmission (TX) and in reception (RX), the sensing capabilities in a particular region of space are the same as the capabilities to send the energy in that same particular region during transmission. In other words, $\mathrm{h_{TX}}(\boldsymbol{r},t)$, the spatial impulse response in (TX) defined in (18), is the same as $\mathrm{h_{TX}}(\boldsymbol{r},t)$, the spatial impulse response in (RX):

$$\mathrm{h_{TX}}(\boldsymbol{r},t) = \mathrm{h_{RX}}(\boldsymbol{r},t) \tag{27}$$

The Point Spread Function (PSF) of an array generating an initial pressure $p_0(t)$ is defined as

$$\mathrm{PSF} = p_0(t) * \mathrm{h_{TX}}(\boldsymbol{r},t) * \mathrm{h_{RX}}(\boldsymbol{r},t) \tag{28}$$

[11] This theorem states that in the acoustic field due to a sound source at point A, the sound pressure received at any other point B is the same as that which would be produced at A if the source were placed at B, and that this can be generalized for multiple sources and receivers.

so that the resulting pressure field response received from a set of N_{scat} scatterers $s(\boldsymbol{r_i}, t)$ located in $\boldsymbol{r_1} \ldots \boldsymbol{r_{N_{\text{scat}}}}$ is:

$$p(\boldsymbol{r}, t) = \text{PSF} * \sum_{i=1}^{N_{\text{scat}}} s(\boldsymbol{r_i}, t) \tag{29}$$

and $p(\boldsymbol{r}, t)$ is called the pulse-echo signal. Again here, all the individual scatterer responses are assumed to be linear.

Several studies (Sciallero and Trucco 2015; Diarra et al. 2013; Tekes, Karaman, and Degertekin 2011; Choe, Oralkan, and Khuri-Yakub 2010; Austeng and Holm 2002; Weber et al. 1994) are based on the pulse-echo (two way) beam pattern. Analyzing the pulse-echo beam pattern is necessary when two different arrays are considered for TX and RX. If the same elements are used in both TX and RX then (27) can be applied and an analysis restricted on the one-way BP in transmission can be performed.

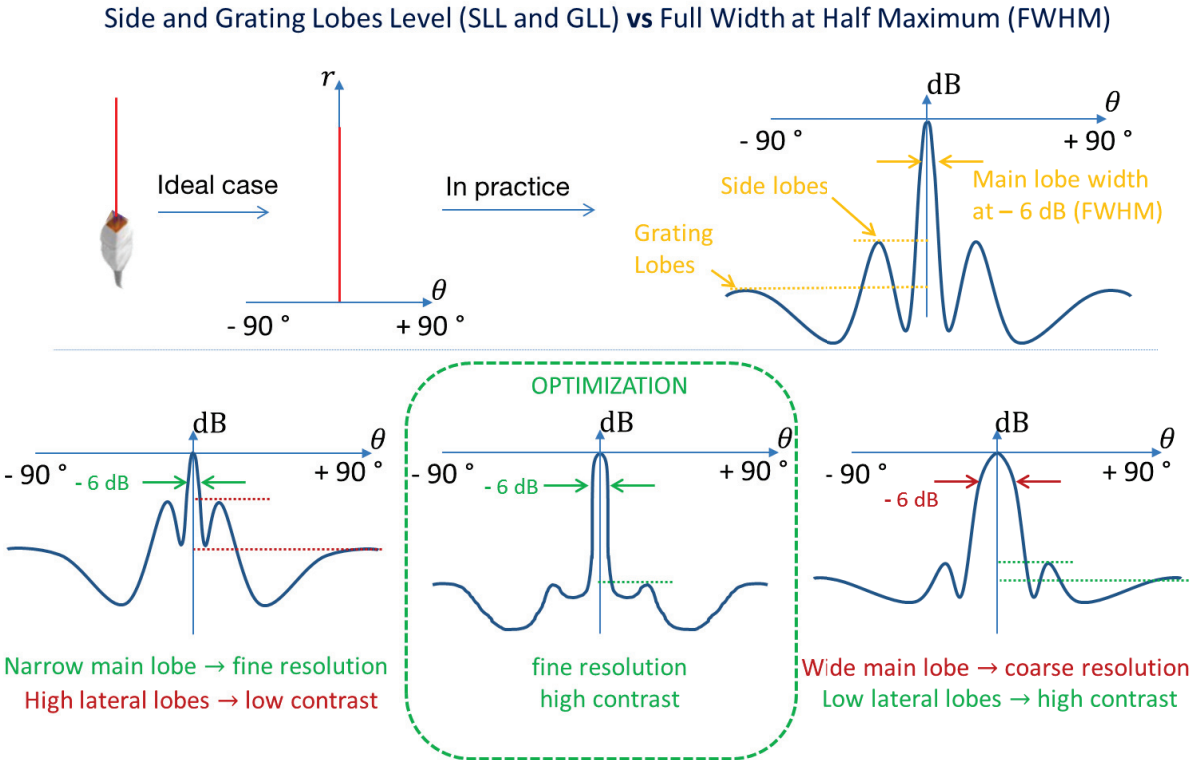


Figure 11 Illustration of the tradeoff between lateral lobes level and main lobe width on the radiated beam pattern.

An ideal beam pattern when transmitting focused waves would be a Dirac of energy in the steering direction of the beam (Figure 11). But in practice there are side lobes, grating lobes and the main lobe has a certain width. The latter has an impact on the image resolution. The lateral lobes impact on the image contrast. A set of acoustic receivers has to trade the available information content between resolution (measured by e.g. the main lobe width at - 6 dB, designated as Full Width Half Maximum - FWHM) and contrast (measured by e.g. Side and Grating Lobe Level, SLL and GLL) of the final image. Because of the direct impact of the BP on the image quality, it is of particular interest to define what the excepted characteristics of the beam pattern are (depending on the application) and what guidelines should be followed to produce ultrasound images of good quality.

As a general trend, the main lobe width is linked with the aperture size: the wider the aperture size the finest the main lobe width. The side lobes are linked to the apodization (weighting window) of the aperture. To understand the influence of the aperture apodization on the BP behavior, the latter can be approximated (under continuous wave –CW- conditions and in the far-field) as the spatial Fourier transform of the active aperture (Brandwood 2012; Brunke and Lockwood 1997; S. W. Smith, Pavy, and von Ramm 1991). The rectangular weighting window produces a sinc (cardinal sine) function in the BP (the larger the spatial window the thinner the FWHM on the BP). On the contrary a punctual source (Dirac of space sampling) radiates a spherical wave with homogeneous front wave energy for any direction. The grating lobes are visible when a regular gridded array of elements has inter-element distance (the pitch d) greater than half the wavelength of the lowest frequency present in the transmitted signal. The space sampling condition $d < \frac{\lambda}{2}$ must be respected in order to avoid the apparition of grating lobes (aliasing effect) which is the consequence of the under sampled surface of the aperture. On the contrary, when the space sampling of the aperture is aperiodic (no periodical pattern) the constraint of having a maximum $\frac{\lambda}{2}$ inter-element distance is relaxed (Diarra et al. 2013; Austeng and Holm 2002). To better understand the BP impact on the image quality the next section details how images are built from the received echoes.

I.B.4 Image reconstruction

The conventional time domain Delay and Sum (DAS) beamforming technique is illustrated on Figure 12. It starts by producing post-beamforming Radio-Frequency (RF) signals $\mathrm{RF}_{\mathrm{post}}(\mathrm{t})$ from the pre-beamforming RF signals (raw data) $\mathrm{RF}_k(t)$ received by the set of N_e elements. Then post-beamforming RF signals are computed with DAS which consists in the summation of the delayed and weighted raw data with individual delays τ_k and weighting coefficient w_k:

$$\mathrm{RF}_{\mathrm{post}}(\mathrm{t}) = \sum_{k=1}^{N_\mathrm{e}} w_k \, \mathrm{RF}_k(t - \tau_k) \tag{30}$$

The individual delays τ_k are computed to focalize the beam, i.e. to compensate the propagation duration (times of flight) between the reconstructed area and the individual sensors:

$$\tau_k = \max_k(\tilde{\tau}_k) - \tilde{\tau}_k \tag{31}$$

with

$$\tilde{\tau}_k = |\boldsymbol{r_k} - \boldsymbol{r_s}|/c \tag{32}$$

where $\boldsymbol{r_s}$ and $\boldsymbol{r_k}$ are the positions of the reconstructed area and the k −th element respectively.

All post-beamforming RF signals are stored side-by-side to form the RF image. The envelope of the RF image is computed using the Hilbert transform in order to cancel the oscillations (induced by the excitation signal applied on the transducers) in the PSF response. Finally to enhance small signal values, the B-mode image is obtained by log-compression. The impact of the pulse-echo BP (in this case the active surface acts in both TX and RX) can be retrieved on the profile of a point scatterer B-mode image (Figure 12, right). The point scatterer does not appear as a single white spot on the B-mode image because of the BP side lobes. When the image pixels are surrounding the scatterer are reconstructed, they are polluted by the echoed energy received by the lateral lobes. More sophisticated beamforming techniques aim at reducing those artefacts and in particular adaptive beamforming investigations (Nilsen and Hafizovic 2009; Synnevag, Austeng, and Holm 2007; Wang,

Li, and Wu 2005) where an active control of the weights w_k associated to each active element is performed depending on the observed data itself.

I.B.4.a Bottleneck of the data amount and DAS complexity

The computational complexity, i.e. the number of multiply-and-accumulate (MAC) operations of DAS in time is domain $N_s(N_e)^2$ where N_s designates the number of samples in a post-beamforming RF signal. The complexity can be reduced to $N_s N_e \log(N_e)$ by computing the DAS beamforming using Fourier-based methods such as frequency remapping (Cheng and Lu 2006; Lu 1997), f-k migration (Garcia et al. 2013), Ultrasound Fourier Slice Imaging (UFSI) (Bernard et al. 2014; Zhang et al. 2015) or Non-Uniform Fast Fourier Transform (NUFFT) (Chi, Li, and Li 2015; Kruizinga et al. 2012). In (Mucci 1984) the hardware implementations of beamforming techniques are described and the authors highlights that the disadvantages raised by a direct implementation of a DAS beamformer are mainly the required high sampling rate, the large amount of memory and huge cable bandwidth (to transfer high data rates). Therefore, directly applying a DAS beamforming on a full array still represents a technological barrier to be provided to general public. Several 3D ultrasonic probe design techniques and strategies have addressed this issue of acquiring 3D ultrasound data in real time. Some of them are already commercially available while others are restricted to the research field as detailed in section I.C.4. One can refer to (Prager et al. 2010) for a complete review about 3D ultrasound imaging.

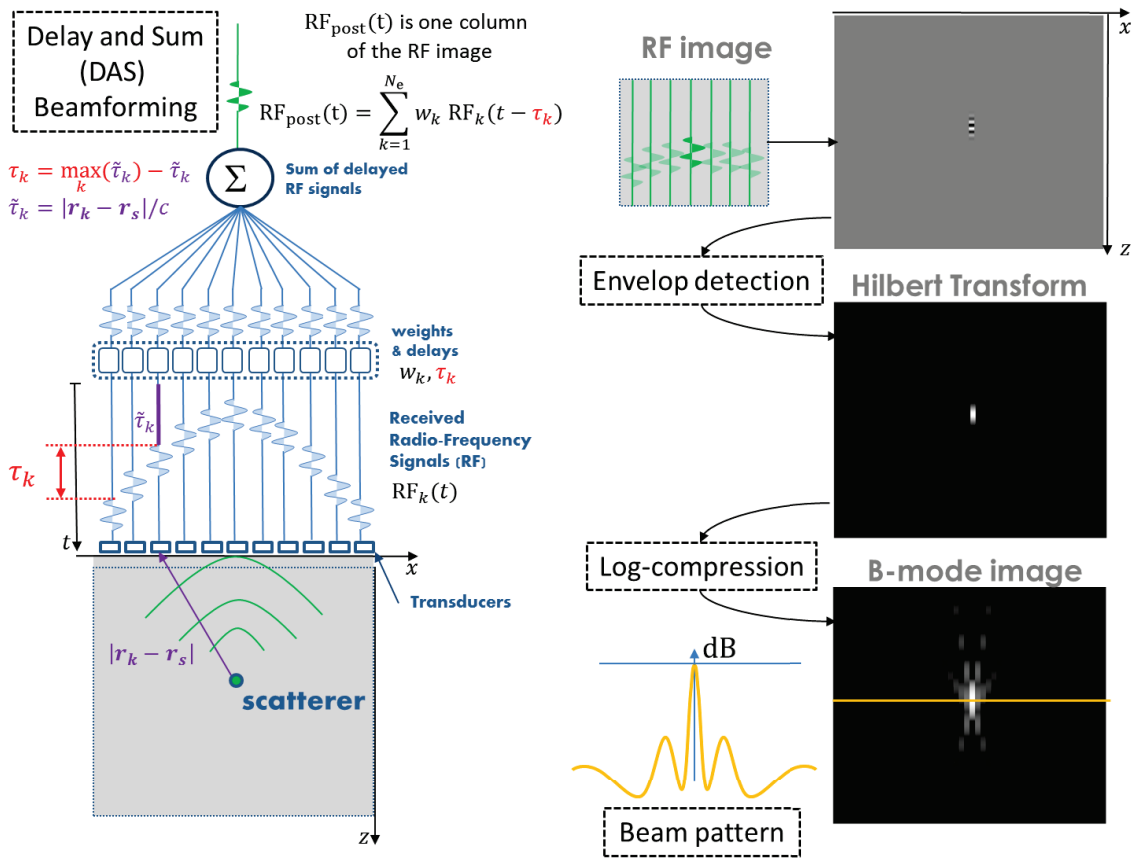


Figure 12 Illustration of the Delays and Sum (DAS) beamforming technique used to produce B-mode images with the echoes received from a scatter in the observed medium.

I.C Interest and current limits of 3D+t (4D) ultrasound imaging

I.C.1 Existing applications of 3D+t (4D) ultrasound imaging

Few imaging systems can be simultaneously defined portable, non-ionizing, relatively inexpensive, and fully interactive thanks to real-time operation. All of these features characterize the two-dimensional ultrasound (2D-US) scanners, which are widely used in clinical environment for the diagnosis of several diseases. Even if highly successful, 2D-US is inherently limited to display 2D slices of the three-dimensional (3D) reality of organs, thus forcing the doctors to mentally reconstruct the observed volume. This also increases the diagnostic variability (operator dependent) because volumetric dimensions (organs or tumors) are estimated by correlating measurements done in distinct planes; this inevitably limits the estimation accuracy. Again, conventional 2D imaging is not convenient for monitoring therapeutic procedure or tracking chirurgical tools since the 2D imaging plane may not fully contained the site of interest (tools like biopsy needles may cross the imaging plane for instance).

This lack of volumetric information has motivated many investigations in both academic and industrial research departments (Fenster, Downey, and Cardinal 2001; Nelson and Pretorius 1998). 3D real-time US imaging (Prager et al. 2010) would allow accessing arbitrary tissue slices (Stetten et al. 1998), assessing 3D mechanical properties of tissues (Deprez et al. 2009; Deffieux et al. 2008), measuring 3D vector blood flow (Billy Y. S. Yiu, Lai, and Yu 2014), assisting surgery (e.g., for biopsy needle tracking) (Nadeau et al. 2015; Zhao et al. 2014), or High Intensity Focused Ultrasound (HIFU) monitoring (Lindseth et al. 2013; Unsgaard et al. 2005). In particular, real-time 3D echocardiography is one of the most challenging US applications (Jean Provost et al. 2014; Sugeng et al. 2006; Light et al. 2001; Stetten et al. 1998) because it requires very high spatio-temporal resolution, i.e. high volume rates while maintaining the precision and robustness in the spatial domain.

I.C.2 Arrays design evolution

Before the development of electronic steering (O. T. V. Ramm and Smith 1983), single-element transducers were manually or mechanically translated to create 2D images. The same trend has taken place in the passage from 2D to 3D imaging, which actually started with position-tracked (free-hand) scanning (Hughes et al. 1996; Rivera et al. 1994; Levine et al. 1989; Moritz et al. 1983) or motorized 1D arrays that were translated (Dabrowski et al. 2001; Guo and Fenster 1996), rotated (Andresen 2006; Tong et al. 1996; Downey et al. 1996), or tilted (Gilja et al. 1995; Delabays et al. 1995) to scan a volume (mechanical scanning).

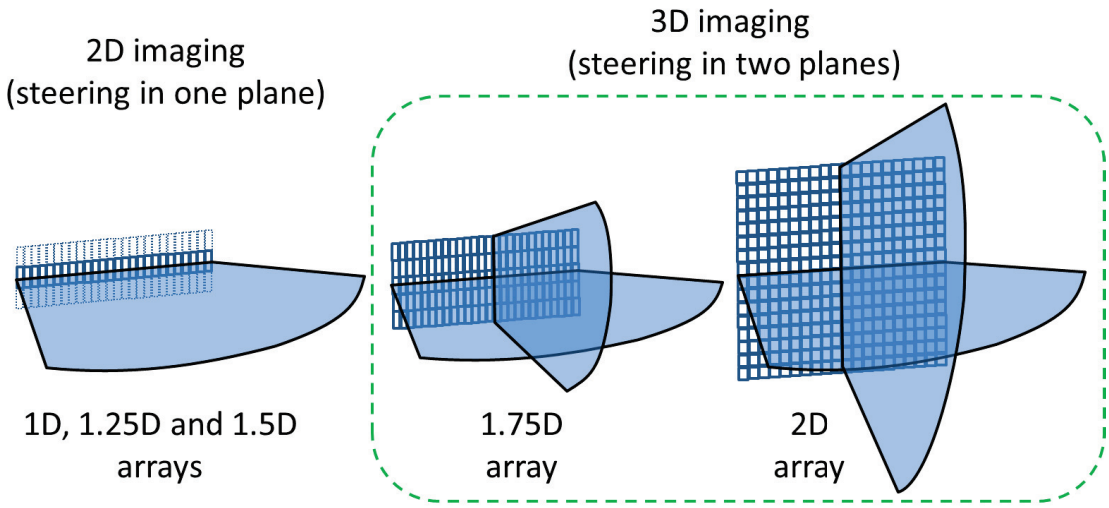


Figure 13 From 2D imaging to 3D imaging using the electronic steering capabilities of 2D arrays.

The evolution from 1D to 2D arrays happened through several intermediate designs described in (Wildes et al. 1997; Fernandez et al. 2003): the 1.25 D, 1.5 D and 1.75 D arrays (Figure 13) successively improved the imaging capabilities up to the full electronic apodization, focusing and steering capabilities of 2D arrays. Just recently, 3D imaging was made more feasible by the introduction of 2D array probes, which are able to steer US waves in both directions (elevation and azimuthal) (Prager et al. 2010; Light et al. 2001; Rasmussen et al. 2015; Christiansen et al. 2015; Jean Provost et al. 2014). In order to run the array with highest flexibility, one channel of the scanner should be continuously connected to one active element, so that each transmission signal, transmit/receive timing and apodization can be independently controlled to implement specific imaging sequences.

I.C.3 A technical challenge for 3D+t ultrasound imaging

I.C.3.a Full array limitations

Unfortunately, in full 2D arrays, the need of maintaining the pitch smaller than half the wavelength, λ, leads to a large number (up to thousands) of small-sized elements. Connecting several thousands of elements in a one-element-to-one-channel (one-to-one) design increases the electronic circuit complexity and makes the connection probe cable unsuitable to clinical practice. For example, let us assume a 20 mm aperture (e.g., for parasternal cardiac imaging) and a central frequency of 3 MHz. The 513 $\mu\mathrm{m}$ ($\lambda/2$) pitch condition (for a speed of sound=1540 m/s) leads to a 40x40 = 1600 elements array. A possible one-to-one design would also be very demanding in terms of data transfer rate (1600 elements produce ≈1500 Gb/s with 12-bit ADC sampling at 80 MHz), data storing capability (almost 2 TB for each second of acquisition), and computational load (I.B.4.a).

I.C.3.b Volume data reconstruction load

The computational reduction is particularly important when considering volumetric data reconstruction (Figure 14): the computational load for a volume of 128x128 lines, each of 2048 samples, requires 54 Giga multiply-and-accumulate (MAC) operations with DAS reconstruction.

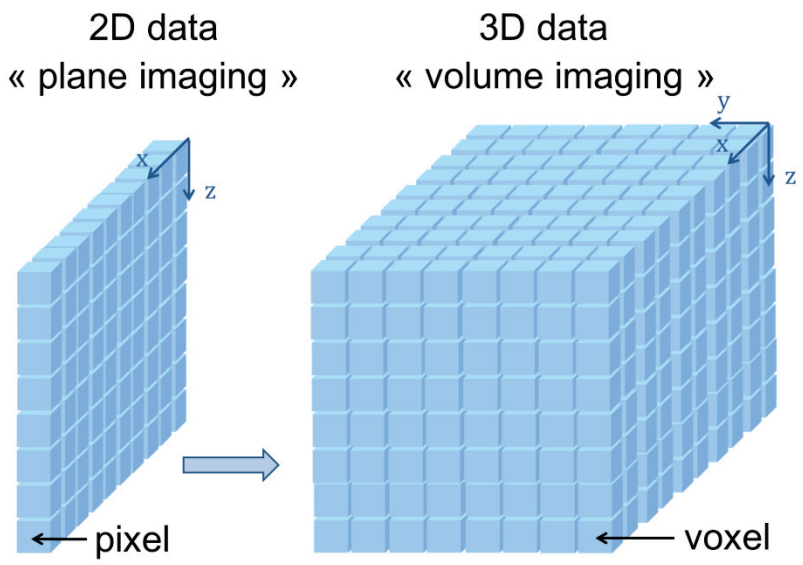


Figure 14 The amount of data to be acquired and beamformed when switching from 2D to 3D imaging is increased drastically which raises technical challenges.

Several technical solutions have made 4D ultrasound imaging possible (I.C.4) but it is still a technological challenge to acquire a full myocardium volume during a single-heartbeat. Today such acquisitions are gated over several cardiac cycles to avoid pulsatility motion (not suitable in case of arrhythmias) and under apnea to avoid breathing motion (contra-indicated for some patients).

I.C.4 Existing probe designs for 3D imaging

An elegant solution to reduce the cable size and the amount of data to be transferred to and processed by the scanner is represented by the micro-beamforming technique (Kortbek, Jensen, and Gammelmark 2013; Matrone et al. 2014; Fisher et al. 2005; Wygant et al. 2009). This allows maintaining thousands of active elements while sending only a reduced number of signals through the probe cable. This is possible thanks to the implementation of a first beamforming step in the probe handle (Figure 15), which delays and sums the signals related to a group of elements (called sub-aperture).

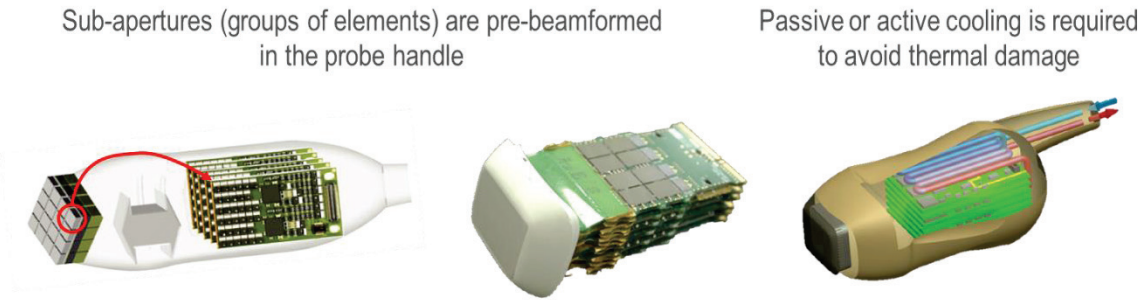


Figure 15 Illustration of the hardware located in the probe handle to perform a first beamforming stage in the probe head (micro-beamforming) (original images http://www.mehradco.com and https://www.healthcare.siemens.com)

An available commercial solution combines the 4Z1c matrix array transducer with the Acuson SC2000 scanner[12] (Siemens Healthcare, Ultrasound Business Unit, Moutain View, CA)(Barnes, Bolorforosh, and Phelps 2005): the 4Z1c probe integrates six electronic boards on which more than 120 custom ASIC are performing a partial-beamforming step, improving the electrical impedance mismatch and reducing the number of cables connecting the transducer to the SC2000 scanner. The Acuson SC2000 system performs a second beamforming stage and process the obtained image for display. The probe handle also integrates an active cooling technology to draw heat away from the transducer in order to maximize the information rate which in general is linked with the amount of transmitted energy while staying under regulatory limits avoiding an overheating of the skin. Another commercial solution, the X6-1 xMatrix probe with the iE33 Echocardiography system[13] (Koninklijke Philips Electronics N.V., Amsterdam, Netherlands) (B. J. Savord 2012; Robinson et al. 2003; B. Savord and Solomon 2003; B. J. Savord and Thiele 1999) also integrates a pre-beamforming stage in the probe handle. The 3V probe with the Vivid 7 dimension scanner[14] (General Electric Company, Fairfield, Connecticut, U.S.) (Thomenius, Wodnicki, and Li 2010) also integrated a pre-beamforming stage in the probe head but the new generation of General Electric scanners are based on the cSound™ hardware architecture[15] which could be structured on a fully digital beamformer similar to the very exciting one described in (Hager, Bartolini, and Benini 2016). The micro-beamforming technique allows the scanner to control a reduced number of channels but involves the expensive development of Application Specific Integrated Circuits (ASIC) and limits the flexibility in the image reconstruction process.

Row-column addressing (Rasmussen et al. 2015; Christiansen et al. 2015; K. Chen 2014; Logan et al. 2011) and channel multiplexing techniques (B. Savord and Solomon 2003; O. T. von Ramm and Smith 1987) are also promising techniques, but they do not allow continuously running the full array during transmission and reception since only part of the elements can be connected to the front-end of the scanner at each time. Performing systems approaching a full flexibility (continuous and simultaneous sampling of thousands of channels) are restricted to few research laboratories: 1024-channels and 512-channels are available in TX and RX respectively with the combination of four 256-transmit/128-receive channels units of Aixplorer systems (Supersonic Imagine, Aix-en-Provence, France) at Institut Langevin in Paris, France (J. Provost et al. 2015) and the Synthetic Aperture real-time Ultrasound System (SARUS) offers 1024 independent channels (256 channels can be processed in real time) at the *Danmarks Tekniske Universitet* in Lyngby (Jensen et al. 2013).

To sum up, as described in I.B.4.a and I.C.3, the combination of a huge amount of active elements and the desire to reconstruct large volume images raise a bottleneck for standard ultrasound imaging architecture. Few very flexible experimental research ultrasound platforms and few high-end commercial probe designs have successfully enabled 4D imaging capabilities. The research ultrasound platforms need to be fully flexible so the extreme information rate and computation power requirements have been tackled by exploiting huge hardware infrastructure. In main commercial solutions, these limitations have been tackled by implementing active probes (pre-

[12] More information at https://www.healthcare.siemens.com (visited July 2016)
[13] More information at http://www.usa.philips.com (visited July 2016)
[14] More information at http://www.mehradco.com (visited July 2016)
[15] More information at http://www3.gehealthcare.com (visited July 2016)

beamforming the raw data in the probe handle) at the expense of a decreased the flexibility in the volume reconstruction. A countercurrent approach is represented by sparse array designs where the tendency to use highly integrated electronic circuits to yield high performance is reversed by directly reducing the number of active elements that need to be controlled by the scanner: 3D ultrasound imaging can be performed keeping the full flexibility of a one-to-one design without increasing the circuit complexity. In the next section I.D, the state-of-the-art and the limitations of 2D sparse array designs are presented.

I.D 2D sparse array optimization methods

I.D.1 State-of-the-Art and limitations

The 2D sparse array design consists in directly reducing the number of active elements that need to be connected and controlled by the scanner, according to the sparse array methodology (S. Holm et al. 2001). The active elements configuration emerging out of this reduction must, of course, fit the desired imaging features in terms of resolution and contrast over the entire field-of-view. These features are directly bound by the 2D array beam pattern (BP), whose main lobe width (full width at half maximum - FWHM at - 6 dB), side lobe level (SLL) and grating lobe level (GLL) affect the 2D image quality. In literature, two main approaches have been investigated to find the smartest "sparse" configuration of active elements: the first one corresponds to deterministic designs (Table I) and the second one corresponds to stochastic designs (Table II). The lists of reviewed publications for the two groups are the following:

- Deterministic designs (Table I) (Ramalli et al. 2015; Ramadas et al. 2014; Tekes, Karaman, and Degertekin 2011; Martínez-Graullera et al. 2010; Karaman et al. 2009; Austeng and Holm 2002; Schwartz and Steinberg 1998; Brunke and Lockwood 1997; Lockwood and Foster 1996; S. W. Smith, Pavy, and von Ramm 1991)
- Stochastic designs requiring optimization (Table II) (Sciallero and Trucco 2015; Diarra et al. 2013; Choe, Oralkan, and Khuri-Yakub 2010; P. Chen et al. 2010; Trucco 1999; Austeng et al. 1997; S. Holm et al. 2001; S. Holm, Elgetun, and Dahl 1997; S. Holm and Elgetun 1995; Davidsen, Jensen, and Smith 1994; Weber et al. 1994; Boni, Richard, and Barbarossa 1994; Turnbull and Foster 1991).

TABLE I FEATURES COMPARISON BETWEEN THE PRINCIPAL DETERMINISTIC 2D ARRAY DESIGNS IN THE LITERATURE

Features / Works	On-grid / Out-of-grid	Wideband simulations	Shape sensitive	One-way BP / Two-way BP	Multi-depth	Number of elements known in advance	Symmetry free / Fabrication constraints	TX elements = RX elements	No use of apodization	optimization	online BP computation (not pre-computed)	No a priori on SLL
Smith, 1991	✓ / ×	×	✓	× / ✓	×	✓	× / ✓	×	×	×		
Lockwood, 1996	✓ / ×	✓	✓	× / ✓	×	✓	× / ✓	×	×	×		
Brunke, 1997	✓ / ×	×	✓	× / ✓	×	×	× / ✓	×	×	×		
Schwartz, 1998	✓ / ×	✓	×	✓ / ✓	✓	✓	× / ×	×	×	×		
Austeng, 2002	✓ / ×	×	×	× / ✓	×	×	× / ×	×	✓	×		
Karaman, 2009	✓ / ×	✓	×	× / ✓	✓	✓	× / ✓	×	✓	×		
Martínez-Graullera, 2010	× / ✓	✓	×	× / ✓	×	✓	× / ✓	×	✓	×		
Tekes, 2011	× / ✓	✓	×	× / ✓	×	✓	× / ✓	×	✓	✓	×	✓
Ramadas, 2014	× / ✓	×	×	✓ / ×	✓	✓	× / ×	✓	✓	×		
Ramalli, 2015	× / ✓	✓	✓	✓ / ×	✓	✓	× / ✓	✓	✓	×		

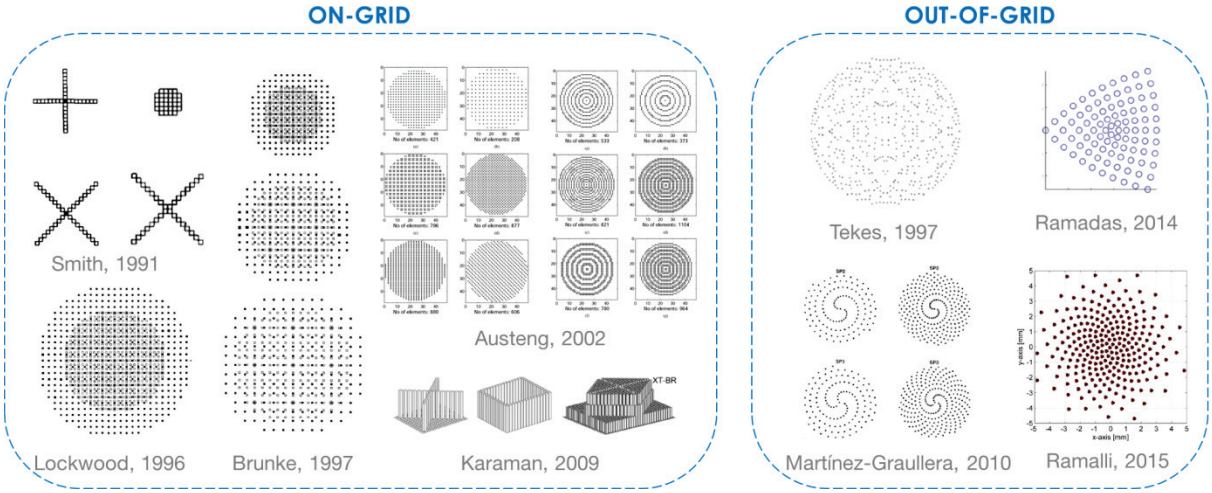


Figure 16 Deterministic 2D array designs proposed in Literature, on the left configurations with the on-grid arrays (elements located on a regular lattice) and on the right configurations out-of-grid arrays.

Deterministic sparse array designs include conformal array (Ramadas et al. 2014), regular and radially periodic arrays (Austeng and Holm 2002; Brunke and Lockwood 1997), or Mills[16] cross arrays (S. W. Smith, Pavy, and von Ramm 1991) which can be quickly defined, with small computational effort, and immediately tested through simulations because the layout geometry is known in advance. As drawbacks, there is limited design flexibility, and their performance, in terms of SLL/GLL, depends on the use of one set of elements in transmission (TX) and another one in reception (RX), addressed to cancel the grating lobes in the pulse-echo (two-way) BP. If multiplexing cannot be adopted, the total number of elements in TX and RX is limited by the number of scanner channels. Using all of the available channels to activate the same group of elements in both TX and RX maximizes the active surface, which helps compensating for the lack of sensitivity often reproached to sparse arrays. Quite recently, the use of special spiral array configurations has been proposed (Ramalli et al. 2015; Martínez-Graullera et al. 2010), and the related simulations show promising results.

[16] In reference to the Mills Cross Telescope built by Bernard Yarnton Mills in 1954.

TABLE II FEATURES COMPARISON BETWEEN THE PRINCIPAL STOCHASTIC 2D ARRAY DESIGNS IN THE LITERATURE

Works \ Features	On-grid / Out-of-grid	Wideband simulations	Shape sensitive	One-way BP / Two-way BP	Multi-depth	Number of elements known in advance	Symmetry free / Fabrication constraints	TX elements = RX elements	No use of apodization	optimization	online BP computation (not pre-computed)	No a priori on SLL
Turnbull and Foster, 1991	✓ / ×	✓	✓	× / ✓	✓	✓	× / ✓	✓	×	×		
Boni, 1994	× / ✓	×	×	✓ / ×	×	×	× / ×	✓	×	✓	✓	✓
Weber, 1994	✓ / ×	×	×	✓ / ×	×	×	✓ / ✓	✓	✓	✓	✓	×
Davidsen, 1994	✓ / ×	✓	✓	× / ✓	✓	✓	✓ / ✓	×	✓	×		
Holm, 1997	✓ / ×	×	×	✓ / ×	×	×	× / ×	✓	×	✓	✓	×
Austeng, 1997	✓ / ×	×	×	× / ✓	×	✓	✓ / ✓	×	✓	✓	✓	✓
Trucco, 1999	✓ / ×	×	×	✓ / ×	×	×	× / ✓	✓	×	✓	✓	×
Austeng, 2002	✓ / ×	×	×	× / ✓	×	×	× / ×	×	✓	×		
Chen, 2010	✓ / ×	×	×	✓ / ×	×	×	✓ / ✓	✓	×	✓	✓	×
Choe, 2010	✓ / ×	✓	✓	× / ✓	✓	✓	× / ✓	×	✓	✓	×	✓
Diarra, 2013	✓ / ✓	×	×	× / ✓	×	×	✓ / ✓	✓	×	✓	✓	×
Sciallero, 2015	✓ / ✓	✓	✓	× / ✓	×	✓	× / ✓	×	×	✓	✓	×
Roux, 2016	✓ / ✓	✓	✓	✓ / ×	✓	✓	✓ / ✓	✓	✓	✓	✓	✓

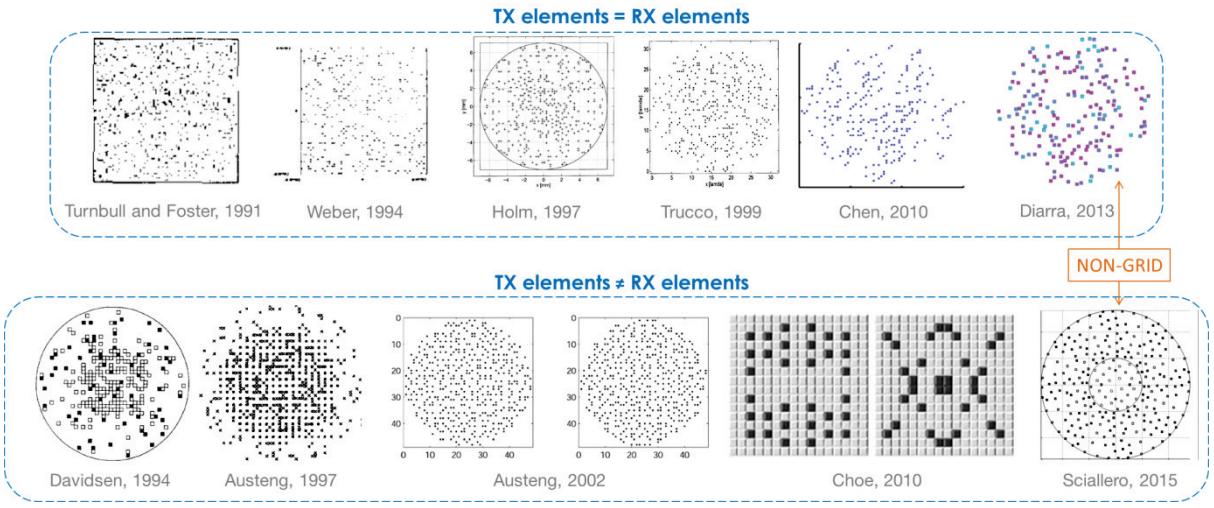


Figure 17 Stochastic 2D array designs proposed in literature. At the top, configurations with the same arrays used in both transmission (TX) and reception (RX) and at the bottom configurations with two different set of elements used in TX and RX.

In stochastic random sparse arrays, a number of configurations, each obtained by randomly choosing part of the elements of the fully populated 2D array, is initially defined. Among them, the configuration yielding the best performance (e.g., in terms of GLL) is selected. With this approach, the number of explored configurations is typically limited (Davidsen, Jensen, and Smith 1994; Austeng and Holm 2002; Turnbull and Foster 1991) and it is not possible to ensure that the best achievable performance is actually obtained. This lack of robustness comes from the fact that each random array is generated independently from the previous tested configurations.

Stochastic approaches based on stochastic optimization take advantage from the previous trials to iteratively search for the "optimum" configuration. Since searching for an optimal configuration among all possible sparse arrays is a very large scale combinatorial optimization problem, simulated annealing (Sciallero and Trucco 2015; Diarra et al. 2013; Tekes, Karaman, and Degertekin 2011; P. Chen et al. 2010; Choe, Oralkan, and Khuri-Yakub 2010; S. Holm et al. 2001; Trucco 1999; S. Holm

and Elgetun 1995) is better suited than genetic algorithms (S. Holm et al. 2001; Austeng et al. 1997; Weber et al. 1994; Haupt 1994). Indeed, the main difficulty in solving a large scale optimization problem using a genetic algorithm is to manage a large population of candidate solutions, which is expensive in terms of both computation time and memory requirements; besides, genetic algorithms have other drawbacks: they usually converge prematurely and have poor hill-climbing capability (see, e.g., (Hwang and He 2006; Adler 1993)). For best performance, the cost functions to be optimized by stochastic methods should be based on the BP features, which is often unpractical since computing a realistic BP for each configuration is time consuming. In order to reduce the computational load, the majority of stochastic 2D array design methods (Diarra et al. 2013; Tekes, Karaman, and Degertekin 2011; P. Chen et al. 2010; S. Holm et al. 2001; Trucco 1999; Austeng et al. 1997; S. Holm and Elgetun 1995; Weber et al. 1994; Haupt 1994) approximate the BP by a narrowband BP in the far field. The far-field approximation implies that each active element is reduced to a pointwise source defined by its center and weight (the element size and orientation are not taken into account). The narrowband BP, also known as the Continuous Wave (CW) response, assumes that the transmitted signal is a monochromatic wave at the central frequency of the array (no realistic excitation signal and impulse response are considered). To our knowledge, the only two exceptions are (Sciallero and Trucco 2015; Choe, Oralkan, and Khuri-Yakub 2010), where stochastic optimization is performed using a wideband two-way Point Spread Function (PSF) simulation. In addition, layout symmetry is usually enforced to further reduce the computational load and the number of possible configurations (Sciallero and Trucco 2015; Choe, Oralkan, and Khuri-Yakub 2010).

A further distinction between on-grid (Brunke and Lockwood 1997; Trucco 1999; Sciallero and Trucco 2015; P. Chen et al. 2010) and out-of-grid (Diarra et al. 2013; Roux et al. 2014; Diarra et al. 2014; Roux, Ramalli, Tortoli, et al. 2015; Roux, Ramalli, Robini, et al. 2015; Ramalli and Tortoli 2014; Ramalli et al. 2015) sparse arrays can be made. The former have all of the elements aligned along rows and columns, while in the latter ones the elements do not have any position restriction (except that they cannot overlap). The additional degrees of freedom achieved in this case, permit to increase the obtainable acoustic performance (Diarra et al. 2013; Ramalli et al. 2015). Indeed, out-of-grid designs present the advantage of reducing the grating lobe level even when the inter-element distance is greater than $\lambda/2$ thanks to a non-periodical spatial sampling. Releasing the spatial sampling condition also enables the use of wider elements and compensates for the sparse array sensitivity lack by increasing the active surface of the aperture. However, increasing the element size can potentially limit the field of view (FOV): the wider the elements the weaker their steering capability. However, manufacturing out-of-grid arrays impose additional requirements on the fabrication process, which could require laser machining technique if piezoelectric technology is involved or CMUT technology (Savoia, Caliano, and Pappalardo 2012). The CMUT fabrication process is very close to that of integrated circuits and, as such, is extremely flexible but, at the same time, more expensive unless thousands of identical probes are fabricated.

Based on this state of the art, the chapters are organized as follows to introduce the contributions of this thesis:

- Chapter II presents the speed-up techniques that enable the introduction of realistic acoustic simulations and the use of wideband and shape sensitive energy functions in a general 2D sparse array optimization framework.

- Chapter III presents an application on 2D out-of-grid sparse arrays of the general optimization framework introduced in Chapter II. New multi-depth energy functions are also introduced and their impact is enhanced analyzing the obtained optimized out-of-grid arrays.
- Chapter IV presents the guidelines to introduce fabrication constraints in the optimization framework and results are obtained searching for the best selection of a fixed number of elements in a 2D on-grid full array.

IIChapter II Realistic acoustic simulations in a general 2D sparse array optimization framework

II.A Introduction: motivations and limitations

This chapter presents implementation techniques to integrate realistic acoustic simulations in a general 2D sparse array optimization framework. The motivation for integrating wideband and shape sensitive (realistic) acoustic simulations in the 2D sparse array optimization process was clearly stated in (S. Holm, Elgetun, and Dahl 1997, 97): *"The issue of pulsing with broad bandwidth pulses is also important. In this paper, the assumption is that there is only a single frequency present. In general pulsing will tend to smear out sidelobe peaks. To some extent this happens to the sparse arrays also, but the peaks are still there, although smaller, after pulsing".* The interest is even more stressed in (Trucco 1999): *"Other developments will concern the application of the synthesis based on [Simulated Annealing] to wide-band sparse arrays. Thanks to the different definition of the BP* [(Davidsen, Jensen, and Smith 1994; Turnbull and Foster 1991; Murino, Trucco, and Tesei 1997)]*, the synthesis of arrays working under wide-band conditions may yield further improved results, e.g., BPs that show lower side-lobe profiles, even when the same number of elements is used*". In short, Martínez-Graullera writes the following hypothesis: *"Then, it is supposed that better results […] can be obtained if the search is repeated in wideband"* (Martínez-Graullera et al. 2010).

Moreover, several expectations arise when integrating wideband and shape sensitive acoustic simulations in the optimization process, for instance the following: enabling new degrees of freedom (size, shape, orientation, excitation signal) and improving the distinctive capability between arrays with respect to the previous omnidirectional narrow band acoustic model; taking into account the single elements acoustic radiation contributions means to optimize the array in a realistic way, with no approximation model in the middle. Finally, the optimization process evolves and converges through solutions with the same performance as if they were physically built.

For the limitations, again we can cite (Trucco 1999): "*The major problem to be solved lies in the load imposed by the computation of the BP under wide-band conditions".*

II.B Speed-up of the realistic acoustic simulations

The main drawback of using realistic acoustic simulations is the time required to compute the pressure field (PF) around the array of transducers. In our work all the simulations are done using FIELD II (Jensen 1996; Jensen and Svendsen 1992). To achieve a sufficiently fast implementation, two strategies are introduced. The first technique consists in reducing the number of Pressure Measurement Points (PMP) used to compute the PF around the array. The second technique is an ergonomic data management enabling a fast PF update.

II.B.1 Pressure measurement points (PMP) reduction technique

The computation time limitation is mostly due to the acoustic simulation, which in turns depends on the number of active elements and on the number of PMP used to evaluate the beam pattern. To

evaluate the beam pattern radiated by the array, the pressure field is evaluated on a hemisphere of radius

$$R_\mathrm{f} = \sqrt{x_\mathrm{f}^2 + y_\mathrm{f}^2 + z_\mathrm{f}^2} \tag{33}$$

where $(x_\mathrm{f}, y_\mathrm{f}, z_\mathrm{f})$ are the coordinates of the focal point (Figure 18).

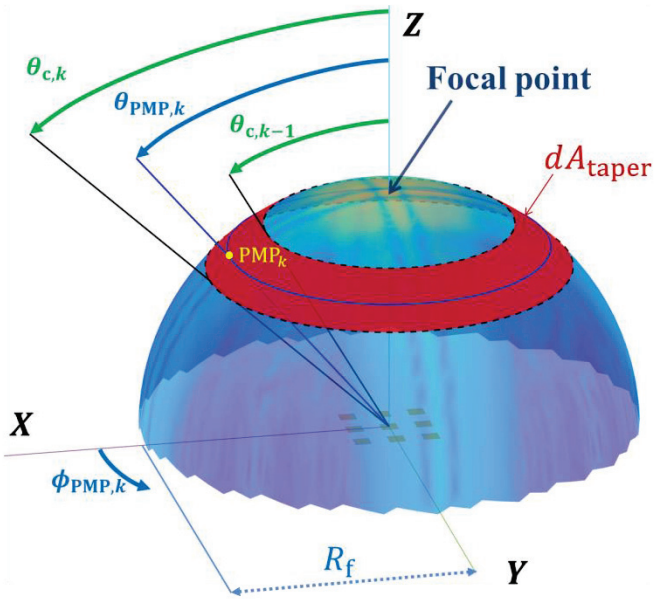


Figure 18 Circles delimiting the tapered stripes of surface dA_taper used for the placement of the pressure measurement points (PMP). The first PMP is located on the z-axis at focal depth R_f, then each k-th PMP is located at angle $\theta_{\mathrm{PMP},k}$ splitting in two equal tapered surfaces dA_taper which is delimited by two angles $\theta_{\mathrm{c},k-1}$ and $\theta_{\mathrm{c},k}$.

Usually the spherical coordinates are discretized (N_θ samples on θ and N_ϕ samples on ϕ) and the k-th PMP is located at $(R_\mathrm{f}, \theta_{\mathrm{PMP},k}, \phi_{\mathrm{PMP},k})$ with $k = 1 \dots N_\theta N_\phi$, which results in a non-uniform and periodic distribution of the PMP. To faster compute the beam pattern without losing precision, the elements placement strategy used in (Viganó et al. 2009) was transposed in a 3D spiral arm and applied to the placement of the PMP so that no periodicity is introduced (or hidden) in the measurements. To adapt (Viganó et al. 2009) in 3D a hemisphere with density tapered surface is considered with surface density varying with θ (Figure 19). The positioning of the PMP along θ is performed in three steps:

1. A density law $A_\mathrm{taper}(\theta)$ and the number N_PMP of sampling points are defined to yield the desired density of PMP along the $\theta-$angle. On Figure 19 three different density laws are presented: on the top line of the figure, the PMP are more densely located close to the focal point, on the second line the PMP are concentrated at the bottom of the hemisphere (denser sampling for values of θ close to $\pi/2$) and on the third line the distribution is homogeneous on $\theta-$angle. The three density laws are illustrated using different number of points: $N_\mathrm{PMP} = \{300, 3000, 30\,000\}$.
2. The second step consists in determining the angles $\theta_{\mathrm{c},k}$ of the delimiting circles on the hemisphere surface surrounding each PMP (Figure 18). Using the density law $A_\mathrm{taper}(\theta)$ the surface of the stripe contained between two circles which are located at angles $\theta_{\mathrm{c},k-1}$

and $\theta_{c,k}$ defines an elementary surface dA_{taper} of the tapered hemisphere (Figure 19). The key concept is that the unknown $\theta_{c,k}$ angles are found iteratively through the numerical integration of (35) obtained from (34).

3. The precise location $\theta_{\text{PMP},k}$ of the k-th PMP on θ is obtained founding the angle splitting the k-th stripe in two equal tapered surfaces.

In practice, each PMP is located in between two delimiting angles $\theta_{c,k-1}$ and $\theta_{c,k}$ which are the angles of the consecutive circles on the tapered hemisphere surface delimiting a stripe of elementary surface dA_{taper} (note that in (34) and (35) the unknown $\theta_{c,k}$ is found iteratively starting with $\theta_{c,1} = 0$ rad):

$$\begin{aligned} dA_{\text{taper}} &= \int_{\theta_{c,k-1}}^{\theta_{c,k}} \int_{0}^{2\pi} A_{\text{taper}}(\theta)\, R_f^2 \sin\theta \, \mathrm{d}\theta \mathrm{d}\phi \\ &= \frac{1}{N_{\text{PMP}}} \int_{0}^{\pi/2} \int_{0}^{2\pi} A_{\text{taper}}(\theta)\, R_f^2 \sin\theta \, \mathrm{d}\theta \mathrm{d}\phi. \end{aligned} \tag{34}$$

Integrating on ϕ we get

$$dA_{\text{taper}} = 2\pi R_f^2 \int_{\theta_{c,k-1}}^{\theta_{c,k}} A_{\text{taper}}(\theta)\ \sin\theta \, \mathrm{d}\theta = \frac{2\pi R_f^2}{N_{\text{PMP}}} \int_{0}^{\pi/2} A_{\text{taper}}(\theta)\ \sin\theta \, \mathrm{d}\theta. \tag{35}$$

The $\theta_{c,k}$ angles are computed from (35) and the PMP can then be precisely placed in the barycenter θ_k of the tapered stripe surface using (36):

$$2\pi R_f^2 \int_{\theta_{c,k}}^{\theta_{\text{PMP},k}} A_{\text{taper}}(\theta)\ \sin\theta \, \mathrm{d}\theta = \frac{dA_{\text{taper}}}{2} \tag{36}$$

Combined with the following ϕ_k angle computation method, it resulted in a 3D spiral PMP setup avoiding periodical patterns:

$$\phi_{\text{PMP},k} = 2k\pi . \left(\frac{1+\sqrt{5}}{2} \right) \tag{37}$$

The uniform and aperiodic coverage of the hemisphere surface permits to reduce the number of the PMP while maintaining satisfying beam pattern analysis (II.B.3.b).

As an example, if the target is a uniform distribution of the PMP along θ, the density law $A_{\text{taper}}(\theta)$ must be set equal to $\frac{1}{\sin\theta}$ (Figure 19, bottom line). It results that the delimiting circles and the PMP are equi-spaced on $\theta-$ angle with $\delta\theta_c = \frac{\pi/2}{N_{PMP}}$. So, the equidistant (along θ angle) circles are located at angles

$$\theta_{c,k} = \frac{\pi}{2} \frac{k}{N_{\text{PMP}}}. \tag{38}$$

The positioning method starts by placing a first PMP at the focal point and the following PMP positions are computed using (36) so that the θ angle of the k-th PMP $\theta_{\mathrm{PMP},k}$ equally splits the tapered stripe surface delimited by two consecutive circles.

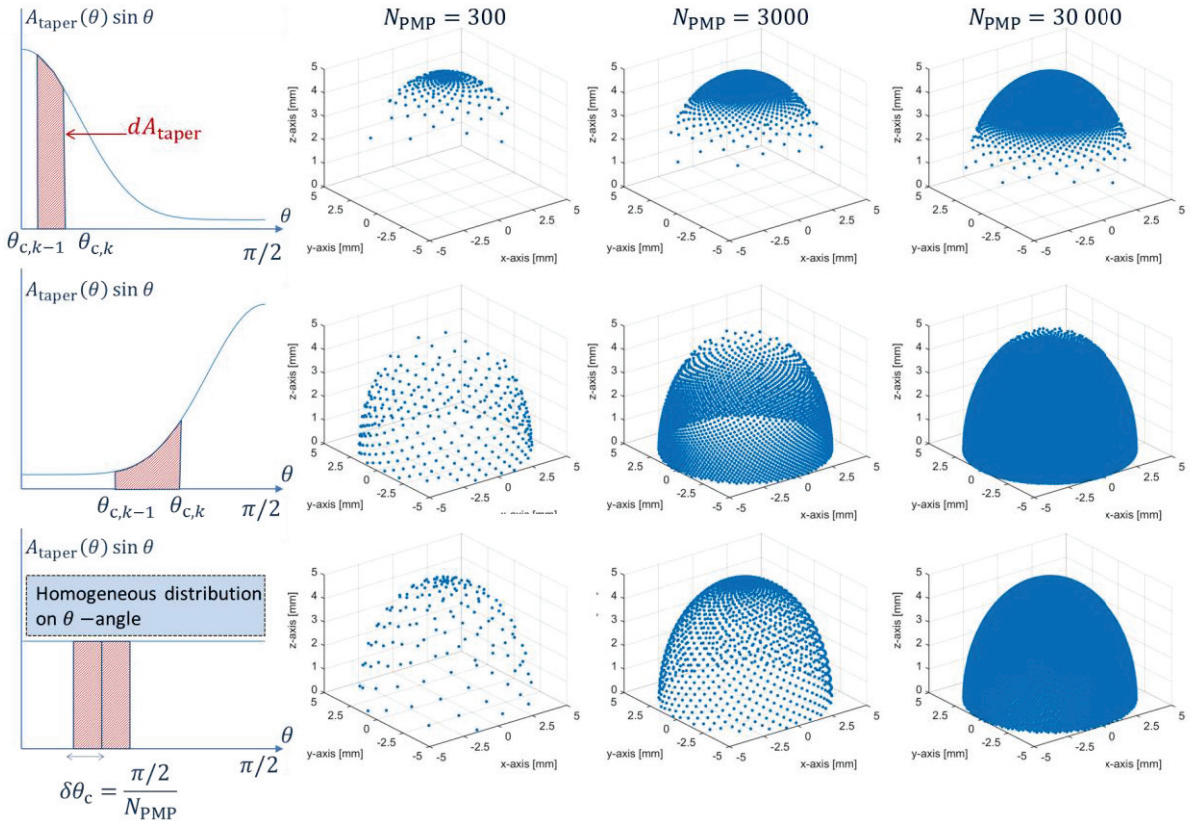


Figure 19 Illustration of the density tapering of the pressure measurement points (PMP) distribution using different density laws $A_{\mathrm{taper}}(\theta)$: a new circle is delimited each time an elementary stripe surface dA_{taper} is integrated under the curve of $A_{\mathrm{taper}}(\theta)\sin\theta$. It results that the PMP are wound along a 3D spiral on the tapered surface of the hemisphere of radius R_{f}. Three density laws (lines) are illustrated for three number of PMP (columns) $N_{\mathrm{PMP}} = \{300, 3000, 30\,000\}$.

II.B.2 Ergonomic data management

Since Field II simulations assume linear propagation conditions, the superposition of individual elements contribution was exploited for fast PF computation as described in Figure 20. In particular, only the new pressure field contribution $\mathrm{PF}_{\mathbf{e}_{n+1}}$ of the perturbed element, $\mathbf{e}$ placed in $(x_{\mathbf{e}}, y_{\mathbf{e}}, z_{\mathbf{e}})$, was updated. The initial PF_{S_0} was first computed and for the following iterations it was updated as

$$\mathrm{PF}_{S_{n+1}} = \mathrm{PF}_{S_n} - \mathrm{PF}_{\mathbf{e}_n} + \mathrm{PF}_{\mathbf{e}_{n+1}} \tag{39}$$

Note that in (39) and in Figure 20 the index n designate the iteration number.

In order to facilitate calculation and avoid matrix dimension variations due to the elements moves, two PMP^* were added above every single element $\mathbf{e}$. The reason for introducing the PMP^* is strictly related to the way Field II renders the simulated pressure, i.e. in the form of uniformly sampled signals and a "starting time" that is not an integer multiple of the sampling time. Indeed, when controlling where the acoustic radiation is measured at first and at last, it is possible to guarantee the same individual signals duration and phase (Figure 21). The RF signals (raw data) are

safely memorized for each element not to lose track of the temporal dimension of its contribution to the PF so that after any perturbation the new phase interferences can be accurately computed.

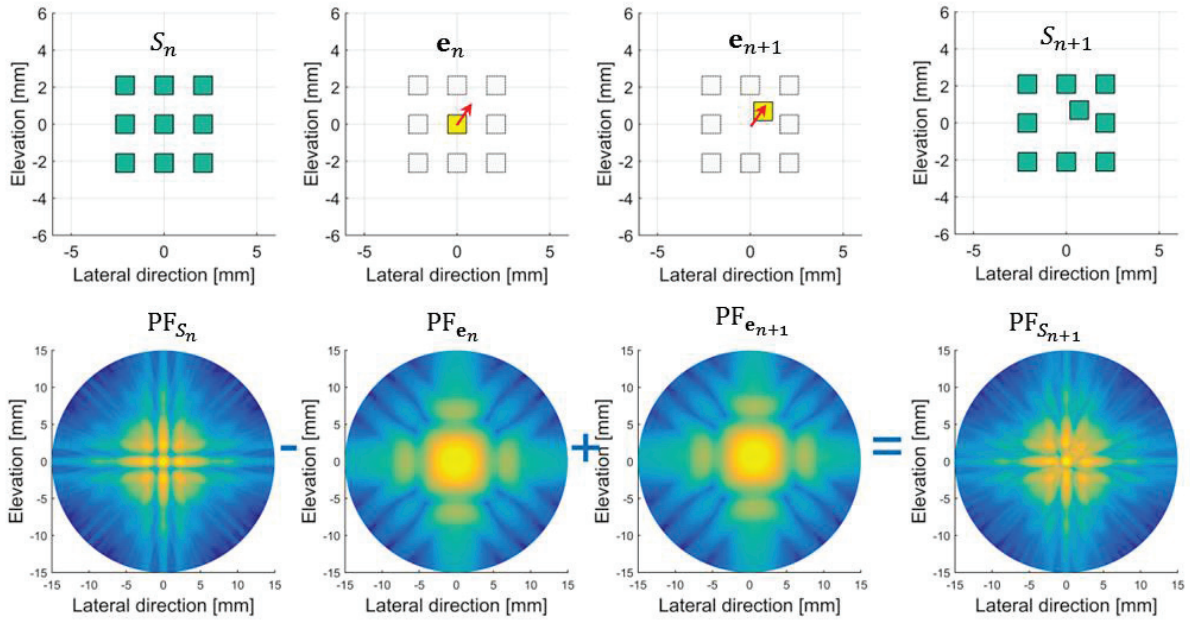


Figure 20 Detailed steps of a fast pressure field update when translating one element $\mathbf{e}_n \rightarrow \mathbf{e}_{n+1}$ of the array S_n to create a new solution S_{n+1}. The layouts of the initial array S_n, the element $\mathbf{e}_n$ before translation, the element $\mathbf{e}_{n+1}$ after the translation and the new solution S_{n+1} are presented at the top from left to right. The respective associated pressure fields (PF_{S_n}, $\mathrm{PF}_{\mathbf{e}_n}$, $\mathrm{PF}_{\mathbf{e}_{n+1}}$, $\mathrm{PF}_{S_{n+1}}$) are presented from left to right at the bottom.

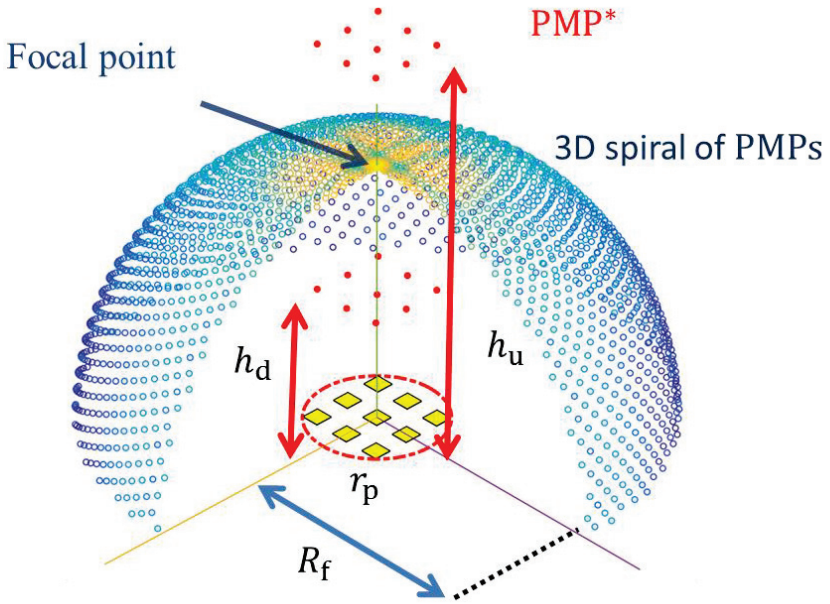


Figure 21 Illustration of the PMP* located over each transducer element. Two PMP*, one down and one up, are associated to each elements of the array; they are located above the element at respective height h_u and h_d. The radius of the aperture is designated as r_p (dotted red circle).

The first PMP* of coordinates $(x_\mathrm{d}^*, y_\mathrm{d}^*, z_\mathrm{d}^*)$ was located under the hemisphere but as far as possible from its associated element along the steering direction $\hat{\boldsymbol{r}}_\mathrm{steer}$ in order to reduce the simulation time. On the contrary, the second PMP* of coordinates $(x_\mathrm{u}^*, y_\mathrm{u}^*, z_\mathrm{u}^*)$ had to be as close as

possible to its associated element along the direction $\hat{\boldsymbol{r}}_{\text{steer}}$. The equations (41)-(46) details how to compute the location of the PMP^*:

$$(x_{\text{d}}^*, y_{\text{d}}^*, z_{\text{d}}^*) = (x_{\text{e}}, y_{\text{e}}, z_{\text{e}}) + (h_{\text{d}} + \Delta D_{\text{E}} - \Delta D_{\max}).\hat{\boldsymbol{r}}_{\text{steer}} \tag{40}$$

$$(x_{\text{u}}^*, y_{\text{u}}^*, z_{\text{u}}^*) = (x_{\text{e}}, y_{\text{e}}, z_{\text{e}}) + (h_{\text{u}} + \Delta D_{\text{E}} - \Delta D_{\min}).\hat{\boldsymbol{r}}_{\text{steer}} \tag{41}$$

with

$$h_{\text{d}} = 0.95\big(R_{\text{f}} - r_{\text{p}}\big) \tag{42}$$

$$h_{\text{u}} = 1.05\big(R_{\text{f}} + r_{\text{p}}\big) \tag{43}$$

$$\Delta D_{\min} = c \cdot |\tau_{\min}| \tag{44}$$

$$\Delta D_{\max} = c \cdot |\tau_{\max}| \tag{45}$$

and,

$$\Delta D_{\text{E}} = \left\| \begin{matrix} x_{\text{e}} - x_{\text{f}} \\ y_{\text{e}} - y_{\text{f}} \\ z_{\text{e}} - z_{\text{f}} \end{matrix} \right\|_2 - \left\| \begin{matrix} x_{\text{f}} \\ y_{\text{f}} \\ z_{\text{f}} \end{matrix} \right\|_2 \tag{46}$$

where c is the speed of sound (set to 1540 m/s here), r_{p} is the aperture radius, and $\tau_{\max}$ and $\tau_{\min}$ are, respectively, the maximum and minimum delays applied to do the focalization (I.B.2.a). Since the applied delays for focusing depend on the element position, each time an element was translated during the optimization process, the two associated PMP^* also had to be updated.

II.B.3 Benefits

II.B.3.a Speed-up factors

To quantify the speed-up gain of the PMP reduction, the execution time to update the pressure field was compared for twenty values of N_{PMP}: starting from 1000 up to 20 000 by steps 1000. Experimentally the PMP reduction yields a speed-up gain

$$g_1(\varepsilon) = \frac{102}{(\varepsilon + 0.74)} \tag{47}$$

where $N_{\text{REF}} = 20\,000$ is the reference amount of PMP from which only N_{PMP} are maintained and $\varepsilon = \frac{N_{\text{PMP}}}{N_{\text{REF}}} \times 100$ is the downsampling factor. The numerical values were the best parameters to fit with the experimental computation time speed-up.

To quantify the speed-up gain of the fast pressure field update, the execution time to do one fast update was compared to the time needed to compute the entire array PF when the number of elements vary from N_{e}=64 up to 1024 by steps of 64 elements. The execution time ratio between the entire array PF update and the fast PF update defines a speed-up gain

$$g_2(N_e) = 1 + \frac{42}{1000} N_e \quad (48)$$

where N_e is the number of active elements. Here also the numerical values were the best parameters to fit with the experimental computation time speed-up. It must be underlined that the speed-up gain increases linearly with the number of array elements.

The two acceleration techniques were combined to achieve the optimization of a 256-element 7 MHz array of radius r_p = 6 mm ≈ 30 λ with focus at 25 mm on z-axis. 10 000 PMP were located on the hemisphere of radius R_f = 25 mm resulting in a space sampling resolution smaller than 3λ. Compared to the standard pressure field sampling setting (65536 PMP: 256 on θ × 256 on ϕ) the total speed-up gain was here increased to $g_T = g_1 \cdot g_2 \sim 75$ for the radiated pressure field update. With the same number of PMP, the optimization of a 1024-element array would be accelerated 280 times.

II.B.3.b Dimension reduction for the 2D BP analysis

A noteworthy property of PMP distribution on a 3D spiral arm is that it allows a simple representation of the 2D BP in only one dimension. The dimension reduction comes from the combination of a scanning of the θ-angle along with the rotation of the ϕ-angle: it appears by plotting the beam profile which is the normalized pressure field measured by each PMP against their θ-angle (Figure 22). The worst-case and the best-case beam profiles can be plotted by detecting the upper and lower envelops respectively (full red line and full green respectively on Figure 22).

On Figure 22 two PF sampling strategies are compared, the standard strategy with $N_\theta = 64$ and $N_\phi = 64$ which gives 4096 PMP (mainly concentrated close to the focal point) and the proposed strategy (3D spiral with homogeneous distribution along $\theta - \text{angle}$) using the same amount of PMP ($N_{PMP} = 4096$). The proposed strategy allows analyzing the BP more precisely because the number of PMP per degree (on θ angle) is 64 times greater.

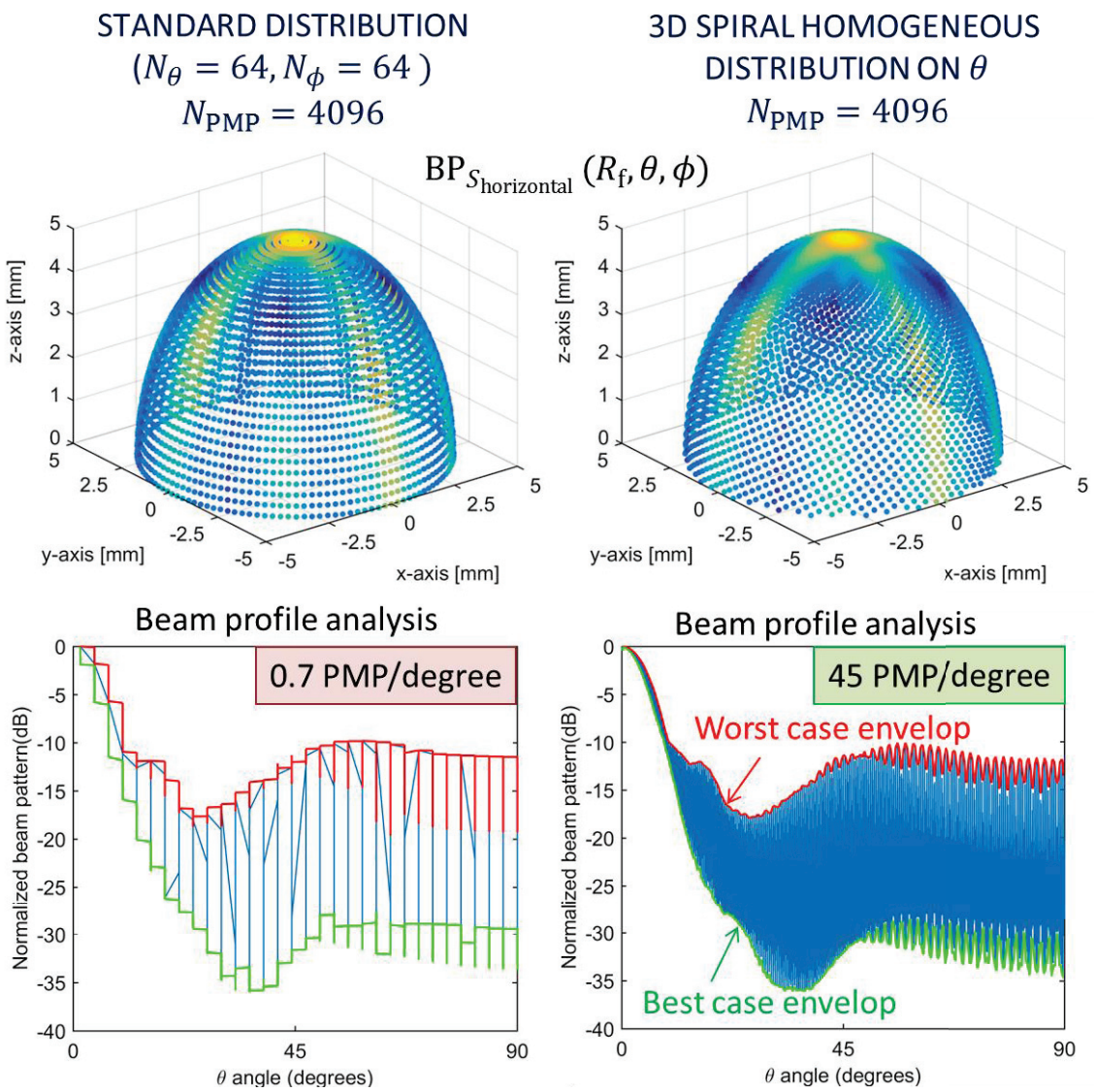


Figure 22 Comparison of the standard PMP distribution method (64 samples on θ and 64 samples on ϕ) with the proposed reduction technique (4096 PMP homogeneously distributed along θ − angle). The beam profile analyses at the bottom illustrate the interest of the dimension reduction implied by the homogeneous and aperiodic sampling of the PF. The worst case and the best case envelops are displayed on the beam profiles analysis in full red line and full green line respectively.

II.B.3.c New degrees of freedom and distinctive capability enhancement

The greatest benefit of the integrating realistic acoustic simulations in the 2D sparse array optimization process is that new degrees of freedom (size, shape, orientation, excitation signal) can be investigated. Indeed during the optimization the energy function, that defines the desired array acoustic behavior, can take into account these new parameters. In other words, now the optimization algorithm is sensitive to arrays that were considered identical with a pointwise monochromatic acoustic radiation model: the integration of realistic acoustic simulations enhances the distinctive capability of the optimization algorithm.

To illustrate the enhancement of this distinctive capability, two 5x5 array arrays having elements with the same rectangular size and position, but perpendicular orientations (Figure 23), were designed and their respective BP, $\mathrm{BP}_{S_{\mathrm{vertical}}}(\theta, \phi)$ and $\mathrm{BP}_{S_{\mathrm{horizontal}}}(\theta, \phi)$, were compared. The

arrays were centered at the origin point (0,0,0) and the 5x5 rectangular active elements laid on the x0y plane. The size of the elements was set to $\lambda/2 = 0.22\ \mathrm{mm}$ for the short side and to $(1+\sqrt{5})\,\lambda/4 = 0.36\ \mathrm{mm}$ on the long side with pitch equal to 1.31 λ on x-axis and pitch equal to λ on y-axis.

Using the proposed PMP reduction technique, 3000 PMP were uniformly distributed on the hemisphere of radius $R_\mathrm{f} = 5\ \mathrm{mm}$ centered on the array. Moreover, the 72 % bandwidth impulse response of the elements was implemented as a 2.5-period-sinusoidal signal weighted by Hanning window (central frequency $f_0 = 3.5\ \mathrm{MHz}$ and sampling frequency $F_\mathrm{s} = 100\ \mathrm{MHz}$). The elements were excited by a 62 % bandwidth 3-period-sinusoidal signal weighted by Hanning window (central frequency $f_0 = 3.5\ \mathrm{MHz}$ and sampling frequency $F_\mathrm{s} = 100\ \mathrm{MHz}$) with individual delay laws to make the array focus at R_f on the z-axis.

Figure 23 (a) and Figure 23 (b) show $\mathrm{BP}_{S_\mathrm{vertical}}(R_\mathrm{f},\theta,\phi)$ and $\mathrm{BP}_{S_\mathrm{horizontal}}(R_\mathrm{f},\theta,\phi)$ over the respective vertical and horizontal layouts S_vertical and $S_\mathrm{horizontal}$. To localize the beam region where the BPs are appreciably different, the normalized BP difference is displayed in Figure 23 (c). The two normalized BPs were compared and the maximum difference reached 7 dB:

$$\max\left(\left|\mathrm{BP}_{S_\mathrm{vertical}}(R_\mathrm{f},\theta,\phi)\right| - \left|\mathrm{BP}_{S_\mathrm{horizontal}}(R_\mathrm{f},\theta,\phi)\right|\right) = 7\ \mathrm{dB} \tag{49}$$

In conclusion of this distinctive capability enhancement, it is clear that an energy function defined on the BP calculated with the proposed realistic simulation approach, will be able to finely distinguish arrays that were considered identical using the omnidirectional model (the centers of the elements are the same for both S_vertical and $S_\mathrm{horizontal}$). From now on, if it is expected by the probe designer, the optimization algorithm will be able to distinguish more degrees of freedom in the elements configurations, enabling the investigation of a large amount of yet unexplored solutions.

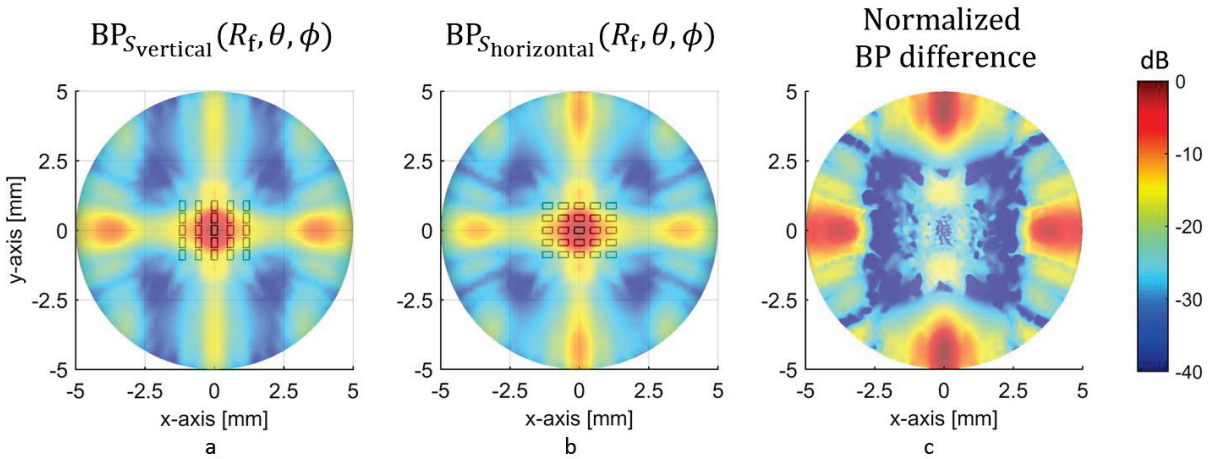


Figure 23 The vertical rectangles layout overlaid by the associated radiated pattern $\mathrm{BP}_{S_\mathrm{vertical}}(R_\mathrm{f},\theta,\phi)$ (a), the horizontal rectangles layout overlaid by the associated radiated pattern $\mathrm{BP}_{S_\mathrm{horizontal}}(R_\mathrm{f},\theta,\phi)$ (b), normalized difference between $\mathrm{BP}_{S_\mathrm{vertical}}(R_\mathrm{f},\theta,\phi)$ and$\mathrm{BP}_{S_\mathrm{horizontal}}(R_\mathrm{f},\theta,\phi)$ (c). A 40dB dynamic range is displayed

II.C General 2D sparse array optimization framework

An optimal 2D sparse array S_{opti} is searched by minimizing an energy function U over a large (but finite) state space of 2D sparse arrays Ω. The optimization is performed by a Metropolis-type Simulated Annealing (SA) algorithm (Kirkpatrick et al. 1983; Van Laarhoven and Aarts 1987) ,(Robini and Reissman 2013; Robini 2013) which explores Ω iteratively by means of a communication mechanism Θ specifying the possible state transitions. The key feature of SA is that a cooling sequence controls the acceptance probability of the uphill transitions in the Markov chain of the explored solutions. The state space Ω of 2D sparse arrays is presented in section II.C.1, the communication mechanism Θ is introduced in section II.C.2, and the energy function U is defined in section II.C.3. The SA optimization workflow is described in section II.D.

II.C.1 General state space

From a general point of view, a 2D sparse array consists of a reduced number of elements N_{e} compared to a full array of same aperture size. A general state space of 2D sparse arrays with N_{e} elements is of the form

$$\begin{aligned}\{S = (\mathbf{e}_1, \dots, \mathbf{e}_{N_{\text{e}}}) \in \text{E}_1 \times \dots \times \text{E}_{N_{\text{e}}} \mid \text{A}_i \cap \text{A}_j = \emptyset, \\ \text{for all } i, j \in [1..N_{\text{e}}] \text{ such that } i \neq j\}\end{aligned} \tag{50}$$

where E_k and A_k are respectively the set of properties and the spatial region occupied by the k-th element $\mathbf{e}_k$. In other words, a sparse array S is a collection of N_{e} non-overlapping elements, each of which is represented by a vector in some space E_k. The spaces E_k can differ from one another, meaning that the elements in a sparse array S can have different types or geometries as long as they do not overlap. However, for computational complexity reasons, the full set of parameters describing each element cannot be optimized. For example, a rectangular element can be described by a vector

$$\mathbf{e}_k = \begin{bmatrix} (x_k, y_k, z_k) \\ (\theta_k, \phi_k) \\ (a_k, b_k) \\ w_k \\ \text{Imp}_k \\ \text{Exc}_k \\ \tau_k \end{bmatrix} \in \text{E}_k, \tag{51}$$

where (x_k, y_k, z_k) are the three dimensional Cartesian coordinates of the element center, (θ_k, ϕ_k) are the spherical orientation coordinates of the normal vector to the element surface, (a_k, b_k) are the element sizes along the x- and y-axes when $(\theta_k, \phi_k) = (0,0)$, w_k is the element weight for apodization, Imp_k and Exc_k are respectively the impulse response and the excitation signal of the element, and τ_k is the transmission delay. In practice, for a given focal point, the individual delays τ_k are determined by the element positions. Note that here the index k designates the element index in the array whereas in II.B.2 the index n designates the optimization iteration. If necessary, the k-th element at iteration n can be written $\mathbf{e}_{k,n}$ and a property such as the individual delay can be written $\tau_{k,n}$ as well.

Moreover, the components of $\mathbf{e}_k$ to be optimized are classically either (x_k, y_k, z_k) or w_k, the other components being fixed and equal for all the elements. So the actual state space Ω is of the form (50) with each E_k replaced by its subset obtained by fixing all the components except the Cartesian coordinates or the weights.

II.C.2 Communication mechanism

During the exploration of the state space Ω, the transition from a state $S = (\mathbf{e}_1, \ldots, \mathbf{e}_{N_\mathrm{e}})$ to a candidate solution $\tilde{S} = (\tilde{\mathbf{e}}_1, \ldots, \tilde{\mathbf{e}}_{N_\mathrm{e}})$ is controlled by a so-called communication mechanism (Robini 2013; Robini and Reissman 2013). This mechanism, say Θ, is a Markov matrix on Ω whose entries $\Theta(S, \tilde{S})$ are the probabilities to move from a given state $S \in \Omega$ to a candidate solution $\tilde{S} \in \Omega$. Usually, the possible moves in Ω are defined via a neighborhood system $\mathcal{G}$ on Ω, that is, $\mathcal{G} = \{\mathcal{G}(S) : S \in \Omega\}$, where the neighborood $\mathcal{G}(S)$ of a state S is a subset of Ω such that (i) $S \notin \mathcal{G}(S)$ and (ii) $\tilde{S} \in \mathcal{G}(S) \Leftrightarrow S \in \mathcal{G}(\tilde{S})$ (in other words a state cannot belong to its neighborhood and the neighborhood relation is symmetric). The mechanism Θ is then of the form

$$\Theta(S, \tilde{S}) = \begin{cases} \gamma\, \Gamma(S, \tilde{S}) & \text{if } \tilde{S} \in \mathcal{G}(S), \\ 1 - \gamma \displaystyle\sum_{S' \in \mathcal{G}(S)} \Gamma(S, S') & \text{if } \tilde{S} = S, \\ 0 & \text{otherwise,} \end{cases} \tag{52}$$

where Γ is a positive function defined on $\{(S, \tilde{S}) \subset \Omega \mid \tilde{S} \in \mathcal{G}(S)\}$ and γ is a positive constant which is small enough to guarantee that Θ is indeed a Markov matrix. In practice, Γ and γ are not defined explicitly; they are fixed implicitly by the implementation of the communication transitions. In our experiments, we use a simple neighborhood system defined by

$$\mathcal{G}(S) = \{\tilde{S} \in \Omega \mid \exists!\, k \in [1..N_\mathrm{e}], \tilde{\mathbf{e}}_k \neq \mathbf{e}_k\}. \tag{53}$$

In other words, $\mathcal{G}(S)$ is the set of arrays in Ω that differ from S in exactly one element, and Θ generates candidate solutions by changing one element at a time. This mechanism satisfies the symmetric support and irreducibility conditions required for the probabilistic convergence of SA. The symmetric support means that if $\Theta(S, \tilde{S})$ is not equal to zero it implies that $\Theta(\tilde{S}, S)$ is not either equal to zero. The irreducibility condition means that any state can be reached from any other state in a finite number of moves (to refer to (Robini and Reissman 2013; Robini 2013) for technical details).

The transition matrix $\mathrm{P}(S_{n+1}|S_n)$ of the SA Markov chain $(S_n)_{n\in\mathbb{N}}$ is defined by

$$\mathrm{P}(S_{n+1} = \tilde{S} \mid S_n = S) = \begin{cases} \Theta(S, \tilde{S}) & \text{if } \Delta U \leq 0 \text{ and } \tilde{S} \neq S, \\ \Theta(S, \tilde{S})\, \exp(-\beta_n \Delta U) & \text{if } \Delta U > 0, \end{cases} \tag{54}$$

where $\Delta U = U(\tilde{S}) - U(S)$ is the energy variation associated with the transition $S \to \tilde{S}$. In other words, a transition with negative energy variation is accepted unconditionally, whereas a transition with positive energy variation at iteration n is accepted with probability $\exp(-\beta_n \Delta U)$; this probability is called the acceptation rate. The annealing theory (Robini 2013; Robini and Reissman 2013) suggests to control this rate by a piecewise-constant cooling sequence $(\beta_n)_{n\in\mathbb{N}}$ of the form

$$\beta_n = \beta_{\mathrm{inf}} \left(\frac{\beta_{\mathrm{sup}}}{\beta_{\mathrm{inf}}}\right)^{\frac{1}{\sigma-1}\left(\left\lceil\frac{n}{K}\right\rceil-1\right)}, \tag{55}$$

where β_{inf} is the initial inverse temperature, β_{sup} is the final inverse temperature, $\lceil\cdot\rceil$ is the ceiling function, and σ is the number of constant temperature stages, each of length K (so the total number of iterations is $N_{\mathrm{iter}} = \sigma K$).

To determine β_{inf} and β_{sup} (which depends on the energy function difficulty) the first step consists in randomly choosing an initial state S_0. Then a vector, say ΔU^+, is defined to store the first M positive variations of the energy function that occurs during the evolution of the Markov chain $(S_n)_{n\in\mathbb{N}}$ at infinite temperature (all transitions are accepted unconditionally). Finally β_{inf} and β_{sup} are computed solving

$$\sum_{i=1}^{M} \exp(-\beta\,(\Delta U_i^+)) \;= \chi\, M_{\mathrm{uphill}} \tag{56}$$

with $\chi_{\mathrm{inf}} = 0.85$ and $\chi_{\mathrm{sup}} = 0.005$ respectively. The number M of positive variations of the energy function must be set in accordance with the size of the optimization problem; for instance choosing M_{uphill} of the order of $100q$ is suitable for the case where Ω is a Cartesian product space included in $\mathbb{R}^q$ (Robini 2013).

II.C.3 Energy function

The energy function U is the heart of the 2D array design because its definition gives the objective to the optimization process. In general the aim of the energy function U is to control the shape of the BP in order to obtain an array that yields good image quality in terms of resolution (narrow beam width – Full Width at Half Maximum FWHM) and contrast (low Side and Grating Lobe Levels - SLL and GLL). To achieve this goal the BP can now be simulated under wideband conditions using the two acceleration techniques introduced in II.B and the energy function U can be defined using $\mathrm{BP}_S(R,\theta,\phi)$, the wideband BP of S. As a consequence, wideband and shape sensitive energy functions can be defined.

To compute the normalized Beam Pattern $\mathrm{BP}_{S_n}(R,\theta,\phi)$ of the array S at iteration n, the associated transmitted Pressure Field PF_{S_n} is first simulated using FIELDII (Jensen 1996; Jensen and Svendsen 1992)

$$\mathrm{BP}_{S_n}(R,\theta,\phi) = \frac{\max\limits_{t} \mathrm{PF}_{S_n}(R,\theta,\phi,t)}{\max\limits_{\theta,\phi,t} \mathrm{PF}_{S_n}(R,\theta,\phi,t)}, \tag{57}$$

where $\mathrm{PF}_{S_n}(R,\theta,\phi,t)$ is the one-way transmitted pressure field of S_n depending on spherical coordinates (R,θ,ϕ) and time t, the origin of which is the center of the probe layout.

As specified in II.B.1, in order to simulate $\mathrm{PF}_{S_n}(R,\theta,\phi,t)$, N_{PMP} Pressure Measurement Points (PMP) are positioned on a 3D spiral arm laying on a hemisphere of radius R_{f} (focal depth) so that no periodicity is introduced (or hidden) in the measurements. In the optimization, using a hemisphere of PMP allows taking into account the pressure field behavior over the full range of (θ,ϕ) angles and not only along two orthogonal directions.

II.D Simulated annealing workflow

Once the state space Ω, the communication mechanism Θ and the energy function U are defined, the number of iterations N_{iter} can be chosen based on the time and computational power available. The flowchart given in Figure 24 summarizes the different steps of the SA algorithm:

(A) Random choice of the initial solution $S_0 \in \Omega$ and computation of the initial pressure field (FIELD II) $\text{PF}_{S_0}(R, \theta, \phi, t)$ and associated energy $U(S_0)$. The initial and final inverse temperatures β_{inf} and β_{sup} are computed using the methods described in II.C.2.
(B) Generation of a new solution $\tilde{S}_n$ using the communication mechanism Θ described in section II.C.2.
(C) Acoustic simulation (FIELD II) to compute the PF update associated with the candidate solution $\tilde{S}_n$.
(D) Computation of the energy difference ΔU between the current solution S_n and the candidate solution $\tilde{S}_n$.
(E) Acceptation or rejection of the candidate solution: $\tilde{S}_n$ is accepted with probability $\min(\exp(-\beta_n \Delta U), 1)$.
(F) Update of the iterate S_{n+1}, which is either $\tilde{S}_n$ or S_n depending on the decision taken in step (E).
(G) Update of the iteration index and the inverse-temperature value.
(H) Output of the best solution S_{opti} encountered during the optimization process.

In summary, the energy function U specifies the goals in terms of acoustic performance (II.C.3) and the search of the optimal array is performed by exploring the finite state space Ω (II.C.1) using the communication mechanism Θ (II.C.2). The specificity of SA is that the probability to accept a transition $S \to \tilde{S}$ (step (E) on Figure 24) is controlled by a cooling sequence $(\beta_n)_{n \in \mathbb{N}}$.

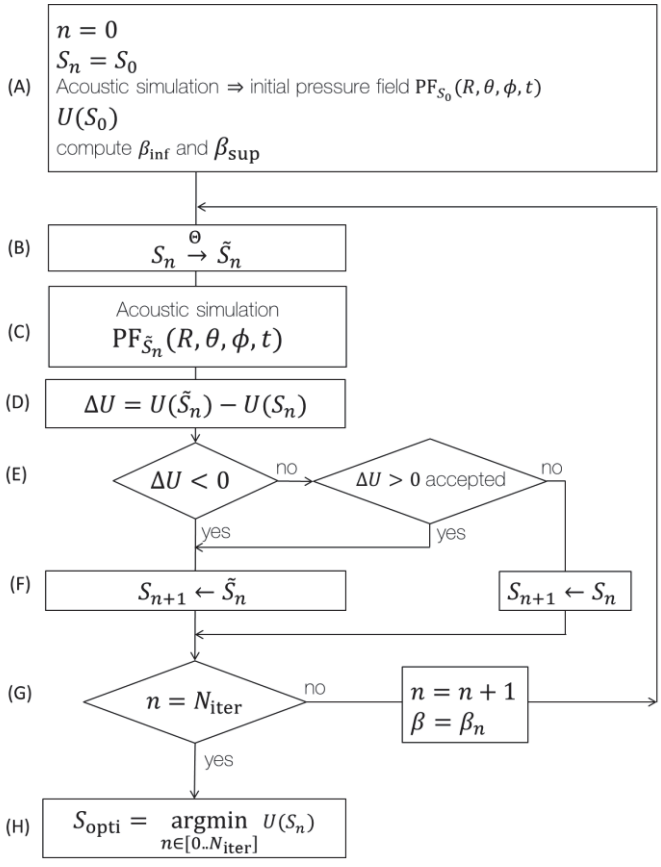


Figure 24 Simulated Annealing flowchart

II.E Discussion

In the analysis of the radiated pressure field at distances closer than the array radius r_{p}, the PMP^{*} can potentially limit the minimum value of R_{f}. Indeed, the minimum distance of the hemisphere is linked to the radius of the array, r_{p}, because the PMPs^{*} down (the lower group of PMP stars) must stay under the hemisphere of radius R_{f}.

An alternative solution to the signal synchronization using the PMPs^{*} consists in performing each time the zero-padding and the interpolation of all the signals vectors. It remains a more general solution but with the inconvenient of requiring an additional computation step which can potentially introduce some errors depending on the precision of the interpolation. Further investigations could be handled to evaluate the error implied by a series of interpolation strategies. The required time to perform the interpolation on the signals should then be compared to the required time to compute two extra RF signals per active element (one for each PMPs^{*}).

The optimization of the pressure field surrounding the array could be done at several depths (this will be further detailed in chapter III and chapter IV) by using several hemispheres of PMP. In this case, the value of h_{d} must be computed to place the group of PMPs^{*} down below the smallest hemisphere: in equation (42) R_f should be replaced by the radius of the hemisphere with minimum radius R_{min}. Similarly, considering h_{u} for the group of PMPs^{*} up in equation (43), R_f should be replaced by the radius of the hemisphere with maximum radius R_{max}.

A limitation of the fast pressure field update is linked to the initial hypothesis of linear propagation. Indeed, the field update is impracticable when a non-linear simulation is employed (F. Varray et al. 2011) and it is mandatory to compute the beam pattern considering the contributions of each element of the full array and not only of the element which is perturbed.

In future, an additional acceleration technique could be implemented by memorizing all the already explored individual contributions $\mathrm{PF}_{\mathbf{e}}$, so that only the simulation of the newly explored situations would be necessary. However, storing all the previously investigated active element positions may require a very large amount of memory, especially in the case of non-grid arrays.

II.F Conclusion

To speed-up the optimization of 2D sparse arrays for 3D ultrasound imaging two techniques were proposed in order to accelerate the acoustic simulations of the pressure field radiated by the transducer. The first technique is a sampling strategy that allows reducing the number of pressure measurement points. The second technique allows a fast update of the pressure field to avoid a simulation of the entire array at each iteration. The benefits of integrating realistic acoustic simulations in the 2D sparse array optimization framework are an improved distinctive capability between arrays new degrees of freedom (size, shape, orientation, excitation signal) available and the acoustic behavior of the tested arrays is more accurately modeled, closer to if they were physically manufactured during the optimization. The wideband simulation acceleration techniques also enable a flexible PF sampling strategy (density law can be adapted as desired) and a dimension reduction of the BP sampling to perform a smart beam profile analysis. The free-positioning of the elements on the aperture surface to optimize the design of 2D non-grid arrays is investigated in the next Chapter III.

III Chapter III Multi-depth radiation optimization of non-grid 2D ultrasound sparse arrays

III.A Introduction

In this chapter, we present a non-grid 2D sparse array design strategy to optimize the wideband beam pattern (BP) at several depths by permitting arbitrary positions of the array elements over the entire aperture. Properties and features of the proposed non-grid 2D sparse array optimization strategy are illustrated in Figure 25.

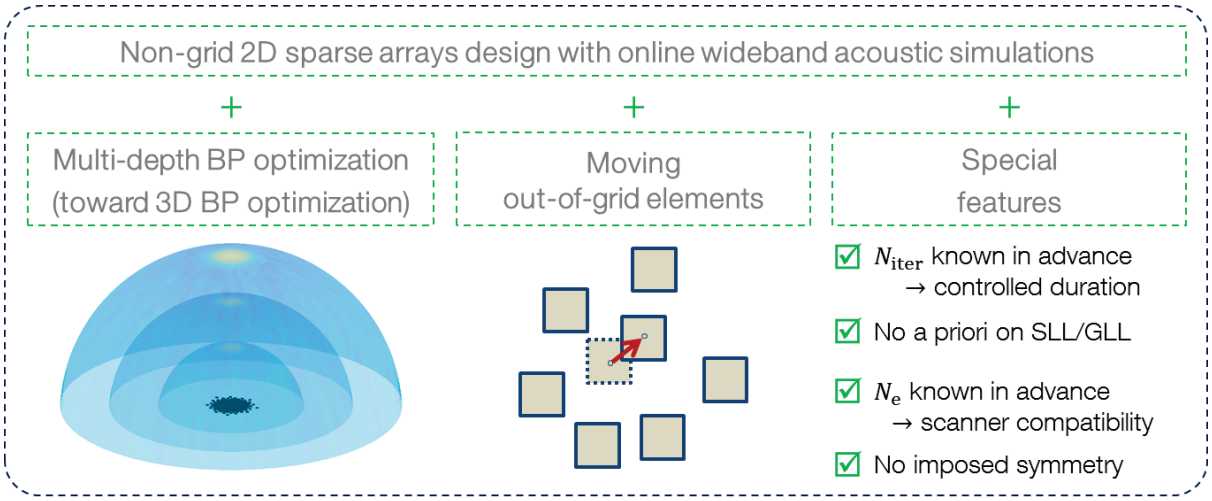


Figure 25 Properties of the proposed non-grid 2D sparse array optimization strategy: wideband acoustic simulations, multi-depth energy function and out-of-grid moving elements. Additional features such as the known number of iterations and the known number of active elements allow better controlling the duration of the optimization and the compatibility of the obtained results with a specific ultrasound scanner. The fact that no a priori is imposed neither on the symmetry nor on the targeted SLL/GLL opens the proposed method to non-expert users.

Multi-depth energy functions are introduced providing a better control of the BP behavior in the volume which is a step toward 3D BP optimization. The realistic acoustic simulation allows taking into account the radiated pressure field (PF) at several depths, and not only at the focal depth. In order to control the PF behavior at multiple depths, the acoustic performance is evaluated by means of fast wideband and shape sensitive realistic BP simulations (chapter II) repeated at each optimization step over several concentric hemispheres placed at defined depths. Moreover, three innovative energy functions, inspired by the PF radiated by a Blackman-tapered spiral array, are introduced and the performance are evaluated from 3D PF simulations as the one used in (Ramalli et al. 2015). The objective of the introduced energy functions is reducing, the Side Lobe Levels and Grating Lobe Levels (SLL and GLL) while maintaining a narrow main lobe at multiple depths. It is noteworthy that the lateral lobe reduction is performed without any a priori on the targeted levels: the goal is to yield the best SLL and GLL performance that is effectively achievable for given application.

In the literature, only (Choe, Oralkan, and Khuri-Yakub 2010) introduced a multi-depth (even 3D) energy function performing PF volume simulations using the FIELD II software. But the individual PF contributions of all elements were computed and stored in memory before running the optimization. This was possible because they assumed horizontal and vertical symmetry of the

layout and because the element positions were restricted to a 16×16 regular grid. The same approach is not convenient when moving the active elements out-of-grid on the surface of the layout (the required amount of memory to store all possible PF contributions would drastically increase). Let us recall here the advantage of out-of-grid 2D sparse array designs which are presented in section I.D.1: the grating lobes are reduced (even with inter-element distance greater than $\lambda/2$) thanks to a non-periodical spatial sampling. Because the spatial sampling condition is relaxed, it also enables the use of wider elements to increase the active surface of the aperture (sensitivity enhancement). However, wider elements present weaker steering capabilities so the element size must be kept small enough not to limit the field of view (FOV).

In the presented investigation, the fast BP computation allows optimizing the out-of-grid element positions without any BP pre-calculation or any a priori layout symmetry condition. The elements can arbitrarily move over the surface of the aperture which is restricted to a circular footprint since it is intended to have homogeneous radiating properties over the widest possible range of steering angles (Turnbull and Foster 1991). During the optimization process and for each new candidate solution the associated BP is simulated. At each iteration step of the optimization process, one element is freely translated (under non-overlapping conditions) and the ergonomic PF update (presented in II.B.2) is computed considering the newly translated element contribution to the radiated PF. In few words, non-grid 2D sparse arrays can be optimized under wideband conditions by freely translating the active elements on the surface of the layout (with no symmetry a priori) during the optimization process.

An important practical aspect of the proposed optimization strategy is that the final number of active elements can be fixed in advance. This can be relevant for instance to have a final number of element equal to the number of available independent channels on a scanner. Moreover, the finite time convergence properties of the simulated annealing algorithm (Kirkpatrick et al. 1983; Van Laarhoven and Aarts 1987; Robini 2013; Robini and Reissman 2013) also allows setting the number of iteration in advance. The required time to perform an optimization process can thus better be controlled.

III.B Methods

III.B.1 Non-grid 2D sparse array optimization

The non-grid 2D sparse array optimization is based on the framework presented in section II.C where the optimization problem formalism was introduced: an energy function U is minimized on a finite state space Ω using a Metropolis-type Simulated Annealing (SA) algorithm which is a Markov chain $(S_n)_{n\in\mathbb{N}}$ on Ω whose transitions are guided by a communication mechanism Θ and controlled by a cooling sequence $(\beta_n)_{n\in\mathbb{N}}$.

III.B.2 State space of non-grid 2D sparse arrays

The state space Ω of the possible solutions S, in which an optimal configuration S_{opti} has to be found, is the set of planar ($z_k = 0$ for all the elements) non-grid 2D sparse arrays with N_{e} non-overlapping active elements in a disk of radius r_{p}. Actually the elements of a non-grid 2D sparse array are located on a regularly sampled grid but the lattice has resolution $\ll \lambda$. In practice the grid spacing has no impact on the outputs as long as it is smaller than $\sim \lambda/100$. So, the degrees of

freedom are the element positions (x_k, y_k) on a fine Cartesian grid G superimposed on the disk of radius r_p, hence Ω is defined by:

$$\Omega = \left\{ \left((x_1, y_1), \dots, \left(x_{N_\mathrm{e}}, y_{N_\mathrm{e}}\right) \right) \in G^{N_\mathrm{e}} \mid \mathrm{A}_i \cap \mathrm{A}_j = \emptyset, \text{ for all } i, j \in [1..N_\mathrm{e}] \text{ such that i} \neq \text{j} \right\} \tag{58}$$

where A_k is the area occupied by the k-*th* element. A minimum inter-element distance (kerf) may also be parametrized according to the technology used to build the active elements in order to respect the constraints of the manufacturing process.

III.B.3 Communication mechanism

As stated in section II.C.2, the state space Ω is explored via the communication mechanism Θ. The possible transitions from a state S to a new candidate $\tilde{S}$ are defined by the neighborhood $\mathcal{G}(S)$ of state S. Here the allowed moves from S to $\tilde{S}$ are restricted to a single element translation (under non-overlapping conditions), hence $\mathcal{G}(S)$ is given by:

$$\begin{aligned} \mathcal{G}(S) = &\left\{ \tilde{S} \in \Omega \mid \exists! \, k \in [1..N_\mathrm{e}], \quad \tilde{S}(k) \neq S(k) \right\} \\ &\cap \left\{ \tilde{S} \in \Omega \mid \exists! \, k \in [1..N_\mathrm{e}], \quad 0 < \left\| \tilde{S}(k) - S(k) \right\|_2 < t_\mathrm{r} \right\} \end{aligned} \tag{59}$$

where $S(k)$ denotes the k-*th* element coordinates (x_k, y_k) and t_r is maximum translation value. In other words, the neighborhood $\mathcal{G}(S)$ is the set of arrays in Ω with only one translated element with respect to S and $\Theta\left(S, \tilde{S}\right)$ generates a candidate $\tilde{S}$ from the current state S by translating a single element by a distance in $]0, t_\mathrm{r}[$.

III.B.4 Energy function

III.B.4.a Multi-depth pressure field sampling

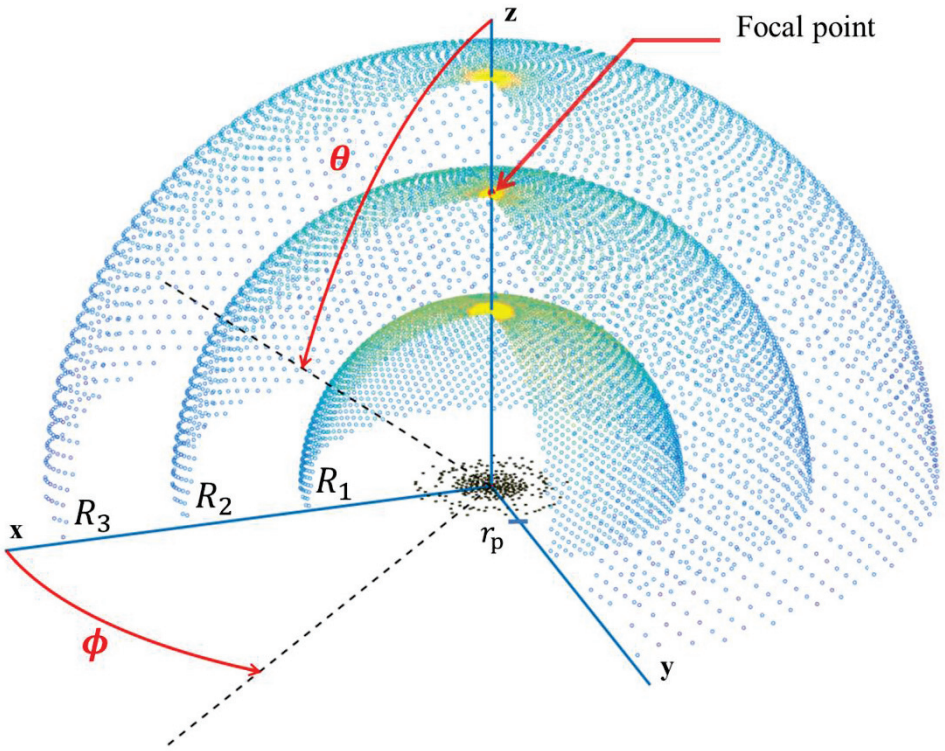


Figure 26 Reference coordinate system for the three hemispheres of radius R_1, R_2 and R_3, each used to estimate the pressure in N_{PMP} Pressure Measurement Points (PMP). The 2D sparse array probe of radius r_{p} is centered on the axes origin. The focal point is on the z-axis at depth z =R_2.

The proposed multi-depth BP optimization represents a first step toward an optimization of the 3D BP. It requires the introduction of multi-depth energy functions. Multi-depth energy functions can be defined and the acoustic radiated BP of the array can be optimized performing simulations at different depths. Our method allows adding hemispheres of PMP to take into account the pressure field behavior below and above the focal depth in the optimization (example with 3 hemispheres in Figure 26). In order to compute the normalized beam pattern $\mathrm{BP}_S(R,\theta,\phi)$ at several depths, N_{PMP} Pressure Measurement Points (PMP) are positioned on the 3D spiral arms laying on N_{H} hemispheres of radius $R_1,\ldots,R_{N_{\mathrm{H}}}$ (Figure 26). The PMP are homogeneously distributed along θ −angle as specified in section II.B.1. The multi-depth pressure field control is further discussed in III.D.3.

III.B.4.b Multi-depth energy function expressions

Three innovative multi-depth energy functions, inspired by the Blackman-tapered spiral array performance, are introduced. The common goal of the three energy functions U_1, U_2 and U_3 ((60), (61) and (65)) is to obtain a “good” resolution and contrast in the image. In other words, they are aimed at minimizing the SLL and GLL beyond the main lobe which has a fixed width $\theta_{\mathrm{ML}}(R)$ chosen as the - 30 dB main lobe width of the spiral array (Ramalli et al. 2015) beam pattern at depth R.

The first energy function $U_{1,R}$ is the square of the maximum of pressure outside the main lobe region at depth R:

$$U_{1,R}(S_n) = \left(\max_{(\theta,\phi)\notin L} \left(\mathrm{BP}_{S_n}(R,\theta,\phi) \right) \right)^2 \tag{60}$$

where $L(R) = \left\{ (\theta,\phi) \mid \theta < \frac{\theta_{\mathrm{ML}}(R)}{2} \right\}$ is the main lobe region delimited by half of $\theta_{\mathrm{ML}}(R)$.

The second energy function $U_{2,R}$ is the product of $U_{1,R}$ with the squared pressure ratio at depth R.

$$U_{2,R}(S_n) = U_{1,R}(S_n) \left(\frac{\mathrm{P}_{\mathrm{out}}(R)}{\mathrm{P}_{\mathrm{in}}(R)} \right)^2 \tag{61}$$

with

$$\mathrm{P}_{\mathrm{out}}(R) = \iint_{(\theta,\phi)\notin L} \left(\mathrm{BP}_{S_n}(R,\theta,\phi) \right) \mathrm{d}\theta \mathrm{d}\phi \tag{62}$$

and

$$\mathrm{P}_{\mathrm{in}}(R) = \iint_{(\theta,\phi)\in L} \left(\mathrm{BP}_{S_n}(R,\theta,\phi) \right) \mathrm{d}\theta \mathrm{d}\phi \tag{63}$$

Note that for convenience and generality the integral operator is used for summation in (62) and (63) but it is implemented by a discrete summation on the values measured by the PMP. A capital-sigma notation would be closer to the implementation but it is intended to present it in the continuous case not to lose the value of the continuous case as in (Diarra et al. 2013; Trucco 1999).

For the third energy function $U_{3,R}$, a sculpting mask $\mathrm{MASK}(R,\theta,\phi)$ is defined as follows:

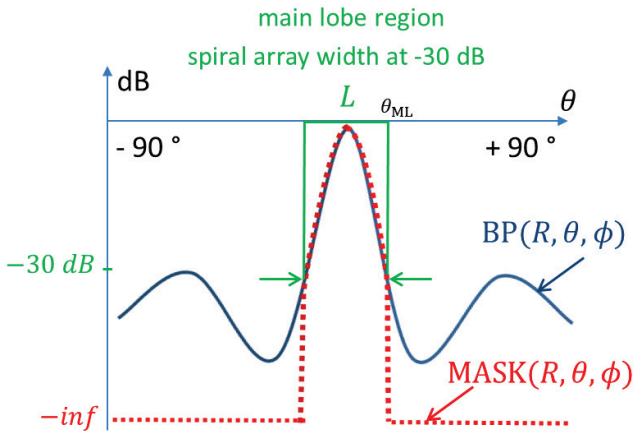
$$\mathrm{MASK}(R,\theta,\phi) = \begin{cases} \mathrm{IFT}\left(\mathrm{Blackman}\left(r_{\mathrm{p}} \right) \right) & \text{if } (\theta,\phi) \in L(R) \\ 0 & \text{if } (\theta,\phi) \notin L(R) \end{cases} \tag{64}$$

In other words, inside the main lobe region $L(R)$ the sculpting mask $\mathrm{MASK}(R,\theta,\phi)$ is given by the inverse Fourier Transform (IFT) of the Blackman window applied to a disk of radius r_{p}, and outside the main lobe region, the mask is set to zero. The introduction of such a sculpting mask creates a new constraint in the main lobe region: the main lobe shape must fit under the main lobe of the Blackman-tapered spiral array (Ramalli et al. 2015). The motivation to sculpt the main lobe shape is to better control the beam profile and avoid undesired lobes inside the main lobe region. The constraint outside the main lobe region is still to reach the minimum GLL and SLL: the sculpting mask is set to zero in this region. The energy function $U_{3,R}$ is the square of the product between the pressure ratio $\mathrm{P}_{\mathrm{out}}/\mathrm{P}_{\mathrm{in}}$ and $M_+(R)$, the maximum positive pressure difference with $\mathrm{MASK}(R,\theta,\phi)$:

$$U_{3,R}(S_n) = \left(M_+(R) \frac{\mathrm{P}_{\mathrm{out}}(R)}{\mathrm{P}_{\mathrm{in}}(R)} \right)^2 \tag{65}$$

where

$$M_+(R) = \max\left[\max_{(\theta,\phi)} \mathrm{BP}_{S_n}(R,\theta,\phi) - \mathrm{MASK}(R,\theta,\phi)\ ,\quad 0\right] \tag{66}$$



$$U_{1,R} = \left(\max_{(\theta,\phi)\notin L}\left(\mathrm{BP}(R,\theta,\phi)\right)\right)^2$$

$$U_{2,R} = U_{1,R}\left(\frac{\iint_{(\theta,\phi)\notin L}\mathrm{BP}(R,\theta,\phi)}{\iint_{(\theta,\phi)\in L}\mathrm{BP}(R,\theta,\phi)}\right)^2$$

$$U_{3,R} = \left(M_+(R)\left(\frac{\iint_{(\theta,\phi)\notin L}\mathrm{BP}(R,\theta,\phi)}{\iint_{(\theta,\phi)\in L}\mathrm{BP}(R,\theta,\phi)}\right)\right)^2$$

with $M_+ = \max(\mathrm{BP} > \mathrm{MASK})$

Figure 27 The three proposed energy functions $U_{1,R}$, $U_{2,R}$ and $U_{3,R}$ are all defined on the radiated beam pattern $\mathrm{BP}(R,\theta,\phi)$ at depth R considering the main lobe region L as the beam width of the spiral array at - 30 dB. In particular $U_{3,R}$ is shaping the main lobe using the sculpting MASK.

In summary (Figure 27),

$U_{1,R}$ measures the maximum of pressure outside the main lobe region $L(R)$.

$U_{2,R}$ combines $U_{1,R}$ with the pressure ratio $\frac{\mathrm{P_{out}}(R)}{\mathrm{P_{in}}(R)}$.

$U_{3,R}$ is similar to $U_{2,R}$ but with a mask sculpting the main lobe shape.

In the optimization, using several hemispheres of PMP allows taking into account the pressure field behavior at focal depth F but also below and above F (Figure 26). As a consequence $U_{1,R}$, $U_{2,R}$ and $U_{3,R}$ can be defined as multi-depth energy functions if the acoustic radiation of the array is optimized using simulations performed at different depths. To do so, N_H hemispheres of PMP are considered and the overall energy function is the weighted sum of the energy functions associated with each hemisphere

$$U^{N_\mathrm{H}}(S_n) = \sum_{i=1}^{N_\mathrm{H}} \rho_i U_{R_i}(S_n) \tag{67}$$

with ρ_i the weight coefficient of the energy function value $U_{R_i}(S_n)$ computed at depth R_i. Note that U_{R_i} can be either U_{1,R_i}, U_{2,R_i} or U_{3,R_i}.

III.B.5 Optimization setup

In this study the targeted application is for peripheral vessel imaging. The state space Ω, the communication mechanism Θ, and the acoustic parameters listed in Table III are the same for all of the sixteen performed optimizations.

About the state space Ω, Table III gives the amount of active elements ($N_\mathrm{e} = 256$), the central frequency ($f_\mathrm{c} = 7$ MHz), the bandwidth (72 %) and the aperture radius ($r_\mathrm{p} = 6\ \mathrm{mm} \sim 30\lambda$) of the considered arrays. The elements are squares of same size ($a_k = b_k = 200\ \mu\mathrm{m} \sim \lambda$) as the reference

spiral array to improve the sensitivity of the sparse array probe. The spatial region occupied by the each active element is broadened of a $\lambda/20$ safeguard margin in each direction assuming that below such an inter-element distance the electro-acoustic coupling effect would be too high to separate the elements (Felix et al. 2000). Each element orientation is set to $(\theta_k, \phi_k) = (0,0)$, the element weight is set to $w_k = 1$ (no apodization is applied to maximize the sensitivity of the array), the impulse response Imp_k is implemented by sampling at $F_s = 70$ MHz a 2.5-sine cycles at 7 MHz weighted by a Hamming window, and the excitation signal Exc_k is implemented by sampling at $F_s = 70$ MHz a 3-sine cycles at 7 MHz weighted by a Hamming window (62 % bandwidth).

About the communication mechanism Θ, the maximum translation value t_r is set equal to the elements size, i.e. $t_\mathrm{r} = 200$ µm. The evaluation of the initial and final inverse temperature β_inf and β_sup are computed as detailed in II.C.2 storing the energy variation implied by the first 2 560 uphill moves and solving equation (56).

About the multi-depth energy functions, a total of three hemispheres $N_\mathrm{H} = 3$ is setup (Figure 26) in order to check the performance before, after and at focal depth. The choice of radius R_1 = 15 mm, R_2 = 25 mm and R_3 = 35 mm (Table III) are motivated by the 25.3 mm depth of field (DOF) of the spiral array, i.e., the main beam pressure is expected to be still over - 6 dB from 15 mm to 35 mm depths. According to section III.B.4.b, for each depth R_1, R_2 and R_3, the main lobe width is set to $\theta_\mathrm{ML}(R_1) = 13.7\,°$, $\theta_\mathrm{ML}(R_2) = 5.5\,°$, and $\theta_\mathrm{ML}(R_3) = 9.6\,°$, i.e. the - 30 dB main lobe width of the spiral array at the respective depths. Moreover, each value of U_R is computed as specified in section III.B.4.b and the overall energy function U^{N_H} is the equi-weighted sum of the energy function values associated with each hemisphere:

$$U^{N_\mathrm{H}} = \sum_{i=1}^{N_\mathrm{H}} U_{R_i}. \tag{68}$$

TABLE III SIMULATION PARAMETERS

Acoustic simulation parameters	
Sampling frequency (F_s)	*70 MHz*
Sound speed (c)	*1540 m/s*
Excitation signal	*3-cycle sine at 7 MHz weighted by a Hamming window*
Focal distance (F)	*25 mm*
Central frequency (f_c)	*7 MHz*
Aperture radius (r_p)	*6 mm ($\sim 30\,\lambda$)*
Bandwidth (- 6 dB)	*72.6 %*
Element size (squares $a_k = b_k$)	*200 µm*
Number of elements (N_e)	*256*
Elements apodization (w_k)	*None*
Minimum kerf	*λ/20*
Communication mechanism Θ	
Maximum single translation value t_r	*200 µm*
Measurement hemisphere radius	
N_H=1	*25 mm*
N_H=3	*15, 25, 35 mm*

The performance of the spiral array (Ramalli et al. 2015) and those of the optimized non-grid 2D sparse arrays are compared in section III.C to evaluate how N_{iter}, N_{PMP}, N_{H}, and the expression of U impacted on the final results.

III.B.6 Post-optimization evaluation: 3D beam pattern performance metrics

Three-dimensional one-way pressure fields were simulated in a 3D volume ($L_{\mathrm{x}} \times L_{\mathrm{y}} \times L_{\mathrm{z}} = 40{\times}40{\times}30\ \mathrm{mm}^3$), compatible with peripheral vessel imaging, for each of the optimized array as performed in (Ramalli et al. 2015). The simulated volume was centered over the array starting at depth $z = 10\ \mathrm{mm}$ and it was sampled with a voxel resolution of $v_{\mathrm{res}} = \delta\mathrm{x} \times \delta\mathrm{y} \times \delta\mathrm{z} = 132\ \mu\mathrm{m} \times 132\ \mu\mathrm{m} \times 264\ \mu\mathrm{m} = 0.43\ \lambda^3$. For each solution, 81 steering angles (θ_{zx} = −32:8:+32 °, θ_{zy}= −32:8:+32 °) were considered and for each simulation the array performance was assessed through the six following parameters (Ramalli et al. 2015):

- The Side Lobe Level (SLL) was estimated as the log compressed ratio between the intensities of the highest secondary lobe and the main lobe.
- The lateral resolution was computed as the average − 6dB width of the main beam (full width half maximum - FWHM) in a plane perpendicular to the US propagation direction.
- The Depth Of Field (DOF) was measured as the − 6 dB length along the steering direction.
- The Side- to Main- lobe Energy Ratio (SMER) was computed as the log compressed ratio between the average intensity outside and inside the focal region, i.e. the region surrounding the focus delimited by the − 6dB iso-surface.
- The sensitivity was estimated as the ratio between the focus intensity and that resulted for the simulation of a 20 λ-radius spiral array having 0.5 λ-wide elements as used in (Ramalli et al. 2015).
- The steering angle error measured the difference between the principal direction of the − 6 dB iso-surface angle and the set steering angle.

Unfortunately the listed 3D performance metrics are not (yet?) computed in the energy functions (it is post-optimization evaluation). However, it is of great interest to analyze how the obtained results behave according to these 3D metrics even though only specific depths are considered in the proposed energy functions. The idea of integrating such evaluation during the optimization process is discussed in III.D.3.

III.C Optimized non-grid 2D sparse arrays and spiral array comparison

III.C.1 Number of iterations

N_{iter} influences the speed of the cooling sequence β_n, i.e. the greater is N_{iter} the slower is the temperature cooling down from $1/\beta_{\mathrm{inf}}$ to $1/\beta_{\mathrm{sup}}$. The optimization process always started from a 256-elements initial sparse array (chosen randomly by activating only $N_{\mathrm{e}} = 256$ elements of a full array with the same acoustic parameters as presented in Table III, which was optimized using $N_{\mathrm{PMP}} = 5000$ on each of the $N_{\mathrm{H}} = 3$ hemispheres (Table III) and U_1 as energy function expression. The effect of changing the number of iterations, $N_{\mathrm{iter}} = \sigma K$, was tested by setting σ to 2500, 5000,

7500, and 10000 while K was kept equal to N_e. The associated values of U_1 are presented in Table IV: the notations k and M in the name of the obtained arrays are the shortcuts for 10^3 and 10^6 respectively.

TABLE IV FINAL ENERGY FUNCTION VALUES FOR DIFFERENT N_{ITER}

Array ID	Iter 640k	Iter 1.28M	Iter 1.92M	Iter 2.56M
σ	2500	5000	7500	10000
N_{iter}	640 000	1 280 000	1 920 000	2 560 000
U_1 ($\times 10^3$)	33.3	25.9	19.6	17.7

The final values of U_1 associated with optimal states (Table IV) decrease when more iterations are done. This result confirms that the higher the number of iterations the higher the probability of reaching a global minimum (Van Laarhoven and Aarts 1987). As expected, the performance of the optimized arrays improved when increasing N_{iter}. In all the following experiments N_{iter} was fixed to the maximum tested ($N_{iter} = 2\ 560\ 000$), unless otherwise stated.

III.C.2 Number of pressure measurement points

The impact of the number of pressure measurement points (PMP) N_{PMP} on the final value of U_1 was assessed by optimizing the sparse array with N_{iter} = 1.28M, N_{H} = 3 and N_{PMP} = 500, 1000, 2000, 3000, 4000, and 5000 (Table V). The configuration obtained when using 3000 PMP (*PMP 3k*) yields the lowest energy function value. Since it provides a good angular resolution sampling for the beam pattern analysis ($\sim$ 30 PMP per degree on θ-angle), N_{PMP} was set to 3000 for the following optimizations.

TABLE V FINAL ENERGY FUNCTION VALUES ASSOCIATED TO THE OPTIMIZATION RESULTS FOR DIFFERENT N_{PMP}

Array ID	PMP 0.5k	PMP 1k	PMP 2k	PMP 3k	PMP 4k	PMP 5k
N_{PMP}	500	1000	2000	3000	4000	5000
U_1 ($\times 10^3$)	74.7	36.5	22.1	11.8	35.1	25.9

III.C.3 Number of hemispheres

The impact of using multi-depth energy functions with N_{H} = 3 measurement hemispheres was evaluated by comparing the optimized configurations obtained with the 1 HS and 3 HS versions of the energy functions U_1, U_2 and U_3. The optimization setup of the multi-depth approach is detailed in III.B.5. Figure 29 shows the layouts of the optimized configurations with 1 HS (U_1 1HS, U_2 1HS, U_3 1HS), 3 HS (U_1 3HS, U_2 3HS, U_3 3HS) and of the reference spiral array, while Figure 30 shows the associated radiating patterns at 0 ° and 30 ° steering angles[17].

Figure 30 qualitatively highlights the benefits of using multi-depth energy functions in both steered and not-steered cases. Indeed for the three definitions of U, at 15 mm and 35 mm depths, the 3HS profiles have much lower SLL than the 1HS profiles and this is valid also when the beam is steered by 30°. A quantitative analysis of the unsteered case can be done from Table VI.c and Table

[17] Supplementary material is available at https://www.creatis.insa-lyon.fr/site7/en/roux. The online material includes the videos illustrating the individual optimization run of the optimized arrays U_1 1HS, U_2 1HS, U_3 1HS, U_1 3HS, U_2 3HS, U_3 3HS. In the appendix II of this manuscript, the last video frame of the U_3 3HS optimization shows the end of the layout evolution, the plot of the energy function evolution, the plot of the acceptation rate evolution and the three optimized beam pattern profiles at depths 15 mm, 25 mm, and 35 mm.

VI.d showing that the SLL at 15 mm depth of U_1 3HS, U_2 3HS, and U_3 3HS are 14.3 dB, 12.3 dB and 13.6 dB lower than in the respective 1HS cases. Similarly, at 35 mm depth, the SLL for 3HS cases are 10.6 dB, 8.7 dB and 11.1 dB lower than for the respective 1HS. This denotes an uncontrolled behavior of the pressure field before and after the focal depth in the 1HS cases and it clearly enlightens the performance improvement thanks to the multi-depth approach. Moreover, even when no steering is done, the main lobes of the 1HS profiles are not centered around $\theta = 0°$ and the bias can reach up to 5 ° at depth R_1=15 mm. On the contrary, the 3HS profiles present a centered main lobe followed by a flat *plateau* up to θ= 40-45°.

However, analyzing Table VI.c and Table VI.d at the focal depth (R_2= 25 mm), with respect to the 1HS versions, the 3HS versions increase, on average, by 1.0 dB and 0.8 ° the SLL and the - 6 dB main lobe width, respectively. This indicates that, at the focal depth, for any expression of U, the 1HS version is slightly more efficient. A possible explanation could be that no compromises have to be done with the pressure behavior at other depths. In spite of the small performance improvement at the focal depth when using the single hemisphere approach, the uncontrolled behavior of the pressure field before and after the focal depth discards such solutions. This remark is corroborated by the 3D performance analysis obtained over 81 steering angles: Figure 31 and Table VII (group c and d) show that the 3D performance clearly improves in terms of SLL, DOF (especially its limited deviation), sensitivity and steering angles error while the resolution gets coarser when comparing 3HS and 1HS optimizations. For example U_3 3HS compared to U_3 1HS yields 2.2 dB reduction of the median SLL, 11.4 mm DOF increase (+75 %), 1.9 dB sensitivity increase, 1.1 ° angle error reduction (-65 %) for only 0.4 mm worse resolution (5% coarser than the spiral, Table VII). The same trend is observed with U_1 and U_2. It is worth noting that the multi-depth energy functions (3HS) strongly improves the steering angle precision (9 % better than the spiral array for U_3 3HS, Table VII); hence the proposed approach not only controls the focal point to be accurate but also leads the beam direction to be aligned with the desired steering angle.

In conclusion, the multi-depth energy function approach improves the array performance in terms of SLL, DOF, sensitivity and angle error even in steering condition and independently from the energy function expression. Although a tradeoff is done on the resolution (at focal depth), a more regular shape of the main lobe close to the array and a better alignment between the beam direction and the steering angle are obtained.

III.C.4 Energy function

The performance of the three optimized layouts U_1 3HS, U_2 3HS, and U_3 3HS and of the reference spiral array were evaluated. A qualitative comparison of the profiles shown in Figure 30 highlights that the energy function U_1 3HS leads to slightly higher SLL with respect to U_2 3HS and U_3 3HS, in both steered and unsteered cases. It can be observed that the spiral array presents a deeper trough at the bottom of the main lobe but also higher SLL than the three optimized results. More quantitatively, Table VII.d shows that U_1 3HS reaches the best resolution median (1.3 mm) but is not as close as U_2 3HS and U_3 3HS to the spiral arrays performance on the other criteria. Compared to the spiral array, U_2 3HS tends to improve the SLL (-0.9 dB) and reaches very similar results in terms of sensitivity (-0.2 dB), SMER (+0.0 dB), and DOF (+0.5 mm), while the resolution is getting slightly worse (+0.1 mm) and the angle error is increased by 0.2°. U_3 3HS is very competitive on SLL (-0.9 dB), DOF (+1.3 mm), SMER (+0.0 dB), sensitivity (+0.0 dB) and angle error (-0.1 °) but the resolution is a little coarser (+ 0.1 mm). Figure 28 helps to conduct an overall comparison among the

3HS optimized arrays and the spiral array. The array performance is represented with the worst case of each parameter close to the center of the radar plot and the best performance on the external web line.

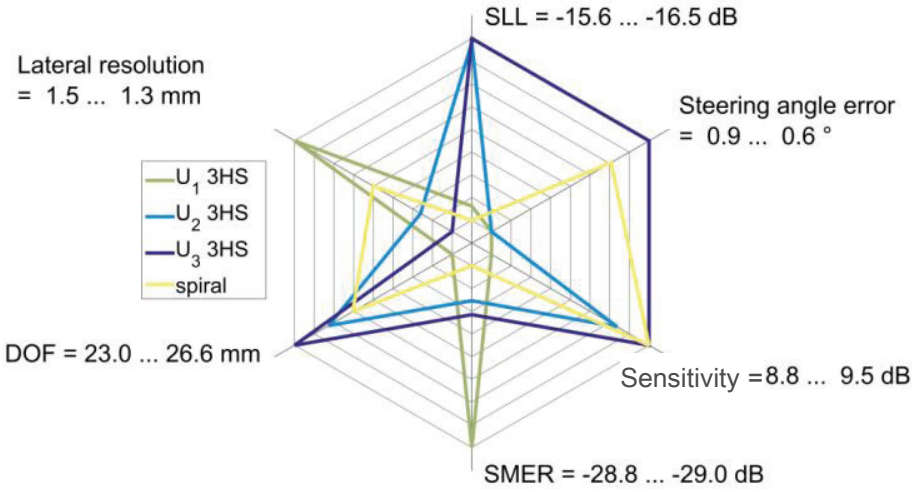


Figure 28 Radar plot comparison for U_1 3HS, U_2 3HS, U_3 3HS and the spiral array

To summarize, it may be concluded that the U_1 energy function, by its definition, tries to push down the SLL only once the main lobe is thinner than expected. Indeed until the entire main lobe gets inside the delimited main lobe region L, the outstripping part is considered as a lateral lobe with very high level compared to the real side lobes. Since the resolution constraint has priority on the contrast constraint, the U_1 energy function is not likely to balance the tradeoff between them. The U_2 expression starts to better integrate the tradeoff thanks to the pressure ratio that implies both a SLL reduction and a concentration of the acoustic energy in the main lobe. Major improvements are reached by U_3 because it also sculpts the main lobe shape.

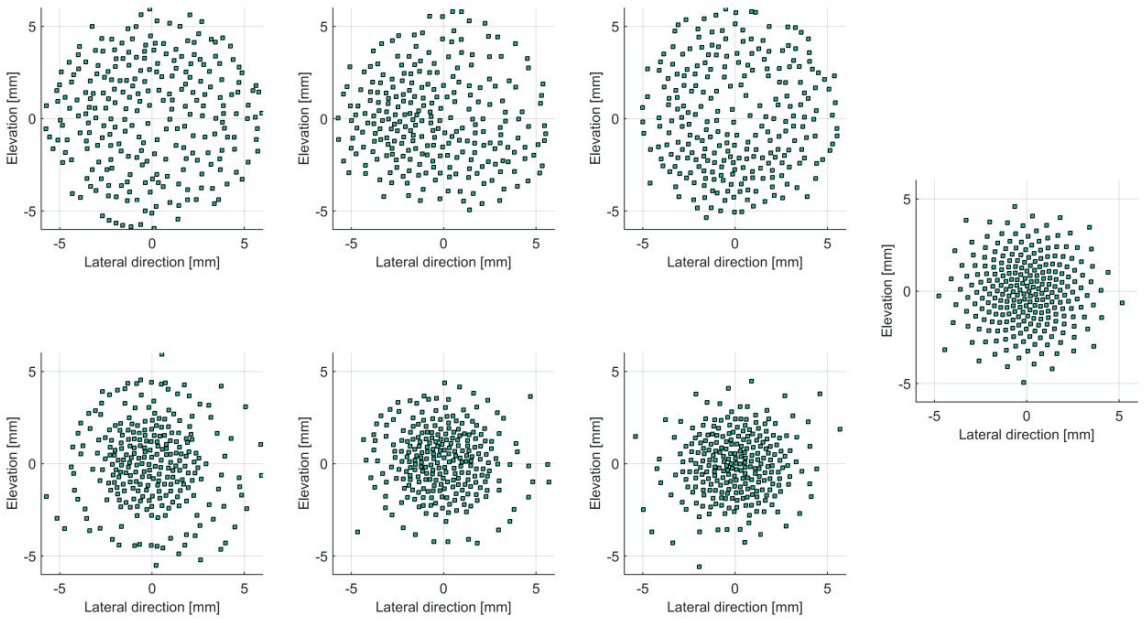


Figure 29 Layouts of the optimization results when using 1 hemisphere (top panels, from left to right: U_1 1HS U_2 1HS, U_3 1HS) and when using 3 hemispheres (bottom panels, from left to right: U_1 3HS, U_2 3HS, U_3 3HS). The layout of the Blackman-tapered spiral array is also shown on the very right hand.

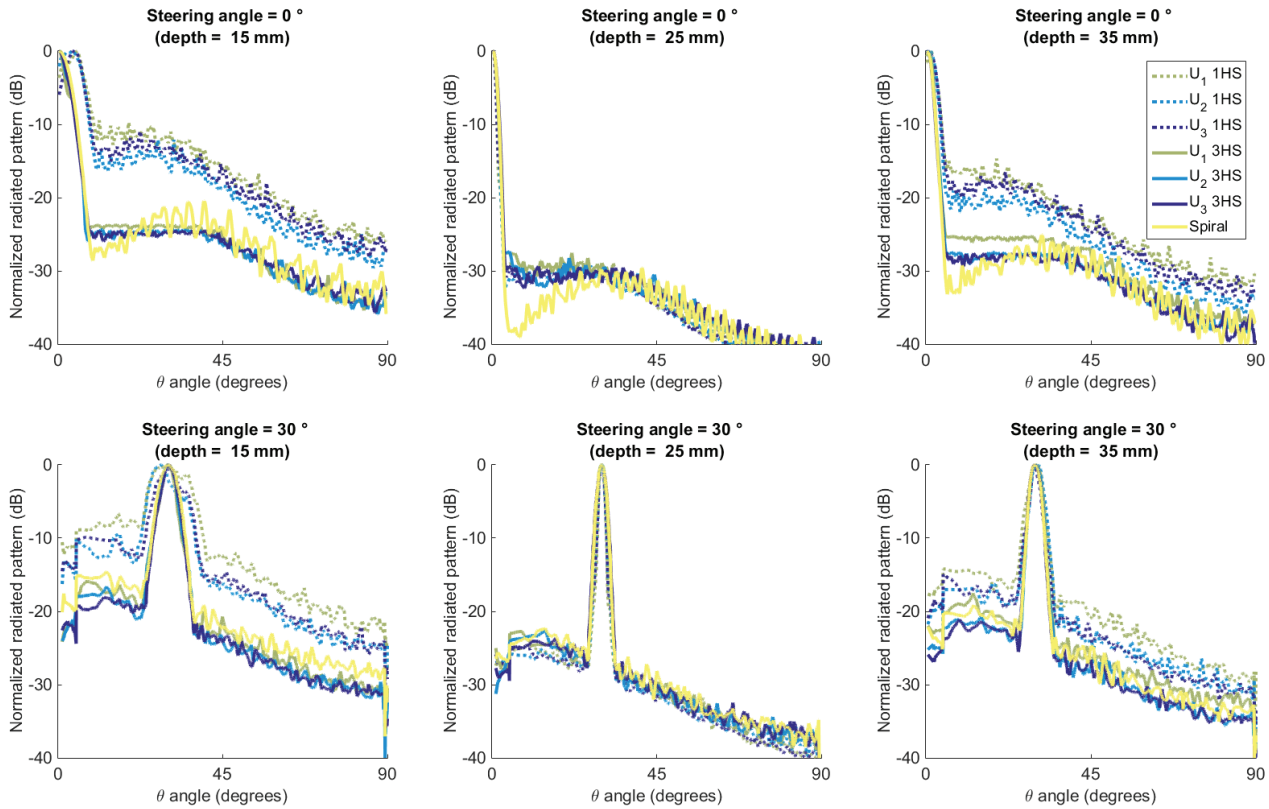


Figure 30 Radiated beam patterns at depths 15 mm (left), 25 mm (center) and 35 mm (right) of the optimization results and the spiral array. The steering angles were 0° (top panels) and 30 ° (bottom panels).

TABLE VI FOR EACH OPTIMAL ARRAY WE PRESENT THE OBTAINED SIDE LOBE LEVEL AND MAIN LOBE WIDTH ON THE THREE HEMISPHERES (HS) OF RADIUS 15 MM, 25 MM AND 35 MM.

	Optimization Setup					Side Lobe Level (in dB)			Main Lobe Width at -6dB (in degree)		
	Array ID	N	PMP (per HS)	N_H	U	15mm	25 mm	35 mm	15mm	25 mm	35 mm
a	Iter 640 k	0.64 M	5k	3	U_1	-20.1	-24.4	-19.8	3.0	1.9	4.2
	Iter 1.28 M	1.28 M	5k	3	U_1	-20.0	-24.8	-22.6	3.9	2.1	2.4
	Iter 1.92 M	1.92 M	5k	3	U_1	-21.1	-26.0	-23.5	4.0	2.1	3.9
	Iter 2.56 M	2.56 M	5k	3	U_1	-21.4	-24.9	-24.1	6.7	2.2	3.9
b	PMP 0.5k	1.28 M	0.5k	3	U_1	-17.4	-23.5	-17.5	5.1	2.0	4.3
	PMP 1k	1.28 M	1k	3	U_1	-19.5	-26.3	-19.8	3.0	2.1	4.5
	PMP 2k	1.28 M	2k	3	U_1	-20.3	-25.1	-22.9	7.5	2.1	4.2
	PMP 3k	1.28 M	3k	3	U_1	-22.3	-26.4	-24.4	5.4	2.0	4.0
	PMP 4k	1.28 M	4k	3	U_1	-19.5	-24.6	-24.1	4.2	2.1	3.4
	PMP 5k	1.28 M	5k	3	U_1	-20.0	-24.8	-22.6	3.9	2.1	2.4
c	U_1 1HS	2.56 M	3k	1	U_1	-9.4	-28.9	-14.7	14.1	1.6	6.1
	U_2 1HS	2.56 M	3k	1	U_2	-12.1	-29.3	-18.8	8.3	1.9	6.0
	U_3 1HS	2.56 M	3k	1	U_3	-10.9	-29.3	-16.5	12.2	1.6	6.6
d	U_1 3HS	2.56 M	3k	3	U_1	-23.7	-27.5	-25.3	4.6	2.2	3.8
	U_2 3HS	2.56 M	3k	3	U_2	-24.4	-27.4	-27.5	5.3	2.7	3.7
	U_3 3HS	2.56 M	3k	3	U_3	-24.5	-29.7	-27.6	6.1	2.6	3.4
	Spiral	-	-	-	-	-20.2	-29.3	-25.2	7.8	2.6	3.8

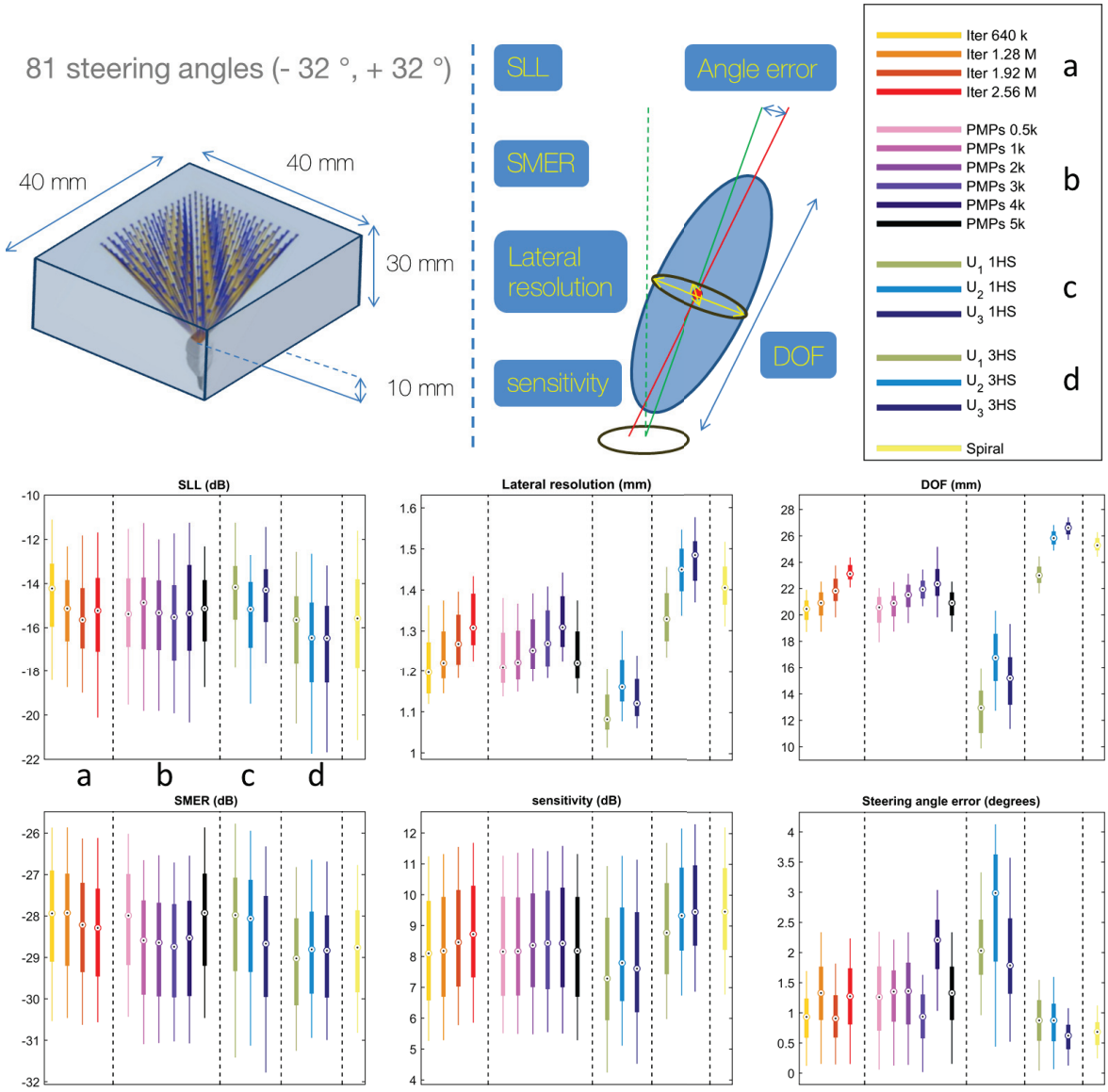


Figure 31 Side Lobe Level (SLL), Lateral resolution, Depth Of Field (DOF), Side- to Main- lobe Energy Ratio (SMER), sensitivity and steering angle error from the 3D pressure field analysis (81 steering angles). Simulations were done in a 40x40x30 mm^3 volume starting at z = 10 mm over the arrays

TABLE VII MEDIAN VALUES OF THE RESULTS PRESENTED IN FIGURE 31. THE 3D PERFORMANCE METRICS WERE EVALUATED OVER 81 STEERING ANGLES.

	Array ID	SLL (in dB)	Resolution (mm)	DOF (mm)	SMER (dB)	Sensitivity (dB)	Steering angle error (°)
a	Iter 640 k	-14.2	1.2	20.5	-27.9	8.1	0.9
	Iter 1.28 M	-15.1	1.2	20.9	-27.9	8.2	1.3
	Iter 1.92 M	-15.6	1.3	21.8	-28.2	8.5	0.9
	Iter 2.56 M	-15.2	1.3	23.1	-28.3	8.7	1.3
b	PMP 0.5k	-15.4	1.2	20.6	-28.0	8.2	1.3
	PMP 1k	-14.9	1.2	20.9	-28.6	8.2	1.4
	PMP 2k	-15.3	1.3	21.5	-28.6	8.4	1.4
	PMP 3k	-15.5	1.3	22.0	-28.7	8.4	0.9
	PMP 4k	-15.4	1.3	22.4	-28.5	8.4	2.2
	PMP 5k	-15.1	1.2	20.9	-27.9	8.2	1.3
c	U_1 1HS	-14.2	1.1	12.9	-28.0	7.3	2.0
	U_2 1HS	-15.2	1.2	16.8	-28.1	7.8	3.0
	U_3 1HS	-14.3	1.1	15.2	-28.7	7.6	1.8
d	U_1 3HS	-15.6	1.3	23.0	-29.0	8.8	0.9
	U_2 3HS	-16.5	1.5	25.8	-28.8	9.3	0.9
	U_3 3HS	-16.5	1.5	26.6	-28.8	9.5	0.6
	Spiral	-15.6	1.4	25.3	-28.8	9.5	0.7

III.D Discussion

2D sparse array probes were so far designed by optimizing the pressure field at only one distance from the array center. The proposed method, including acoustic simulations and multi-depth energy functions, represents a first step toward the 3D optimization of the pressure field around the array. The simulation results also suggest that great care should be taken in the definition of the optimization mask, which, on turn, depends on the targeted application.

The proposed method also raises specific aspects about the transducer design that are discussed below.

III.D.1 Layout characteristics

The results in Figure 29 show that the elements are significantly concentrated in the center of the aperture when the multi-depth (3HS), rather than the single-depth (1HS), energy functions are used. In the case of U_3 3HS they are even more concentrated in the center of the circular footprint than in the spiral array. In the 1HS cases, the highest density region appears to be eccentric. However, considering the circular footprint center as the reference, the bias of the element position barycenter is low (<λ) in most of the cases and it is further reduced with the multi-depth energy functions, Table VIII. A bias of the highest density region, for instance with U_2 1HS, may strongly increase the steering angle error (Figure 31 and Table VII).

TABLE VIII BARYCENTER BIAS OF THE 256 ELEMENTS FOR EACH OPTIMIZATION RESULTS SHOWED IN FIGURE 29

	$1HS$			$3HS$			spiral
	U_1	U_2	U_3	U_1	U_2	U_3	
Barycenter bias (λ)	0.8	2.0	0.3	0.1	0.8	0.4	0.1

In most previous optimization studies a circular symmetry was assumed as a pre-requisite to guarantee the same performance for any ϕ angle (i.e there should be no effect on the image quality if the probe is rotated around the z-axis). A further advantage of assuming the symmetry is the state space reduction, which favors a faster convergence of the algorithm. Even though in our method the elements can arbitrarily move over the aperture, the multi-depth approach yields a circular symmetry without any a priori constraint. Moreover, in both U_1 3HS and U_2 3HS and, at a minor extent in U_3 3HS, an annular array may be observed around the central dense cluster. Usually the resolution is linked to the size of the array and the lateral lobes are related to the sampling of the aperture surface. In this geometry, the annular array widens the size of the array and contributes to improve the resolution performance; while the central cluster contributes to reduce the GLL by the aperiodic space sampling and reduce the SLL by the density tapering. This hypothesis will be further investigated.

The element size is important since it impacts the field of view: the wider the elements, the weaker the steering capability of the array. Here, the choice of an element size close to λ aimed at compensating the sensitivity lack of sparse arrays by increasing the active surface. Yet, the optimized arrays yield good performance over a wide field of view (FOV) (- 32 °; + 32°).

III.D.2 Degrees of freedom and constraints

The fast pressure field update (section II.B.2) allows moving the elements out-of-grid during the optimization without continuous wave approximation. Moreover, the wideband acoustic simulations suggest exploring new degrees of freedom while considering more realistic constraints. Indeed the effects of the excitation signal, the impulse response and the element orientation and size could be taken into account in optimization setups exploring these new degrees of freedom. Furthermore, the proposed approach could permit possible geometrical constraints (like, e.g., the presence of "keep-out" areas on the array surface or curved aperture surface) to be included in the state space. Integrating special geometrical constraints could not be obvious designing the array with a deterministic analytical equation. This raises the possible interest of optimizing the array layout under geometrical constraints required by the application or some accessibility hardships that could influence the general shape of the array.

III.D.3 Multi-depth energy function

The introduction of the new energy functions that shape the beam pattern at several depths represent a first step toward a 3D control of the pressure field. Indeed, the multi-depth energy functions show how the quality of the transmitted beam can be shaped along the propagation direction. The multi-depth spatial coherence of the beam pattern can be seen as the temporal stability of the transmitted wave during its propagation. The scope of the multi-depth optimization was the extraction of 2D arrays design guidelines, from the obtained layouts, that could hopefully yield such a spatio-temporal coherence.

The multi-depth approach yields a strong reduction of the angle error when using 3HS (compared to 1HS, III.C.3), which is important to avoid artefacts implied from the misalignment between the desired steering angle and the direction of the beam. Moreover, even if a reflector in the side lobe region at depth R_1 (or R_3) is time-separated from a pixel reconstructed at depth R_2, it is worth having low side lobes at depths R_2 and R_1 (or R_3) if the same transmission is used to reconstruct pixels located at both depths.

How choosing a tradeoff among resolution, contrast and depth-of-field depends, in general, on the application. In particular, in our experiments the layout was optimized for peripheral vascular applications. For these applications, the deterministic approach presented in (Ramalli et al. 2015) yields satisfying performance with ultra-light computation load. The Blackman-tapered spiral array configuration was thus chosen as the reference to compare our approach. Actually the proposed energy functions (in particular U_3) were directly inspired by the reference spiral array and the resulting constraints directly fit with its radiated beam pattern, as detailed in III.B.4.b. The energy function design could be further developed to influence the tradeoff into a desired direction. For instance, in the presented multi-depth approach a different weight could be applied to each hemisphere, e.g. by giving more weight to the central hemisphere to favor the resolution at the expenses of DOF and image contrast. The distance between the hemispheres and their number could also be increased to optimize specific depths or to extend the DOF. Eventually, an effective 3D sculpt of the pressure field during the optimization process could be included, however with a significant increase of the computation load. A more powerful hardware, exploiting a graphic process unit (GPU) implementation of our method, would enable the extension to 3D-energy functions including 3D performance metrics (III.B.6).

III.D.4 Optimization setup

As observed in section III.C.1, the probability of reaching a global minimum increases with the number of iteration N_{iter}, as confirmed by the evolution of the energy function in Table IV. Moreover, Table VI.a shows that when N_{iter} increases from 0.64 M to 2.56 M the SLL decreases from - 20.1 dB to - 21.4 dB and from - 19.8 dB to - 24.1 dB at depths of 15 mm and 35 mm respectively. However, *Iter 1.92 M* array is an exception: it yielded the lowest SLL over the 25 mm hemisphere (Table VI) and the best median SLL value (Table VII.a). In spite of this isolated result, it is highly recommended to run as many iterations as possible in the available time since it increases the probability of reaching a lower minimum of the global energy (Table IV).

The influence of the number of PMP analyzed in section III.C.2 (Table VI.b) has highlighted the related serious impact: the SLL obtained with *PMP 3k* was 4.9 dB, 2.9 dB and 6.9 dB lower than *PMP 0.5k* at depths 15 mm, 25 mm, and 35 mm, respectively. The peaks of the radiated pattern are more likely to be missed at low resolution. However, according to the Table VI.b, *PMP 3k* yields better results in terms of SLL than *PMP 5k*. Indeed, the SLL of *PMP 3k* were 2.3 dB, 1.6 dB and 1.8 dB lower than for *PMP 5k* at depths 15 mm, 25 mm, and 35 mm, respectively. Moreover, in Table VII.b, the results obtained with *PMP 3k* on the 3D simulations of 81 steering angles were slightly better than with *PMP 5k* in terms of SLL (- 0.4 dB), DOF (+ 1 mm), ER (- 0.8 dB), sensitivity (+ 0.3 dB), and angle error (- 0.4 °). Because it makes the energy topology more difficult, increasing N_{PMP} should be accompanied by an increase of N_{iter} to hope for similar performance. This may explain why, when performing the same number of iterations, better results are obtained with N_{PMP} = 3000 rather than with N_{PMP} = 5000 in III.C.2.

III.E Conclusion

In this chapter, a novel non-grid 2D sparse array optimization strategy was presented. The innovation is based on the integration of acoustic simulations in the simulated annealing optimization process (chapter II) which enabled the definition of multi-depth energy functions that take into account the pressure field behavior at different depths. Moreover, thanks to the acoustic simulation, a wideband excitation signal, the pulse response and the size of the elements were taken into account during the optimization process. The effects of changing the number of iterations, the number of pressure measurement points, the number of hemispheres and, the energy function definition, were studied. Three different energy functions inspired by the Blackman tapered spiral array (here chosen as reference) were defined and their performance was compared. Sixteen optimized arrays were analyzed in terms of lateral lobes level, resolution, sensitivity, side- to main-lobe energy ratio, depth of field and steering angle error. The comparison criteria were based on performance metrics evaluated on 3D pressure field simulations at 81 steering angles (from - 32° to + 32°) for each array. An optimized array (illustration on Figure 32) provided slightly better performance than the reference spiral array. It was shown that sculpting the main beam shape at several depths leads to a circular symmetry of the layouts without imposing any geometrical constraint. The proposed optimization strategy can be extended to a general 2D sparse array optimization framework because it can lead to both out-of-grid (Chapter III) and, on-grid sparse array designs (chapter IV).

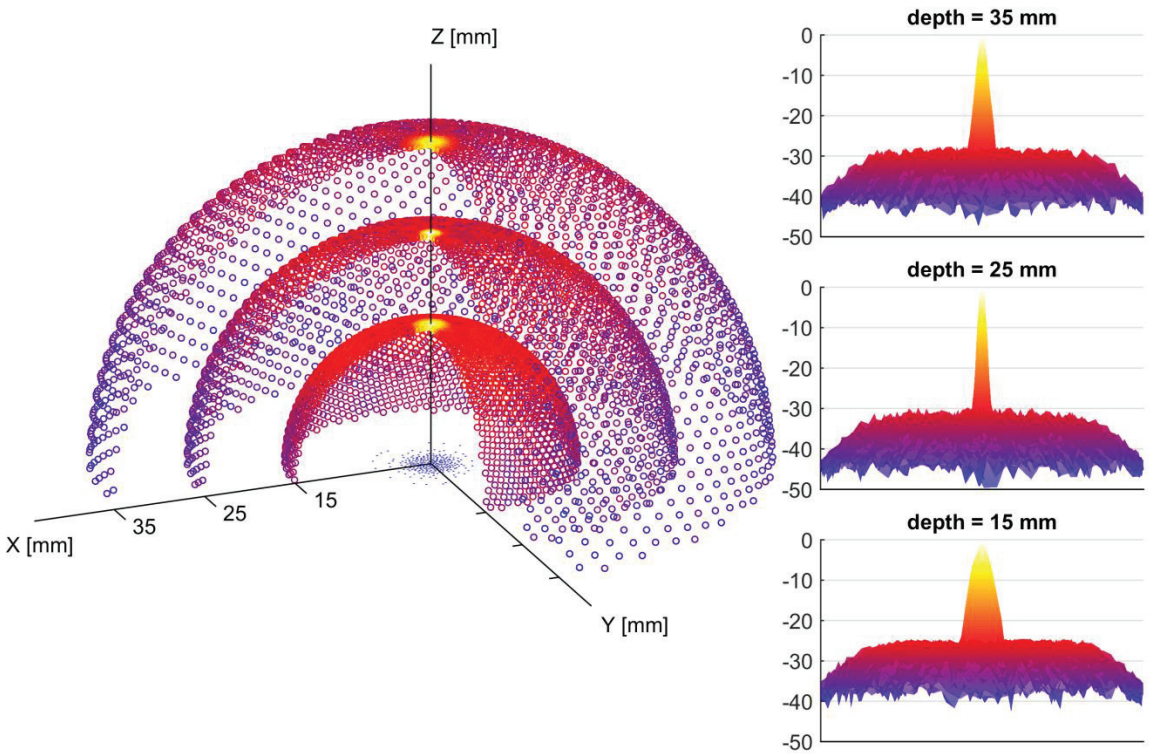


Figure 32 Illustration of the non-grid 2D sparse array (U_3 3HS) performance obtained with a multi-depth energy function optimizing the radiated beam pattern at depths 15 mm, 25 mm and 35 mm (focusing at F = 25 mm) and shaping the main lobe with a sculpting mask.

IV Chapter IV Wideband on-grid 2D array design optimization with fabrication constraints for 3D US imaging

IV.A Introduction

This chapter provides the formalism and the guidelines for a wideband optimization of on-grid (or gridded) 2D sparse arrays capable of fitting specific applications or fabrication/implementation constraints. As detailed in paragraph II.A, new degrees of freedom (element size and orientation, impulse response and excitation signal) can be explored while specific geometrical constraints imposed by the application (e.g. positioning/orientation on a convex surface for HIFU transducers) or the fabrication process (e.g., definition of a suitable spacing between elements to let the circuit lines go through the footprint) can be introduced. The scope here is to present how the proposed method behaves when integrating fabrication or design constraints are applied on the layout.

Moreover, an original tool helping for the definition of multi-depth energy functions is presented. The concept of a multi-depth energy function was already introduced in III.B.4 but the user-friendly interface allows a very intuitive definition of the multi-depth energy function. In particular, the sculpting mask (introduced in III.B.4.b) can be interactively setup using a graphical user interface (GUI) showing the sculpting mask over the beam profile of any ideal array chosen as reference.

Even though out-of-grid arrays have promising performance, as discussed in the previous chapter III.A, only a few prototype samples have been manufactured so far. On the other side, on-grid matrix array probes are already commercially available (B. Savord and Solomon 2003; Barnes, Bolorforosh, and Phelps 2005; Thomenius, Wodnicki, and Li 2010) and their production is expected to increase. For this reason, it looks valuable illustrating the general 2D sparse array optimization framework introduced in section II.C by the design of optimal sparse array probes whose elements are selected from an on-grid array. Simulated annealing is here used to find the smartest combination of a given number, N_{e}, of elements (the same for both TX and RX to maximize the array sensitivity) in a $N_{\mathrm{x}}N_{\mathrm{y}}$ 2D gridded array that produces the best possible acoustic performance for 3D ultrasound imaging. The number of active elements $N_{\mathrm{e}} < N_{\mathrm{x}}N_{\mathrm{y}}$ would ideally be equal to the number of channels available on the scanner to avoid the limitations mentioned in paragraphs I.C.2 and I.C.4. In short, it allows maintaining the acquisition sequence flexibility and potentially enables the obtained 2D array probes to be compatible with currently available scanners. A specific array design for echocardiography is presented to illustrate the general 2D sparse array optimization framework. It is applied to a 32x32 array of central frequency 3 MHz to select the 128, 192 and 256 elements that provide the best acoustic performance. It is shown that the 256-element optimized array yields sidelobe levels even lower (by 5.7 dB) than that of the reference 716-element circular and (by 10.3 dB) than that of the reference 1024-element array.

IV.B Finding the best configuration of N_e active elements in a $N_x N_y$ 2D array

IV.B.1 State space and design constraints

IV.B.1.a 1024-element reference array

Let us consider a generic 2D matrix with $N_x N_y$ elements (N_x columns by N_y rows of elements) and a scanner with $N_e < N_x N_y$ independent channels. Assuming that neither multiplexing nor micro-beamforming are used, N_e can be set equal to the number of independent channels that are usually available in clinical and research ultrasound scanners, i.e. $N_e = \{128, 192, 256\}$. In this example study any full 2D matrix with $N_x N_y$ elements can be considered. In particular, we focus on $\mathrm{ref1024}$ (one of the two references considered for the experimental validation), the effective planar matrix architecture of a 1024 ($N_x = N_y = 32$) active elements array Figure 33) manufactured by Vermon (Tour, France). The central frequency is 3 MHz (bandwidth 72 %), the elements are squares 249 μm wide and, the pitch (distance between consecutive elements centers) is $d = 300$ μm in both x and y directions. Assuming that $\mathrm{ref1024}$ is a gridded 2D array, the k-th element is indexed as the one located on the i-th line ($i \in [1..N_y]$) and j-th column ($j \in [1..N_x]$) of $\mathrm{ref1024}$ using $k = i + (j-1)N_y$, so that $k \in [1..N_x N_y] = [1..1024]$. The elements of $\mathrm{ref1024} = (\mathbf{e}_1, \dots, \mathbf{e}_{N_x N_y})$ are of the form (50) in II.C.1, where the components other than the positions (x_k, y_k) (the array is planar so z_k is set to zero for all elements) and the transmission delays τ_k are fixed in accordance with the array specifications: the element size is set to $a_k = 249$ μm, the element orientation is set to $(\theta_k, \phi_k) = (0,0)$, the element weight is set to $w_k = 1$ (no apodization is applied to maximize the sensitivity of the array), the impulse response Imp_k is implemented by sampling at $F_s = 30$ MHz a 2.5-sine cycles at 3 MHz weighted by a Hanning window, and the excitation signal Exc_k is implemented by sampling at $F_s = 30$ MHz a 3-sine cycles at 3 MHz weighted by a Hanning window (62 % bandwidth).

As mentioned in (Jean Provost et al. 2014), the effective matrix architecture of $\mathrm{ref1024}$ integrates a double pitch distance between the lines n° 8-n°9, n° 16-n°17 and n° 24-n°25 to facilitate the electronic connection (wiring pathway) of the piezo-electric elements. It results that, along the y direction, $N_d = 3$ deactivated lines (not indexed) are empty of elements (Figure 33). The k-th element (located on the i-th line and j-th column) has the following position coordinates:

$$\begin{cases} x_k = \left(j - \frac{N_x+1}{2}\right) d, \\ y_k = \left(\frac{N_y+N_d+1}{2} - \left(i + \left\lfloor \frac{i-1}{8} \right\rfloor\right)\right) d, \\ z_k = 0, \end{cases} \tag{69}$$

where $\lfloor \cdot \rfloor$ is the floor function.

The transmission delay τ_k is computed as follows considering a focal point at 40 mm on z-axis:

$$\tau_k = \frac{1}{c}\left(\sqrt{{x_f}^2 + {y_f}^2 + {z_f}^2} - \sqrt{\left(x_k - x_f\right)^2 + \left(y_k - y_f\right)^2 + \left(z_k - z_f\right)^2}\right), \tag{70}$$

where $c = 1540$ m/s is the speed of sound and $(x_f, y_f, z_f) = (0,0,40)$ mm is the position of the focal point.

IV.B.1.b 716-element reference array

It is known (Turnbull and Foster 1991; Brunke and Lockwood 1997; Austeng and Holm 2002; Diarra et al. 2013) that homogeneous radiating performance (with respect to the ϕ angle) are favored by using circular footprints. Hence a circular reference array $\mathrm{ref}716$ was introduced for comparison. This 716-element circular array results from the deactivation of the elements in $\mathrm{ref}1024$ that are outside a disk of radius $4.8\ \mathrm{mm}$ (centered at x=0, y=0). The diameter of the $\mathrm{ref}716$ aperture was chosen equal to the shorter side of $\mathrm{ref}1024$ to produce a circular footprint. The consequence of corner elements deactivation is that the secondary lobe energy along the axis of the array is reduced at the expense of a wider main lobe.

IV.B.1.c Effective state space

The state space Ω is based on $\mathrm{ref}1024$ (the corner elements are available during the optimization): Ω is isomorphic to the set of N_e-permutations of $\{\mathbf{e}_1, \ldots, \mathbf{e}_{N_\mathrm{x}N_\mathrm{y}}\}$. Indeed, $S = (\mathbf{e}_{k_1}, \ldots, \mathbf{e}_{k_{N_\mathrm{e}}}) \in \Omega$ if and only if $k_u \in [1..1024]$ for all $u \in [1..N_\mathrm{e}]$ and $k_u \neq k_v$ if $u \neq v$. In a nutshell, a given solution $S \in \Omega$ is a 2D sparse array with N_e active elements in the full 1024-elements matrix array.

IV.B.2 Communication mechanism

In this example study, the communication mechanism Θ is implemented by moving a single element from its current position to an available (i.e., non-active) neighboring position in an 8-nearest spatial neighborhood system. This spatial neighborhood system enters into the definition but should not be confused with the communication neighborhood system $\mathcal{G}$ defined in section II.C.2: for every array S, $\mathcal{G}(S)$ is the set of arrays $\tilde{S}$ that differ from S in exactly one element $\tilde{\mathbf{e}}_k$ located in an available position in the 8-nearest spatial neighborhood of $\mathbf{e}_k$.

Because of the boundary constraints, the number of candidate positions around a given element depends on the spatial location of this element: 3 in a corner, 5 on the border, and 8 elsewhere. The double pitch separating the elements of lines n° 8-n°9, n° 16-n°17 and n° 24-n°25 has no impact on the neighborhood structure, as if there were no gaps. Any no-occupied position in an element neighborhood can be picked up with the same probability, and the occupied neighboring positions cannot be selected.

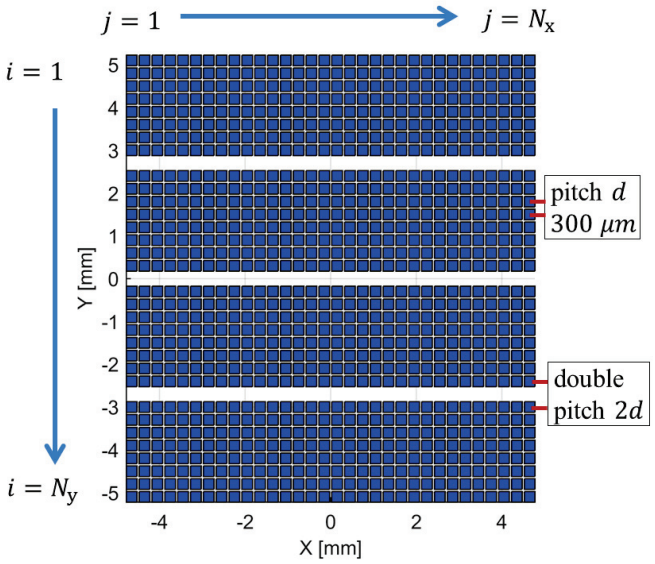


Figure 33 Layout of the 32×32 elements 2D array matrix ref1024 with double pitch distance between lines 8-9, 16-17 and 24-25 to facilitate the electronical connections as described in (Jean Provost et al. 2014).

IV.B.3 Energy function

IV.B.3.a Shaping of the multi-depth BP with a mask

The normalized Beam Pattern $\mathrm{BP}_{S_n}(R,\theta,\phi)$ of the array S at iteration n is computed from the associated transmitted Pressure Field $\mathrm{PF}_{S_n}(R,\theta,\phi,t)$ - section II.C.3, in the equation (57). In order to simulate $\mathrm{PF}_{S_n}(R,\theta,\phi,t)$, N_{PMP} Pressure Measurement Points (PMP) are positioned on each 3D spiral arm laying on the N_{H} hemispheres of radius $R_1,\ldots,R_{N_{\mathrm{H}}}$ surrounding the array respecting the procedure detailed in II.B.1. So multi-depth energy functions can be defined as the weighted sum of the energy functions associated with each of the N_{H} hemisphere (equation (67), section III.B.4.b). A specific array design for echocardiography is presented to illustrate the general method. In this example study $N_{\mathrm{H}} = 3$ and $N_{\mathrm{PMP}} = 3000$ with R_1= 30 mm, R_2= 40 mm (focal depth) and R_3= 50 mm (Figure 34). Similarly to the energy function defined as U_3 (equation (65), section III.B.4.b), the acoustic radiation of the array is here optimized shaping the multi-depth BP with a sculpting mask. A graphical user interface was designed as an innovative tool to easily define the sculpting mask that shapes the BP (section IV.B.3.b).

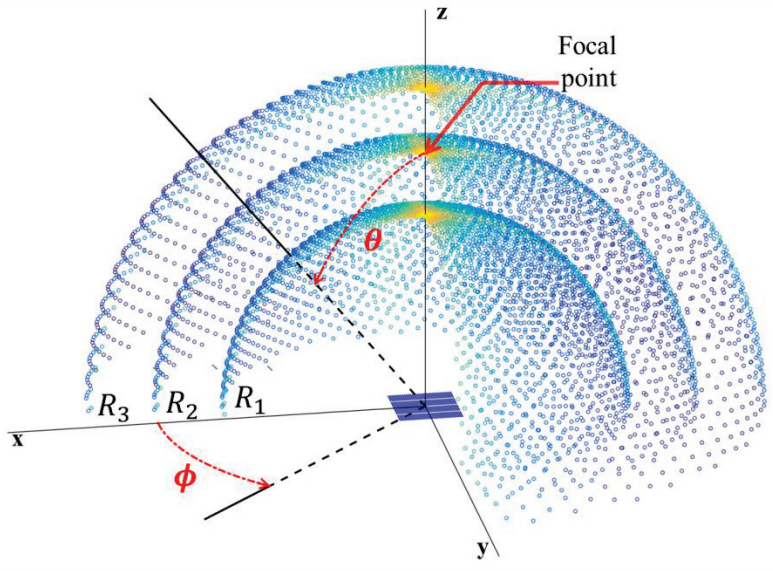


Figure 34 Example of three hemispheres of Pressure Measurement Points (PMP) around ref1024, the reference 32×32 elements 2D array with (θ, ϕ) the spherical angles convention where θ is the angle between a point and the z-axis and ϕ is the angle between the projection of this point in the xOy plane and the x-axis. The focal point is located at depth R_2 on the z-axis.

IV.B.3.b A graphical tool to design the sculpting mask

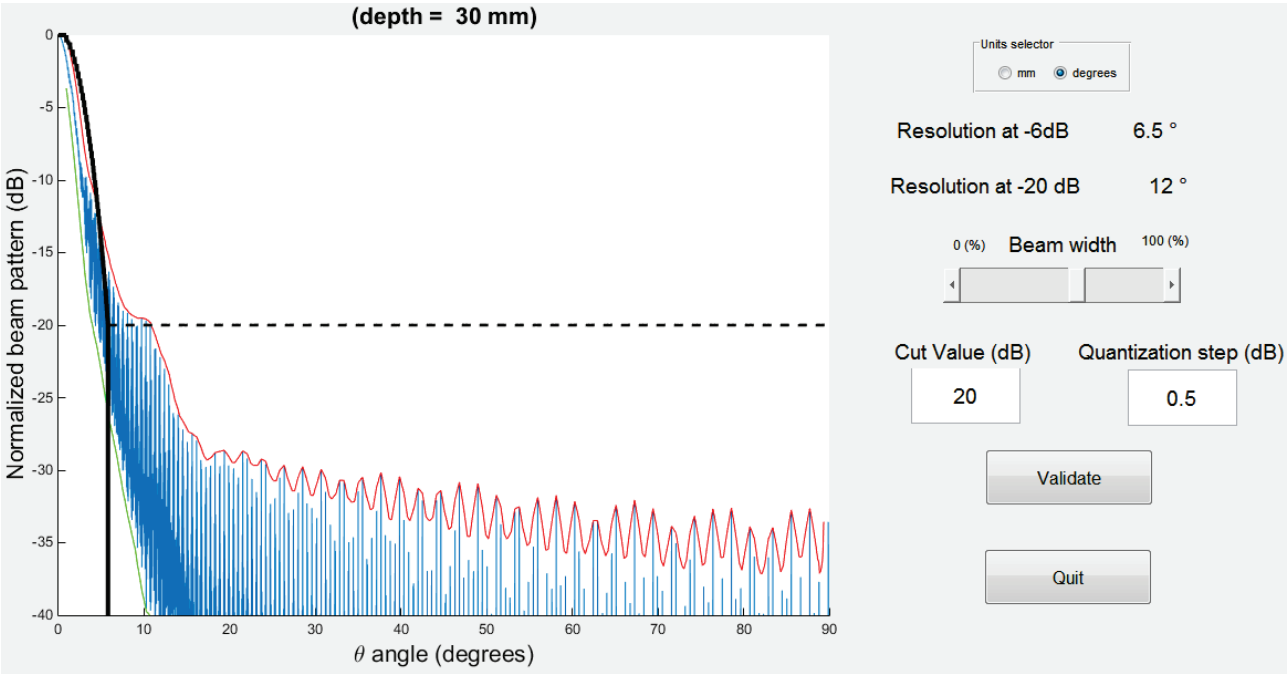


Figure 35 Screenshot of the Graphical User Interface (GUI) used to define the sculpting mask shape based on the beam pattern (BP) of the 1024-element reference array ref1024: the blue line displays the BP value for each pressure measurement point and the red line is the worst case envelope. The beam width constraint, the cut value $C(R)$ (dotted black line) and, the quantization step q_{mask} can be interactively adjusted to define the shape of the sculpting mask (full black line) at each depth where the beam pattern is simulated.

At each depth R where $\text{BP}_S(R, \theta, \phi)$ is simulated, a sculpting mask $\text{MASK}\,(R, \theta, \phi)$ is defined as follows to better control the main lobe shape and reduce the lateral lobes:

$$\text{MASK}\,(R, \theta, \phi) = \begin{cases} f(R, \theta) & \text{if } (\theta, \phi) \in L(R), \\ 0 & \text{if } (\theta, \phi) \notin L(R). \end{cases} \tag{71}$$

Here $L(R) = \{(\theta, \phi) \mid \theta < \theta_{\mathrm{ML}}(R)\}$ is the main lobe (ML) region at depth R delimited by the angle $\theta_{\mathrm{ML}}(R)$. Inside $L(R)$, MASK is given by the function $f(R, \theta)$ which sculpts the ML shape while outside $L(R)$, MASK is set to zero in order to minimize the GLL and SLL.

As a tool to define MASK, a graphical user interface was created to overlap the $\mathrm{MASK}(R, \theta, \phi)$ over $\mathrm{BP}_{\mathrm{REF}}(R, \theta, \phi)$, the BP of any REF array chosen as reference (Figure 35). This tool can be used to adjust both the definition of the function $f(R, \theta)$ and the angle $\theta_{\mathrm{ML}}(R)$ at each depth R.

To make the ML shape fit under $\mathrm{MASK}\ (R, \theta, \phi)$ and concentrate the acoustic energy inside $L(R)$, $U_R(S)$ is defined as the square of the product between $M(R)$, the maximum of pressure above $\mathrm{MASK}\ (R, \theta, \phi)$, and the pressure ratio $\mathrm{P_{out}}(R)/\mathrm{P_{in}}(R)$ respectively

$$U_R(S) = \left(M(R)\left(\frac{\mathrm{P_{out}}(R)}{\mathrm{P_{in}}(R)}\right)\right)^2, \tag{72}$$

with

$$\mathrm{P_{out}}(R) = \iint_{(\theta,\phi)\notin \mathrm{L}} \left(\mathrm{BP}_S(R, \theta, \phi)\right)^2 \mathrm{d}\theta \mathrm{d}\phi, \tag{73}$$

and

$$\mathrm{P_{in}}(R) = \iint_{(\theta,\phi)\in L} \left(\mathrm{BP}_S(R, \theta, \phi)\right)^2 \mathrm{d}\theta \mathrm{d}\phi. \tag{74}$$

In this study U_R is defined by the sculpting function $f(\theta, R)$ and the angle $\theta_{\mathrm{ML}}(R)$ (delimiting the ML region) which are computed at each simulation depth using the graphical user interface (Figure 35) with $\mathrm{ref1024}$ as the reference ($\mathrm{ref1024}$ was used instead of $\mathrm{ref716}$ because it represents the set of available positions for the N_{e} elements during the optimization). The function $f(\theta, R)$ is defined as the inverse Fourier transform (IFT) of a Nuttall window (Nuttall 1981). Then $\theta_{\mathrm{ML}}(R)$ is computed as the beam width of $f(\theta, R)$ at $-\mathrm{C}(R)$ dB where $\mathrm{C}(R)$ is the cut value at depth R. The GUI allows adjusting interactively both the Nuttall window size and the cut value $\mathrm{C}(R)$ so that it is related with reference $\mathrm{BP}_{\mathrm{ref1024}}(R, \theta, \phi)$ over which the MASK is displayed (Figure 35). Finally, the resulting MASK is quantized by steps of q_{mask} dB to avoid a too strict main lobe constraint for very small values of θ.

In this example study the cut value was the same at the three depths: $\mathrm{C}(R_1) = \mathrm{C}(R_2) = \mathrm{C}(R_3) = -20$ dB and the size of the Nuttall window was adjusted, at each depth, to be close to the resolution yielded by $\mathrm{ref1024}$ at focal depth R_2. So the main lobe regions $L(R_1)$, $L(R_2)$ and, $L(R_3)$ were delimited by $\theta_{\mathrm{ML}}(R_1) = 6.0\,°$, $\theta_{\mathrm{ML}}(R_2) = 5.4\,°$ and, $\theta_{\mathrm{ML}}(R_3) = 6.9\,°$ which are respectively $56\,\%$ (R_1), $105\,\%$ (R_2) and $125\,\%$ (R_3) of the half beam widths at - 20 dB of $\mathrm{ref1024}$. Incidentally, it corresponds to $98\,\%$ (R_1), $150\,\%$ (R_2) and $148\,\%$ (R_3) of the respective half beam widths at - 20 dB of $\mathrm{ref716}$. The quantization step was set to be $q_{\mathrm{mask}} = 0.5$ dB.

At the end, each value of U_R was computed as specified in (72) and the overall energy function $U^{N_{\mathrm{H}}}$ was the equi-weighted sum of the energy function values associated with each hemisphere.

IV.B.4 Optimization setup and random design comparison

The optimization process was launched three times with the setup described above and a number of elements $N_{\mathrm{e}} = \{128, 192, 256\}$ to obtain three optimized sparse arrays hereafter

designated as opti128, opti192 and opti256 respectively. The number of iterations $N_{\text{iter}} = \sigma K$ was fixed by dividing the available computation time (168 hours – one week is acceptable for a task duration in a complete probe design pipeline) by the time required to complete a single iteration (0.46 s). In order to give to all of the elements a chance to be moved during each of the σ temperature stages, K was set equal to N_{e} and σ resulted equal to 5000. Thanks to a speed-up of the PF update (section II.B) the number of iterations N_{iter} achievable in a given amount of time is about 70 times greater than that with a standard implementation.

An additional experiment was launched with the same setup as the one that led to opti256 but with all transitions $S_n \rightarrow S_{n+1}$ accepted unconditionally (infinite temperature). The best encountered array, i.e. the array associated with the lowest energy function value, obtained during this "random" exploration of the solutions is designated as rand256. Because rand256 is not designed with the full optimization process (the temperature is not cooled down and stays and infinite value during the N_{iter}= 1 280 000 exploration steps) it is not considered as part of the "optimized arrays" in this study.

IV.B.5 Performance analysis

IV.B.5.a 3D beam pattern

3D one-way pressure fields were simulated in a 3D volume ($L_{\text{x}} \times L_{\text{y}} \times L_{\text{z}} = 100 \times 100 \times 40\ \text{mm}^3$) for all optimized and reference arrays. The simulated volume was centered over the array starting at depth $\text{z} = 20\ \text{mm}$ and it was sampled with a voxel resolution of $v_{\text{res}} = \delta\text{x} \times \delta\text{y} \times \delta\text{z} = 667 \times 667 \times 667\ \mu\text{m}^3 = 0.43\ \lambda^3$. For each solution, 81 steering angles (θ_{zx} = − 32:8:+ 32 °, θ_{zy}= − 32:8:+ 32 °) were considered, and for each simulation the array performance was assessed through the same parameters already defined in III.B.6: Side Lobe Level (SLL), Lateral resolution, Depth Of Field (DOF), Side- to Main-lobe Energy Ratio (SMER) and Sensitivity. The only differences with the metrics presented in chapter III are that the angle error is not displayed in the results (section IV.D.3) and that the sensitivity is normalized on the reference array ref1024.

The corresponding simulation results are presented in IV.C.3 where the boxplots illustrate the distribution of the performance over the 81 tested steering angles.

IV.B.5.b 3D imaging

The imaging capability of the optimized, the random and the reference arrays are compared using a resolution phantom and a contrast phantom. For each array and each phantom, two orthogonal B-mode images (XZ plane when $\phi = 0$ and YZ plane when $\phi = 90°$) were reconstructed with 90° sector angle coverage (- 45°, + 45°) and maximum depth 70 mm. The 90° sector was scanned transmitting 180 beams, focused at depth 40 mm, with 0.5° step between each steering angle. For each transmitted beam a dynamic focalization was applied in reception to beamform the corresponding line in the image. The sector scan images were finally computed as the log compression of the interpolated 180 post-beamforming RF-lines.

The resolution phantom consists of 5 scatterers equi-spaced by 5 mm along the z-axis, with the middle one at the 40 mm focal depth. The lateral resolution was evaluated as the FWHM of the Point Spread Functions of these scatterers. To qualitatively assess the imaging capability of the

arrays with a 30° steering angle, 4 additional scatterers were added in the phantom at respective positions $\{(-23,0,40),(23,0,40),(0,-23,40),(0,23,40)\}$ mm.

The contrast phantom consists of a 3D anechoic cyst of radius 7.5 mm located at 40 mm depth. A total of 1 750 000 scatterers were randomly placed in a volume delimited by x = [- 25 , 25] mm, y = [- 25 , 25] mm and z = [20 , 60] mm (0). Considering the resolution cell of $\mathrm{ref}1024$ at the focal point, it corresponds to 19.6 scatterers per resolution cell of 1.12 mm^3.

The contrast to noise ratio was computed according to:

$$\mathrm{CNR} = 20\log_{10}\left(\frac{|\mu_{\mathrm{in}}-\mu_{\mathrm{out}}|}{\sqrt{(\sigma_{\mathrm{in}}^2+\sigma_{\mathrm{out}}^2)/4}}\right) \tag{75}$$

where $\mu_{\mathrm{in}}/\mu_{\mathrm{out}}$ and $\sigma_{\mathrm{in}}/\sigma_{\mathrm{out}}$ correspond to the respective mean and standard deviation of the B-mode image module inside/outside the cyst. For the evaluation, the inside region was delimited by a circle of radius $7.45\ \mathrm{mm}$. The outside region of the cyst was delimited by an inner circle of radius $7.55\ \mathrm{mm}$ and an outer circle of radius $9\ \mathrm{mm}$.

IV.B.5.c Robustness

To test if the presented results were robust when changing the initial state S_0, the same optimization setup was performed ten times, each time starting from a different initial state. Because of the identical optimization setup the ten obtained results are designated as “clones”. The optimization setup was identical to the one used with opti256 but the main lobe regions $L(R_1)$, $L(R_2)$ and, $L(R_3)$ were respectively delimited by $\theta_{\mathrm{ML}}(R_1) = 4.1°$, $\theta_{\mathrm{ML}}(R_2) = 5.0°$, $\theta_{\mathrm{ML}}(R_3) = 6.5°$ which are $75\ \%$, $106\ \%$ and $135\ \%$ of the half beam widths at - 20 dB of opti256 at the same depths R_1, R_2 and R_3. The motivation and the impact of the resolution constraint strengthening at depth R_1 (while relaxing at depth R_3) is discussed in section IV.D.5.

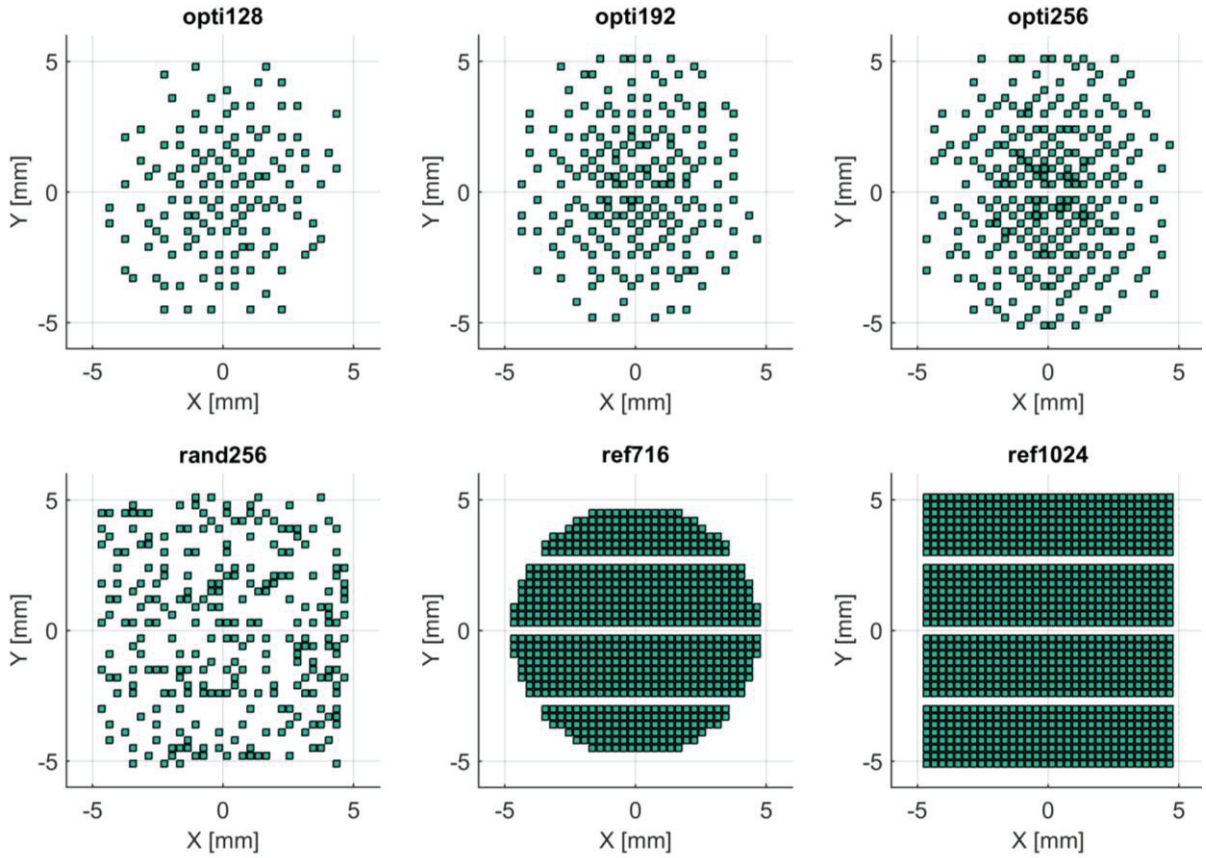


Figure 36 Layouts of the optimization results opti128, opti192, opti256, the best random array rand256 and the two reference arrays ref716 and ref1024. The corner elements deactivation happened spontaneously during the optimization of opti128, opti192 and opti256 whereas it was artificially imposed for ref716.

IV.C Results

IV.C.1 Layouts and energy function values

The layouts obtained with solutions opti128, opti192, opti256, the best random array rand256 and the reference arrays ref716 and ref1024 are presented in Figure 36.

Qualitatively, the optimized layouts[18] do not respect any periodical pattern but they seem to present a circular symmetry. The distances of the layouts barycenter with respect to the origin are $0.2\ \lambda, 0.47\ \lambda, 0.08\ \lambda$ for the respective arrays opti128, opti192, opti256 and $0\ \lambda$ for both ref716 and ref1024. The layouts barycenter of rand256 shows is $0.31\ \lambda$ far from the origin. It can be noticed that the apertures opti128, opti192 and opti256 are confined in disks of radius 5.3 mm, 5.6 mm and 5.7 mm, respectively: the confinement of the elements in a disk shape was not forced but they were spontaneously deactivated by the optimization process itself (the corner elements were available during the optimization, as assessed by rand256 whose corners still have some active elements). On the contrary, the circular array ref716 was produced from ref1024 by intentionally removing the corner elements outside a disk of radius 4.8 mm (maximum size of ref1024 along the x-axis, IV.B.1.b).

[18] Supplementary material is available at https://www.creatis.insa-lyon.fr/site7/en/roux. The online material includes the videos of the individual optimization run of the optimized arrays opti128, opti192 and opti256.

TABLE IX ENERGY FUNCTION VALUES ASSOCIATED TO THE OBTAINED SOLUTIONS OPTI128, OPTI192, OPTI256 AND THE REFERENCE ARRAYS REF716 ANDREF1024.

	opti128	opti192	opti256	rand256	ref716	ref1024
U^{N_H} ($\times 10^6$)	39.9160	8.3111	3.7274	838.5983	3.7265	7.3400

The energy function values $U^{N_H}(\text{opti128})$, $U^{N_H}(\text{opti192})$, $U^{N_H}(\text{opti256})$, $U^{N_H}(\text{rand256})$, $U^{N_H}(\text{ref716})$ and $U^{N_H}(\text{ref1024})$ are reported in Table VII. The energy value decreases with the number of elements for the optimized results. The energy value $U^{N_H}(\text{rand256})$ is the highest compared to all the other results. The energy value $U^{N_H}(\text{opti256})$ is very close but slightly higher than that obtained with ref716. On the contrary, $U^{N_H}(\text{ref1024})$ is higher than $U^{N_H}(\text{opti256})$. The fact that ref1024 is not associated with the best score is discussed in section IV.D.2.

IV.C.2 Comparison of the multi-depth beam patterns

The BP of opti128, opti192, opti256, rand256, ref716 and ref1024 are qualitatively compared in Figure 37 for both steered (bottom) and not steered (top) cases at the three depths of interest (R_1=30 mm, R_2=40 mm and, R_3=50 mm). The BPs of the optimized arrays fit, at all depths, below the sculpting MASK which is plotted (black dashed lines) in Figure 37 (IV.B.3.b for the definition of MASK). The BP main lobes of the optimized arrays are followed by a flat *plateau* up to $\theta = 90$ °. For all optimized arrays and at all depths, when a steering angle of 30 ° is applied the main lobe shape is very regular and the flat *plateau* can still be observed (no grating lobes). The BP of both reference arrays (ref716 and ref1024) present sidelobes close to the main lobe (around 10 °) that tend to rapidly decrease. The BP of rand256 also presents high sidelobes close to the mainlobe but they do not decrease as rapidly as for the reference arrays, i.e. they reach the level of the optimized arrays for θ higher than 20 ° approximately. A more detailed illustration of the optimized arrays BP, the random array BP and the reference arrays BP at depths R_1, R_2 and, R_3 is displayed, with 40 dB dynamic range, in Figure 38 when no steering is applied and in Figure 39 when a 30 ° steering angle is applied. On both Figure 38 and Figure 39, it can be noticed that for ref1024 side lobes over - 40 dB are present along the x and the y directions, whereas for ref716 they are only present along the y direction. For the optimized arrays such side lobes are homogeneously spread over the entire hemisphere (there is no worst-case direction). The side lobes are also homogeneously spread for rand256 but with a higher average level.

A quantitative comparison of the BPs can be done thanks to Table X which gives the SLL (peak and average values measured outside L) and the - 6 dB and - 20 dB main lobe widths for each of the compared arrays. The "peak SLL" (designated as usual by SLL) is defined as a ratio between the main lobe maximum value and the highest side lobe value. By contrast the "average SLL" (SLL_{ave}) is defined as the log-compressed average of the BP (linear values) outside L.

The best SLL performance is obtained by opti256 at the three depths. Compared to opti128, the SLL of opti256 is 1.9 dB, 1.8 dB and 2.2 dB lower at depths R_1, R_2 and R_3, respectively. Compared to opti192, the SLL of opti256 is 0.3 dB (R_1), 0.7 dB (R_2) and 0.9 dB (R_3) lower. The SLL obtained by ref1024 is 6.5 dB (R_1), 10.3 dB (R_2) and 12.9 dB (R_3) higher than with opti256. The SLL obtained by ref716 is still 4.8 dB (R_1), 5.7 dB (R_2) and 4.2 dB (R_3) higher than with opti256. The worst SLL performance is obtained by rand256 at the three depths with SLL 10.9 dB (R_1), 9.6 dB (R_2) and 12.0 dB (R_3) higher than with opti256.

The same trend about the $\text{SLL}_{\text{ave}}$is observed among the optimized arrays where opti256 overmatches the performance of opti128 of 4.5 dB (R_1), 4.8 dB (R_2) and 4.9 dB (R_3). Compared to

opti192, the $\mathrm{SLL_{ave}}$ of opti256 is 1.7 dB (R_1), 1.8 dB (R_2) and 1.9 dB (R_3) lower. Compared to opti256, the $\mathrm{SLL_{ave}}$ of rand256 is 3.4 dB (R_1), 2.8 dB (R_2) and 2.7 dB (R_3) higher (worst performance). Contrary to the SLL, ref1024 shows the best $\mathrm{SLL_{ave}}$ performance which is 9.9 dB (R_1), 11.9 dB (R_2) and 12.4 dB (R_3) lower than with opti256. Similarly to ref1024, ref716 yields $\mathrm{SLL_{ave}}$ performance which is 6.8 dB (R_1), 7.4 dB (R_2) and 8.3 dB (R_3) lower than with opti256. For all optimized arrays, both SLL and $\mathrm{SLL_{ave}}$ are always lower at depth R_2 (focal depth) than at depths R_1 and R_3.

The resolution at - 6 dB is very close for all the optimized arrays with mean 5.4 ° (R_1), 5.2 ° (R_2) and 5.1 ° (R_3). The best resolution at - 6 dB are yielded by ref1024 which overmatches of 1.4 ° (R_1), 1.6 °(R_2) and 1.3 ° (R_3) the - 6 dB resolution of opti256. The - 6 dB resolution obtained with ref716 is also slightly better than with opti256 of 0.7 ° (R_1), 0.9 °(R_2) and 0.7 ° (R_3). The random array rand256 is very close to the best performance (ref1024) with resolution at - 6 dB only 0.1 ° wider than with ref1024 at the three depths.

The resolution at - 20 dB is very similar for all the optimized arrays with mean 11.2° (R_1), 9.3° (R_2) and 9.7° (R_3). The random array rand256 has the coarsest resolution at − 20 dB with + 14.8 °(R_1), + 6.4 °(R_2) and, + 7.8 °(R_3) compared to opti256. Contrary to the resolution at - 6 dB, ref1024 has also a very coarse resolution at - 20 dB with + 10.3 °(R_1), + 0.8 °(R_2) and, + 1.5 °(R_3) compared to opti256. The situation is quite different for ref716 which yields the best - 20 dB resolution performance at both R_2 (7.2 °) and R_3 (9.3 °) but at depth R_1 it is slightly coarser (+ 1.3 °) than opti192 (the latter has yields the best - 20 dB resolution at this depth).

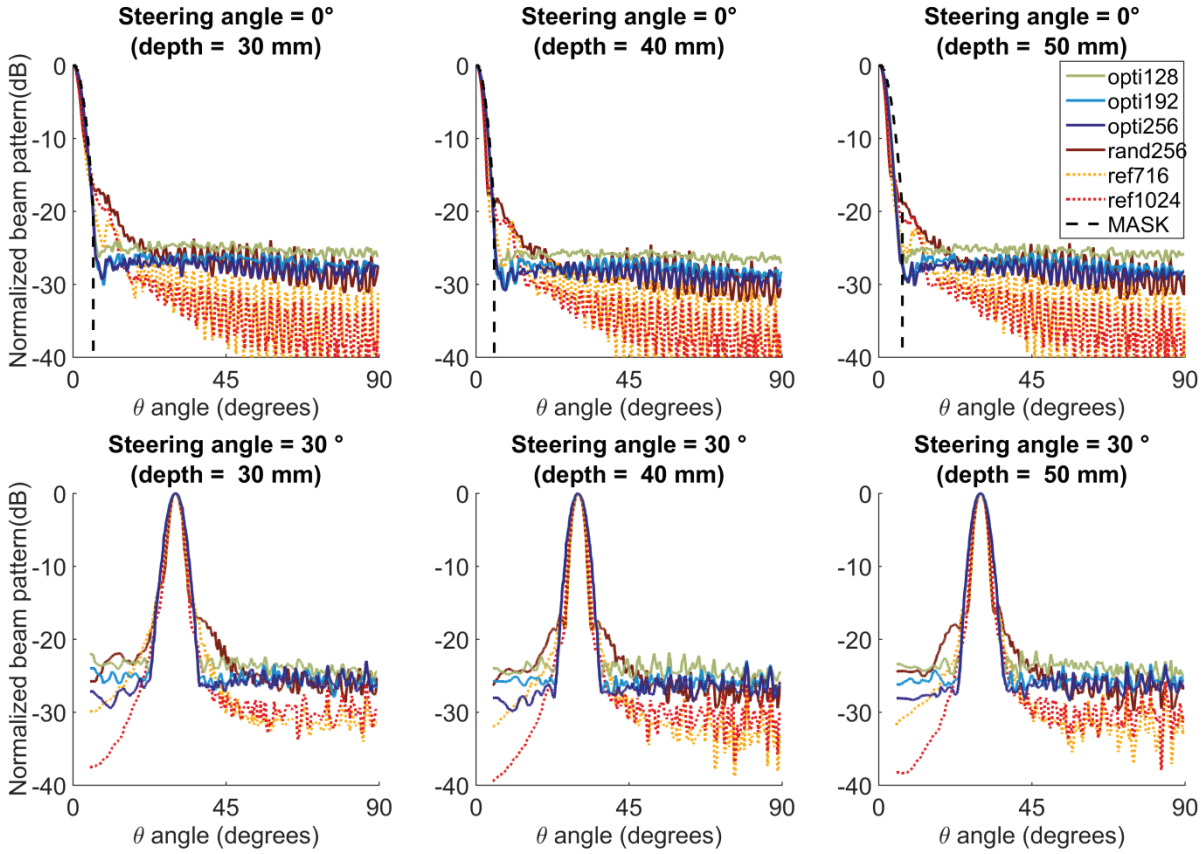


Figure 37 Radiated beam patterns (worst case) at depths 30 mm (left), 40 mm (center) and 50 mm (right) of the optimization results and the reference arrays ref716 and ref1024. The constraints MASK is shown in black dashed lines. The steering angles were 0 ° (top panels) and 30 ° (bottom panels).

TABLE X SIDE LOBE LEVEL AND MAIN LOBE WIDTH EVALUATED ON THE HEMISPHERES OF RADIUS 30, 40 AND 50 MM OBTAINED FOR THE OPTIMIZED AND REFERENCE ARRAYS. THE BEST PERFORMANCE IN EACH COLUMN IS HIGHLIGHTED IN GREEN.

	Side Lobe Level (in dB)						Main Lobe Width at -6dB and -20dB (in degree)					
	R_1 = 30 mm		R_2 =40 mm		R_3 =50 mm		R_1 =30 mm		R_2 =40 mm		R_3 =50 mm	
	SLL	SLL_{ave}	SLL	SLL_{ave}	SLL	SLL_{ave}	at -6 dB	at -20 dB	at -6 dB	at -20 dB	at -6 dB	at -20 dB
opti128	-24.1	-28.4	-25.1	-29.4	-24.4	-28.8	5.4	11.6	5.2	9.4	5.2	10.0
opti192	-25.7	-31.2	-26.2	-32.4	-25.7	-31.8	5.5	10.9	5.1	9.2	5.2	9.6
opti256	-26.0	-32.9	-26.9	-34.2	-26.6	-33.7	5.4	11.1	5.2	9.4	5.0	9.6
rand256	-16.9	-29.5	-17.3	-31.4	-14.6	-31.0	4.1	25.9	3.7	15.8	3.8	17.4
ref716	-21.2	-39.7	-21.2	-41.6	-22.4	-42.0	4.7	12.2	4.3	7.2	4.3	9.3
ref1024	-19.5	-42.8	-16.6	-46.1	-13.7	-46.1	4.0	21.4	3.6	10.2	3.7	11.1

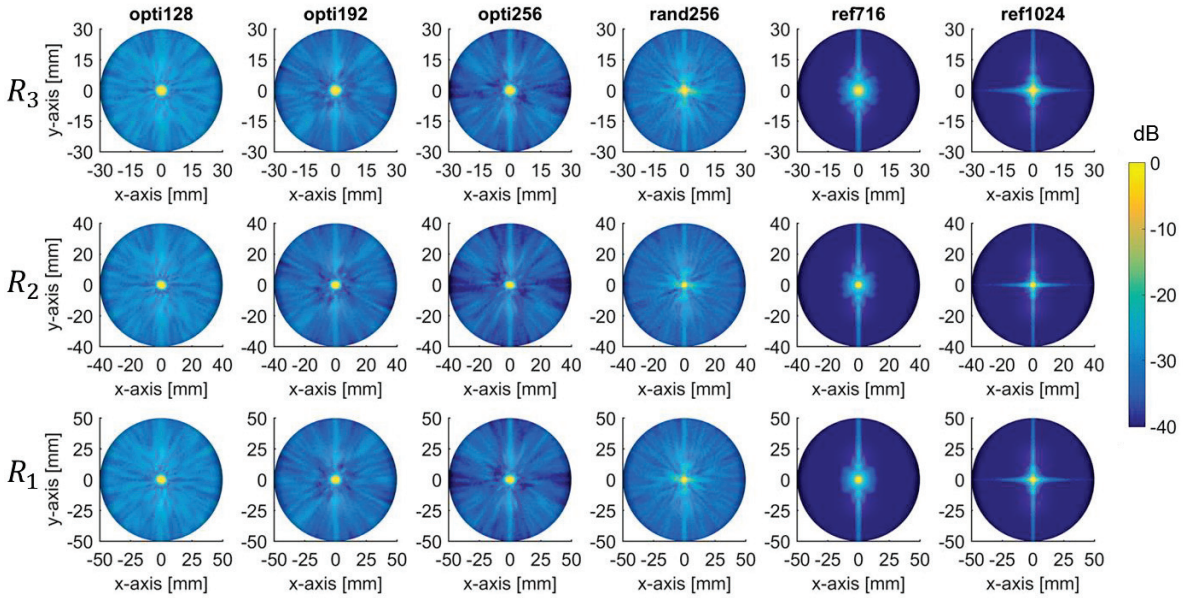


Figure 38 Radiated beam patterns (no steering) of the optimized arrays, the random array and the reference arrays evaluated on the three hemispheres at depths 30 mm (bottom line), 40 mm (middle line) and, 50 mm (top line)

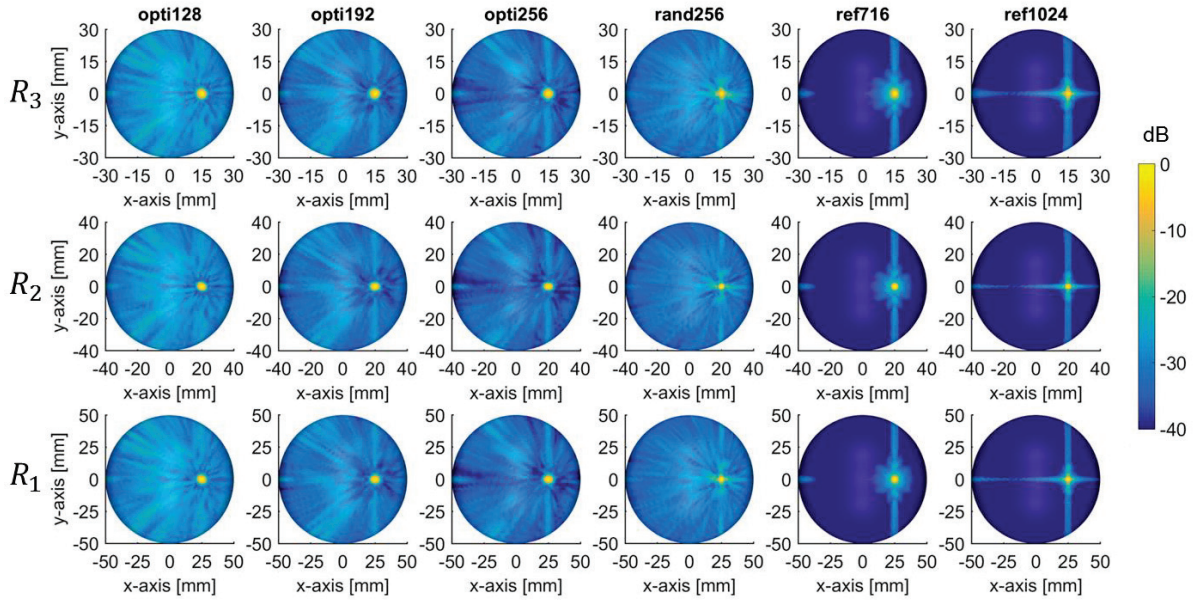


Figure 39 Radiated beam patterns (steering of 30 °) of the optimized arrays, the random array and the reference arrays evaluated on the three hemispheres at depths 30 mm (bottom line), 40 mm (middle line) and, 50 mm (top line)

IV.C.3 3D beam patterns analysis over 81 steering angles

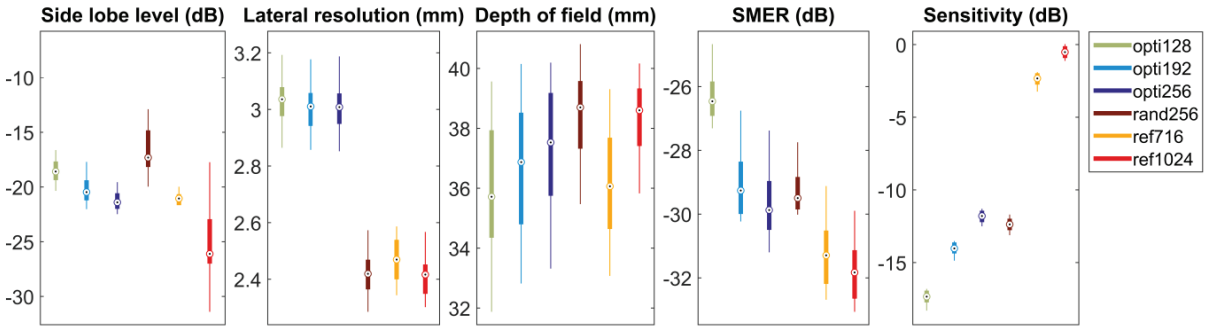


Figure 40 Side Lobe Level, lateral resolution, Depth of field, Side- to Main-lobe Energy Ratio (SMER) and sensitivity from the 3D BP analysis (statistics over 81 steering angles). The plotted whisker extends to the adjacent value, which is the most extreme data value that is not an outlier. Outliers are beyond the 99.3 coverage (normal distribution).

Qualitatively, for the optimized arrays the performance evaluated on the 3D BP (Figure 40) improves with the number of elements. A quantitative analysis of the 3D acoustic performance over 81 steering angles can be done from Figure 40. In terms of SLL, the best median value is obtained by ref1024 (- 26.1 dB) but high peaks can be noticed for extreme steering angles. Moreover, for ref1024, a SLL of - 17.7 dB is observed when no steering is applied which is consistent with the SLL values reported in Table X. The highest median SLL (- 17.3 dB) and peak (- 12.9 dB) SLL is associated with rand256. Furthermore, the range of SLL values showed by rand256 over the 81 steering angles is as large as with ref1024. On the contrary, ref716 yields a SLL performance with - 21 dB median value with a very small range of variation with the steering angles (discussion IV.D.3). Compared to ref716, the median SLL of opti 128 and opti192 is respectively 2.5 dB and 0.6 dB higher while opti256 yields a slightly better SLL median value (- 21.4 dB). The references ref716 and ref1024 have a median lateral resolution of 2.5 mm and 2.4 mm respectively. It can be underlined that rand256 yields the same lateral resolution performance as ref1024 (2.4 mm) which is the best achieved lateral resolution by all the studied arrays. Compared to ref1024, the median lateral resolution of all the optimized arrays is 0.6 mm coarser. In terms of depth of field, the best performance is also achieved by ref1024 (38.6 mm) and rand256 (38.7 mm) which overcome ref716 (36.1 mm). Compared to ref1024, the median DOF of opti128, opti192 and, opti256 is 2.9 mm, 1.7 mm and, 1.1 mm shorter, respectively. The best median value of Side- to Main-lobe Energy Ratio (SMER) is obtained by ref1024 which is 0.5 dB and 1.96 dB lower than with ref716 and opti256 respectively. The SMER yielded by opti256 is itself 3.5 dB and 0.6 dB lower than opti128 and opti192 respectively. The SMER and sensitivity performance of rand256 is slightly worse than with opti256: the SMER is 0.4 dB higher and the sensitivity is 0.6 dB lower than with opti256. Compared to ref1024, the median sensitivity of opti128, opti192, opti256 and, ref716 is respectively 17.1 dB, 13.5 dB, 11.3 dB and, 1.8 dB lower.

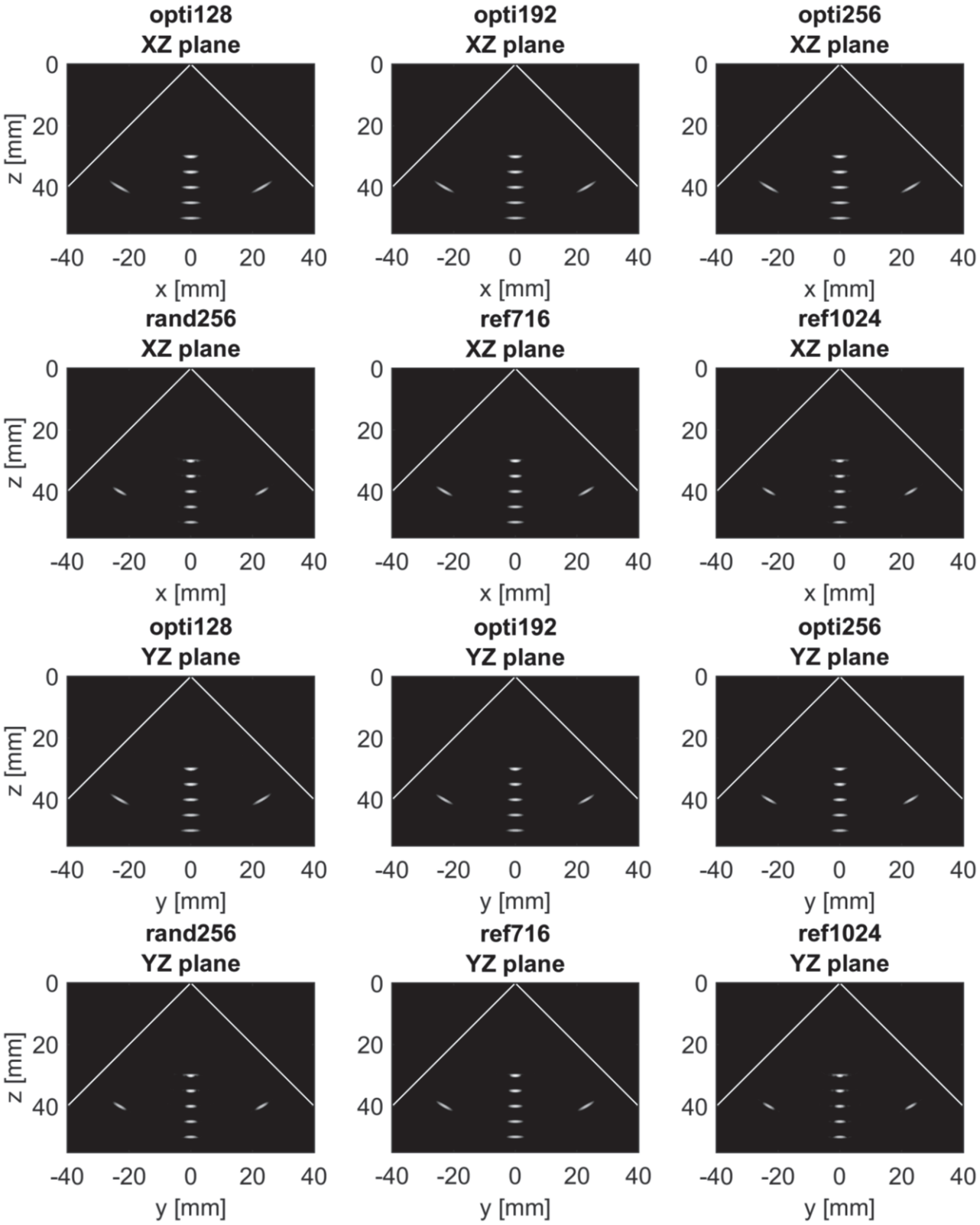


Figure 41 Resolution images (XZ plane at the top and YZ plane at the bottom) of a resolution phantom containing 9 scatterers: 5 equidistant scatterers along z-axis from 30 mm to 50 mm in depth and 2 scatterers on the sides of each XZ and YZ planes. The lateral size of the scatterers (measured at – 6dB) is a consequence of the main lobe width and the artefacts around the bright spots (particularly visible for rand256 and ref1024) are the consequence of the side lobes. The dynamic range is 40 dB.

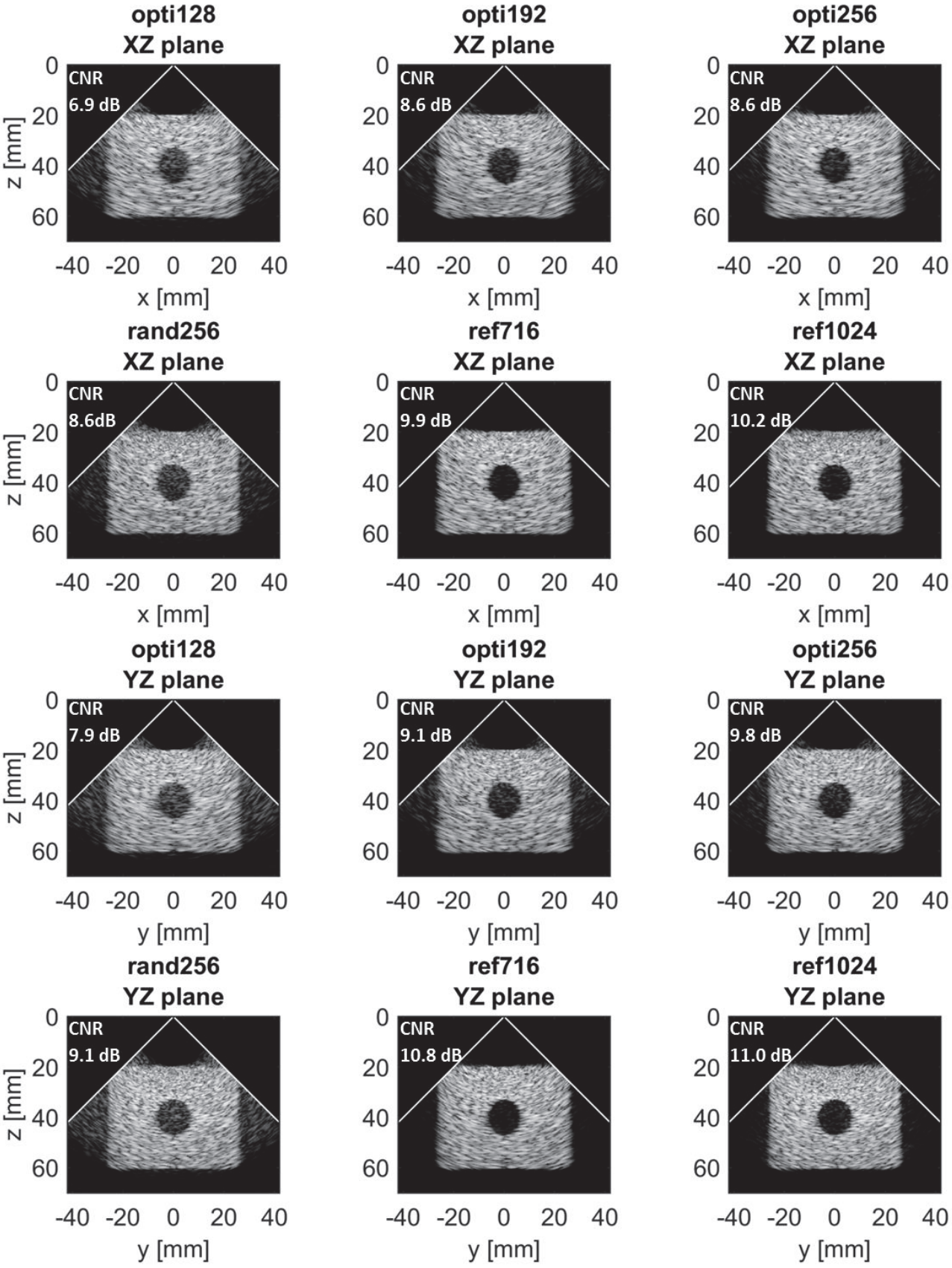


Figure 42 Contrast images (XZ plane on the first two lines and YZ plane on the last two lines) of an anechoic cyst phantom of radius 7.5 mm located at 40 mm in depth. The dynamic range is 40 dB.

TABLE XI LATERAL RESOLUTION AT -6 DB AND CONTRAST-TO-NOISE RATIO (CNR) EVALUATED ON IMAGE SIMULATIONS FOR THE OPTIMAL ARRAYS AND THE REFERENCE. THE BEST PERFORMANCE IN EACH COLUMN IS HIGHLIGHTED IN GREEN.

	Lateral resolution at -6 dB (mm) (average on the 5 scatterers)		CNR (dB) Cyst (z = 40 mm, r = 7,5 mm)	
	XZ	YZ	XZ	YZ
opti128	2.3	2.3	6.9	7.9
opti192	2.4	2.1	8.6	9.1
opti256	2.5	1.9	8.6	9.8
rand256	1.8	1.8	8.6	9.1
ref716	2.3	2.3	9.9	10.8
ref1024	1.7	1.4	10.2	11.0

IV.C.4 Image simulations

Qualitatively, the resolution (Figure 41) appears to be very similar for all of the optimized arrays and ref716. From Figure 41 also, the resolution appears very similar between rand256 and ref1024. The images in Figure 42 clearly show that the contrast improves with the number of elements. Quantitatively, it can be seen from Table XI that the best lateral resolution is obtained by ref1024 in both XZ (1.7 mm) and YZ (1.4 mm) planes. The lateral resolution yielded by rand256 is very close to ref1024 with 1.8 mm in both XZ and YZ planes. For the optimized arrays, the resolution in both XZ and YZ planes is in average 40 % coarser than for ref1024. The resolution of ref716 equals that of opti128 in both XZ (2.3 mm) and YZ (2.3 mm) planes. The relatively coarse resolution of ref716 compared to ref1024 is discussed in IV.D.4. On the contrary, in terms of contrast the CNR of ref716 is very close to that of ref1024 in both XZ plane (- 0.3 dB) and YZ plane (- 0.2 dB). The CNR of opti128, opti192, and, opti256, is 3.0 dB, 1.3 dB and 1.3 dB lower than with reference ref716 on the XZ plane. On the YZ plane, the CNR of ref716 is 2.9 dB, 1.7 dB and 1.0 dB higher than with opti128, opti192 and, opti256 respectively. The random array rand256 has same CNR as opti256 on XZ plane while it is 0.7 dB lower than with opti256 on the YZ plane. It can be noticed from Table XI that the resolution and contrast performance is systematically better on the YZ plane than on the XZ plane (discussion in section IV.D.4).

IV.C.5 Design robustness

The ten “clone” optimizations raised very similar results as it can be inferred from: Figure 43, where the final layouts are shown; TABLE XII, which presents their associated energy value; and Figure 44, where the radiated BP are presented in both steered and not-steered cases. Qualitatively the layouts shown in Figure 43 present a striking similarity in the element distribution over the aperture. The associated energy function values are also very close with mean and standard deviation 111 ± 2. However, the energy value is not a sufficient comparison criterion. For example, the comparison between opti256 and ref716 (section IV.C.1), has shown that for close energy function values the solutions can yield substantially different performance (discussion in section IV.D.2). So to highlight the acoustic performance robustness of the ten clones, their associated radiated BP are displayed in Figure 44. Analyzing the BP of the ten clones, the mean and standard deviation of the SLL is - 24.1 $\pm$ 0.6 dB, - 24.6 $\pm$ 1.4 dB and, - 23.7 $\pm$ 1.4 dB at depths R_1, R_2 and, R_3.

The acoustic performance improvement is highlighted on Figure 44 when comparing in both not-steered (top) and steered cases the BP of the ten initial random arrays (dotted red lines) and the optimized clones (full blue lines). The SLL reduction is about 10 dB in both steered and not steered cases at focal depth 40 mm and it can reach more than 12 dB at depths 30 mm and 50 mm. The resolution at - 6 dB is 0.5 ° coarser for the optimized clones.

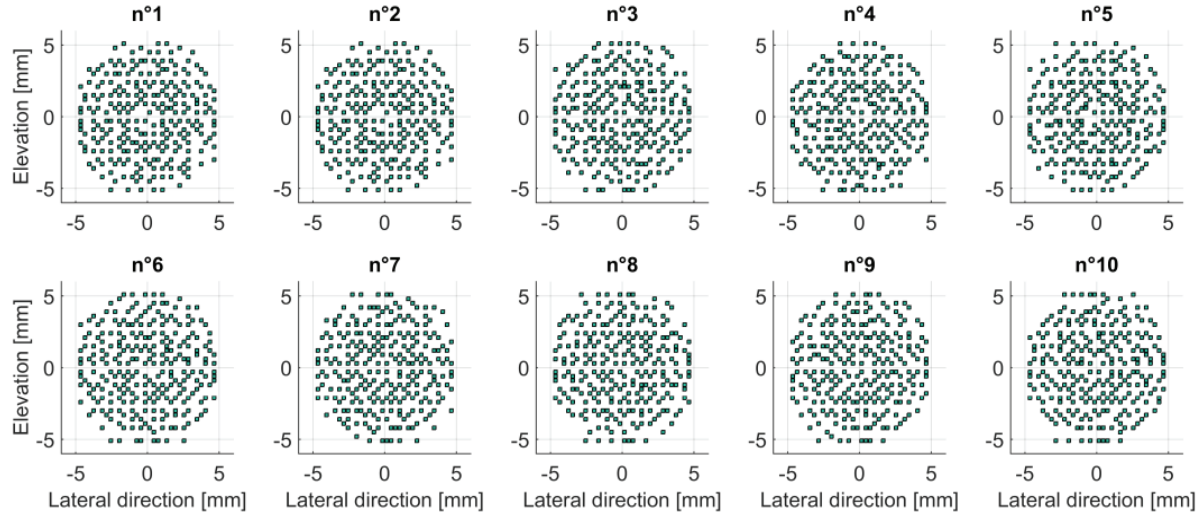


Figure 43 Final layouts of the ten optimized arrays with identical optimization setup but different initial state S_0.

TABLE XII ENERGY FUNCTION VALUES ASSOCIATED TO THE TEN ARRAYS OBTAINED USING AN IDENTICAL OPTIMIZATION SETUP BUT WITH DIFFERENT THE INITIAL STATE.

Clone	n°1	n°2	n°3	n°4	n°5	n°6	n°7	n°8	n°9	n°10
U ($\times 10^6$)	111.5	111.5	108.2	113.7	113.9	110.3	109.5	111.1	108.3	111.4

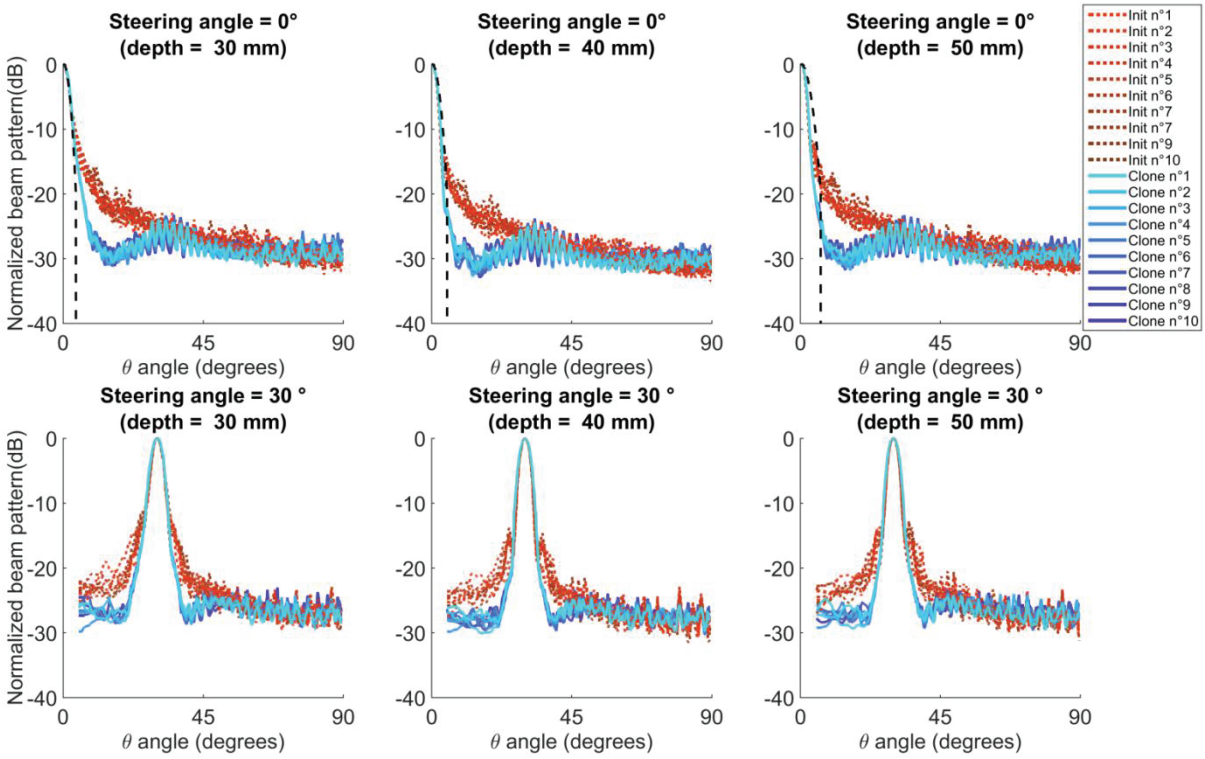


Figure 44 Radiated beam patterns (worst case) at depths 30 mm (left), 40 mm (center) and 50 mm (right) of the ten optimization clones. The constraints MASK is shown in dotted lines. The steering angles were 0 ° (top panels) and 30 ° (bottom panels)

IV.D Discussion

IV.D.1 Generalities

The general purpose of this chapter was essentially to present, step by step, a method combining stochastic optimization and wideband acoustic simulation to design and evaluate 2D ultrasonic sparse arrays. The practical case study illustrates how specific constraints raised by the targeted application and the fabrication process can be taken into account in the optimization design. In particular it is shown how the method can be adapted to the number of independent channels on the available imaging system. The guidelines to define the energy function were also illustrated by the case study in order to make easier the identification of the main challenging specifications that will shape the BP. The presented results aimed at illustrating the link between the layout geometry, the resulting BP (several depths and in 3D) and, the imaging capability in terms of resolution and contrast.

IV.D.2 The multi-depth energy function and the layouts

First of all it can be noticed on Figure 37 (top) that the main lobe of all the optimized arrays fits under the MASK, especially at depth 50 mm (Table X). This is assessed quantitatively from Table X where all the optimized arrays present a main lobe width at - 20 dB which is at least (considering the worst case of $\mathrm{opti128}$) 0.4 ° (R_1), 1.4 ° (R_2) and 3.8 ° (R_3) narrower than the MASK constraint (IV.B.3.b). A broader main lobe at 50 mm would further reduce the SLL, but this would be valuable only if, at the same time, the MASK was still be respected at the other depths. Moreover, in the proposed method, the deactivation of the corner elements was spontaneous, and therefore it might be inferred from the chosen energy function. This function was in fact defined to fit a beam shape with circular symmetry, which is a typical feature of circular apertures. The energy function definition implies that if the resolution constraints is respected, i.e. if the main lobe fits under the sculpting function $f(R,\theta)$, then the optimization continues pushing down the SLL (and indirectly the flat *plateau*) as low as possible. As in (Tekes, Karaman, and Degertekin 2011; S. Holm and Elgetun 1995; Choe, Oralkan, and Khuri-Yakub 2010), there is no a priori on the minimum GLL and SLL values that must be reached, i.e. the goal is the lowest achievable value for $M(R)$. This may explain why, with similar resolution performance, the optimized arrays that yield the lowest values of energy function are those with the lowest SLL.

However, the energy definition is not sufficient to make the beam pattern fit with the sculpting mask and the importance of the temperature variation to reduce the acceptation rate along with the optimization is highlighted with rand256: even though it yields the lowest energy function value (among the N_{iter} randomly explored arrays), rand256 has a - 20 dB main lobe width which is 13.9 ° (R_1), 10.8 ° (R_2) and 3.6 ° (R_3) wider than the MASK constraint. Because the BP main lobe of rand256 does not fit under the MASK, very high SLL are measured which inevitably strongly increases its energy function value. Surprisingly, rand256 yields very competitive imaging capabilities (0) despite its high energy value. This is also the case for ref1024 which is discussed in the next paragraph.

Moreover, as mentioned in IV.C.1, the reference array ref1024 which has the best results in terms of imaging capability (IV.C.3 and 0), is not associated with the lowest value of $U^{N_{\mathrm{H}}}$. This exception of $\mathrm{ref1024}$ can be explained looking at the high side lobes close to its main lobe (- 19.5 dB,

- 16.6 dB, - 13.7 dB at respective depths R_1, R_2 and, R_3) which inevitably penalizes the $\mathrm{ref1024}$ configuration. However, $U^{N_\mathrm{H}}(\mathrm{ref1024})$ does not yield the highest energy function value because the penalty induced by the high SLL is compensated by a low energy ratio ($\mathrm{P_{out}/P_{in}}$) that can be inferred from the very low $\mathrm{SLL_{ave}}$value compared to the optimized arrays. The high SLL of $\mathrm{ref1024}$ can be reduced using an apodization window, for instance the SLL values are - 19.6 dB (R_1), - 20.3 dB (R_2) and - 21.6 dB (R_3) with a 2D Hanning apodization window on $\mathrm{ref1024}$. This is in average 11 dB higher compared to the SLL yielded by the same apodized 32x32 elements array but without deactivated lines. It appears that the three deactivated lines are also responsible for the high SLL. These remarks are also valid for $\mathrm{ref716}$ and the high SLL that are visible along the y-axis on Figure 38 and Figure 39 are also caused by the three deactivated lines. It is noteworthy that integrating the fabrication constraints in the optimization process yielded SLL of the optimized arrays that are lower than with the apodized $\mathrm{ref1024}$ array: it seems that the effect of the three deactivated lines is attenuated by the optimized aperiodic organization of the active elements.

This highlights how crucial the energy function definition is. Although $\mathrm{ref1024}$ is not associated with the lowest energy value, it outperforms the optimized arrays in terms of imaging capabilities (1024 elements are expected to perform better than a quarter of them). This limitation means that solutions with better imaging capabilities may be avoided because the proposed energy function penalizes a high SLL (peak) without considering the $\mathrm{SLL_{ave}}$. However, a quality of the obtained optimized solutions is that the SLL is lower than with rand256, $\mathrm{ref716}$ and $\mathrm{ref1024}$, and this at all of the three considered depths: From this point of view the target of the proposed energy function is achieved but it requires further refinements (section V.C) to match with the best imaging performance. Surprisingly the contrast performance of rand256 is not dramatically different than with opti256. Considering that rand256 has the worst indicators in terms of SLL and $\mathrm{SLL_{ave}}$ (IV.C.2) it could have been expected that the contrast performance would be worse. However, the good contrast imaging capability of rand256 is demonstrated in front of the transducer but the behavior with higher steering angles is less convincing: on Figure 42 the sides ($\theta \sim 30\,°$) of the images of rand256 are noisier than with opti256. This qualitative comparison is assessed quantitatively by the boxplots presented in Figure 40 as discussed in IV.D.3.

IV.D.3 The 3D beam pattern simulations

From Figure 40 it can be seen that for the optimized arrays the median SLL decreases when the number of active elements increases but also it can be noticed that the range of variation of the SLL is higher with $\mathrm{ref1024}$. As general trend for the evaluated 3D metrics a small range of variation should be preferred to guarantee a homogenous imaging capability over the entire volume. The smallest the range of variation, the less the image appearance depends on the steering angle which is desired in practice. As announced in IV.B.1.b for the circular aperture $\mathrm{ref716}$, the confinement of the elements in a disk shape, significantly reduces the range of variation of the SLL compared to $\mathrm{ref1024}$. Moreover, it can be noticed that it impacts on the SLL: the highest SLL encountered with $\mathrm{ref716}$ over the 81 steering angles is 2 dB lower than with $\mathrm{ref1024}$. The trend of reducing the SLL using a circular aperture is also reported in Table X where the values at depth R_1 ($-1.7\,\mathrm{dB}$ with $\mathrm{ref716}$ rather than $\mathrm{ref1024}$) are consistent with the 3D simulations and where the SLL reduction is stronger at depth R_2 ($-4.6\,\mathrm{dB}$) and R_3 ($-8.7\,\mathrm{dB}$). The lateral resolution performance (Figure 40) appears to be very similar with the three optimized arrays. This is mainly due to the MASK that sculpted the same main lobe shape for all the optimized arrays (Figure 37). A low SMER value

indicates that the acoustic energy is concentrated inside the -6 dB iso-surface, i.e. the remaining amount of pressure that could create the lateral artefacts is reduced. The sensitivity indicates the highest pressure value generated by the array (generally at focal point) normalized on the maximum of pressure obtained with $\mathrm{ref1024}$. The sensitivity performance is directly impacted by the number of active elements, and Figure 40 confirms that the sensitivity increases of $\sim 6\ \mathrm{dB}$ when the number of elements i.e. the active surface, is doubled (Figure 40).

For all the optimized arrays, the ranges of variation of lateral resolution ($0.3\ \mathrm{mm}$), depth of field (8 mm), SMER ($3.2\ \mathrm{dB}$) and sensitivity ($1\ \mathrm{dB}$) are very close to those obtained with $\mathrm{ref716}$. The range of variation of the SLL ($3.5\ \mathrm{dB}$) is divided by 4 with the optimized arrays compared to that obtained with $\mathrm{ref1024}$ and rand256. The relatively small variation range obtained on the 3D field metrics with the optimized arrays is positively surprising since only one steering angle at $(\theta, \phi) = (0°, 0°)$ is considered during the optimization process. The optimized layouts yield similar behavior for all of the steering directions, thanks to its circular symmetry. Again, such symmetry may be associated to the chosen energy function, which imposes the minimization of the lateral lobes, at three depths, for all ϕ angles (IV.D.2).

The comparison over all the 3D metrics of Figure 40 shows that opti192 and opti256 performs almost identically and it is also verified on the 3D volume images that were simulated. Eventually, the 3D BP analysis of the random array rand256 illustrates that in the design of an array there is a tradeoff between the SLL and the lateral resolution performance. Compared to opti256, the median SLL of rand256 is 4.1 dB higher but the lateral resolution is 0.6 mm finer.

IV.D.4 The 3D volume images

The resolution images (Figure 41) and Table XI show that all the optimized arrays yield a very similar resolution performance that is 2.4 mm/2.1 mm average in XZ/YZ planes. This may be a consequence of using the same MASK to sculpt the main lobe shape. The resolution yielded by $\mathrm{ref716}$ is 35% (XZ plane) and 64% (YZ plane) coarser compared to $\mathrm{ref1024}$: the trade of switching off the corner elements is an increase of the lateral resolution because it reduces the dimensions of the active aperture (Table XI). The lateral resolution yielded by rand256 is very close to the one obtained with ref1024 and the images look very similar: this may be explained by the wide aperture size which is also very similar to ref1024 since the corners of rand256 are not deactivated. The key point here is on the contrast images (Figure 42) where opti192 yields almost the same results as opti256. From Table XI, compared to opti128 it can be noticed that opti192 and opti256 improve the CNR of 1.7 dB (XZ plane) / 1.7 dB (YZ plane) and 1.7 dB (XZ plane) / 1.9 dB (YZ plane), respectively. This highlights a relationship between the imaging contrast capability of the optimized array and the level of their BP *plateau* (Figure 37) described in IV.C.2: the *plateau* of opti192 and opti256 are both $\sim 2\ \mathrm{dB}$ below the *plateau* of opti128. But the level of the BP *plateau* is not the only indicator for the image CNR because again, even if on YZ plane opti256 has higher CNR than rand256, it is rather surprising for rand256 to yield the same CNR level (8.6 dB) as opti256 on XZ plane (discussion IV.D.2).

Moreover, the fact that better images are obtained on the YZ rather than on the XZ plane can be explained by the rectangular geometry of the footprint caused by the 3 inactive lines. Indeed the aperture dimension of ref1024 on the x-axis (9.6 mm) is slightly narrower than on the y-axis (10.5 mm). The same trend can be observed on the optimized layouts: a wider aperture dimension along

the y-axis provides better imaging capabilities in a plane containing this same direction. On the contrary, in Table XI the resolution performance raised by $\mathrm{ref716}$ is the same in both XZ and YZ planes because it has the same aperture dimension along the x-axis and the y-axis.

IV.D.5 The design robustness

The design robustness was analyzed through the optimization of ten "clones" as described in IV.B.5.c. It can be seen from Figure 44 that the obtained BP are robust with the initial state. The comparison with the initial states clearly shows the improvement yielded by the optimization on the radiated BP, and this at the three depths R_1, R_2 and R_3. The resolution at - 6 dB presented in Table X suggests that for all the optimized arrays the resolution constraint was not strong enough to reach the performance of the reference arrays $\mathrm{ref716}$ and $\mathrm{ref1024}$. So a new MASK definition (IV.B.5.c) was tested to improve the resolution performance. Unfortunately, compared to opti256 the SLL is 2.5 dB (R_1), 2.3 dB (R_2) and, 2.9 dB (R_3) higher with the clones (mean over the ten clones), which may be due to a too strong resolution constraint at depth R_1. Indeed, it can be noticed on Figure 44 that at depth R_1= 30 mm the main lobe goes beyond the MASK whereas at depth R_3= 50 mm there is a little space between the main lobe and the MASK. To some extent the resolution improvement was achieved since the mean - 6 dB resolution for the clones is respectively 92 %, 95 % and 86 % the one of opti256. Hence the energy function should be carefully defined, taking into consideration that it is not possible to reach a resolution as thin as desired without a strong increase of the SLL.

IV.D.6 Tension and metastability

The fact that rand256 yields surprisingly good imaging performance despite the low measured acoustic performance considered in the energy function is not the main interest of this experiment. It is true that the proposed energy function does not ideally describe the required acoustic characteristic to obtain the best imaging capabilities (as discussed in IV.D.2), but it is based on the criteria that were optimized in the Literature and enhanced them with an original sculpting mask: the idea of "sculpting" at several depth the PF can be very useful for applications such as HIFU transducers and it represents a step toward 3D BP optimization that is claimed as a novel approach. Moreover it suggests revisiting the acoustic criteria on which the optimization is usually based, for instance by defining optimization criteria directly based in the image quality (there appears a connection with adaptive beamforming).

The « random » exploration of N_{iter} =1 280 000 solutions from which rand256 is extracted as the best random array is not exactly a random selection for two reasons: the first reason is that the exploration is done respecting the same communication mechanism as in the optimization so that each explored solution was obtained from the previous one by translating one element as described in IV.B.2. The second reason is that the extraction of rand256 as the best array was based on the same energy function as opti256. For those two reasons the « random » exploration was done on the same state space Ω, with the same communication mechanism Θ and with the same energy function $U^{N_{\mathrm{H}}}$ as in the optimization but the difference was on the cooling sequence. Hence, the most significative information that can be learnt from the process that led to rand256 is about the temperature cooling sequence. The latter is clearly essential to regulate the acceptation rate of positive variation of the energy function. In particular, the challenge is to reach, at each instant, a fare rate, i.e. a smart balance (metastable equilibrium) for the individuation speed of the array. A right speed is just in between a too fast individuation process (temperature cooled very rapidly as in

thermal toughening), which enclose the solution in local minima, and a too slow individuation process where no tension exists toward the “ideal behavior” fixed by the energy function. The “random” process that led to rand256 corresponds to the situation where no tension leads the iterative exploration of the state space toward a specific goal.

IV.E Conclusion

The optimization of on-grid 2D sparse arrays for 3D ultrasound imaging has been addressed using a simulated annealing algorithm with wideband acoustic simulations. An innovative control of the 3D acoustic behavior was achieved thanks to a multi-depth energy function that sculpts the beam pattern at multiple depths. A specific graphical tool was design on purpose to help for the definition of the function sculpting the BP main lobe shape at several depths. The proposed approach was illustrated with an example of 2D sparse optimization where the aim was to find the best selection of 128, 192 and 256 active elements within a 3 MHz 32x32 gridded 2D array. The performance of the obtained 256-element optimal array (opti256) is displayed on Figure 45. The 1024-element 2D array and the 716-element circular array, obtained after corner deactivation, were both considered as references. The best 256-elements “random” array encountered during N_{iter}= 1 280 000 exploration steps, at infinite temperature, was also considered in the study. The obtained layout geometries were compared in terms of SLL and resolution on the radiated beam pattern at depths of 30 mm, 40 mm (focal depth) and 50 mm. Additional 3D beam pattern simulations with 81 steering angles for each array were performed to evaluate the performance homogeneity over a wide range of steering angles. Both resolution and contrast phantoms were simulated to quantify the 3D imaging capabilities of the arrays. The robustness of the results was assessed through the comparison of the optimized arrays obtained from ten identical experiments. The “random” experiment highlighted the decisive influence of the temperature cooling sequence on the obtained results. Finally, possible fabrication constraints can be taken into account before starting the design of the transducer.

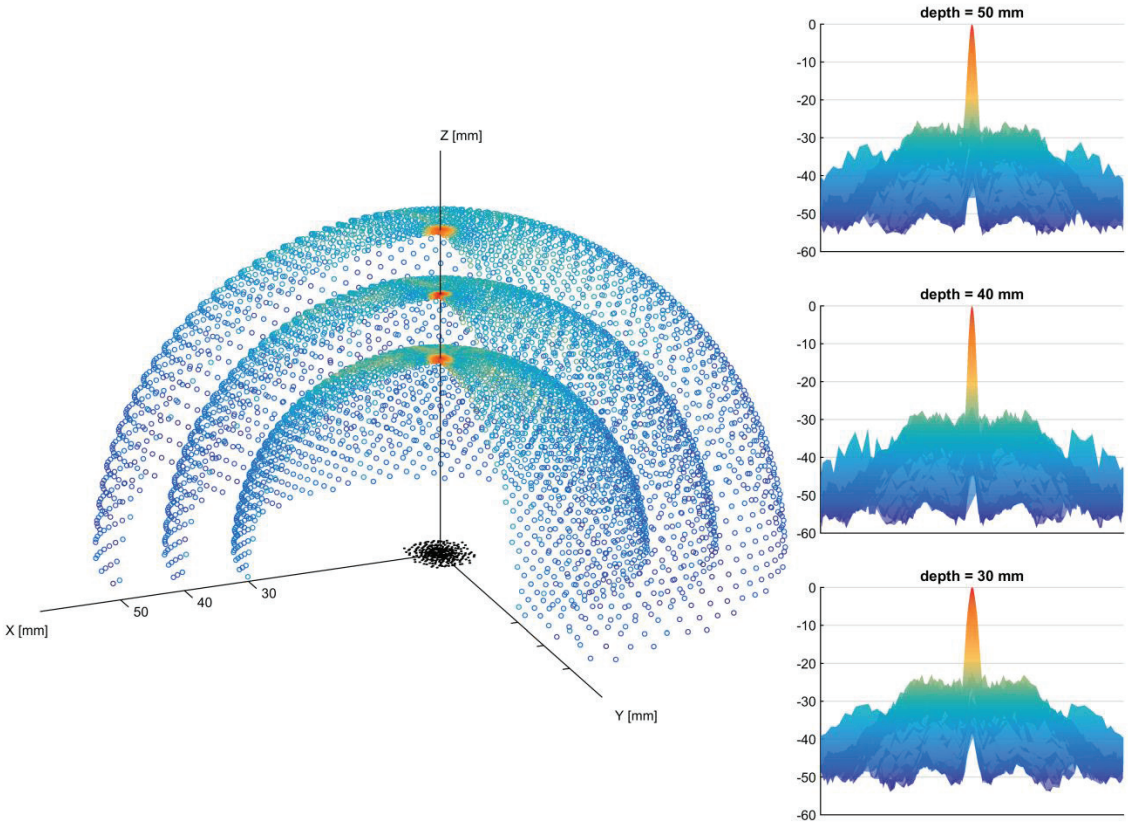


Figure 45 Illustration of the grid 2D sparse array (opti256) performance obtained with a multi-depth energy function optimizing the radiated beam pattern at depths 30 mm, 40 mm and 50 mm (focusing at F = 40 mm) and shaping the main lobe with a sculpting mask.

V General discussion: limits and perspectives

V.A Lack of experimental 3D images and prototyping

One of the most critical limitations of this work is the lack of satisfying experimental 3D images acquisitions. Indeed the 3D images that are presented on Figure 41 (p. 76) and Figure 42 (p. 77) are reconstructed from simulated signals. Besides, no prototypes were manufactured on the basis of the optimized layouts obtained from the performed optimizations. Nonetheless, some experimental 3D images acquisitions were done with the help of Lorena Petrusca (Post-Doc in CREATIS laboratory) using the 32x32 elements layout (ref1024) described in IV.B.1.a. Only a quarter of the array could be controlled using 256 channels of a Verasonics scanner but it was intended to combine several acquisition systems to fully control the 1024 elements independently. Unfortunately, the experiments did not yield satisfying 3D image acquisitions in the available amount of time.

V.B The state space and acoustic simulations

The state space of possible arrays, i.e. the types of solutions that are investigated during the optimization can be enriched by exploring more degrees of freedom. But the state space definition depends on the parameters that can be taken into account by the acoustic simulator. A limitation of the fast pressure field update (section II) is linked to the initial hypothesis of linear propagation. Indeed, the field update is impracticable when a non-linear simulation is employed (F. Varray et al. 2011) and it is mandatory to compute the beam pattern considering the contributions of each element of the full array and not only of the element which is perturbed.

Currently the following degrees of freedom are available and their impact on the image quality will be investigated in future works: element size and orientation, excitation signal and, individual impulse response of the elements. An extension to a more complex model of the array of transducers (especially to consider the electrical and acoustic interface, i.e. the materials involved in the transduction) would be possible using a Multiphysics simulator but it may require a specific implementation and more computation power. A possibility to be more realistic with the presented work would be to physically measure the individual impulse response of all the 1024 elements of $\mathrm{ref1024}$ and integrate them in the acoustic simulation used for the optimization. This could penalize the elements with a very bad quality response –dead elements- and prevent from connecting them in the optimal array. Following the same idea, the state space could be restricted to the elements that show a satisfying impulse response which means to withdraw any defective element from the possible candidates.

In the presented work, the same array is used for both TX and RX of the ultrasound waves aiming at maximizing the array sensitivity. But, a simple modification of the state space would enable optimizing the combination of two arrays, one with N_{TX} elements in TX and another one with N_{RX} elements in RX as in (Sciallero and Trucco 2015; Tekes, Karaman, and Degertekin 2011; Choe, Oralkan, and Khuri-Yakub 2010; Austeng and Holm 2002; Brunke and Lockwood 1997). The number of elements of each array could be part of the optimization with for instance $N_{\mathrm{TX}} + N_{\mathrm{RX}}$ = 256 if 256 independent channels are available (part of the TX and RX elements could be shared). In this case,

however, the presented multi-depth energy function sculpting the main lobe shape would be adapted to the two-way (pulse-echo) BP and not to the one-way BP.

V.C The energy function

As discussed in section IV.D.2, the energy function may be improved by mixing the minimization of the SLL with the minimization of the average SLL ($\mathrm{SLL_{ave}}$) which may enable higher SLL while lowering the $\mathrm{SLL_{ave}}$ values. If the computation power could yield ultrafast beamforming it would be possible to define the energy function directly on the B-mode images (or RF images). To a certain extent, this hypothesis follows the field of research in adaptive beamforming. The connection between stochastic optimization and such beamforming techniques may be fruitful in terms of future investigations.

As mentioned in IV.D.3, a homogenous imaging capability over the entire volume is desired to avoid any dependencies between the image quality and the orientation of the probe handle. In the presented work a relatively good homogeneity of the acoustic properties is obtained (see IV.C) over a 3D sector of - 32°,+ 32° with only one steering angle ($\theta = 0\,°, \phi = 0\,°$) considered in the optimization. However, one could think about integrating in the energy function the steering capability of the array. This could be implemented by simulating the BP for N_{steer} angles of steering at each step of the optimization but the optimization would last N_{steer} times longer because of the required additional simulation.

As mentioned in III.D.3, a different weighting for the different hemispheres can be implemented (67) to give priority to the performance at a particular depth. One could add more hemispheres, or also investigate the impact of an energy function directly defined on the 3D BP of an array. But for an effective sculpting of the 3D BP, the PMP should be located in the entire 3D volume above the array (not only at three depths). It would require a lot more computation power, demanding GPU implementation, to define an energy function based on the transmitted 3D BP in the volume.

V.D The communication mechanism

More investigations could be done also on the communication mechanism. In particular the neighborhood system could be changed by adjusting the maximum authorized translation during one perturbation in the case of non-grid arrays. In the case of gridded-arrays, the size of the area where elements positions are considered as connected can be changed to allow movements of larger dimension. The possibility of customizing the allowed moves during the exploration of the state space is another technique for integrating specific fabrication constraints in the design of the array. Such constraints are different from the one imposed on the state space and their influence on the obtained results is also a source of methodological investigations. For instance, a possible refinement of the communication mechanism, would be to set it up as the combination of two different communication mechanism Θ_1 and Θ_2 used during the optimization process with probability α_1 and α_2 respectively.

$$\Theta = \alpha_1 \Theta_1 + (1 - \alpha_1)\Theta_2$$

For instance, a non-zero probability of randomly moving an element in a much larger neighborhood can be introduced through Θ_2. This could avoid staying in a local minimum when very strong requirements are imposed by the energy function.

V.E The computation time

Three years of computation are reduced to two weeks. This is the exact speed-up that was achieved to obtain the 256-elements optimized arrays presented in chapter III. More in details, all the presented optimization results were obtained using a cluster[19] of computers available in CREATIS laboratory. The range computation time stands within two days and five weeks depending on the optimization setup (number and location of the PMP, number of active elements, and number of iterations) and the capacity of the machine that was available on the cluster. This is acceptable for a complete probe design pipeline and the implementation of the graphical interface significantly reduced the time required to adapt the proposed method to acoustic constraints that are specific to the targeted application. However, these long jobs (few weeks are long job in the laboratory) needed to by compiled first in order to run on the cluster letting the limited number of MATLAB licenses available in the laboratory free.

But, why is it needed to reduce the computation time of the acoustic simulations, i.e. why do we want to go faster? And what is going faster better for? At first it appears obvious that obtaining the results quicker can be appreciated in a probe design pipeline. This is especially convenient thanks to the finite time convergence property of the simulated annealing which allows knowing the duration of the optimization task in advance. But a deeper interest is that, in the same amount of time, the exploration of the possible solutions is vaster and the temperature sequence can cool down slower which increase the probability to reach global optima. Incidentally, a systematic method enabled to control the state of the running optimization process at any time of the optimization. This method allowing the evolution check of the optimization process is presented in the appendix (APPENDIX I: Optimization and analysis pipeline, p. 109). The electrical power or a full update of the cluster machine could (did…) happen unexpectedly so the implementation also included an “after-crash” mode with dedicated scripts that allowed restarting the optimization from the “crash point” of the cluster. This permits not to restart everything from scratch thanks to regular savings of the optimization process.

There are still two main possibilities for increasing the speed of the optimization process. The first one is technological the second one is methodological. Technologically, there is always a tradeoff between fast computation and a huge amount of memory. Faster simulations could be achieved simply by changing the hardware implementation for instance with a faster Central Process Unit (CPU), or by changing both hardware and software implementations with for instance exploiting parallel computing on GPU. Instead of increasing the computation speed, another acceleration idea

[19] In 2015 the cluster of the CREATIS laboratory which was used in this work, was upgraded with a park of 24 heterogeneous machines gathering together a total of 274 CPU and 942 GB RAM on a gigabit network where 14 TB of disk data can be shared. Two additional machines (one with 32 CPU and 128 GB RAM and one with 2 Nvidia Tesla GPU) are also available for specific tasks. All machine runs under Fedora 20 (64 bits) operating system. More information about job submission and batch manager are given in APPENDIX I: Optimization and analysis pipeline, p. 109.

could be to increase the amount of memory. By pre-computing and storing the individual active elements pressure field contributions for all possible positions on the layout would replace the computation step done at each iteration by a simple load from memory. However, this solution may be feasible in the case of gridded arrays while for non-grid arrays the huge amount of possible positions would require to have access to a yet unthinkable memory system. From a methodological approach there is space in increasing the optimization speed-up in particular by upgrading the simulated annealing algorithm to stochastic continuation. This would enable a multi-scale approach with a progressive refinement of the goals targeted by the energy function during the optimization process.

V.F Stochastic continuation and continuous modulation

In our work the simulated annealing (SA) optimization algorithm was "fixed", i.e. the energy function and the communication mechanism could not change during the optimization. Despite the use of a "static" algorithm definition, the videos of the obtained results allows seeing the evolution of the running optimization process which helps illustrating that the array design may be seen as a dynamic process[20] instead of an absolute solution given by pre-determined pattern. A detailed description of the content which is displayed on the running optimization videos[21] is given in appendix (APPENDIX II: Online video description, p. 115). More than the obtained result, the really important topic here is the pathway/operation that leads to it. The quote written by Deleuze and Guattari in (Deleuze and Guattari 1987) extracted by Andrew Iliadis in (Iliadis 2013) is particularly relevant here: "*In short, what Simondon criticizes the hylomorphic model for is taking form and matter to be two terms defined separately, like the ends of two half-chains whose connection can no longer be seen, like a simple relation of molding behind which there is a perpetually variable, continuous modulation that it is no longer possible to grasp*". The fact that in our work the SA algorithm is not modified during the optimization can be associated with the quoted idea of a simple molding operation which is missing the continuous modulation of the energy function. To link with the beam pattern optimization of the ultrasound 2D arrays it could be seen as the necessity to make a "continuous modulation" of the sculpting mask. It does not mean only that the mask should evolve with temperature to gradually change the constraint on the array design, but also that the arrays explored during the optimization process may impact on the sculpting mask shape also. As for the matter, the reciprocity of influences should connect each order taking part in the "individuation" which can be seen as the mode of operation in the design process (section V.G).

The presented work is based on a "static" algorithm definition but it can easily be adapted such that a progressive operation makes the optimization process evolve with the temperature cooling

[20] « One could assess without any doubt that the transduction could not be presented as a logic process having a proof value: as well, we do not want to say that the transduction is a logic process in the current sense of the word; it is a mental process, and even more than a process it is discovery reasoning. This reasoning consists in *tracking the being in its genesis*, performing the genesis of mind along with performing the object genesis. », (Simondon 2005), p. 34, personal translation.

[21] As mentioned in footnotes 17 (p. 53), and 18 (p. 71) the running optimization videos are available online as supplementary material at https://www.creatis.insa-lyon.fr/site7/en/roux.

sequence, i.e. during the optimization run. Stochastic continuation (SC) designates a class of algorithms obtained from the generalization of temperature-dependent SA with simple sufficient conditions for global convergence. The key feature of SC is an evolution of the energy function and the communication mechanism while the iteration index gradually increases. The interest of the concept is clearly announced and further detailed in (Robini and Reissman 2013): *"The first idea is to ease the annealing process by gradually revealing the complexity of the optimization problem. The second idea is to facilitate the exploration of the state space by adapting the communication mechanism to the temperature regime."* These two ideas yielded by SC are very complementary to what happens by integrating the acoustic simulations in the optimization process. There is more flexibility in the state space of explored arrays thanks to new degrees of freedom and thanks to SC there is more flexibility in the energy function and the communication mechanism design. Hence combining the presented work with SC represents a rich source of investigations by joining together increased design flexibilities in the state space, the energy function and the communication mechanism.

V.G Multi orders individuation of ultrasound 2D sparse arrays

The ultrasound 2D sparse array design, seen as a dynamic operation and not as an absolute deterministic solution, takes the shape of a tension-resolving process toward a goal fixed by the application (via the energy function definition). The evolution is performed while maintaining a meta-stable equilibrium. This meta-stable equilibrium is the kernel of the array definition and paradoxically it exists only thanks to the subtle and delicate evolution of the disequilibrium tolerance rate (the acceptation rate of uphill moves gradually decreases while optimization progresses). In his own thesis *Difference and repetition,* Deleuze writes the following in 1968 (note that the following reference is a re-edition) (Deleuze 1994):

"Gilbert Simondon has shown recently that individuation presupposes a prior metastable state—in other words, the existence of a "disparateness" such as at least two orders of magnitude or two scales of heterogeneous reality between which potentials are distributed. […]. An "objective" problematic field thus appears, determined by the distance between two heterogeneous orders. Individuation emerges like the act of solving such a problem, or—what amounts to the same thing—like the actualisation of a potential and establishing of communication between disparates". (1994, p. 246)

The concept of disparation is "*the process of two-way becoming via a universal problematic*" (Iliadis 2013). This brings forward to the idea of transductive process (footnote 4). Here three scales (meaning orders of magnitude) of processes are interacting: the array design is a central scale of processes surrounded by two other scales of processes: an inner scale of processes associated with the crystallization (annealing) which produces the piezoelectric material and an outer scale of processes associated with the optimization algorithm (Using SC enables the continuous modulation of the energy function and the communication mechanism). A very interesting multi order design process can then be individuated with adjacent orders "communicating" with each other in the

individuation operation they form in order to solve the problematic tensions embodied by the energy function minimization[22].

V.H Other fields of applications

In a field were apparently there was not much space to improve what has already been known, the integration of wideband simulations during the optimization process reopens the possibility to explore solutions in a more practical way (fabrication design constraints), with more flexibility (new degrees of freedom) as a source of new investigations tightly connected with current manufacturing process. Moreover, the presented work could also be applied in other scientific and technical fields.

Other imaging sequences such as plane or diverging waves strategies could possibly take advantage of the multi-depth energy functions, for instance by optimizing the array to have the beam pattern as homogeneous as possible at each depths or by exploiting the following concept inferred from section I.B.2.a: for a given point (x, y, z) in space, the configuration that yields the "best" focal spot in (x, y, z) will also be the best configuration to transmit a diverging wave from the virtual source point $(x, y, -z)$. Further studies would be required to demonstrate the suggested perspectives.

As a potential perspective, the multi-depth energy functions could be adapted to high intensity focused ultrasound (HIFU) and dual mode (HIFU and B-mode) transducers where the minimization of the spread energy outside of the target located at focal point is critical to preserve safe tissues. For instance, when considering the optimization setup used in chapter III (three hemispheres of radius R_1, R_2 and R_3, focusing at depth R_2) it could be implemented by maximizing the pressure intensity at focal depth R_2 and minimizing the pressure intensity at depth R_1 and R_3. For HIFU operations, an array could be optimized using an energy function defined inspired from (Choe, Oralkan, and Khuri-Yakub 2010) by adjusting the focal region to fit with the targeted focal spot. However, the computation of the 3D PSF energy ratio outside/inside the focal region requires the (pre-) computation of 3D PF and it can be considered only in the case of gridded arrays (section I.D.1).

Underwater investigations (P. Chen, Tian, and Chen 2010; Trucco, Palmese, and Repetto 2008) represent another field of application where, sound navigation and ranging (sonar) systems could possibly take advantage of the proposed optimization framework.

The entertainment industry currently develops innovative 3D image systems (glasses 3D in cinema theaters, Samsung Gear VR[23] developed by Oculus VR[24]) to create the illusion of a 3D virtual reality. What about 3D sound systems for virtual reality and multimedia (Begault and Trejo 2000) ? Today it is relatively easy to produce a multi-phonic audio[25] track which can be rendered on a set of loudspeakers. In the abstract[26] of the EDISON 3D European project (Project ID ANR-13-CORD-0008),

---

[22] « While potential energy (higher order condition) is being actualized, matter is being organized and distributed (lower order condition) into structured individuals at a middle range order, developing by a mediate amplifying process. », (Simondon 2005), p. 27, personal translation.

[23] http://www.samsung.com/global/galaxy/gear-vr/ (visited on August 2016)

[24] https://www.oculus.com/ (visited on August 2016)

[25] http://multiphonie.free.fr/ (in French; visited on August 2016)

[26] http://www.agence-nationale-recherche.fr/?Project=ANR-13-CORD-0008 (visited on August 2016)

the project coordinator Etienne Corteel from sonic emotion labs[27] writes: "*Ongoing initiatives in standardization bodies (MPEG, ITU) and from the major players in the movie industry (Dolby, Barco, etc.) suggest that 3D audio content productions for audio and audiovisual consumer applications will emerge in the next years. However, there is no consensus yet on the tools for the creation of contents, the formats or the distribution methods of 3D sound."* Contrary to binaural listening where each individual listener needs a set of headphones and a specific rendering taking into account its own head related transfer function (HRTF) to enjoy a 3D sound illusion, a more interesting approach consists in rendering a truly 3D sound field (holophonic sound) with techniques such as wave field synthesis (WFS) (Berry, Dia, and Robin 2012; Berkhout, Vries, and Vogel 1993), high-order ambisonics (Daniel, Moreau, and Nicol 2003) or spherical harmonics (Poletti 2005). Noise cancellation may also be another field of application with optimal acoustic panel designs or active noise control (S. M. Kuo and Morgan 1999; Sen M. Kuo and Morgan 1995) to preserve the opportunity of listening to the silence[28].

[27] http://www2.sonicemotion.com/ (visited on August 2016)

[28] http://soundtracker.com/ website of Gordon Hempton, the author of *One Square Inch of Silence, 2010*

General conclusion

The context of 3D ultrasound imaging (3D US) was presented starting with the physical principles up to the current technical solutions (and their limits) for real-time 3D US proposed by leader academic research laboratories and the commercially available solutions. A first section was dedicated to explain how acoustic waves are generated from matter thanks to the electroacoustic transduction property of piezoelectric materials. Ultrasound waves were then described as they are used in medical environment focusing on the transmission strategies and how images are beamformed from the echoes back propagating from the observed medium. It was detailed how the pressure field produced by a group of transducers is associated to its so called beam pattern (BP). The relation between the imaging capabilities of an array and the shape of BP was illustrated presenting the basic principles of image reconstruction. The difficulties to be faced for 3D+t image rendering were exposed. The existing ultrasound probes, based on electronically steered 2D arrays, which allow 3D diagnostic echography to be achieved, were reviewed. The 2D sparse array designs, which drastically reduce the number of active elements, were presented as a solution to perform 3D ultrasound imaging by keeping the full flexibility of a one-element-to-one-channel configuration without increasing the circuit complexity. The need of integrating wideband acoustic simulations in the design framework was highlighted from the 2D sparse array design strategies and optimization techniques that have been explored in literature.

The first contribution of this thesis is the integration of realistic acoustic simulations in a general 2D sparse array optimization framework. Two acceleration techniques were implemented to speed-up the acoustic simulations so that the optimization duration becomes reasonable. The first technique consists in reducing the amount of pressure measurement points (PMP) used to evaluate the beam pattern radiated by the array. The second technique consists in an ergonomic data management to quickly update the radiated pressure field when a perturbation is done on one element of the array. The following benefits of performing realistic acoustic simulations during the optimization were studied: the speed-up factor of the implementation, the dimension reduction yielded in the 2D BP analysis, the new degrees of freedom (size, shape, orientation, and excitation signal) and a distinctive capability enhancement thanks to the use of shape sensitive and wideband acoustic simulations. Another benefit is the convergence to realistic solutions because during the optimization the tested arrays acoustically behave as if they were physically manufactured. A general 2D sparse array optimization framework was introduced based on simulated annealing whose constitutive components (state space, energy function, communication mechanism and cooling sequence) were described in the context of ultrasound array design. The limitations and possible improvements of the presented implementation were discussed.

The second contribution of this thesis is the introduction of a multi depth energy function as a step toward 3D pressure field optimization with an application to non-grid sparse array design. In this second study, sixteen radiation optimizations of 256-element sparse arrays were performed. The solutions were explored by moving the elements out-of-grid in order to optimize their position to the sense of three proposed energy functions. One of the energy functions shapes the main beam via the introduction of a sculpting mask. In particular, the energy function of the optimization checks the radiated beam patterns over three concentric hemispheres at selected depths to evaluate the quality of the acoustic performance in 3D and not only at focal depth. In the presented investigation,

the beam patterns were evaluated at 15, 25 (focal depth) and 35 mm, and the optimization process aimed at obtaining the same width of the main lobe and lower side lobe level of the radiated pattern of a Blackman-tapered spiral array. This array was assumed as reference to compare the obtained results since it is known to produce an almost uniform sidelobe distribution. A post-optimization evaluation was performed through the comparison of 3D beam pattern performance metrics. The impact of the number of iterations, the number of PMP, the number of hemispheres, and the impact of the energy function definition were studied on the obtained results. An optimized array provided slightly better performance than the reference spiral array. It was shown that sculpting the main beam shape at several depths leads to a circular symmetry of the layouts without imposing any geometrical constraint. The circular symmetry of the optimized layouts was discussed as well as the possibility of integrating additional degrees of freedom and constraints. The proposed multi depth energy functions and the implemented optimization setup were also discussed.

The third contribution of this thesis is an on-grid 2D array optimization study, which gives the guidelines to integrate specific fabrication constraints in the general wideband optimization framework. The issue of finding the best configuration of a given number of active elements in a 2D matrix array was formulated. It was here addressed with 128, 192 and 256 active elements to be chosen on a 32x32 matrix array. Here again the energy function was intended to shape the multi depth BP with a sculpting mask. Additionally, a graphical user interface was developed to help for setting up the sculpting mask used in the energy function definition. The obtained results were compared in terms of main lobe width at – 6dB and – 20 dB and in terms of side lobe level (SLL) and average SLL ($\mathrm{SLL_{ave}}$) that were computed from their multi-depth beam patterns. As in the previous chapter, the 3D BP performance analysis was also performed. To evaluate the imaging capabilities of the obtained arrays, 3D volume images were simulated and both lateral resolution and contrast to noise ratio were computed on orthogonal planes. The design robustness to the initial state was assessed through the comparison of ten identical experiments which all started from different initial states. A random array was also obtained by maintaining the acceptation rate of uphill moves to one (infinite temperature). Its comparison with the optimized results highlighted the precious role of the temperature cooling sequence. It is claimed that integrating manufacturing constraints in the optimization process enriches the theoretically defined array designs. For a given application, it constitutes a new tool which is available for the manufacturer to choose between technological solutions.

A general discussion allowed dealing with the limitations of the proposed optimization framework and its requirements in terms of computation. But it was also the occasion for suggesting potential of extension and analogies for this thesis. It finally contains an attempt to place the *present*ed state of the work into a fascinating dynamic design perspective, which is, hopefully, not restricted to the design of 2D ultrasound sparse arrays. Medical imaging, and ultrasound imaging in particular, have changed the way medicine has been practiced over the last 50-60 years. In return, the medical doctors have influenced what information should be extracted and how it should be displayed (this is also true for 3D US imaging). Unfortunately, the interactions between medical doctors and engineers are typically less frequent and constructive than they should be. However, when such a happy situation occurs, it is very likely that both edge innovative technological ideas and efficient health practices emerge. It seems that for transdisciplinarity (Nicolescu 2016; Nicolescu 2008), a meta-stable state is required, characterized by a partial “disturbance” acceptation (uphill move, effort?) by both disciplines. Great progressive solutions may happen from a two-way

transductive process. Without a *central operating zone* (Simondon 2005) included in the middle, they could not be invented because each environment would remain closed and stable about itself. Interestingly, very precious persons can embody this “included middle” when they bravely achieve both engineering and medicine studies.

Personal publications

Journal

Roux, E., A. Ramalli, P. Tortoli, C. Cachard, M. Robini, and H. Liebgott. 2016. "2D Ultrasound Sparse Arrays Multi-Depth Radiation Optimization Using Simulated Annealing and Spiral-Array Inspired Energy Functions." *IEEE Transactions on Ultrasonics, Ferroelectrics, and Frequency Control,* Dec. 2016, vol. 63, no. 12, pp. 2138–2149. doi:10.1109/TUFFC.2016.2602242

Roux, E., A. Ramalli, H. Liebgott, C. Cachard, M. Robini, and P. Tortoli. 2016. "Wideband 2D Array Design Optimization with Fabrication Constraints for 3D US Imaging." *IEEE Transactions on Ultrasonics, Ferroelectrics, and Frequency Control,* Jan. 2017, vol. 64, no. 1, pp. (published Oct. 2016, 3rd on IEEE Explore - printed release in Jan. 2017). doi:10.1109/TUFFC.2016.2614776

Journal front cover images

Ramalli, A., E. Boni, E. Roux, and P. Tortoli. 2015. "Density-Tapered Sunflower: A Deterministic Sparse Array Solution." *IEEE Transactions on Ultrasonics, Ferroelectrics, and Frequency Control [Cover]* 62 (8): c1–2. doi:10.1109/TUFFC.2015.620801

International conferences

Diarra, B., **E. Roux**, H. Liebgott, S. Ravi, M. Robini, P. Tortoli, and C. Cachard, "Comparison of different optimized irregular sparse 2D ultrasound arrays," in Ultrasonics Symposium (IUS), 2016 IEEE International, 2016, pp. 1-4 doi:10.1109/ULTSYM.2016.7728414

Diarra, B., M. Robini, **E. Roux**, H. Liebgott, C. Cachard, and P. Tortoli. 2014. "Optimization of Free-Moving Elements in 2D Ultrasound Sparse Arrays." In Ultrasonics Symposium (IUS), 2014 IEEE International, pp. 2189–92. doi:10.1109/ULTSYM.2014.0545

Roux, E., B. Diarra, M. Robini, C. Cachard, P. Tortoli, and H. Liebgott. 2014. "Realistic Acoustic Simulation of 2-D Probe Elements in Simulated Annealing Sparse Array Optimization." In Ultrasonics Symposium (IUS), 2014 IEEE International, pp. 2125–28.
doi:10.1109/ULTSYM.2014.0529

Roux, E., A. Ramalli, M. Robini, H. Liebgott, C. Cachard, and P. Tortoli. 2015. "Spiral Array Inspired Multi-Depth Cost Function for 2D Sparse Array Optimization." In Ultrasonics Symposium (IUS), 2015 IEEE International, pp. 1–4. doi:10.1109/ULTSYM.2015.0096

Roux, E., A. Ramalli, P. Tortoli, C. Cachard, M. Robini, and H. Liebgott. 2015. "Speed-up of Acoustic Simulation Techniques for 2D Sparse Array Optimization by Simulated Annealing." In Ultrasonics Symposium (IUS), 2015 IEEE International, pp. 1–4.
doi:10.1109/ULTSYM.2015.0431

National conferences

Roux, Emmanuel, Marc C. Robini, Alessandro Ramalli, Piero Tortoli, Christian Cachard, and Hervé Liebgott. 2015. "Modélisation et Simulation Acoustique Pour L'optimisation de Sondes Échographiques 2D Par Recuit Simulé." In XXVème Colloque GRETSI. Lyon, France.
https://hal.archives-ouvertes.fr/hal-01286079

Roux, Emmanuel, Alessandro Ramalli, Piero Tortoli, Marc Robini, Hervé Liebgott, and Christian Cachard. 2015. "Optimisation du rayonnement acoustique de sondes parcimonieuses pour l'échographie 3D temps-réel." 22ème Congrès Français de Mécanique, 24 au 28 août 2015, Lyon, France (FR).
http://documents.irevues.inist.fr/handle/2042/57698

Other

My PhD in 180 seconds



Figure 46 Screenshot of the video of my PhD in 180 seconds presentation
(Youtube link https://www.youtube.com/watch?v=iIxG-7y3pV4)

In April 2016 I participated in the challenge called "My PhD in 180 seconds" (local finalist of University of Lyon, Figure 46). You can find a video of my presentation on Youtube (link https://www.youtube.com/watch?v=iIxG-7y3pV4, in French).

CREATIS' Image of the year 2013

Each year in CREATIS there is a little challenge to select "the image of the year" that is then printed on the all the grating cards for New Year celebration. I produced the image (Figure 47) that won in 2013 on the base of the optimization results obtained by Bakary Diarra. It was accompanied with the following caption "Simulation of a 3D ultrasound optimized sparse array by random positioning of 256 active elements and apodization". B. Diarra, **E. Roux**, M. Robini, C. Cachard, H. Liebgott. Collaboration : P. Tortoli, MSD-Lab, Université de Florence, Italie

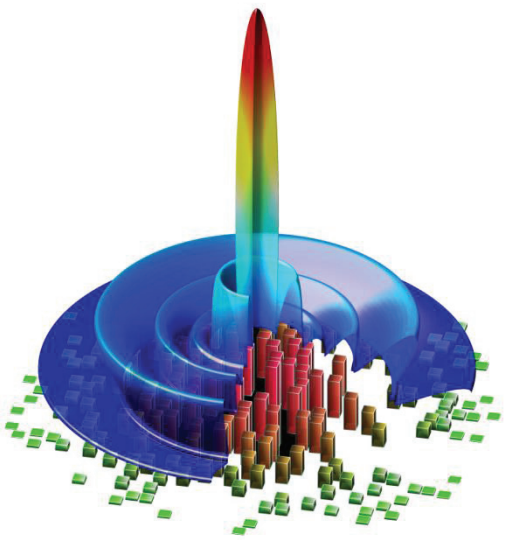


Figure 47 Wining image of the year 2013 at CREATIS Laboratory: Simulation of a 3D ultrasound optimized sparse array by random positioning of 256 active elements and apodization. B. Diarra, **E. Roux**, M. Robini, C. Cachard, H. Liebgott. Collaboration : P. Tortoli, MSD-Lab, Université de Florence, Italie

References

Adler, D. 1993. “Genetic Algorithms and Simulated Annealing: A Marriage Proposal.” In *, IEEE International Conference on Neural Networks, 1993*, 1104–9 vol.2. doi:10.1109/ICNN.1993.298712.

Andresen, Henrik. 2006. “Three-Dimensional Ultrasound Imaging Using a Rotating Array.” Technical University of Denmark, DTU, DK-2800 Kgs. Lyngby, Denmark.

Austeng, A, and S. Holm. 2002. “Sparse 2-D Arrays for 3-D Phased Array Imaging - Design Methods.” *IEEE Transactions on Ultrasonics, Ferroelectrics, and Frequency Control* 49 (8): 1073–86. doi:10.1109/TUFFC.2002.1026019.

Austeng, A., S. Holm, P.K. Weber, N. Aakvaag, and K. Iranpour. 1997. “1D and 2D Algorithmically Optimized Sparse Arrays.” In *, 1997 IEEE Ultrasonics Symposium, 1997. Proceedings*, 2:1683–86 vol.2. doi:10.1109/ULTSYM.1997.663319.

Azhari, Haim. 2010. “Appendix A: Typical Acoustic Properties of Tissues.” In *BASIC of Biomedical Ultrasound for Engineers*, 313–14. John Wiley & Sons, Inc. http://onlinelibrary.wiley.com/doi/10.1002/9780470561478.app1/summary.

Barnes, Stephen, Mirsaid Bolorforosh, and Robert Phelps. 2005. System and method for 2D partial beamforming arrays with configurable sub-array elements. US20050228277 A1, filed April 5, 2004, and issued October 13, 2005. http://www.google.com/patents/US20050228277.

Begault, Durand R., and Leonard J. Trejo. 2000. “3-D Sound for Virtual Reality and Multimedia.” http://ntrs.nasa.gov/search.jsp?R=20010044352.

Berg, Wendie A., David O. Cosgrove, Caroline J Doré, Fritz K. W. Schäfer, William E. Svensson, Regina J. Hooley, Ralf Ohlinger, et al. 2012. “Shear-Wave Elastography Improves the Specificity of Breast US: The BE1 Multinational Study of 939 Masses.” *Radiology* 262 (2): 435–49. doi:10.1148/radiol.11110640.

Berkhout, A. J., D. de Vries, and P. Vogel. 1993. “Acoustic Control by Wave Field Synthesis.” *The Journal of the Acoustical Society of America* 93 (5): 2764–78. doi:10.1121/1.405852.

Bernard, O., M. Zhang, F. Varray, P. Gueth, J. P. Thiran, H. Liebgott, and D. Friboulet. 2014. “Ultrasound Fourier Slice Imaging: A Novel Approach for Ultrafast Imaging Technique.” In *2014 IEEE International Ultrasonics Symposium*, 129–32. doi:10.1109/ULTSYM.2014.0033.

Berry, Alain, Rokhiya Dia, and Olivier Robin. 2012. “A Wave Field Synthesis Approach to Reproduction of Spatially Correlated Sound Fields.” *The Journal of the Acoustical Society of America* 131 (2): 1226–39. doi:10.1121/1.3675942.

Beyer, Robert Thomas, and Stephen V Letcher. 1969. *Physical Ultrasonics*. Vol. 32. Academic Press.

Boni, C., M. Richard, and S. Barbarossa. 1994. “Optimal Configuration and Weighting of Nonuniform Arrays according to a Maximum ISLR Criterion.” In , *1994 IEEE International Conference on Acoustics, Speech, and Signal Processing, 1994. ICASSP-94*, v:V/157-V/160 vol.5. doi:10.1109/ICASSP.1994.389424.

Brandwood, David. 2012. *Fourier Transforms in Radar and Signal Processing, Second Edition*. Artech House.

Brunke, S.S., and G.R. Lockwood. 1997. “Broad-Bandwidth Radiation Patterns of Sparse Two-Dimensional Vernier Arrays.” *IEEE Transactions on Ultrasonics, Ferroelectrics, and Frequency Control* 44 (5): 1101–9. doi:10.1109/58.655635.

Caliano, G., R. Carotenuto, E. Cianci, Vittorio Foglietti, A. Caronti, A. Iula, and M. Pappalardo. 2005. “Design, Fabrication and Characterization of a Capacitive Micromachined Ultrasonic Probe for Medical Imaging.” *IEEE Transactions on Ultrasonics, Ferroelectrics, and Frequency Control* 52 (12): 2259–69. doi:10.1109/TUFFC.2005.1563268.

Caronti, Alessandro, G. Caliano, R. Carotenuto, A. Savoia, M. Pappalardo, E. Cianci, and V. Foglietti. 2006. “Capacitive Micromachined Ultrasonic Transducer (CMUT) Arrays for Medical Imaging.” *Microelectronics Journal* 37 (8): 770–77. doi:10.1016/j.mejo.2005.10.012.

Chen, Kailiang. 2014. “A Column-Row-Parallel ASIC Architecture for 3D Wearable / Portable Medical Ultrasonic Imaging.” Thesis, Massachusetts Institute of Technology. http://dspace.mit.edu/handle/1721.1/87916.

Chen, Peng, Bin-jian Shen, Li-sheng Zhou, and Yao-wu Chen. 2010. “Optimized Simulated Annealing Algorithm for Thinning and Weighting Large Planar Arrays.” *Journal of Zhejiang University SCIENCE C* 11 (4): 261–69. doi:10.1631/jzus.C0910037.

Chen, Peng, Xiang Tian, and Yaowu Chen. 2010. “Optimization of the Digital Near-Field Beamforming for Underwater 3-D Sonar Imaging System.” *IEEE Transactions on Instrumentation and Measurement* 59 (2): 415–24. doi:10.1109/TIM.2009.2024368.

Cheng, Jiqi, and Jian-yu Lu. 2006. “Extended High-Frame Rate Imaging Method with Limited-Diffraction Beams.” *IEEE Transactions on Ultrasonics, Ferroelectrics, and Frequency Control* 53 (5): 880–99. doi:10.1109/TUFFC.2006.1632680.

Chi, C., Z. Li, and Q. Li. 2015. “Fast Broadband Beamforming Using Nonuniform Fast Fourier Transform for Underwater Real-Time 3-D Acoustical Imaging.” *IEEE Journal of Oceanic Engineering* PP (99): 1–13. doi:10.1109/JOE.2015.2429251.

Choe, Jung Woo, O. Oralkan, and P.T. Khuri-Yakub. 2010. “Design Optimization for a 2-D Sparse Transducer Array for 3-D Ultrasound Imaging.” In *2010 IEEE Ultrasonics Symposium (IUS)*, 1928–31. doi:10.1109/ULTSYM.2010.5935854.

Christiansen, T.L., M.F. Rasmussen, J.P. Bagge, L. Nordahl Moesner, J.A. Jensen, and E.V. Thomsen. 2015. “3-D Imaging Using Row-Column-Addressed Arrays with Integrated Apodization - Part Ii: Transducer Fabrication and Experimental Results.” *IEEE Transactions on Ultrasonics, Ferroelectrics, and Frequency Control* 62 (5): 959–71. doi:10.1109/TUFFC.2014.006819.

Corry, Leo. 1992. “Nicolas Bourbaki and the Concept of Mathematical Structure.” *Synthese* 92 (3): 315–48.

Curie, Jacques, and Pierre Curie. 1880. “Développement, Par Pression, de L’électricité Polaire Dans Les Cristaux Hémièdres À Faces Inclinées.” Comptes rendus hebdomadaires des séances de l’Académie des sciences / publiés... par MM. les secrétaires perpétuels -- 1880-07 -- periodiques. http://gallica.bnf.fr/ark:/12148/bpt6k30485.

———. 1881. “Contractions et Dilatations Produites Par Des Tensions Électriques Dans Les Cristaux Hémièdres À Faces Inclinées.” Comptes rendus hebdomadaires des séances de l’Académie des sciences / publiés... par MM. les secrétaires perpétuels -- 1881-07 -- periodiques. http://gallica.bnf.fr/ark:/12148/bpt6k3049g.

Dabrowski, Waldemar, Joy Dunmore-Buyze, H. Neale Cardinal, and Aaron Fenster. 2001. “A Real Vessel Phantom for Flow Imaging: 3-D Doppler Ultrasound of Steady Flow.” *Ultrasound in Medicine & Biology* 27 (1): 135–41. doi:10.1016/S0301-5629(00)00277-5.

Daher, N.M., and J.T. Yen. 2006. “2-D Array for 3-D Ultrasound Imaging Using Synthetic Aperture Techniques.” *IEEE Transactions on Ultrasonics, Ferroelectrics, and Frequency Control* 53 (5): 912–24. doi:10.1109/TUFFC.2006.1632682.

Daniel, Jerome, Sebastien Moreau, and Rozenn Nicol. 2003. “Further Investigations of High-Order Ambisonics and Wavefield Synthesis for Holophonic Sound Imaging.” In *Audio Engineering Society Convention 114*. http://www.aes.org/e-lib/browse.cfm?elib=12567.

Davidsen, R. E., J. A. Jensen, and S. W. Smith. 1994. “Two-Dimensional Random Arrays for Real Time Volumetric Imaging.” *Ultrasonic Imaging* 16 (3): 143–63. doi:10.1006/uimg.1994.1009.

Deffieux, T., J.-L. Gennisson, M. Tanter, and M. Fink. 2008. “Assessment of the Mechanical Properties of the Musculoskeletal System Using 2-D and 3-D Very High Frame Rate Ultrasound.” *IEEE Transactions on Ultrasonics, Ferroelectrics, and Frequency Control* 55 (10): 2177–90. doi:10.1109/TUFFC.917.

Delabays, Alain, Natesa G. Pandian, Qi-Ling Cao, Lissa Sugeng, Gerald Marx, Achi Ludomirski, and Steven L. Schwartz. 1995. “Transthoracic Real-Time Three-Dimensional Echocardiography Using a Fan-Like Scanning Approach For Data Acquisition.” *Echocardiography* 12 (1): 49–59. doi:10.1111/j.1540-8175.1995.tb00521.x.

Deleuze, Gilles. 1994. *Difference and Repetition*. New York: Columbia University Press.

Deleuze, Gilles, and Félix Guattari. 1987. *A Thousand Plateaus: Capitalism and Schizophrenia*. Minneapolis: University of Minnesota Press.

Deprez, Jean-François, Elisabeth Brusseau, Cédric Schmitt, Guy Cloutier, and Olivier Basset. 2009. “3D Estimation of Soft Biological Tissue Deformation from Radio-Frequency Ultrasound Volume Acquisitions.” *Medical Image Analysis*, Includes Special Section on Medical Image Analysis on the 2006 Workshop Microscopic Image Analysis with Applications in Biology, 13 (1): 116–27. doi:10.1016/j.media.2008.07.003.

Diarra, B., M. Robini, E. Roux, H. Liebgott, C. Cachard, and P. Tortoli. 2014. “Optimization of Free-Moving Elements in 2D Ultrasound Sparse Arrays.” In *Ultrasonics Symposium (IUS), 2014 IEEE International*, 2189–92. doi:10.1109/ULTSYM.2014.0545.

Diarra, B., M. Robini, P. Tortoli, C. Cachard, and H. Liebgott. 2013. “Design of Optimal 2-D Nongrid Sparse Arrays for Medical Ultrasound.” *IEEE Transactions on Biomedical Engineering* 60 (11): 3093–3102. doi:10.1109/TBME.2013.2267742.

Doherty, R. D., D. A. Hughes, F. J. Humphreys, J. J. Jonas, D. Juul Jensen, M. E. Kassner, W. E. King, T. R. McNelley, H. J. McQueen, and A. D. Rollett. 1997. “Current Issues in Recrystallization: A Review.” *Materials Science and Engineering: A* 238 (2): 219–74. doi:10.1016/S0921-5093(97)00424-3.

Downey, Dónal B., David A. Nicolle, Morris F. Levin, and Aaron Fenster. 1996. “Three-Dimensional Ultrasound Imaging of the Eye.” *Eye* 10 (1): 75–81. doi:10.1038/eye.1996.11.

Felix, Nicolas, Marc Lethiecq, Caroline Millar, and Louis P Tran-Huu-Hue. 2000. “Influence of Piezoceramic Composition, Pitch, and Layout on the Performances of Sparse 2D Array Transducers for Medical Imaging.” In *Medical Imaging 2000*, 225–233. International Society for Optics and Photonics.

Fenster, Aaron, Dónal B. Downey, and H. Neale Cardinal. 2001. “Three-Dimensional Ultrasound Imaging.” *Physics in Medicine and Biology* 46 (5): R67. doi:10.1088/0031-9155/46/5/201.

Fernandez, A. T., K. L. Gammelmark, J. J. Dahl, C. G. Keen, R. C. Gauss, and G. E. Trahey. 2003. “Synthetic Elevation Beamforming and Image Acquisition Capabilities Using an 8 /spl Times/ 128 1.75D Array.” *IEEE Transactions on Ultrasonics, Ferroelectrics, and Frequency Control* 50 (1): 40–57. doi:10.1109/TUFFC.2003.1176524.

Fink, M. 1992. “Time Reversal of Ultrasonic Fields. I. Basic Principles.” *IEEE Transactions on Ultrasonics, Ferroelectrics, and Frequency Control* 39 (5): 555–66. doi:10.1109/58.156174.

Fisher, R, K Thomenius, R Wodnicki, R Thomas, S Cogan, C Hazard, W Lee, et al. 2005. “Reconfigurable Arrays for Portable Ultrasound.” In *Proc. IEEE Ultrason. Symp*, 1:495–499.

Garcia, D., L.L. Tarnec, S. Muth, E. Montagnon, J. Porée, and G. Cloutier. 2013. “Stolt’s F-K Migration for Plane Wave Ultrasound Imaging.” *IEEE Transactions on Ultrasonics, Ferroelectrics, and Frequency Control* 60 (9): 1853–67. doi:10.1109/TUFFC.2013.2771.

Gazdag, J., and P. Sguazzero. 1984. “Migration of Seismic Data.” *Proceedings of the IEEE* 72 (10): 1302–15. doi:10.1109/PROC.1984.13019.

Gennisson, J.-L., J. Provost, T. Deffieux, C. Papadacci, M. Imbault, M. Pernot, and M. Tanter. 2015. “4-D Ultrafast Shear-Wave Imaging.” *IEEE Transactions on Ultrasonics, Ferroelectrics, and Frequency Control* 62 (6): 1059–65. doi:10.1109/TUFFC.2014.006936.

Gilja, Odd Helge, Alf Inge Smievoll, Nils Thune, Knut Matre, Trygve Hausken, Svein Ødegaard, and Arnold Berstad. 1995. “In Vivo Comparison of 3D Ultrasonography and Magnetic Resonance Imaging in Volume Estimation of Human Kidneys.” *Ultrasound in Medicine & Biology* 21 (1): 25–32. doi:10.1016/0301-5629(94)00082-4.

Guo, Zhenyu, and Aaron Fenster. 1996. “Three-Dimensional Power Doppler Imaging: A Phantom Study to Quantify Vessel Stenosis.” *Ultrasound in Medicine & Biology* 22 (8): 1059–69. doi:10.1016/S0301-5629(96)00125-1.

Hager, P. A., A. Bartolini, and L. Benini. 2016. “Ekho: A 30.3W, 10k-Channel Fully Digital Integrated 3-D Beamformer for Medical Ultrasound Imaging Achieving 298M Focal Points per Second.” *IEEE Transactions on Very Large Scale Integration (VLSI) Systems* 24 (5): 1936–49. doi:10.1109/TVLSI.2015.2488020.

Hasegawa, Hideyuki, and Hiroshi Kanai. 2011. “High-Frame-Rate Echocardiography Using Diverging Transmit Beams and Parallel Receive Beamforming.” *Journal of Medical Ultrasonics* 38 (3): 129–40. doi:10.1007/s10396-011-0304-0.

Haupt, Randy L. 1994. “Thinned Arrays Using Genetic Algorithms.” *IEEE Transactions on Antennas and Propagation* 42 (7): 993–99. doi:10.1109/8.299602.

Holm, S., A. Austeng, K. Iranpour, and J.-F. Hopperstad. 2001. “Sparse Sampling in Array Processing.” In *Nonuniform Sampling*, edited by Farokh Marvasti, 787–833. Information Technology: Transmission, Processing, and Storage. Springer US. http://link.springer.com/chapter/10.1007/978-1-4615-1229-5_19.

Holm, S., and B. Elgetun. 1995. “Optimization of the Beampattern of 2D Sparse Arrays by Weighting.” In *, 1995 IEEE Ultrasonics Symposium, 1995. Proceedings*, 2:1345–48 vol.2. doi:10.1109/ULTSYM.1995.495805.

Holm, S., B. Elgetun, and G. Dahl. 1997. “Properties of the Beampattern of Weight- and Layout-Optimized Sparse Arrays.” *IEEE Transactions on Ultrasonics, Ferroelectrics, and Frequency Control* 44 (5): 983–91. doi:10.1109/58.655623.

Holm, Sverre. 2001. “Ultrasim-a Toolbox for Ultrasound Field Simulation.” *University of Oslo*. http://heim.ifi.uio.no/~sverre/papers/01_Matlab.pdf.

Hughes, S. W., T. J. D’Arcy, D. J. Maxwell, W. Chiu, A. Milner, J. E. Saunders, and R. J. Sheppard. 1996. “Volume Estimation from Multiplanar 2D Ultrasound Images Using a Remote Electromagnetic Position and Orientation Sensor.” *Ultrasound in Medicine & Biology* 22 (5): 561–72. doi:10.1016/0301-5629(96)00022-1.

Hwang, Shun-Fa, and Rong-Song He. 2006. “Improving Real-Parameter Genetic Algorithm with Simulated Annealing for Engineering Problems.” *Advances in Engineering Software* 37 (6): 406–18. doi:10.1016/j.advengsoft.2005.08.002.

Iliadis, Andrew. 2013. “A New Individuation: Deleuze’s Simondon Connection.” *MediaTropes* 4 (1): 83–100.

Jensen, J.A. 1996. “FIELD: A Program for Simulating Ultrasound Systems.” In *10th NordicBaltic Conference on Biomedical Imaging, Vol. 4, Supplement 1, Part 1:351–353*, 351–353.

Jensen, J. A., M. F. Holten-Lund, R. T. Nilsson, M. Hansen, U. D. Larsen, R. P. Domsten, B. G. Tomov, et al. 2013. “SARUS: A Synthetic Aperture Real-Time Ultrasound System.” *IEEE Transactions on Ultrasonics, Ferroelectrics, and Frequency Control* 60 (9): 1838–52. doi:10.1109/TUFFC.2013.2770.

Jensen, J.A., and N.B. Svendsen. 1992. “Calculation of Pressure Fields from Arbitrarily Shaped, Apodized, and Excited Ultrasound Transducers.” *IEEE Transactions on Ultrasonics, Ferroelectrics, and Frequency Control* 39 (2): 262–67. doi:10.1109/58.139123.

Jespersen, Søren K., Jens E. Wilhjelm, and Henrik Sillesen. 1998. “Multi-Angle Compound Imaging.” *Ultrasonic Imaging* 20 (2): 81–102. doi:10.1177/016173469802000201.

Karaman, Mustafa, I.O. Wygant, O. Oralkan, and B.T. Khuri-Yakub. 2009. “Minimally Redundant 2-D Array Designs for 3-D Medical Ultrasound Imaging.” *IEEE Transactions on Medical Imaging* 28 (7): 1051–61. doi:10.1109/TMI.2008.2010936.

Kelly, J. F., and R. J. McGough. 2006. “A Time-Space Decomposition Method for Calculating the Nearfield Pressure Generated by a Pulsed Circular Piston.” *IEEE Transactions on Ultrasonics, Ferroelectrics, and Frequency Control* 53 (6): 1150–59. doi:10.1109/TUFFC.2006.1642513.

Kirkpatrick, Scott, C Daniel Gelatt, Mario P Vecchi, and others. 1983. “Optimization by Simulated Annealing.” *Science* 220 (4598): 671–680.

Kortbek, Jacob, Jørgen Arendt Jensen, and Kim Løkke Gammelmark. 2013. “Sequential Beamforming for Synthetic Aperture Imaging.” *Ultrasonics* 53 (1): 1–16. doi:10.1016/j.ultras.2012.06.006.

Kruizinga, P., F. Mastik, N. de Jong, A.F.W. van der Steen, and G. van Soest. 2012. “Plane-Wave Ultrasound Beamforming Using a Nonuniform Fast Fourier Transform.” *IEEE Transactions on Ultrasonics, Ferroelectrics, and Frequency Control* 59 (12). doi:10.1109/TUFFC.2012.2509.

Kuo, S. M., and D. R. Morgan. 1999. “Active Noise Control: A Tutorial Review.” *Proceedings of the IEEE* 87 (6): 943–73. doi:10.1109/5.763310.

Kuo, Sen M., and Dennis Morgan. 1995. *Active Noise Control Systems: Algorithms and DSP Implementations*. 1st ed. New York, NY, USA: John Wiley & Sons, Inc.

Levine, R. A., M. D. Handschumacher, A. J. Sanfilippo, A. A. Hagege, P. Harrigan, J. E. Marshall, and A. E. Weyman. 1989. “Three-Dimensional Echocardiographic Reconstruction of the Mitral Valve, with Implications for the Diagnosis of Mitral Valve Prolapse.” *Circulation* 80 (3): 589–98. doi:10.1161/01.CIR.80.3.589.

Light, Edward D, Salim F Idriss, Patrick D Wolf, and Stephen W Smith. 2001. “Real-Time Three-Dimensional Intracardiac Echocardiography.” *Ultrasound in Medicine & Biology* 27 (9): 1177–83. doi:10.1016/S0301-5629(01)00421-5.

Lindseth, Frank, Thomas Langø, Tormod Selbekk, Rune Hansen, Ingerid Reinertsen, Christian Askeland, Ole Solheim, Geirmund Unsgård, Ronald Mårvik, and Toril A Nagelhus Hernes. 2013. “Ultrasound-Based Guidance and Therapy.” *Advancements and Breakthroughs in Ultrasound Imaging*, 28–82.

Lockwood, G.R., and F.S. Foster. 1996. “Optimizing the Radiation Pattern of Sparse Periodic Two-Dimensional Arrays.” *IEEE Transactions on Ultrasonics, Ferroelectrics, and Frequency Control* 43 (1): 15–19. doi:10.1109/58.484458.

Lockwood, G.R., J.R. Talman, and S.S. Brunke. 1998. “Real-Time 3-D Ultrasound Imaging Using Sparse Synthetic Aperture Beamforming.” *IEEE Transactions on Ultrasonics, Ferroelectrics, and Frequency Control* 45 (4): 980–88. doi:10.1109/58.710573.

Logan, A.S., L.L.P. Wong, A.I.H. Chen, and J.T.W. Yeow. 2011. “A 32 X 32 Element Row-Column Addressed Capacitive Micromachined Ultrasonic Transducer.” *IEEE Transactions on Ultrasonics, Ferroelectrics, and Frequency Control* 58 (6): 1266–71. doi:10.1109/TUFFC.2011.1937.

Lu, Jian-Yu. 1997. “2D and 3D High Frame Rate Imaging with Limited Diffraction Beams.” *IEEE Transactions on Ultrasonics, Ferroelectrics, and Frequency Control* 44 (4): 839–56. doi:10.1109/58.655200.

Martínez-Graullera, Oscar, Carlos J. Martín, Gregorio Godoy, and Luis G. Ullate. 2010. “2D Array Design Based on Fermat Spiral for Ultrasound Imaging.” *Ultrasonics*, Selected Papers from ICU 2009, 50 (2): 280–89. doi:10.1016/j.ultras.2009.09.010.

Matrone, G., F. Quaglia, and G. Magenes. 2010. “Modeling and Simulation of Ultrasound Fields Generated by 2D Phased Array Transducers for Medical Applications.” In *2010 Annual International Conference of the IEEE Engineering in Medicine and Biology Society (EMBC)*, 6003–6. doi:10.1109/IEMBS.2010.5627588.

Matrone, G., A.S. Savoia, M. Terenzi, G. Caliano, F. Quaglia, and G. Magenes. 2014. “A Volumetric CMUT-Based Ultrasound Imaging System Simulator with Integrated Reception and µ-Beamforming Electronics Models.” *IEEE Transactions on Ultrasonics, Ferroelectrics, and Frequency Control* 61 (5): 792–804. doi:10.1109/TUFFC.2014.2971.

Mills, D. M., and S. W. Smith. 2002. “Multi-Layered PZT/polymer Composites to Increase Signal-to-Noise Ratio and Resolution for Medical Ultrasound Transducers. II. Thick Film Technology.” *IEEE Transactions on Ultrasonics, Ferroelectrics, and Frequency Control* 49 (7): 1005–14. doi:10.1109/TUFFC.2002.1020171.

Montaldo, G., M. Tanter, J. Bercoff, N. Benech, and M. Fink. 2009. “Coherent Plane-Wave Compounding for Very High Frame Rate Ultrasonography and Transient Elastography.” *IEEE Transactions on Ultrasonics, Ferroelectrics, and Frequency Control* 56 (3): 489–506. doi:10.1109/TUFFC.2009.1067.

Moritz, W. E., A. S. Pearlman, D. H. Mc Cabe, D. K. Medema, M. E. Ainsworth, and M. S. Boles. 1983. “An Ultrasonic Technique for Imaging the Ventricle in Three Dimensions and Calculating Its Volume.” *IEEE Transactions on Biomedical Engineering* BME-30 (8): 482–92. doi:10.1109/TBME.1983.325151.

Mucci, Ronald A. 1984. “A Comparison of Efficient Beamforming Algorithms.” *IEEE Transactions on Acoustics, Speech and Signal Processing* 32 (3): 548–58. doi:10.1109/TASSP.1984.1164359.

Murino, Vittorio, Andrea Trucco, and Alessandra Tesei. 1997. “Beam Pattern Formulation and Analysis for Wide-Band Beamforming Systems Using Sparse Arrays.” *Signal Processing* 56 (2): 177–83. doi:10.1016/S0165-1684(96)00166-1.

Nadeau, C., Hongliang Ren, A. Krupa, and P. Dupont. 2015. “Intensity-Based Visual Servoing for Instrument and Tissue Tracking in 3D Ultrasound Volumes.” *IEEE Transactions on Automation Science and Engineering* 12 (1): 367–71. doi:10.1109/TASE.2014.2343652.

Nelson, Thomas R., J. Brian Fowlkes, Jacques S. Abramowicz, and Charles C. Church. 2009. “Ultrasound Biosafety Considerations for the Practicing Sonographer and Sonologist.” *Journal of Ultrasound in Medicine* 28 (2): 139–50.

Nelson, Thomas R., and Dolores H. Pretorius. 1998. “Three-Dimensional Ultrasound Imaging.” *Ultrasound in Medicine & Biology* 24 (9): 1243–70. doi:10.1016/S0301-5629(98)00043-X.

Nicolescu, Basarab. 2008. *Transdisciplinarity: Theory and Practice*. Cresskill, NJ: Hampton Press.

———. 2016. *Le Tiers caché dans les domaines de la connaissance*. L’Isle-sur-la-Sorgue: Le Bois d’Orion.

Nilsen, C. I. C., and I. Hafizovic. 2009. “Beamspace Adaptive Beamforming for Ultrasound Imaging.” *IEEE Transactions on Ultrasonics, Ferroelectrics, and Frequency Control* 56 (10): 2187–97. doi:10.1109/TUFFC.2009.1301.

Ningning, Song. 2014. “Quantitative Photoacoustic Tomography for Breast Cancer Screening.” Theses, Centrale Marseille. https://hal.archives-ouvertes.fr/tel-01280134.

Nuttall, A. 1981. “Some Windows with Very Good Sidelobe Behavior.” *IEEE Transactions on Acoustics, Speech, and Signal Processing* 29 (1): 84–91. doi:10.1109/TASSP.1981.1163506.

Oralkan, O., A. S. Ergun, J. A. Johnson, M. Karaman, U. Demirci, K. Kaviani, T. H. Lee, and B. T. Khuri-Yakub. 2002. “Capacitive Micromachined Ultrasonic Transducers: Next-Generation Arrays for Acoustic Imaging?” *IEEE Transactions on Ultrasonics, Ferroelectrics, and Frequency Control* 49 (11): 1596–1610. doi:10.1109/TUFFC.2002.1049742.

Papadacci, C., M. Pernot, M. Couade, M. Fink, and M. Tanter. 2014. “High-Contrast Ultrafast Imaging of the Heart.” *IEEE Transactions on Ultrasonics, Ferroelectrics, and Frequency Control* 61 (2): 288–301. doi:10.1109/TUFFC.2014.6722614.

Piwakowski, B., and K. Sbai. 1999. “A New Approach to Calculate the Field Radiated from Arbitrarily Structured Transducer Arrays.” *IEEE Transactions on Ultrasonics, Ferroelectrics, and Frequency Control* 46 (2): 422–40. doi:10.1109/58.753032.

Poletti, Mark A. 2005. “Three-Dimensional Surround Sound Systems Based on Spherical Harmonics.” *J. Audio Eng. Soc* 53 (11): 1004–1025.

Prager, R. W., U. Z. Ijaz, A. H. Gee, and G. M. Treece. 2010. “Three-Dimensional Ultrasound Imaging.” *Proceedings of the Institution of Mechanical Engineers, Part H: Journal of Engineering in Medicine* 224 (2): 193–223. doi:10.1243/09544119JEIM586.

Provost, J., C. Papadacci, C. Demene, J. L. Gennisson, M. Tanter, and M. Pernot. 2015. “3-D Ultrafast Doppler Imaging Applied to the Noninvasive Mapping of Blood Vessels in Vivo.” *IEEE Transactions on Ultrasonics, Ferroelectrics, and Frequency Control* 62 (8): 1467–72. doi:10.1109/TUFFC.2015.007032.

Provost, Jean, Clement Papadacci, Juan Esteban Arango, Marion Imbault, Mathias Fink, Jean-Luc Gennisson, Mickael Tanter, and Mathieu Pernot. 2014. “3D Ultrafast Ultrasound Imaging in Vivo.” *Physics in Medicine and Biology* 59 (19): L1. doi:10.1088/0031-9155/59/19/L1.

Ramadas, S., J. Jackson, J. Dziewierz, R. O’Leary, and A. Gachagan. 2014. “Application of Conformal Map Theory for Design of 2-D Ultrasonic Array Structure for Ndt Imaging Application: A Feasibility Study.” *IEEE Transactions on Ultrasonics, Ferroelectrics, and Frequency Control* 61 (3): 496–504. doi:10.1109/TUFFC.2014.2933.

Ramalli, A., E. Boni, A.S. Savoia, and P. Tortoli. 2015. “Density-Tapered Spiral Arrays for Ultrasound 3-D Imaging.” *IEEE Transactions on Ultrasonics, Ferroelectrics, and Frequency Control* 62 (8): 1580–88. doi:10.1109/TUFFC.2015.007035.

Ramalli, A., and P. Tortoli. 2014. “256-Element Density-Tapered Spiral Matrices for Ultrasound Phased Imaging.” In *Ultrasonics Symposium (IUS), 2014 IEEE International*, 2087–90. doi:10.1109/ULTSYM.2014.0520.

Ramm, Olaf T. Von, and Stephen W. Smith. 1983. “Beam Steering with Linear Arrays.” *IEEE Transactions on Biomedical Engineering* BME-30 (8): 438–52. doi:10.1109/TBME.1983.325149.

Ramm, Olaf T. von, and Stephen W. Smith. 1987. Three-dimensional imaging system. US4694434 A, filed June 12, 1984, and issued September 15, 1987. http://www.google.com/patents/US4694434.

Rasmussen, M.F., T.L. Christiansen, E.V. Thomsen, and J.A. Jensen. 2015. “3-D Imaging Using Row-Column-Addressed Arrays with Integrated Apodization - Part I: Apodization Design and Line Element Beamforming.” *IEEE Transactions on Ultrasonics, Ferroelectrics, and Frequency Control* 62 (5): 947–58. doi:10.1109/TUFFC.2014.006531.

Rivera, J. Miguel, Samuel C. Siu, Mark D. Handschumacher, Jean-Paul Lethor, J. Luis Guerrero, Gus J. Vlahakes, John D. Mitchell, Arthur E. Weyman, Mary Etta E. King, and Robert A. Levine. 1994. “Three-Dimensional Reconstruction of Ventricular Septal Defects: Validation Studies and in Vivo Feasibility.” *Journal of the American College of Cardiology* 23 (1): 201–8. doi:10.1016/0735-1097(94)90521-5.

Robini, Marc C. 2013. “Theoretically Grounded Acceleration Techniques for Simulated Annealing.” In *Handbook of Optimization*, edited by Ivan Zelinka, Václav Snášel, and Ajith Abraham, 311–35. Intelligent Systems Reference Library 38. Springer Berlin Heidelberg. http://link.springer.com/chapter/10.1007/978-3-642-30504-7_13.

Robini, Marc C., and Pierre-Jean Reissman. 2013. “From Simulated Annealing to Stochastic Continuation: A New Trend in Combinatorial Optimization.” *Journal of Global Optimization* 56 (1): 185–215. doi:10.1007/s10898-012-9860-0.

Robinson, Andrew L., David N. Roundhill, Brent Stephen Robinson, and Paul Detmer. 2003. 2D ultrasonic transducer array for two dimensional and three dimensional imaging. US6582367 B1, filed September 15, 2000, and issued June 24, 2003. http://www.google.com/patents/US6582367.

Roux, E., B. Diarra, M. Robini, C. Cachard, P. Tortoli, and H. Liebgott. 2014. “Realistic Acoustic Simulation of 2-D Probe Elements in Simulated Annealing Sparse Array Optimization.” In *Ultrasonics Symposium (IUS), 2014 IEEE International*, 2125–28. doi:10.1109/ULTSYM.2014.0529.

Roux, E., A. Ramalli, M. Robini, H. Liebgott, C. Cachard, and P. Tortoli. 2015. “Spiral Array Inspired Multi-Depth Cost Function for 2D Sparse Array Optimization.” In *Ultrasonics Symposium (IUS), 2015 IEEE International*, 1–4. doi:10.1109/ULTSYM.2015.0096.

Roux, E., A. Ramalli, P. Tortoli, C. Cachard, M. Robini, and H. Liebgott. 2015. “Speed-up of Acoustic Simulation Techniques for 2D Sparse Array Optimization by Simulated Annealing.” In *Ultrasonics Symposium (IUS), 2015 IEEE International*, 1–4. doi:10.1109/ULTSYM.2015.0431.

Savoia, A. S., G. Caliano, and M. Pappalardo. 2012. “A CMUT Probe for Medical Ultrasonography: From Microfabrication to System Integration.” *IEEE Transactions on Ultrasonics, Ferroelectrics, and Frequency Control* 59 (6): 1127–38. doi:10.1109/TUFFC.2012.2303.

Savord, B., and R. Solomon. 2003. “Fully Sampled Matrix Transducer for Real Time 3D Ultrasonic Imaging.” In *2003 IEEE Symposium on Ultrasonics*, 1:945–953 Vol.1. doi:10.1109/ULTSYM.2003.1293556.

Savord, Bernard J. 2012. System and method for amplifying transmit waveforms generated by an ultrasonic system. US8257260 B2, filed June 27, 2005, and issued September 4, 2012. http://www.google.fr/patents/US8257260.

Savord, Bernard J., and Karl E. Thiele. 1999. Phased array acoustic systems with intra-group processors. US5997479 A, filed May 28, 1998, and issued December 7, 1999. http://www.google.com/patents/US5997479.

Schwartz, J. L., and B. D. Steinberg. 1998. "Ultrasparse, Ultrawideband Arrays." *IEEE Transactions on Ultrasonics, Ferroelectrics, and Frequency Control* 45 (2): 376–93. doi:10.1109/58.660149.

Sciallero, Claudia, and Andrea Trucco. 2015. "Design of a Sparse Planar Array for Optimized 3D Medical Ultrasound Imaging." In . Nice, FRANCE.

Seyed-Bolorforosh, Mir Said, Michael Greenstein, Douglas Harriott, and Turuvekere R. Gururaja. 1997. Hybrid piezoelectric for ultrasonic probes. US5638822 A, filed June 30, 1995, and issued June 17, 1997. http://www.google.com/patents/US5638822.

Simondon, Gilbert. 2005. *L'individuation à la lumière des notions de forme et d'information*. Editions Jérôme Millon.

Smallman, Raymond E, and Ray J Bishop. 1999. *Modern Physical Metallurgy and Materials Engineering*. Butterworth-Heinemann.

Smith, Lowell S., and Axel F. Brisken. 1980. Front surface matched piezoelectric ultrasonic transducer array with wide field of view. US4211948 A, filed November 8, 1978, and issued July 8, 1980. http://www.google.com/patents/US4211948.

Smith, S.W., Jr. Pavy H.G., and O.T. von Ramm. 1991. "High-Speed Ultrasound Volumetric Imaging System. I. Transducer Design and Beam Steering." *IEEE Transactions on Ultrasonics, Ferroelectrics, and Frequency Control* 38 (2): 100–108. doi:10.1109/58.68466.

Stepanishen, Peter R. 1971. "Transient Radiation from Pistons in an Infinite Planar Baffle." *The Journal of the Acoustical Society of America* 49 (5B): 1629–38. doi:10.1121/1.1912541.

Stetten, GEORGE D, TAKAHIRO Ota, CHIKAI J Ohazama, CRAIG Fleishman, JOHN Castellucci, JOHN Oxaal, THOMAS Ryan, J Kisslo, and OT von Ramm. 1998. "Real-Time 3D Ultrasound: A New Look at the Heart." *Journal of Cardiovascular Diagnosis and Procedures* 15 (2): 73–84.

Sugeng, Lissa, Victor Mor-Avi, Lynn Weinert, Johannes Niel, Christian Ebner, Regina Steringer-Mascherbauer, Frank Schmidt, et al. 2006. "Quantitative Assessment of Left Ventricular Size and Function Side-by-Side Comparison of Real-Time Three-Dimensional Echocardiography and Computed Tomography With Magnetic Resonance Reference." *Circulation* 114 (7): 654–61. doi:10.1161/CIRCULATIONAHA.106.626143.

Synnevag, J. F., A. Austeng, and S. Holm. 2007. "Adaptive Beamforming Applied to Medical Ultrasound Imaging." *IEEE Transactions on Ultrasonics, Ferroelectrics, and Frequency Control* 54 (8): 1606–13. doi:10.1109/TUFFC.2007.431.

Szabo, Thomas L. 2004. *Diagnostic Ultrasound Imaging: Inside Out*. Academic Press.

Tanter, M., J. Bercoff, L. Sandrin, and M. Fink. 2002. "Ultrafast Compound Imaging for 2-D Motion Vector Estimation: Application to Transient Elastography." *IEEE Transactions on Ultrasonics, Ferroelectrics, and Frequency Control* 49 (10): 1363–74. doi:10.1109/TUFFC.2002.1041078.

Tekes, C., M. Karaman, and F.L. Degertekin. 2011. "Optimizing Circular Ring Arrays for Forward- Looking IVUS Imaging." *IEEE Transactions on Ultrasonics, Ferroelectrics, and Frequency Control* 58 (12): 2596–2607. doi:10.1109/TUFFC.2011.2123.

Thomenius, Kai E., Robert Gideon Wodnicki, and Ye-Ming Li. 2010. Transmit and receive interface array for highly integrated ultrasound scanner. US7775979 B2, issued August 17, 2010. http://www.google.com/patents/US7775979.

Tong, S., D. B. Downey, H. N. Cardinal, and A. Fenster. 1996. "A Three-Dimensional Ultrasound Prostate Imaging System." *Ultrasound in Medicine & Biology* 22 (6): 735–46. doi:10.1016/0301-5629(96)00079-8.

Trucco, A. 1999. "Thinning and Weighting of Large Planar Arrays by Simulated Annealing." *IEEE Transactions on Ultrasonics, Ferroelectrics, and Frequency Control* 46 (2): 347–55. doi:10.1109/58.753023.

Trucco, A., M. Palmese, and S. Repetto. 2008. "Devising an Affordable Sonar System for Underwater 3-D Vision." *IEEE Transactions on Instrumentation and Measurement* 57 (10): 2348–54. doi:10.1109/TIM.2008.922111.

Turnbull, D.H., and F.S. Foster. 1991. "Beam Steering with Pulsed Two-Dimensional Transducer Arrays." *IEEE Transactions on Ultrasonics, Ferroelectrics, and Frequency Control* 38 (4): 320–33. doi:10.1109/58.84270.

Unsgaard, G., O. M. Rygh, T. Selbekk, T. B. Müller, F. Kolstad, F. Lindseth, and T. A. Nagelhus Hernes. 2005. "Intra-Operative 3D Ultrasound in Neurosurgery." *Acta Neurochirurgica* 148 (3): 235–53. doi:10.1007/s00701-005-0688-y.

Van Laarhoven, Peter JM, and Emile HL Aarts. 1987. *Simulated Annealing*. Springer.

Varray, F., A. Ramalli, C. Cachard, P. Tortoli, and O. Basset. 2011. "Fundamental and Second-Harmonic Ultrasound Field Computation of Inhomogeneous Nonlinear Medium with a Generalized Angular Spectrum Method." *IEEE Transactions on Ultrasonics, Ferroelectrics, and Frequency Control* 58 (7): 1366–76. doi:10.1109/TUFFC.2011.1956.

Varray, François, Olivier Basset, Piero Tortoli, and Christian Cachard. 2013. "CREANUIS: A Non-Linear Radiofrequency Ultrasound Image Simulator." *Ultrasound in Medicine & Biology* 39 (10): 1915–24. doi:10.1016/j.ultrasmedbio.2013.04.005.

Varslot, T., and G. Taraldsen. 2005. "Computer Simulation of Forward Wave Propagation in Soft Tissue." *IEEE Transactions on Ultrasonics, Ferroelectrics, and Frequency Control* 52 (9): 1473–82. doi:10.1109/TUFFC.2005.1516019.

Verhoeven, John D. 1975. *Fundamentals of Physical Metallurgy*. Wiley New York.

Viganó, Maria Carolina, Giovanni Toso, Gerard Caille, Cyril Mangenot, and Ioan E. Lager. 2009. "Sunflower Array Antenna with Adjustable Density Taper." *International Journal of Antennas and Propagation* 2009 (April): e624035. doi:10.1155/2009/624035.

Vray, D., E. Brusseau, V. Detti, F. Varray, A. Basarab, O. Beuf, O. Basset, C. Cachard, H. Liebgott, and P. Delachartre. 2014. "Ultrasound Medical Imaging." In *Medical Imaging Based on Magnetic Fields and Ultrasounds*, 1–72. John Wiley & Sons, Inc. http://dx.doi.org/10.1002/9781118761236.ch1.

Wang, Zhisong, Jian Li, and Renbiao Wu. 2005. "Time-Delay- and Time-Reversal-Based Robust Capon Beamformers for Ultrasound Imaging." *IEEE Transactions on Medical Imaging* 24 (10): 1308–22. doi:10.1109/TMI.2005.857222.

Weber, P.K., R.M. Schmitt, B.D. Tylkowski, and J. Steck. 1994. "Optimization of Random Sparse 2-D Transducer Arrays for 3-D Electronic Beam Steering and Focusing." In , *1994 IEEE Ultrasonics Symposium, 1994. Proceedings*, 3:1503–6 vol.3. doi:10.1109/ULTSYM.1994.401875.

Wildes, D. G., R. Y. Chiao, C. M. W. Daft, K. W. Rigby, L. S. Smith, and K. E. Thomenius. 1997. "Elevation Performance of 1.25D and 1.5D Transducer Arrays." *IEEE Transactions on Ultrasonics, Ferroelectrics, and Frequency Control* 44 (5): 1027–37. doi:10.1109/58.655628.

Wu, Junru, and Jie Tong. 1998. “Measurements of the Nonlinearity Parameter BA of Contrast Agents.” *Ultrasound in Medicine & Biology* 24 (1): 153–59. doi:10.1016/S0301-5629(97)00207-X.

Wygant, I.O., N. Jamal, H. Lee, A. Nikoozadeh, O. Oralkan, Mustafa Karaman, and B. Khuri-yakub. 2009. “An Integrated Circuit with Transmit Beamforming Flip-Chip Bonded to a 2-D CMUT Array for 3-D Ultrasound Imaging.” *IEEE Transactions on Ultrasonics, Ferroelectrics, and Frequency Control* 56 (10): 2145–56. doi:10.1109/TUFFC.2009.1297.

Yiu, Billy Y. S., Simon S. M. Lai, and Alfred C. H. Yu. 2014. “Vector Projectile Imaging: Time-Resolved Dynamic Visualization of Complex Flow Patterns.” *Ultrasound in Medicine & Biology* 40 (9): 2295–2309. doi:10.1016/j.ultrasmedbio.2014.03.014.

Yiu, B.Y.S., IK.H. Tsang, and AC.H. Yu. 2011. “GPU-Based Beamformer: Fast Realization of Plane Wave Compounding and Synthetic Aperture Imaging.” *IEEE Transactions on Ultrasonics, Ferroelectrics, and Frequency Control* 58 (8): 1698–1705. doi:10.1109/TUFFC.2011.1999.

Zhang, M., A. Besson, R. E. Carrillo, F. Varray, M. Viallon, H. Liebgott, J. P. Thiran, D. Friboulet, and O. Bernard. 2015. “Extension of Ultrasound Fourier Slice Imaging Theory to Sectorial Acquisition.” In *Ultrasonics Symposium (IUS), 2015 IEEE International*, 1–4. doi:10.1109/ULTSYM.2015.0185.

Zhao, Yue, Adeline Bernard, Christian Cachard, and Hervé Liebgott. 2014. “Biopsy Needle Localization and Tracking Using ROI-RK Method.” *Abstract and Applied Analysis* 2014 (October): 973147. doi:10.1155/2014/973147.

APPENDIX CONTENT

I. Optimization and analysis pipeline

II. Online video description

III. Dissemination activities

IV. Résumé substantiel en français

APPENDIX I: Optimization and analysis pipeline

The pipeline that was used to perform the optimizations (Figure 48) was presented in the "Developers' Club"[29] that took place in CREATIS laboratory on the 15th of January, 2016.

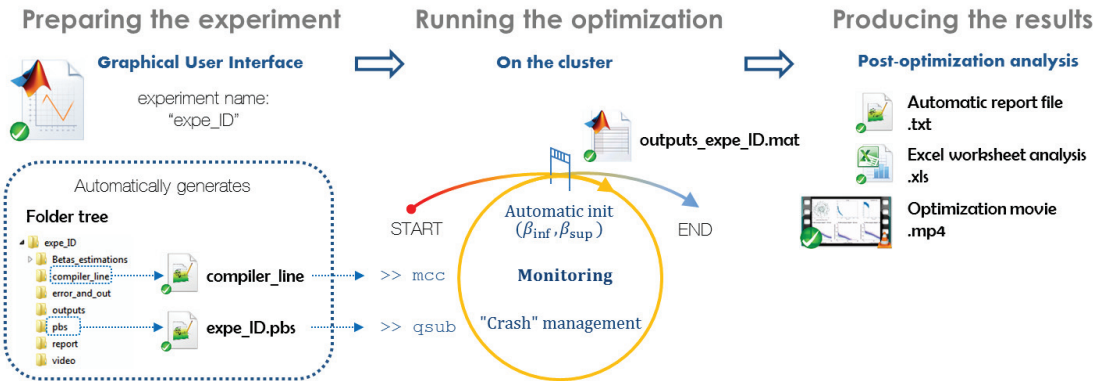


Figure 48 Illustration of the optimization and analysis pipeline

The pipeline description starts with the files and folders organization of the implementation of the proposed general 2D array optimization framework (named optibox) before detailing the three steps (preparing the experiment, running the optimization and producing the results) highlighted on Figure 48.

Optibox: files and folders organization

As displayed on Figure 49, the implementation of the proposed general 2D array optimization framework (named optibox) is made of two main folders: *data* (green area on Figure 49) and *src* (blue area on Figure 49). For example, let "expe_ID" be the identifier of a new experiment.

- The main folder *data* contains specific information for the new experiment "expe_ID", in a subfolder named *data/experiments/expe_ID*. But *data* also contains information that can be shared by all the experiments under the *data/notouch* subfolder.
- The main folder *src* contains the ultrasound simulation software FIELD II (footnote 10 p. 13) in *src/FIELDII*, the Graphical User Interface (GUI) (brown area on Figure 49) in *src/GUI* subfolder, and the implementation of the simulated annealing (SA) process in *src/SA_box.* It also contains the following main files:
  - *init_inf_fun.m* and *init_sup_fun.m*: to estimate the initial parameters β_{inf} and β_{sup}.
  - *monitoring.m* (ex *check_it_out.m)*: to process the intermediate results and perform the optimization run monitoring. This same file is executed once the optimization is finished to produce the post- optimization analysis.
  - *optimize.m*: to start the optimization process. It calls the two initializing scripts *init_inf_fun.m* and *init_sup_fun.m* automatically.

[29] The concepts of object oriented programing (OOP) were presented by Emmanuel Roux and Eduardo Davila during the session of the « developers' club » that took place in CREATIS laboratory on the 29th of May, 2016. The example of OOP MATLAB code that is available online at https://www.creatis.insa-lyon.fr/site7/en/roux

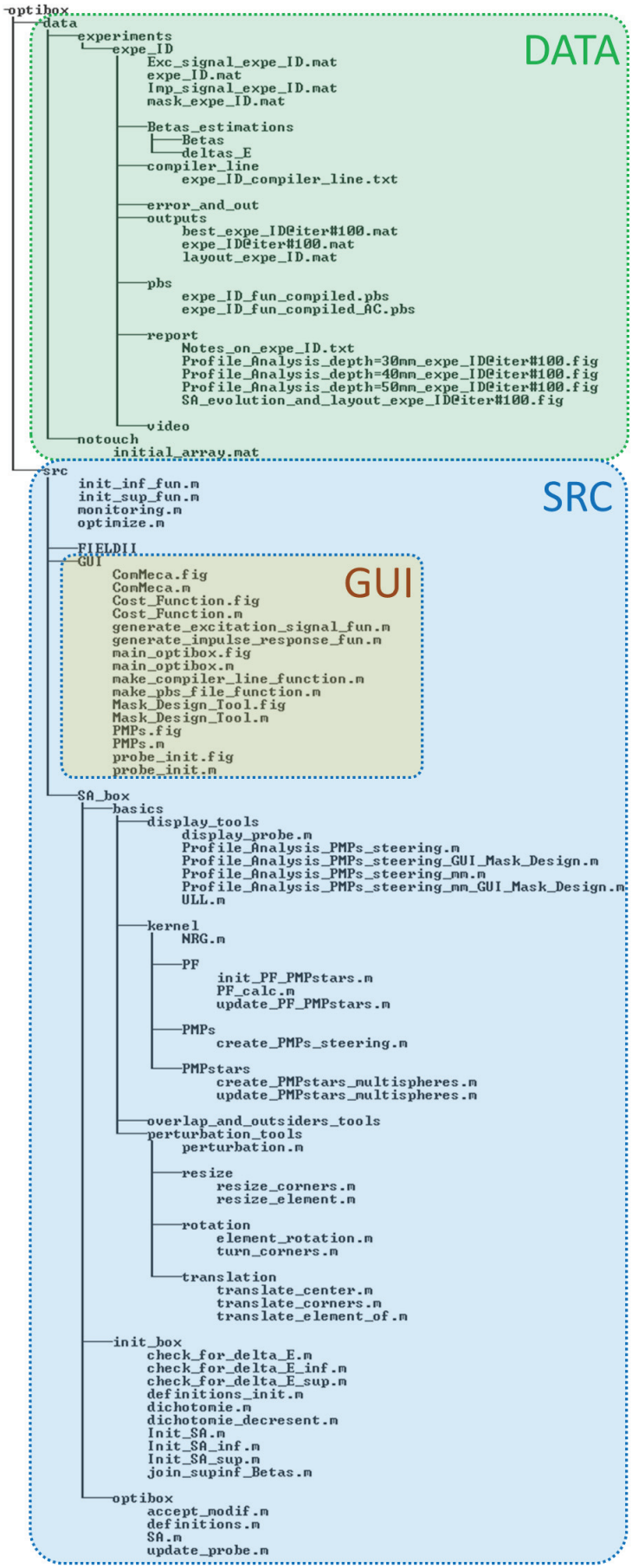


Figure 49 Folder tree of the ultrasound 2D array optimization framework (optibox)

Preparing the experiment

The GUI is used to set up all the optimization parameters. Five of the six entities which compose the GUI are displayed on Figure 50. The sixth entity was already presented in Figure 35 and it would appear automatically if the third energy function U_3 is selected in the *Cost_Function* entity.

The inputs of the five entities displayed on Figure 50 are the following:

- *main_optibox*:
  - The sampling frequency F_s in Hz
  - The value of σ to fix the number of iterations
  - The focal point coordinates (x_f, y_f, z_f) in mm
  - The experiment identifier (for example "expe_ID")
- *probe_init*:
  - The file of the initial probe (generated outside the optibox)
  - The maximum radius of the aperture r_{p} (if required) in mm
  - The central frequency f_c in Hz
  - The speed of sound c in m/s
  - The non-overlapping margin (the inverse of the value is multiplied by λ)
- *PMP*:
  - The radius of the hemispheres (R_1, R_2 and R_3) where the pressure field is computed in mm. For example to have three hemispheres at depths 15 mm, 25 mm and 35 mm this field should contain "15,25,35".
  - The number of PMP to set on each hemisphere
- *Cost_Function*:
  - The button group allows selecting the energy function (here named cost function) definition between (60) (top button), (61) (middle button) and (72) (bottom button).
  - When (60) or (61) are selected it is necessary to enter in mm the desired resolution (width of the main lobe region θ_{ML}) at the level entered in dB for the mask limit (equivalent to the cut value C). This is done at each depth where a hemisphere of PMP is located by separating values with a comma.
  - When (72) is selected, the resolution and the mask limits are not considered but they will be automatically computed by the *MASK_Design_Tool* entity (Figure 35) that will start when clicking on the "Run" button after that all the other entities are correctly filled up.
- *ComMeca*:
  - The perturbation type to enable (yet the translation, rotation and the size variation are implemented).
  - When the translation perturbation is activated, the maximum range of translation must be entered in $\mu\mathrm{m}$.

When all the entities are correctly filled up, clicking on the "Run" button of *main_optibox* will optionally open the *MASK_Design_Tool* entity (Figure 35) if the energy function (72) has been selected (bottom button) in the *Cost_function* entity. In any case and for each new experiment it will create a specific folder tree (and specific files in it) under *data/experiments/expe_ID*.

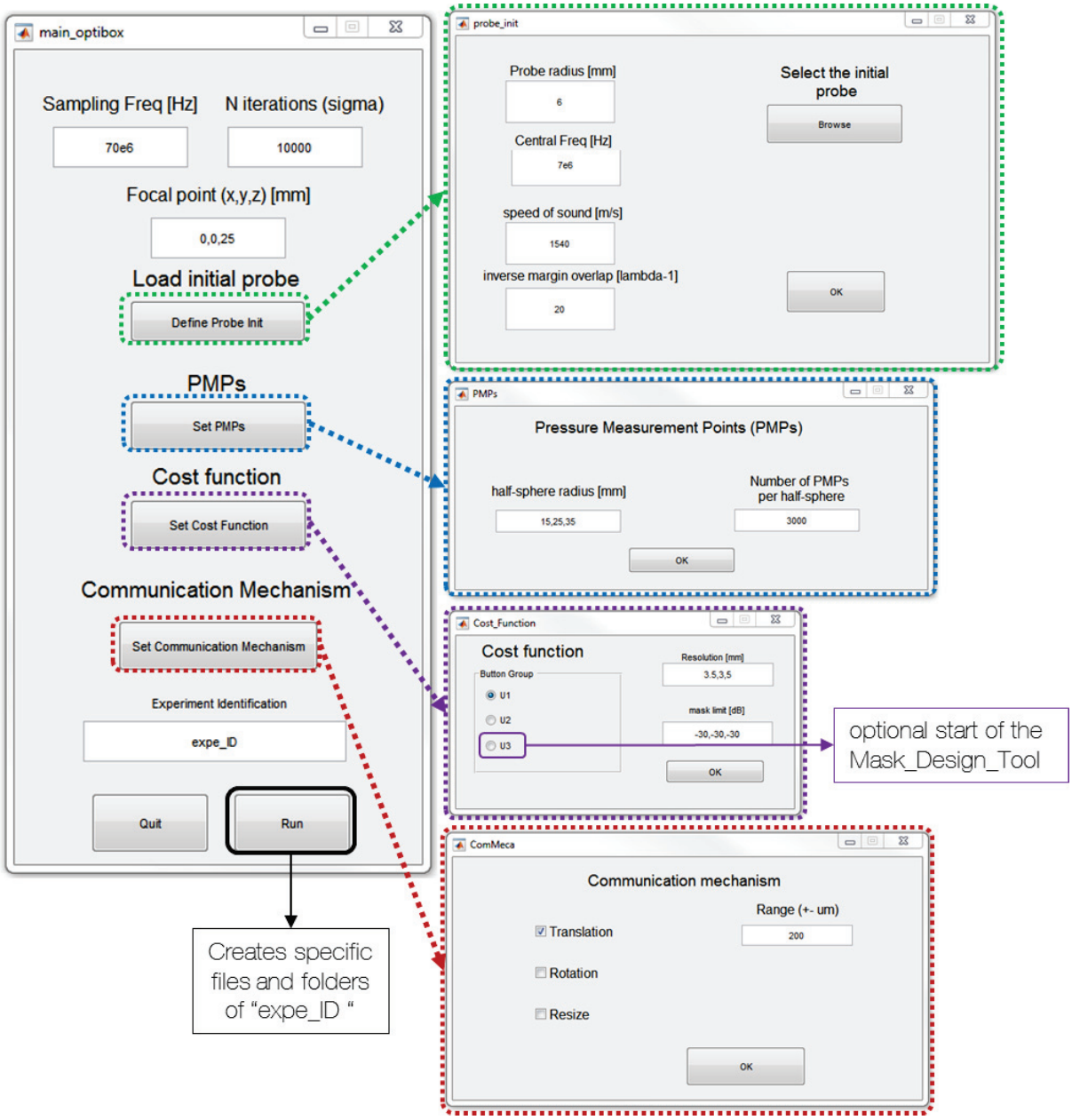


Figure 50 Detailed screenshot of the graphical user interface (GUI) implemented to setup the optimization experiment parameters.

The specific folders that are automatically created and their intended content are the following:

- *Betas_estimations*: to store the estimated initial parameters β_{inf} and β_{sup} and the ΔU^{+} vectors which contain the energy variations that were used to compute β_{inf} and β_{sup}.
- *compiler_line*: a command line is automatically generated and stored in a text file so that a simple copy/paste is required to compile the job on the cluster.
- *error_and_out*: in case of "crash" (error or shutdown of the cluster) this folder will contain (in text files) the error and out messages generated by the cluster machine.
- *outputs*: to store the final and intermediate results (used for monitoring the experiment)
- *pbs*: to store the pbs files that are used to submit a job request on the cluster.
- *report*: to store the monitoring graphs (current beam profiles analysis, evolution of the optimization) and the automatically generated report file (*Notes_on_expe_ID.txt).*
- *video*: to store the movie of the optimization run once it is finished.

The specific files that are automatically created by the GUI are the following:

- *expe_ID.mat*: this file contains all the experiment setup information.
- *Exc_signal_expe_ID.mat*: this file contains the excitation signal (transmitted wave form).
- *Imp_signal_expe_ID.mat*: this file contains the impulse response of the transducers.
- *mask_expe_ID.mat* (optional): the sculpting mask generated by the *MASK_Design_Tool*.
- *expe_ID_compiler_line.txt*: the command line to compile the job on the cluster.
- *expe_ID_fun_compiled.pbs*: the pbs normal file used to submit the optimization job request on the cluster.
- *expe_ID_fun_compiled_AC.pbs*: the pbs file used after a "crash" of the cluster. It is useful to continue the optimization from the last stored intermediate result.

Running the optimization

To start the optimization the entire optibox folder is first uploaded, or even better, synchronized on the cluster. For convenience of the other cluster users, the compilation of the MATLAB code is necessary in order not to use too many licenses when several optimizations are running in parallel (it is never sure that same machine is selected by the batch manager). The compilation is done in MATLAB on the cluster[30] by executing the following command:

```
>>mcc -R -nodisplay -R -singleCompThread -m optimize_expe_ID.m -a
.././data/ -a .././src/FIELDII -a .././src/SA_box
```

Once the compilation is done, the job request can be submitted via the batch manager using the qsub command with the pbs file as argument:

```
>>qsub expe_ID_fun_compiled.pbs
```

After this step (and maybe after queueing a while if the resources are not immediately available), the optimization starts to run (initialization included). It is possible to check the evolution of the optimization by executing (on any personal computer, not on the cluster) the *monitoring.m* file. This would create the Beam profile analysis of the intermediate result and update the report file in the *data/experiments/expe_ID/report* subfolder. Note that if the *optibox* folder is not synchronized it is necessary to download the intermediate results located in *data/experiments/expe_ID/outputs*.

Moreover, the run of the optimization may be interrupted by an unexpected "crash" of the cluster. To manage this situation a dedicated pbs file (in the *data/experiments/expe_ID/pbs* subfolder) can be submitted (`>>qsub expe_ID_fun_compiled_AC.pbs`) in order to continue the optimization from the last intermediate result that is stored.

When ending, the optimization produces an output file *outputs_expe_ID.mat* in the *data/experiments/expe_ID/outputs* subfolder. This files contains all the information required for the post-optimization analysis.

[30] Here an interactive connection to the cluster is required (`>>qsub -I`) and then MATLAB should be opened setting the *optibox/src* folder as the working directory.

Producing the results

The post-optimization analysis consists in executing the *monitoring.m* file once the optimization is finished (the *outputs_expe_ID.mat* file must have been generated). This script performs the beam profile analysis of the best configuration encountered during the optimization run. It also updates the report file not by overwriting but by appending the new information at the end of the report file. Eventually, it produces the video of the optimization run and stores it in the dedicated subfolder *data/experiments/expe_ID/video*.

All the optimization results are then listed and analyzed in an Excel worksheet. For example, the worksheet that was used to produce Table VI in III.C.4 (p. 54) is displayed on Figure 51. A click on the sixth column opens the report file location of the selected experiment and a click on the last column plays the video of the optimization run. The description of the displayed content on the video of the optimization run is detailed in the appendix II.

						SLL (dB)			Resolution @6dB (in degrees)			ID array	video
Experiment name	#iterations	#HS	#PMPs/HS	U	Report files location	R = 15 mm	R = 25 mm	R = 35 mm	R = 15 mm	R = 25 mm	R = 35 mm		
nts spiral (Blackman Density	-	-	-	-	l_256_Blackman_tapered\re	-20.2	-29.3	-25.2	7.8	2.6	3.8	spiral	
#Iterations study													
3PMPspheres_equitheta_NR	2500	3	5000	U1	MPspheres_equitheta_NRG_	-20.1	-24.4	-19.8	3.0	1.9	4.2	Iter 640 k	video
3PMPspheres_equitheta_NR	5000	3	5000	U1	MPspheres_equitheta_NRG_	-20.0	-24.8	-22.6	3.9	2.1	2.4	Iter 1.28 M	video
3PMPspheres_equitheta_NR	7500	3	5000	U1	MPspheres_equitheta_NRG_	-21.1	-26.0	-23.5	4.0	2.1	3.9	Iter 1.92 M	video
pti256_3PMPspheres_equi	10000	3	5000	U1	256_3PMPspheres_equitheta	-21.4	-24.9	-24.1	6.7	2.2	3.9	Iter 2.56 M	video
#PMPs study													
0612_256e_3HS_500p_ma	5000	3	500	U1	12_256e_3HS_500p_max_	-17.4	-23.5	-17.5	5.1	2.0	4.3	PMPs 0.5k	video
612_256e_3HS_1000p_m	5000	3	1000	U1	2_256e_3HS_1000p_max_	-19.5	-26.3	-19.8	3.0	2.1	4.5	PMPs 1k	video
612_256e_3HS_2000p_m	5000	3	2000	U1	2_256e_3HS_2000p_max_	-20.3	-25.1	-22.9	7.5	2.1	4.2	PMPs 2k	video
612_256e_3HS_3000p_m	5000	3	3000	U1	2_256e_3HS_3000p_max_	-22.3	-26.4	-24.4	5.4	2.0	4.0	PMPs 3k	video
612_256e_3HS_4000p_m	5000	3	4000	U1	2_256e_3HS_4000p_max_	-19.5	-24.6	-24.1	4.2	2.1	3.4	PMPs 4k	video
3PMPspheres_equitheta_NR	5000	3	5000	U1	MPspheres_equitheta_NRG_	-20.0	-24.8	-22.6	3.9	2.1	2.4	PMPs 5k	video
1HS (U1, U2, U3)													
609_256e_1HS_3000p_ma	10000	1	3000	U1	9_256e_1HS_3000p_max_	-9.4	-28.9	-14.7	14.1	1.6	6.1	U1 1HS	video
_256e_1HS_3000p_max_x	10000	1	3000	U2	56e_1HS_3000p_max_x_ra	-12.1	-29.3	-18.8	8.3	1.9	6.0	U2 1HS	video
e_1HS_3000p_q_sculpt_m	10000	1	3000	U3	1HS_3000p_q_sculpt_max	-10.9	-29.3	-16.5	12.2	1.6	6.6	U3 1HS	video
3HS (U1, U2, U3)													
610_256e_3HS_3000p_ma	10000	3	3000	U1	0_256e_3HS_3000p_max_	-23.7	-27.5	-25.3	4.6	2.2	3.8	U1 3HS	video
ti256_3HS_3000PMPs_ma	10000	3	3000	U2	56_3HS_3000PMPs_max_x	-24.4	-27.3	-27.5	5.3	2.7	3.7	U2 3HS	video
_3HS_3000PMPs_q_sculpt	10000	3	3000	U3	HS_3000PMPs_q_sculpt_m	-24.5	-29.7	-27.6	6.1	2.6	3.4	U3 3HS	video

Figure 51 Screenshot of the Excel worksheet used for the primary analysis done in chapter III.

APPENDIX II: Online video description

The optimization run videos of the following results are available online at https://www.creatis.insa-lyon.fr/site7/en/roux

Chapter III

Single-depth

- U_1 1HS
- U_2 1HS
- U_3 1HS

Multi-depth

- U_1 3HS
- U_2 3HS
- U_3 3HS

Chapter IV

- opti128
- opti192
- opti256

The content that is displayed on each video screen (Figure 52) is the following:

- Top-left panel: the evolution of the active elements distribution on the layout.
- Top-center panel: the evolution of the energy function values.
- Top-right panel: the evolution of the acceptation rate values.
- Bottom line panels: the evolution of the beam pattern profiles at the depths where the optimization occurred.

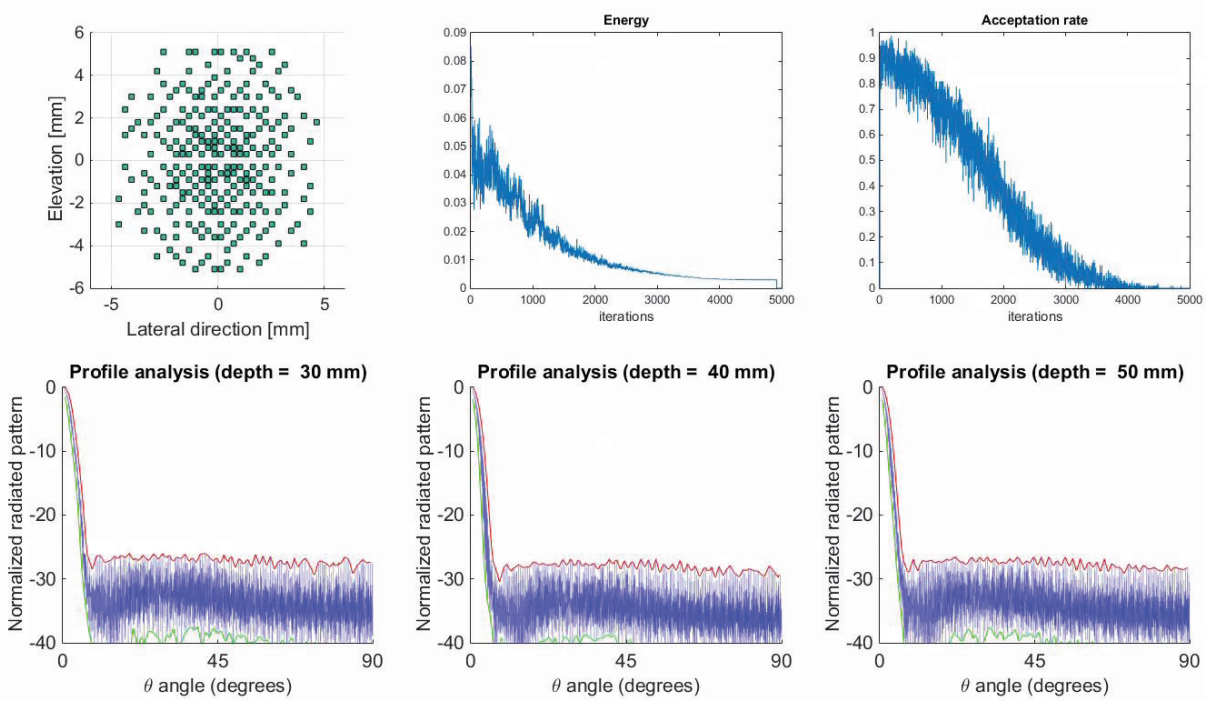


Figure 52 Screenshot of running optimization video (opti256 chapter IV). This screenshot displays (top-left) the end of the layout evolution, (top-center) the plot of the energy function evolution, (top-right) the plot of the acceptation rate evolution and (bottom line from left to right) the three optimized beam pattern profiles at depths 15 mm, 25 mm, and 35 mm.

APPENDIX III: Dissemination activities

Thèse's Art



Figure 53 Thèse's Art picture by Eric Le Roux.
The picture was printed in large format (1.80m x 2.50m) and displayed in the city center in October 2015.
(p. 48 in the press book available at http://www.univ-lyon1.fr/medias/fichier/cataloguethesesart_1465548618561-pdf).

Eric Le Roux took this picture (Figure 53) on the rooftop of the laboratory building (the 7th floor is now closed) to be part of the *Thèse's Art* project (Université Claude Bernard Lyon 1): photographs captured/projected the spirit of some PhD students into large format pictures (1.80m x 2.50m) which were displayed in the Lyon city center on the 3rd of October, 2015. All pictures of the project and an introduction by Cédric Villani (p.3) can be found at (visited August 2016):

http://www.univ-lyon1.fr/medias/fichier/cataloguethesesart_1465548618561-pdf

APPENDIX IV: Résumé substantiel en français

Glossaire

2D	Deux dimensions
3D	Trois dimensions
A/D	Analogique/Digital (convertisseurs)
ADCs	Conversions analogique digitale
ASICs	Circuits intégrés dédiés
BP	Diagramme de rayonnement acoustique
CMUT	Transducteur ultrasonore capacitif micro-usiné
CNR	Rapport de contraste
CPU	Processeur
CW	Onde continue
DAS	Retards et Sommes
DOF	Profondeur de champ
FDA	Agence américaine des produits alimentaires et médicamenteux
FOV	Champ de vue
FWHM	Pleine largeur à mi-hauteur
Gb	Giga bit
GLL	Lobes de réseau
GPU	Processeur graphique
GUI	Interface graphique
HIFU	Ultrasons focalisés de haute intensité
HRTF	Fonction de transfert relative à la tête
HS	Hémisphère
MAC	Multiplication-accumulation
OOP	Programmation orientée objet
PF	Champ de pression
PMP	Points de mesure de pression
PSF	Fonction d'étalement du point
RF	Signal radiofréquence
RX	Réception
SA	Recuit simulé
SC	Continuation stochastique
SIR	Réponse impulsionnelle spatiale
SLL	Niveau des lobes secondaires
SMER	Rapport du niveau du lobe principal sur celui des lobes secondaires
TB	Téra octet
TGC	Compensation temporelle du gain en réception
TX	Transmission
US	Ultrasons
WFS	Synthèse de champ d'onde
WSS	Large bande et sensible à la forme des éléments actifs

Liste des symboles

Géométrie

$\boldsymbol{r}$	Vecteur de position
x, y, z	Coordonnées Cartésiennes $\boldsymbol{r} = x\hat{\mathbf{x}} + y\hat{\mathbf{y}} + z\hat{\mathbf{z}}$ (vecteurs unitaires $\hat{\mathbf{x}}, \hat{\mathbf{y}}, \hat{\mathbf{z}}$)
R, θ, ϕ	Coordonnées sphériques $\boldsymbol{r} = R\hat{\boldsymbol{r}}$ (vecteur unitaire $\hat{\boldsymbol{r}}$)
t	Temps

Ondes acoustiques

$\Upsilon_{\text{reflect}}$	Coefficient de réflexion
$\Upsilon_{\text{transmit}}$	Coefficient de transmission
$\alpha_{\text{i}}, \alpha_{\text{t}}, \alpha_{\text{r}}$	Angles d'incidence, de transmission et de réflexion
c	Vitesse de propagation (vitesse du son)
F_{s}	Fréquence d'échantillonnage
f_{c}	Fréquence centrale du transducteur
h	Épaisseur d'un élément transducteur
u	Déplacement de la membrane du transducteur
v	Vecteur vitesse de la particule
Z	Impédance acoustique du milieu
λ	Longueur d'onde
ρ	Densité du milieu
φ	La phase de l'onde
ψ	Potentiel de vitesse
ω	Vitesse angulaire

Transducteurs

A_k	Région de l'espace occupée par l'élément $\mathbf{e}_k$
d	Pitch (distance entre les centres des éléments consécutifs)
$\mathbf{e}_k$	k-ième élément de la sonde matricielle
E_k	Ensemble des propriétés de l'élément $\mathbf{e}_k$
θ_k, ϕ_k	Orientation du vecteur normal à la surface de l'élément $\mathbf{e}_k$.
τ_k	Retard appliqué à l'élément $\mathbf{e}_k$
a_k, b_k	Taille de l'élément $\mathbf{e}_k$ selon la direction x (a_k) et la direction y (b_k)
Exc_k	Signal d'excitation de l'élément $\mathbf{e}_k$
Imp_k	Réponse impulsionnelle de l'élément $\mathbf{e}_k$
w_k	Poids (coefficient d'apodisation) de l'élément $\mathbf{e}_k$
x_k, y_k, z_k	Position du centre de l'élément $\mathbf{e}_k$

G	Grille Cartésienne
$\text{h}(\boldsymbol{r}, t)$	Réponse impulsionnelle spatiale
N_{e}	Nombre d'éléments actifs
N_x	Nombre d'éléments selon la direction x (sondes matricielles 2D régulières)
N_y	Nombre d'éléments selon la direction y (sondes matricielles 2D régulières)
r_{p}	Rayon d'ouverture

$\boldsymbol{P_i}$	Polarisation du transducteur selon la direction $\boldsymbol{i}$
$\boldsymbol{T_j}$	Tenseur des contraintes appliquées au transducteur selon la direction $\boldsymbol{j}$
d_{ij}	Tenseur des constantes de déformations élastiques du transducteur ($\boldsymbol{i} \rightarrow \boldsymbol{j}$)

Stratégies de reconstruction d'image

$\delta_{\mathrm{l}}, \delta_{\mathrm{a}}$	Dimensions latérale et axiale de la tâche focale (région au-dessus de -6 dB)
$\theta_{\mathrm{steer}}, \phi_{\mathrm{steer}}$	Angles de dépointage du faisceau (steering)
D	Taille de l'ouverture (dans le cas d'un disque $\mathrm{D} = 2\mathrm{r_p}$)
F	Profondeur focale ($= \mathrm{z_f}$)
N_{s}	Nombre de diffuseurs
$p_0(t)$	Pression initiale au niveau de la surface du transducteur
$p(\boldsymbol{r}, t)$	Signal d'écho-impulsion reçu (réponse d'un ensemble de diffuseur)
$\mathrm{RF}_{\mathrm{post}}(t)$	Signaux RF après la formation de voies
$\mathrm{RF}_k(t)$	Signaux radiofréquences (RF) avant la formation de voies (raw data)
$\boldsymbol{r}_{\mathrm{f}}$	Vecteur de position du point focal
$\boldsymbol{r}_{\mathrm{s}}$	Position de la source virtuelle (transmission d'ondes divergentes)
$\mathrm{s}(\boldsymbol{r}, t)$	Diffuseurs dans le milieu
$x_{\mathrm{f}}, y_{\mathrm{f}}, z_{\mathrm{f}}$	Coordonnées Cartésiennes du point focal

Recuit simulé

$(\beta_n)_{n\in\mathbb{N}}$	Séquence de refroidissement (inverse de la température)
β_n	Inverse de la température à l'itération n
K	Nombre d'itérations des plateaux de température constante
N_{iter}	Nombre d'itérations
n	Numéro d'itération
$\mathrm{P}(S_{n+1}\|S_n)$	Matrice de transition
$(S_n)_{n\in\mathbb{N}}$	Chaîne de Markov du recuit simulé
S_0	Solution initiale
S_n	Solution à l'itération n
$\tilde{S}_n$	Nouvelle proposition à partir de la perturbation de S_n
S_{opti}	Meilleure solution rencontrée au cours du processus $(S_n)_{n\in\mathbb{N}}$ d'optimisation.
Θ	Mécanisme de communication
Ω	Espace d'état des solutions
$\mathcal{G}(S)$	Voisinage de la solution S
σ	Nombre de plateaux de température constante

Fonction d'énergie

$\theta_{\mathrm{ML}}(R)$	Angle délimitant la région du lobe principal à la profondeur R
$\rho_1, \dots, \rho_{N_{\mathrm{H}}}$	Poids associés à $U_{R_1}(S) \dots U_{R_{N_{\mathrm{H}}}}(S)$
$\mathrm{BP}_S(R, \theta, \phi)$	Diagramme de rayonnement normalisé du faisceau acoustique transmis par S à la profondeur R
$L(R)$	Région du lobe principal à la profondeur R
MASK (R, θ, ϕ)	Masque de sculpture à la profondeur R
$\mathrm{C}(R)$	Valeur de coupure du MASK (R, θ, ϕ)
q_{mask}	Pas de quantification du MASK (R, θ, ϕ)
$M_+(R)$	Maximum des différences positives de pression avec MASK (R, θ, ϕ)
$M(R)$	Maximum de pression au-dessus du MASK (R, θ, ϕ)
N_{H}	Nombre d'hémisphères de PMP
N_{PMP}	Nombre de points de mesure de pression (PMP)
$\mathrm{PF}_S(R, \theta, \phi, t)$	Champ de pression produit par S sur l'hémisphère de rayon R
$R_1, \dots, R_{N_{\mathrm{H}}}$	Rayon des hémisphères de PMP
$U^{N_{\mathrm{H}}}(S)$	Fonction d'énergie multi-profondeurs associée à la solution S
$U_R(S)$	Fonction d'énergie associée à la solution S calculée à la profondeur R

Table des matières

GLOSSAIRE 119

LISTE DES SYMBOLES 120

TABLE DES MATIERES 122

INTRODUCTION GENERALE: RELIER DES SIMULATIONS ACOUSTIQUES LARGE BANDE AVEC UNE OPTIMISATION PAR RECUIT SIMULE POUR L'INDIVIDUATION DE SONDES ULTRASONORES 2D PARCIMONIEUSES. 125

I CHAPITRE I CONTEXTE DE L'IMAGERIE ULTRASONORE 3D 127

I.A ACOUSTIQUE DE L'IMAGERIE ULTRASONORE: DE LA MATIERE AUX ONDES. 127
I.B LA FORMATION DE VOIES: DES ONDES AUX IMAGES 130
I.C INTERETS ET LIMITES ACTUELLES DE L'IMAGERIE ULTRASONORE 3D+T (4D) 134
I.D DEFINITIONS DE SONDES PARCIMONIEUSES, ETAT DE L'ART ET LIMITATIONS 137

II CHAPITRE II SIMULATIONS ACOUSTIQUES REALISTES DANS UN CADRE GENERAL D'OPTIMISATION DES SONDES 2D PARCIMONIEUSES 141

II.A ACCELERATION DES SIMULATIONS ACOUSTIQUES REALISTES 141
II.B CADRE GENERAL D'OPTIMISATION DES SONDES 2D PARCIMONIEUSES. 145

III CHAPITRE III OPTIMISATION MULTI-PROFONDEURS DU RAYONNEMENT ACOUSTIQUE DE SONDES 2D NON-REGULIERES PARCIMONIEUSES. 147

III.A PARAMETRAGE DE L'OPTIMISATION ET DEFINITION DES FONCTIONS D'ENERGIE MULTI-PROFONDEUR 147
III.B SONDES NON-REGULIERES OPTIMISEES ET COMPARAISON AVEC UNE SONDE SPIRALE 148

IV CHAPITRE IV OPTIMISATION LARGE BANDE DE LA DEFINITION DE SONDES 2D REGULIERES PARCIMONIEUSES AVEC CONTRAINTES DE FABRICATION 153

IV.A PARAMETRAGE DE L'OPTIMISATION ET DE LA FONCTION D'ENERGIE MULTI-PROFONDEUR (AVEC INTERFACE GRAPHIQUE) 153
IV.B PERFORMANCES DES SONDES OPTIMISEES 154

V DISCUSSION GENERALE: LIMITES ET PERSPECTIVES 161

V.A LE MANQUE D'IMAGES EXPERIMENTALES 3D ET DE PROTOTYPE DE SONDE OPTIMALE. 161
V.B L'ESPACE D'ETAT ET LES SIMULATIONS ACOUSTIQUES 161

V.C LA FONCTION D'ENERGIE 161
V.D LE TEMPS DE CALCUL 162
V.E CONTINUATION STOCHASTIQUE ET MODULATION CONTINUE 162
V.F ORDRES D'INDIVIDUATION MULTIPLES DES SONDES ULTRASONORES 2D PARCIMONIEUSES 163
V.G AUTRES CHAMPS D'APPLICATION 164

CONCLUSION GENERALE 165

PUBLICATIONS PERSONNELLES 169

REFERENCES 171

ANNEXES 175

ANNEXE I: PIPELINE D'OPTIMISATION ET D'ANALYSE 177
ANNEXE II: DESCRIPTION DES VIDEOS EN LIGNE 183
ANNEXE III: ACTIVITES DE DISSEMINATION 185

Introduction générale: Relier des simulations acoustiques large bande avec une optimisation par recuit simulé pour l'individuation de sondes ultrasonores 2D parcimonieuses.

La capacité à appréhender son environnement sonore (sens auditif) apparaît comme essentiel à la vie car il est partagé par toutes les espèces vivantes sur la Terre. Mais la vue est également le sens prédominant dans nos sociétés organisées. Entre les deux, la production d'images à partir du son est un processus fascinant qui est à l'origine des images de diagnostic (échographies) utilisées quotidiennement en médecine. L'échographie 3D (imagerie ultrasonore d'un volume) est l'extension en trois dimensions de l'échographie traditionnelle 2D (imagerie ultrasonore d'un plan). Les ondes ultrasonores sont transmises (« chantées ») et reçues (« écoutées ») par la sonde qui est l'appareil que le médecin tient dans sa main lors d'un examen d'échographie.

Comment des ondes acoustiques peuvent-elles être générées à partir de la matière ? À cette échelle, la propriété de transduction électromécanique présentée par certains matériaux est fondamentale. Les *transducteurs* (désignés comme éléments actifs) présents dans la sonde échographique sont capables de convertir de l'énergie électrique en une énergie mécanique (et vice-versa). Leur propriété *transductive* émane de la structure cristalline[31] qui est elle-même le résultat d'un processus de recuit du matériau qui les constitue. Connectés à l'échographe par un câble, ils sont à la fois utilisés pour transmettre des ondes ultrasonores et recevoir les échos.

La problématique de conception des sondes 2D pour l'échographie 3D se place à une échelle d'ordre supérieur. Cette opération consiste à organiser un groupe d'éléments actifs sur la surface de l'ouverture pour former un « capteur 3D d'information acoustique ». Le traitement de ce type d'antennes acoustiques exploite le balayage électronique du faisceau acoustique qu'elles émettent. La qualité des images reconstruites dépend du diagramme de rayonnement du faisceau de sonde et, selon les besoins de l'application visée, la forme du faisceau peut être modulée en ajustant les positions relatives des éléments actifs. Il existe deux principales approches[32] pour résoudre la

[31] « Un cristal qui, à partir d'un germe très petit, grossit et s'étend selon toutes les directions dans son eau-mère fournit l'image la plus simple de l'opération transductive : chaque couche moléculaire déjà constituée sert de base structurante à la couche en train de se former ; le résultat est une structure réticulaire amplifiante. » (Simondon 2005), p. 33.

« Le phénomène de croissance est par la suite automatique et indéfini, toutes les couches successives du cristal ayant la capacité de structurer le milieu amorphe qui les entoure, tant que ce milieu reste métastable ; en ce sens, un cristal est doué d'un pouvoir indéfini de croissance ; un cristal peut avoir sa croissance arrêtée, mais jamais achevée, et il peut toujours continuer à croître si on le remet dans un milieu métastable qu'il puisse structurer. Il importe de remarquer tout particulièrement que le caractère d'extériorité ou d'intériorité des conditions est modifié par la genèse elle-même. Au moment où le cristal n'est pas encore constitué, on peut considérer les conditions énergétiques comme extérieures au germe cristallin, alors que les conditions structurales sont portées par ce germe lui-même. Au contraire, lorsque le cristal a grandi, il a incorporé, au moins partiellement, des masses de substances qui, au temps où elles étaient amorphes, constituaient le support de l'énergie potentielle de l'état métastable. », *Ibidem*, p. 86.

[32] L'opposition entre le monisme et le dualisme est exposé dès les tout premiers mots de l'introduction de la thèse de Simondon : « Il existe deux voies selon lesquelles la réalité de l'être comme individu peut être abordéee : une voie substantialiste, considérant l'être comme consistant en son unité, donné à lui-même, fondé

problématique de conception des sondes 2D. La première est basée sur une définition déterministe où une théorie produit des solutions rationnelles et immédiates. La seconde est basée sur une optimisation stochastique où l'exploration d'un grand nombre de solutions prend du temps. L'intention ici est de présenter les avantages et inconvénients de chacune de ces approches et le but est de monter l'intérêt du lien entre un aspect pratique de la conception (grâce à la simulation réaliste où la dimension temporelle est considérée) et une opération *transductive* d'optimisation[33]. En effet, l'algorithme d'optimisation du recuit simulé est directement inspiré par le procédé de recuit de la matière qui a produit chaque élément actif individuel. Le même procédé opère donc, à une échelle microscopique, pour structurer les particules des cristaux et, à une échelle macroscopique, pour organiser les éléments actifs qui forment le réseau de transducteurs de la sonde. L'optimisation des sondes ultrasonores 2D par recuit simulé est analogue à un *processus transductif d'individuation* en accord avec la définition de *transduction*[34] défendue par Gilbert Simondon dans sa thèse d'état (Simondon 2005).

Les travaux portant sur la définition de sondes 2D pour l'échographie 3D ont débuté dans l'unité CREATIS il y a six ans avec la thèse de Bakary Diarra qui a étudié l'optimisation des sondes 2D parcimonieuses non régulières. En considérant que les sondes régulières sont plus souvent utilisées en pratique et qu'elles sont plus faciles à produire, cette présente thèse n'aurait pu se limiter à l'étude des sondes parcimonieuses non-régulières. Par conséquent elle est destinée à regrouper les définitions de sondes régulières et non-régulières dans un cadre général d'optimisation des sondes matricielles 2D.

---

sur lui-même, inengendré, résistant à ce qui n'est pas lui-même ; un voie hylémorphique, considérant l'individu comme engendré par la rencontre d'une forme et d'une matière. », *Ibidem*, p. 24. Sa conception centrale du processus d'individuation est complétée par Andrew Iliadis comme une opération potentiellement capable de résoudre la tension entre ces deux points de vue opposés : « De façon importante, la conception Simondonienne de l'information comme ontologiquement signifiante peut être vue comme une solution aux problèmes esprit-corps et sujet-objet. » (Iliadis 2013) p. 87, traduction personnelle.

[33] Paradoxalement les simulations acoustiques réalistes sont fondées sur un modèle théorique de radiation acoustique alors qu'au contraire le procédé d'optimisation (recuit simulé) est fondé sur la cristallisation de la matière.

[34] « Nous entendons par transduction une opération, physique, biologique, mentale, sociale, par laquelle une activité se propage de proche en proche à l'intérieur d'un domaine, en fondant cette propagation sur une structuration du domaine opérée de place en place : chaque région de structure constituée sert à la région suivante de principe de constitution, si bien qu'un modification s'étend ainsi progressivement en même temps que cette opération structurante. », (Simondon 2005), p. 32. « La transduction […] est ce par quoi une structure apparaît dans un domaine de problématiques comme apportant la résolution des problèmes posés. Mais […] la transduction ne va pas chercher ailleurs un principe pour résoudre le problème d'un domaine : elle tire la structure résolutrices des tensions mêmes de ce domaine, comme la solution sursaturée se cristallise grâce à ses propres potentiels et selon l'espèce chimique qu'elle renferme, non par apport de quelque forme étrangère. », *Ibidem*, p. 34.

I Chapitre I Contexte de l'imagerie ultrasonore 3D

I.A Acoustique de l'imagerie ultrasonore: de la matière aux ondes.

L'effet piézoélectrique direct a été découvert en 1880 par les frères Jacques et Pierre Curie (Curie and Curie 1880): un cristal piézoélectrique se polarise électriquement lorsqu'il est soumis à une contrainte mécanique. L'année suivante, l'effet piézoélectrique inverse était prédit par Gabriel Lippmann[35] (1845 – 1921) et immédiatement vérifié expérimentalement par les frères Curie (Curie and Curie 1881) : un cristal piézoélectrique subit une déformation lorsqu'on lui applique un champ électrique. En échographie, les éléments actifs exploitent les effets piézoélectriques direct et indirect pour jouer respectivement le rôle de « microphones » (réception, RX) et de « haut-parleurs » (transmission, TX) à ultrasons (Figure 54).

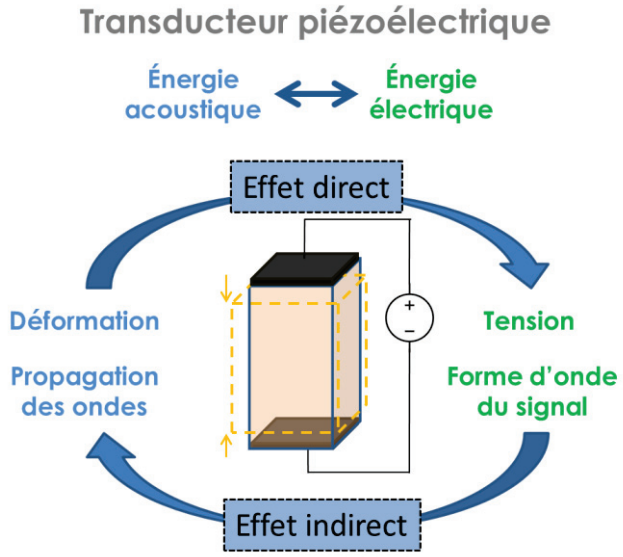


Figure 54 Illustration de l'effet piézoélectrique: l'effet direct (de l'énergie acoustique à l'énergie électrique) est utilisé en réception alors que l'effet indirect (de l'énergie électrique à l'énergie acoustique) est utilisé en émission.

La précédente description de l'effet piézoélectrique est une vision macroscopique d'une structuration particulière du cristal. Plus en détails, la structure cristalline d'un matériau piézoélectrique n'est pas symétrique de telle sorte que l'application d'une contrainte de déformation vient séparer les centres de charges positives et négatives, c'est à dire polariser électriquement le cristal (effet direct). L'effet piézoélectrique est un phénomène linéaire ce qui signifie que la polarisation $\boldsymbol{P_i}$ et le tenseur des contraintes $\boldsymbol{T_j}$ sont linéairement reliés par

[35] Gabriel Lippmann a supervisé Pierre Curie pour son doctorat (Pierre Curie 1985) à l'Université de Paris et à l'École Supérieure de Physique et de Chimie Industrielles (1895). Par la suite, Pierre Curie (ainsi que Joseph John Thomson and Gabriel Lippmann) a supervisé Paul Langevin pour son doctorat à l'Université de Paris (1902).

$$\boldsymbol{P_i} = d_{ij}\boldsymbol{T_j} \tag{76}$$

où d_{ij} est le tenseur des constantes de déformation élastiques du transducteur (en $\mathrm{C.N^{-1}}$).

Certains minéraux sont naturellement piézoélectriques comme le minerai de Pérovskite ($\mathrm{CaTiO_3}$), mais il est également possible de synthétiser des cristaux présentant cette propriété. C'est le cas du très utilisé PZT (Titano-Zirconate de Plomb ou $\mathrm{Pb[Zr_XTi_{1-X}]O_3}$) qui possède la structure cristalline dite pérovskite (Figure 3).

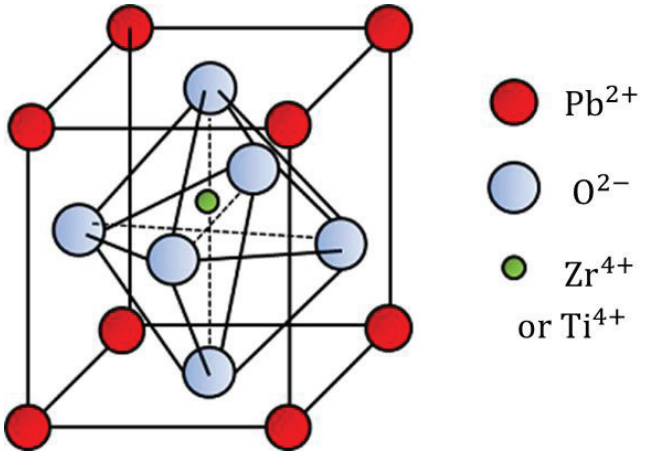


Figure 55 La structure cristalline pérovskite du Titano-Zirconate de Plomb (PZT). Les ions Zr^{4+} ou Ti^{4+} ne sont pas centrés ce qui est à l'origine des propriétés piézoélectriques du cristal de PZT. (image originale sur www.comsol.com)

Synthétiser une substance piézoélectrique nécessite un procédé complexe d'ingénierie des matériaux (dopage, mélanges, pressage à sec, broyage, laminage, découpage, frittage, métallisation…). Il est intéressant de remarquer qu'au début du processus de synthèse le matériau est chauffé pour enlever les tensions internes : il s'agit de l'étape de recuit. De plus, les performances de conversion électroacoustiques peuvent être ajustées très finement en combinant une phase piézoélectrique avec une phase en polymère (époxy, par exemple) de façon à créer un matériau piézo-composite. Les géométries de connectivité les plus connues sont 1-3 et 2-2 : les chiffres indiquent le nombre de dimensions continues des phases piézoélectrique-polymérique. L'efficacité de la transduction, l'impédance électrique, l'impédance acoustique et la fréquence centrale du transducteur dépendent de la proportion de chaque phase. La géométrie de l'arrangement de ces phases influence également la manière dont les transducteurs vibrent. Chaque transducteur est caractérisé par sa réponse impulsionnelle (la déformation subit lorsque l'excitation est un Dirac) qui dépend en partie de sa dimension. En particulier, sa fréquence de résonnance correspond à sa fréquence centrale f_c $[\mathrm{Hz}]$ et elle dépend de l'épaisseur h $[\mathrm{m}]$ de l'élément et de la vitesse c $[\mathrm{m.s^{-1}}]$ de propagation longitudinale de la perturbation dans le cristal :

$$f_\mathrm{c} = \frac{c}{2h} \quad \text{or} \quad h = \frac{\lambda_\mathrm{c}}{2} \tag{77}$$

avec $\lambda_\mathrm{c} = c/f_\mathrm{c}$, la longueur d'onde centrale $[\mathrm{m}]$ associée au transducteur.

En transmission, le déplacement $u(t)$ $[\mathrm{m}]$ de la membrane du transducteur est la convolution $(*)$ entre le signal d'excitation $\mathrm{Exc}(t)$ et la réponse impulsionnelle du transducteur $\mathrm{Imp}(t)$

$$u(t) = \mathrm{Exc}(t) * \mathrm{Imp}(t) \tag{78}$$

Par linéarité de la transduction piézoélectrique, le même phénomène se produit en réception quand l'effet inverse produit un signal électrique mesurable qui correspond à la convolution entre le signal acoustique reçu à la surface du transducteur et la réponse impulsionnelle de ce dernier. La technologie récente des « transducteurs ultrasonores capacitifs micro-usinés » ou *Capacitive Micromachined Ultrasonic Transducers* (CMUT) (Caronti et al. 2006; Caliano et al. 2005; Oralkan et al. 2002) permet une conception beaucoup plus flexible des transducteurs (Savoia, Caliano, and Pappalardo 2012) en terme de de formes, de tailles et de positionnement.

Le mouvement de la surface d'un transducteur (considéré uniforme) est transmis au milieu avec lequel il interagit sous la forme d'une onde ultrasonore se propageant à la vitesse $[\mathrm{m.s}^{-1}]$.

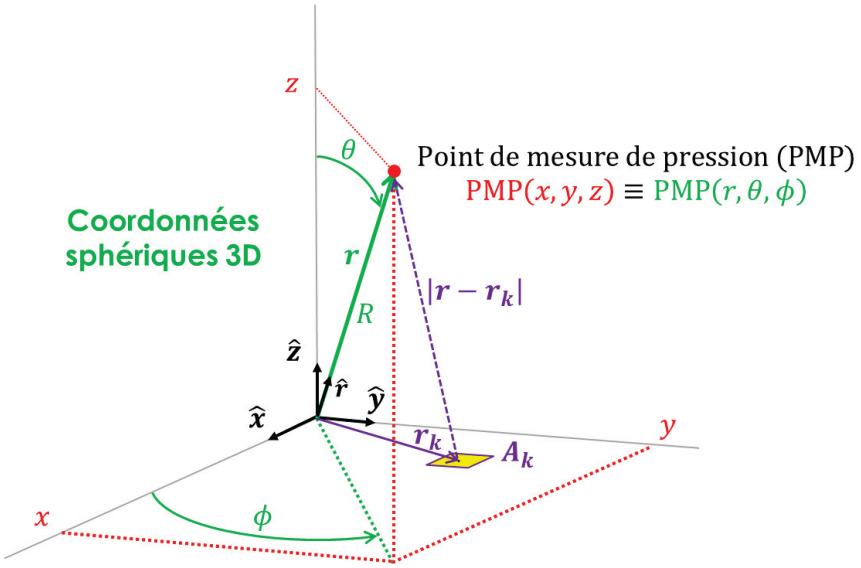


Figure 56 Convention des coordonnées sphériques 3D (ISO-80000-2) et distance entre une surface active A_k et une point de mesure de pression (PMP) localisé en $\boldsymbol{r}$.

La convention des coordonnées sphériques (ISO 80000-2) est présentée en Figure 4 et leurs formules de conversions avec les coordonnées Cartésiennes sont :

$$\begin{cases} x = R\sin\theta\cos\phi \\ y = R\sin\theta\sin\phi \\ z = R\cos\theta \end{cases} \leftrightarrow \begin{cases} R = \sqrt{x^2 + y^2 + z^2} \\ \theta = \arccos(z/R) \\ \phi = \arctan(y/x) \end{cases} \tag{79}$$

Donc pour tout point localisé en (R, θ, ϕ), il est possible de définir un vecteur de position $\boldsymbol{r}$:

$$\boldsymbol{r} = R\hat{\boldsymbol{r}} = x\hat{\boldsymbol{x}} + y\hat{\boldsymbol{y}} + z\hat{\boldsymbol{z}} \tag{80}$$

où $\hat{\boldsymbol{r}}$ est le vecteur unitaire pointant vers (x, y, z).

Une source ponctuelle monochromatique (oscillant à f_c Hz) localisée en $\boldsymbol{r_k}$ rayonne, en tout point $\boldsymbol{r}$ de l'espace, une onde sphérique de la forme

$$\mathbf{v}(\boldsymbol{r},t)=\frac{\rho}{2\pi|\boldsymbol{r}-\boldsymbol{r_k}|}w_k\,e^{j(\frac{2\pi}{\lambda}|\boldsymbol{r}-\boldsymbol{r_k}|-\omega t)} \tag{81}$$

avec $\omega=2\pi f_c$ $[\mathrm{rad}.s^{-1}]$ la vitesse angulaire, w_k l'amplitude de la source, et ρ $[\mathrm{kg}.\mathrm{m}^{-3}]$ la densité du milieu. La phase φ $[\mathrm{rad}]$ de l'onde est définie comme l'argument de $\mathbf{v}(\boldsymbol{r},t)$.

Une source ponctuelle monochromatique n'est pas un modèle réaliste pour représenter le rayonnement acoustique d'un élément actif utilisé en imagerie ultrasonore. Une première contribution de ce travail de thèse est d'intégrer un modèle plus réaliste (large bande et sensible à la forme) dans le processus d'optimisation (Chapitre II). Cependant, par rapport à la réalité, ce travail assume plusieurs hypothèses simplificatrices qui ne sont pas détaillées dans ce résumé.

I.B La formation de voies: des ondes aux images

En mode d'imagerie passive, la sonde ultrasonore ne fait que recevoir les vibrations acoustiques provenant du milieu observé pour ensuite les convertir en signaux électriques, les amplifier et enfin les transposer en images par la formation de voie. Ce mode d'imagerie en « écoute passive » est utilisé en photo-acoustique (Ningning 2014) et en sismologie (Gazdag and Sguazzero 1984). En échographie les transducteurs sont utilisés pour recevoir mais aussi pour émettre des ondes acoustiques.

En imagerie multiéléments, le front d'onde qui définit la forme du faisceau acoustique émis est contrôlée en ajustant les poids w_k et les retards τ_k individuels appliqués aux éléments (Figure 8). Les principales stratégies de transmission sont représentées sur la Figure 8 : les ondes focalisées, les ondes divergentes et les ondes planes (Kruizinga et al. 2012; Montaldo et al. 2009).

Le dépointage du faisceau en transmission consiste à orienter la direction du front d'onde dans la direction θ_{steer}en ajustant les retards individuels τ_k (Figure 8 et Figure 9). Cette technique est habituellement utilisée pour balayer le milieu observé avec des ondes focalisées en émission. Cependant le dépointage du faisceau peut également être utilisé pour changer l'angle d'incidence des ondes planes (Montaldo et al. 2009; Tanter et al. 2002; Jespersen, Wilhjelm, and Sillesen 1998) ou des ondes divergentes (Jean Provost et al. 2014; Papadacci et al. 2014; Hasegawa and Kanai 2011). Cette technique permet d'améliorer le contraste et la résolution des images effectuant plusieurs émissions selon plusieurs angles de dépointage et en les combinant ensemble.

La pondération des éléments actifs à l'aide de fenêtres d'apodisation peut être utilisée pour contrôler la taille et la forme de la tâche focale (cas des ondes focalisées) ainsi que réduire les artefacts tels que la hauteur des lobes latéraux. Le but étant d'obtenir une tâche focale la plus fine possible tout en réduisant la quantité d'énergie acoustique située hors de cette tâche focale. La fenêtre d'apodisation modifie la forme du diagramme de rayonnement acoustique (BP) des éléments actifs.

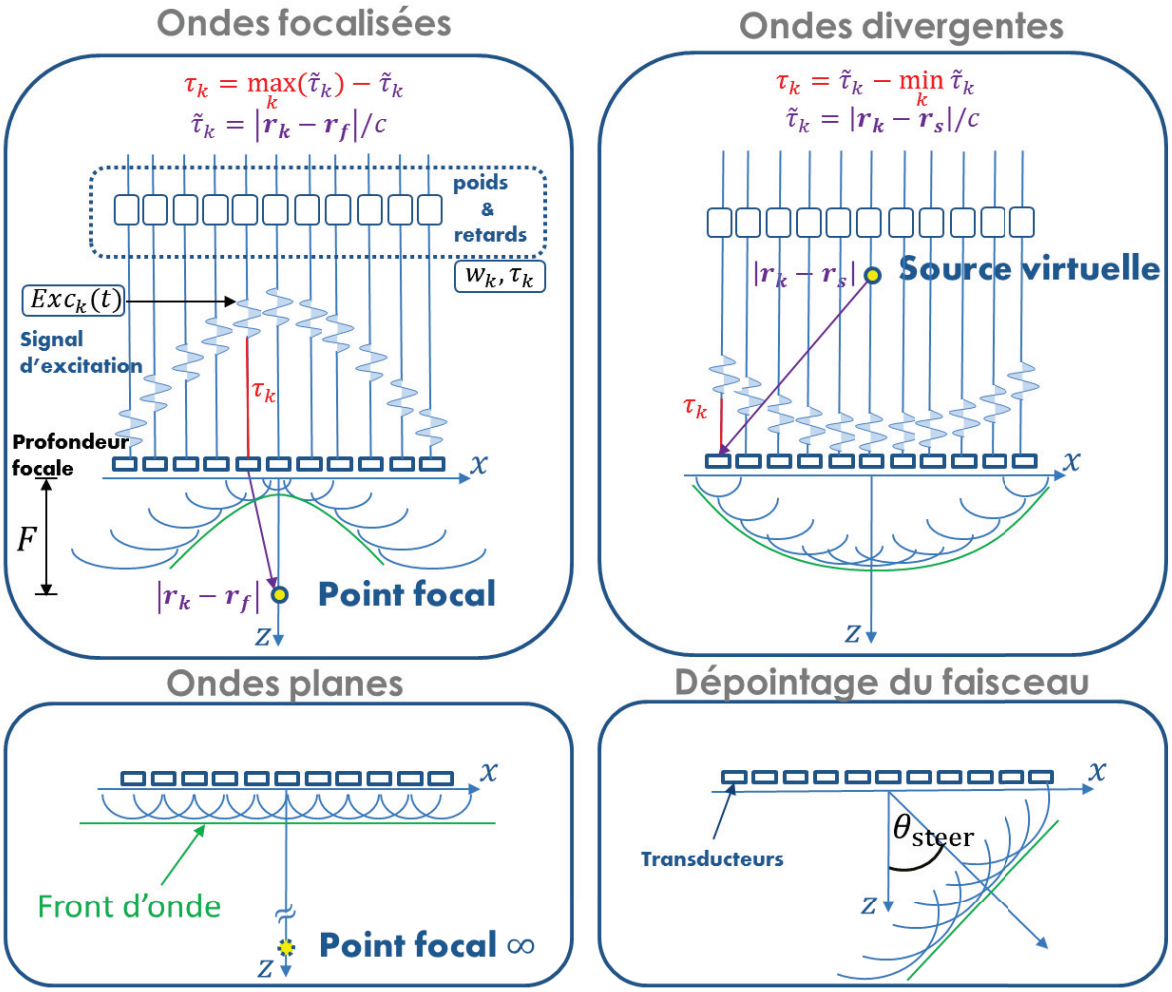


Figure 57 Illustration des principales stratégies de transmission. Les ondes focalisées (haut-gauche) qui convergent vers un point focal. Les ondes divergentes (haut-droite) propagent une onde crée par une source virtuelle localisée derrière le transducteur. Un front d'onde plan est obtenu en fixant le même retard pour tous les éléments actifs (bas-gauche). Les ondes planes peuvent s'obtenir en définissant un point focal localisé à l'infini. Le dépointage du faisceau (bas-droite) correspond à l'orientation du front d'onde dans la direction θ_{steer} en ajustant les retards τ_k.

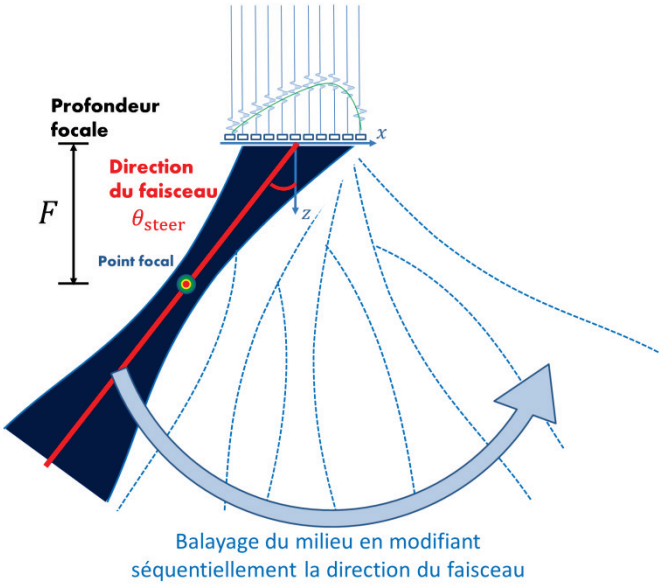


Figure 58 Illustration du balayage du milieu grâce au dépointage du faisceau ultrasonore lorsque des ondes focalisées sont utilisées en émission.

En phase d'émission, les ondes générées par l'ensemble des transducteurs de la sonde se propagent dans le milieu et le champ de pression (PF) correspond à la distribution de la pression dans le milieu. Plus précisément, le champ de pression $\mathrm{PF}(R,\theta,\phi,t)$= $\mathrm{PF}(\boldsymbol{r},t)$ en $[\mathrm{kg.\,m^{-1}.\,s^{-2}}]$ ou en $[\mathrm{Pa}] = [\mathrm{Pascal}]$ est l'évolution de la différence de pression avec la pression d'équilibre $\mathrm{PF}_0(R,\theta,\phi,t)$ en tout point de mesure (R,θ,ϕ). Il existe plusieurs logiciels[36] de simulations acoustiques dédiés aux simulations d'ondes ultrasonores. Certains sont plus ou moins réalistes en fonction du modèle acoustique sur lequel ils reposent. Dans ce travail il a été choisi de travailler avec le logiciel FIELD II (Jensen and Svendsen 1992; Jensen 1996) développé à la *Danmarks Tekniske Universitet.* Ce logiciel permet de réaliser des simulations réalistes car la dimension temporelle et la réponse impulsionnelle spatiale de chaque élément actif sont prises en compte : en d'autre termes, le signal transmis possède une bande passante réaliste et le champ de pression généré par un élément actif dépend de sa forme, de son orientation et de sa taille. Ce simulateur (ainsi que DREAM (Piwakowski and Sbai 1999)) est basé sur le papier de (Stepanishen 1971) où le champ de pression est calculé à partir du principe d'Huygens-Fresnel. Le PF généré par une surface active A se calcule comme l'intégration des contributions en ondes sphériques rayonnées par chaque élément infinitésimal de surface dA localisé en $\boldsymbol{r_{dA}}$:

$$\mathrm{PF}(R,\theta,\phi,t) = \mathrm{PF}(\boldsymbol{r},t) = \rho \int_A \frac{1}{2\pi|\boldsymbol{r}-\boldsymbol{r_{dA}}|} \frac{\partial v_n(t-|\boldsymbol{r}-\boldsymbol{r_{dA}}|/c)}{\partial t}\, dA \qquad (82)$$

avec ρ la densité du milieu $[\mathrm{kg.\,m^{-3}}]$ et v_n la vitesse normale $[\mathrm{m.\,s^{-1}}]$ de la surface dA en train d'émettre.

La qualité du rayonnement acoustique d'un groupe d'éléments actifs est évaluée sur le diagramme de rayonnement (BP) qui représente la distribution angulaire de l'énergie acoustique transmise par l'ouverture. La procédure de calcul du BP à partir du champ de pression (PF) est illustrée sur la Figure 10: tout d'abord le PF est mesuré autour de la sonde par des points de mesure de pression (PMP), ensuite le maximum de signal mesuré au cours du temps par chaque PMP est normalisé puis log-compressé pour enfin être tracé en fonction de l'angle θ du PMP associé.

Un BP idéal en ondes focalisées (cas traité dans ce travail) serait un Dirac d'énergie dans la direction de propagation du front d'onde (Figure 11). Mais en pratique il y a des lobes latéraux et le lobe principal possède une certaine largeur. Cette dernière propriété a un impact sur la résolution des images alors que les lobes latéraux impactent sur le contraste des images. Avec un groupe d'éléments actifs il y a un compromis entre l'extraction de l'information disponible avec meilleure résolution (mesurée par exemple comme la largeur du lobe principal à – 6 dB, FWHM) ou meilleur contraste (mesuré par exemple comme le niveau des lobes secondaires -SLL- ou des lobes de réseau -GLL).

---

[36] FIELD II: http://field-ii.dk/
FOCUS: http://www.egr.msu.edu/~fultras-web/
Abersim©: http://www.ntnu.edu/isb/ultrasound/abersim/download
Ultrasim: http://www.mn.uio.no/ifi/english/research/groups/dsb/resources/software/ultrasim/
DREAM: http://www.signal.uu.se/Toolbox/dream/
CREANUIS: https://www.creatis.insa-lyon.fr/site/fr/CREANUIS.html

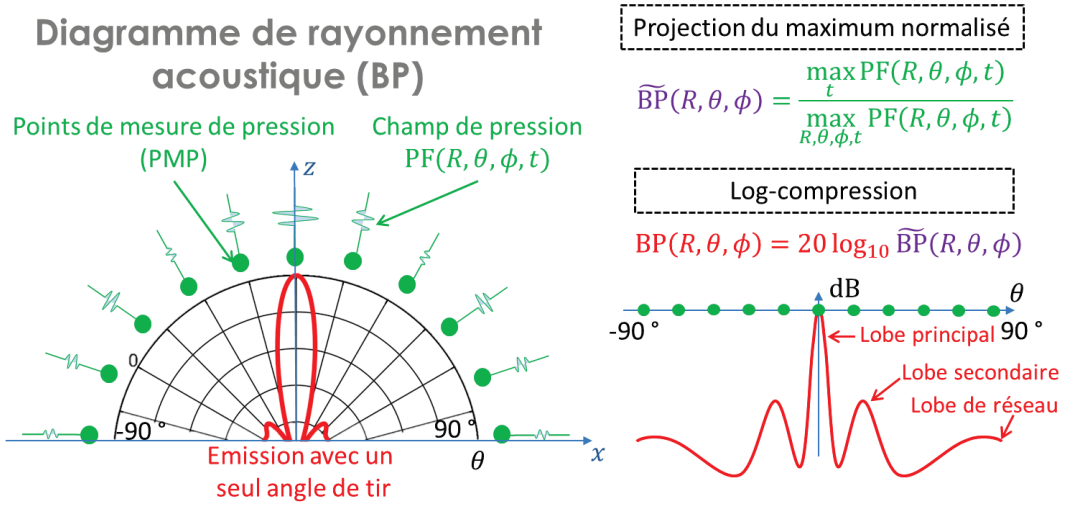


Figure 59 Illustration du calcul du diagramme de rayonnement acoustique (BP) à partir du champ de pression (PF) mesuré en plusieurs points de mesure de pression (PMP).

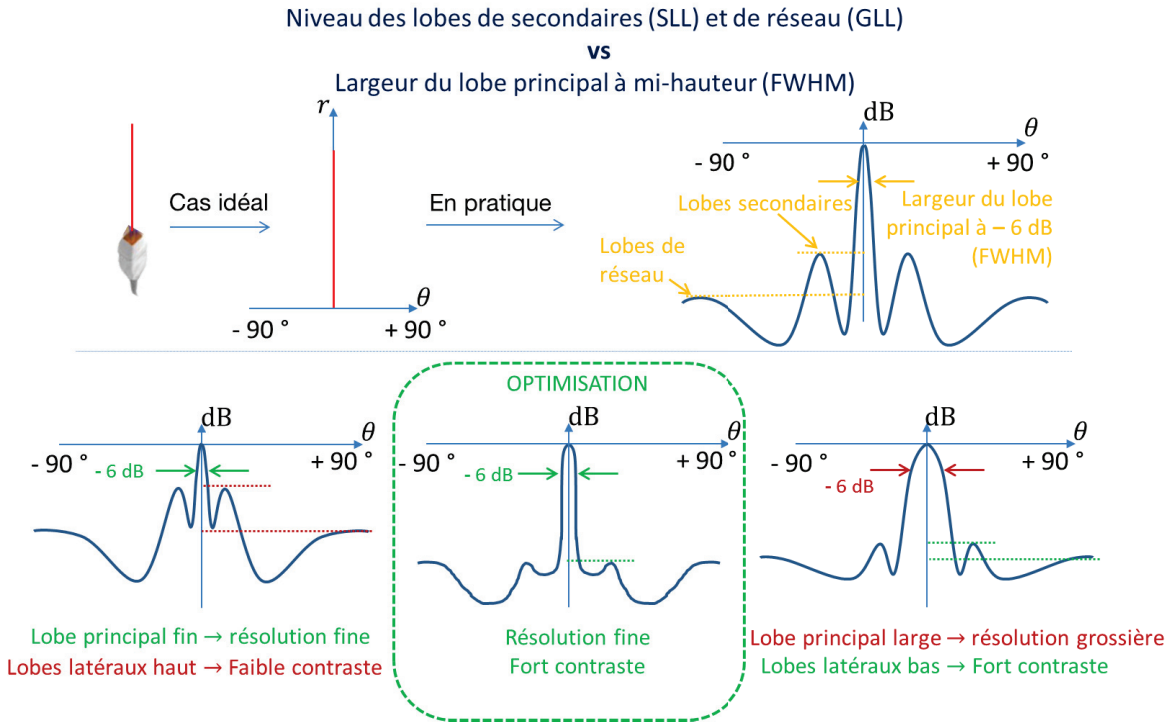


Figure 60 Illustration du compromis entre le niveau des lobes latéraux et la largeur de lobe principal sur le BP.

La méthode de reconstruction d'images conventionnelles dite des retards et sommes (DAS) est détaillée sur la Figure 12. Les délais individuels τ_k sont appliqués aux signaux radiofréquence (RF) bruts pour compenser les différences de temps de vol (durée de la propagation) entre la zone reconstruite et les éléments actifs. Ensuite ces signaux sont sommés entre eux (avec la pondération des coefficients w_k) pour former les « lignes » de l'image RF (ce sont plutôt les colonnes sur la Figure 12). L'enveloppe de l'image RF est ensuite détectée puis log-compressée pour obtenir l'image mode B. Il est possible d'observer l'impact du BP (à double sens car effectif une fois en TX et une autre fois en RX) sur le profil d'une image B-mode d'un diffuseur ponctuel (Figure 12, droite). La tâche du diffuseur n'est pas un simple point à cause de la largeur du lobe principal et des lobes latéraux du BP. En effet, les régions proches du diffuseur n'apparaissent pas vides car elles sont affectées par l'énergie des échos reçus par les lobes latéraux.

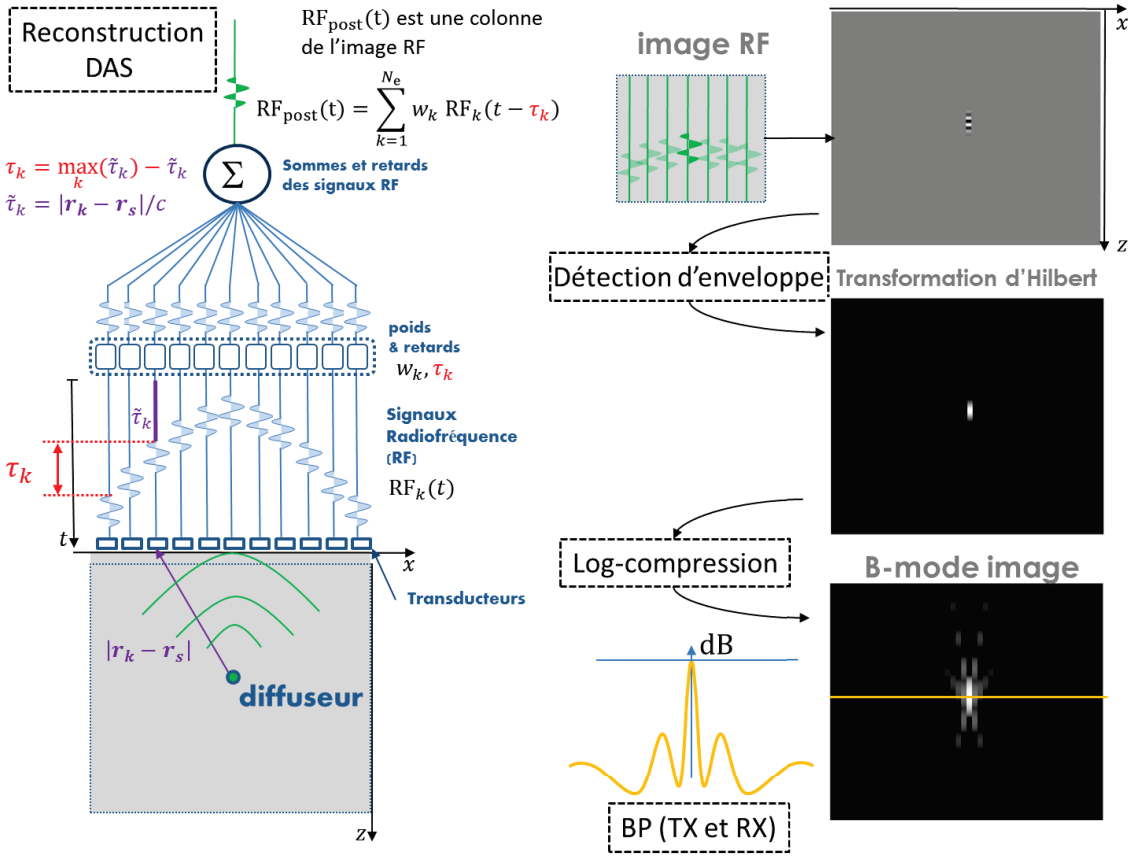


Figure 61 Illustration de la méthode de reconstruction d'image par « retards et sommes » (DAS) afin de produire des images mode B à partir des échos reçus des diffuseurs présents dans le milieu observé.

I.C Intérêts et limites actuelles de l'imagerie ultrasonore 3D+t (4D)

L'imagerie ultrasonore est l'une des rares modalités d'imagerie qui soient à la fois portable, non-ionisante, économiquement relativement accessible, et totalement interactive grâce à son opérativité en temps-réel. Toutes ces caractéristiques sont à la base du succès de l'échographie traditionnelle 2D largement utilisée en clinique. En revanche, l'échographie 2D est intrinsèquement limitée à produire des images 2D en plan de la réalité des organes qui elle est tridimensionnelle (3D). Par conséquent les médecins reconstruisent mentalement cette réalité 3D à partir des images 2D qu'ils observent ce qui requière une formation spécifique et augmente la variabilité des diagnostics (opérateur dépendant). De plus l'imagerie 2D n'est pas idéale pour le suivi d'actes chirurgicaux comme le suivi d'aiguille de biopsie ou de thérapie car l'outil est difficilement contenu dans le plan d'imagerie. Ce manque d'information volumétrique a motivé de nombreuses études à la fois dans les secteurs académiques et industriels (Fenster, Downey, and Cardinal 2001; Nelson and Pretorius 1998). L'imagerie ultrasonore 3D (Prager et al. 2010) permettrait d'accéder à des coupes arbitraires dans les tissus imagés (Stetten et al. 1998), mais aussi de valider les propriétés mécaniques 3D de ces tissus (Deprez et al. 2009; Deffieux et al. 2008), de mesurer le flux 3D dans les vaisseaux (Yiu, Lai, and Yu 2014), de mieux assister les actes chirurgicaux comme le suivi d'aiguilles de biopsie (Nadeau et al. 2015; Zhao et al. 2014) ou le contrôle des traitements par ultrasons focalisés de haute intensité (Lindseth et al. 2013; Unsgaard et al. 2005). En particulier l'échocardiographie 3D temps-réel (Jean

Provost et al. 2014; Sugeng et al. 2006; Light et al. 2001; Stetten et al. 1998) est l'un des plus gros challenge de l'imagerie ultrasonore car une très haute résolution spatio-temporelle est nécessaire. En d'autres termes, la cadence d'imagerie doit être très élevée (typiquement 30 à 50 volumes par secondes car le cœur bat autour de 1-2 Hz) tout en conservant la précision et la robustesse des acquisitions dans le domaine spatial.

Bien que les sondes linéaire 1D (utilisées pour l'imagerie ultrasonore 2D) puissent être déplacées mécaniquement par un moteur afin de balayer la 3ème dimension, le balayage électronique des sondes matricielles 2D est plus rapide et donc plus prometteur pour une imagerie en temps-réel. Le passage des sondes linéaires 1D aux sondes 2D (utilisées pour l'imagerie ultrasonore 3D) s'est déroulé à travers plusieurs étapes intermédiaires décrites dans (Wildes et al. 1997; Fernandez et al. 2003): les sondes 1.25 D, 1.5 D et 1.75 D ont successivement amélioré les capacités d'imager en 3D (Figure 13) jusqu'à atteindre la possibilité de focaliser et de dépointer le faisceau dans toutes les directions avec les sondes 2D (Prager et al. 2010; Light et al. 2001; Rasmussen et al. 2015; Christiansen et al. 2015; Jean Provost et al. 2014).

En revanche une sonde 2D pleinement peuplée (par exemple 40×40 = 1600 éléments) nécessite autant de canaux indépendants que d'éléments pour être pilotée avec la plus haute flexibilité permettant d'explorer de nouvelles stratégies d'imagerie. Outre les complications des connexions électroniques dans la sonde, un trop grand nombre d'éléments actifs conduit également à des difficultés d'ordre pratique, notamment en ce qui concerne la taille du câble reliant la sonde à l'échographe. Par ailleurs, les besoins en termes de taux de transfert et de stockage de l'information sont encore aujourd'hui inaccessibles : par exemple une configuration de 1600 éléments fonctionnant à 3 MHz produit environ 1500 Gbit/s avec un convertisseur numérique de 12 bits échantillonnant à 80 MHz ce qui représente presque 2 Téraoctets à stocker pour chaque seconde d'acquisition. De plus la reconstruction DAS d'un volume de 128x128 lignes (chacune de 2048 échantillons) nécessite 54 Giga opérations de multiplication-accumulation (MAC) reconstruction. Il est donc intéressant de chercher comment réduire les contraintes liées à la fois à l'acquisition et à la reconstruction des volumes ultrasonores.

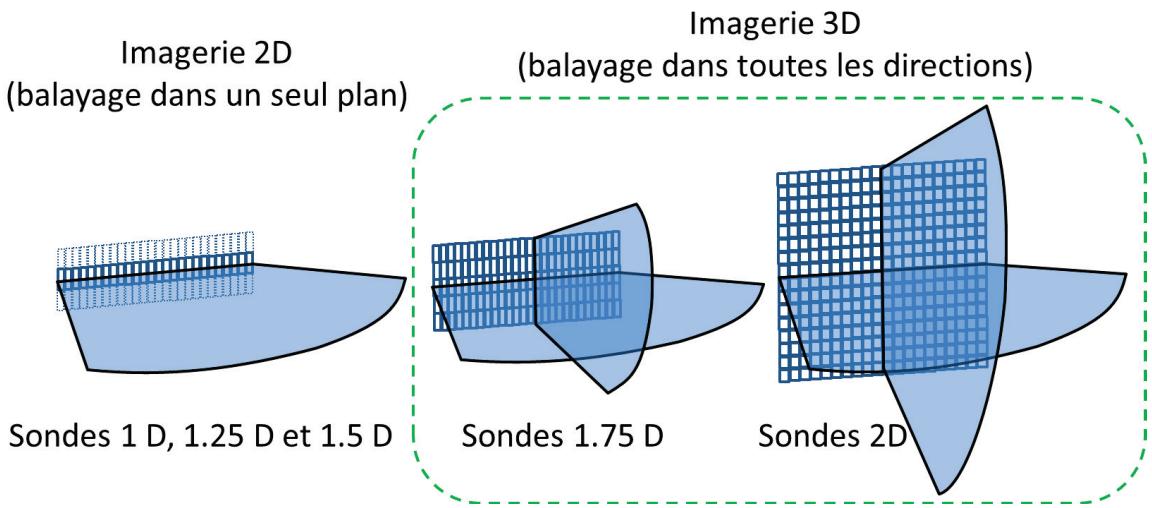


Figure 62 De l'imagerie 2D à l'imagerie 3D avec l'utilisation des sondes matricielles 2D à balayage electronique

Plusieurs solutions existantes permettent à l'échographie 4D d'exister aujourd'hui. Toutefois le challenge d'imager le volume entier du myocarde en un seul battement de cœur reste à relever. Aujourd'hui la totalité du volume du myocarde est acquise sur plusieurs battements cardiaques : les techniques de synchronisation permettant de s'affranchir des mouvements de pulsation du cœur ne sont pas compatibles avec les cas d'arythmie. De même l'apnée nécessaire pour s'affranchir des mouvements de respiration peut être contre-indiquée pour certains patients.

Certaines solutions commerciales prometteuses consistent à combiner l'adressage en ligne-colonnes (Rasmussen et al. 2015; Christiansen et al. 2015; K. Chen 2014; Logan et al. 2011) avec du multiplexage (B. Savord and Solomon 2003) mais elles ne permettent pas de piloter en continu l'intégralité des éléments actifs puisque seule une partie des éléments sont reliés à l'échographe à chaque instant. Voici certaines des solutions industrielles les plus avancées qui donnent actuellement accès à l'imagerie ultrasonore 4D :

- La sonde matricielle 4Z1c combine avec l'échographe Acuson SC2000 [37] (Siemens Healthcare, Ultrasound Business Unit, Moutain View, CA)(Barnes, Bolorforosh, and Phelps 2005).
- La sonde matricielle X6-1 avec l'échographe iE33[38] (Koninklijke Philips Electronics N.V., Amsterdam, Netherlands) (B. J. Savord 2012; Robinson et al. 2003; B. Savord and Solomon 2003; B. J. Savord and Thiele 1999)
- La sonde matricielle 3V avec l'échographe Vivid 7 dimension[39] (General Electric Company, Fairfield, Connecticut, U.S.) (Thomenius, Wodnicki, and Li 2010)

Ces solutions utilisent la technique de *micro-beamforming* (Kortbek, Jensen, and Gammelmark 2013; Matrone et al. 2014; Fisher et al. 2005; Wygant et al. 2009). Cette technique qui consiste à faire une première étape de reconstruction du volume directement dans la sonde (à l'aide d'une électronique embarquée) pour ne transmettre que ces sous-images à l'échographe où elles sont ensuite combinée dans une deuxième étape de reconstruction pour former le volume. Cette technique permet de réduire le nombre de canaux indépendants de l'échographe mais nécessite le développement coûteux de circuits intégrés dédiés (ASICs) qui vont limiter la flexibilité dans la reconstruction des volumes.

Enfin voici les quelques plateformes de recherche où l'échographie 4D est actuellement disponible :

- Institut Langevin à Paris, France (J. Provost et al. 2015) : 1024 canaux and 512 canaux disponibles en TX et en RX respectivement grâce à la combinaison de quatre échographes Aixplorer (Supersonic Imagine, Aix-en-Provence, France).
- *Danmarks Tekniske Universitet* à Lyngby (Jensen et al. 2013) : Système d'imagerie ultrasonore à synthèse d'ouverture temps-réel (SARUS) avec 1024 canaux indépendants dont 256 peuvent être traités en temps-réel.

[37] Plus d'informations sur https://www.healthcare.siemens.com (visité en Juillet 2016)
[38] Plus d'informations sur http://www.usa.philips.com (visité en Juillet 2016)
[39] Plus d'informations sur http://www.mehradco.com (visité en Juillet 2016)

I.D Définitions de sondes parcimonieuses, état de l'art et limitations

Une autre méthode est représentée par la définition de sondes parcimonieuses (Holm et al. 2001) où la tendance est de réduire directement dans la sonde le nombre d'éléments actifs à piloter avec l'échographe. Avec cette technique l'imagerie par ultrasons 3D peut être réalisée en conservant toute la flexibilité d'une situation où un élément est connecté à un canal de l'échographe en continu le tout sans augmenter la complexité du système d'imagerie. La configuration résultant de la réduction du nombre d'éléments actifs doit être capable de réaliser des images volumiques en satisfaisant les contraintes de résolution et de contraste requises par l'application. Dans la littérature, il est possible de distinguer deux principales approches concernant l'étude des sondes parcimonieuses : la première correspond aux conceptions déterministes (Table I) et la seconde correspond aux conceptions stochastiques (Table II). Les listes des publications examinées pour chacune des deux approches sont les suivantes :

- Conceptions déterministes (Table I) (Ramalli et al. 2015; Ramadas et al. 2014; Tekes, Karaman, and Degertekin 2011; Martínez-Graullera et al. 2010; Karaman et al. 2009; Austeng and Holm 2002; Schwartz and Steinberg 1998; Brunke and Lockwood 1997; Lockwood and Foster 1996; Smith, Pavy, and von Ramm 1991)
- Conceptions stochastiques (Table II) (Sciallero and Trucco 2015; Diarra et al. 2013; Choe, Oralkan, and Khuri-Yakub 2010; P. Chen et al. 2010; Trucco 1999; Austeng et al. 1997; Holm et al. 2001; Holm, Elgetun, and Dahl 1997; Holm and Elgetun 1995; Davidsen, Jensen, and Smith 1994; Weber et al. 1994; Boni, Richard, and Barbarossa 1994; Turnbull and Foster 1991).

Une distinction supplémentaire peut être faite entre les sondes régulières (les éléments sont disposés sur une grille régulière) (Brunke and Lockwood 1997; Trucco 1999; Sciallero and Trucco 2015; P. Chen et al. 2010) et les sondes non-régulières (positionnement arbitraire des éléments actifs) (Diarra et al. 2013; Roux et al. 2014; Diarra et al. 2014; Roux, Ramalli, Tortoli, et al. 2015; Roux, Ramalli, Robini, et al. 2015; Ramalli and Tortoli 2014; Ramalli et al. 2015). Les degrés de libertés supplémentaires disponibles dans le cas des sondes non-régulières permettent d'améliorer les performances acoustiques accessibles (Diarra et al. 2013; Ramalli et al. 2015). En effet, les sondes non-régulières présentent l'avantage de réduire les lobes de réseau même lorsque la distance inter-éléments (pitch) dépasse la valeur maximale imposée par la contrainte d'échantillonnage spatiale, à savoir $\lambda/2$. Une telle situation est possible grâce à l'absence de périodicité dans l'échantillonnage de la surface où sont placés les éléments actifs. Le fait de relâcher la contrainte d'échantillonnage spatial permet de définir des éléments de plus grande dimension ce qui aide à compenser la faible sensibilité des sondes parcimonieuses en augmentant la surface active de l'ouverture. Cependant augmenter la taille des éléments peut également limiter le champ de vue (FOV) car plus ils sont grands et plus leur capacité à dépointer le faisceau est limitée. La fabrication de sondes non-régulières impose des contraintes supplémentaire comme l'utilisation de la coupe laser ou l'utilisation d'une technologie CMUT (Savoia, Caliano, and Pappalardo 2012). Le procédé de fabrication des sondes CMUT est très proche de celui mis en œuvre pour la production de circuit intégrés, c'est à dire, extrêmement flexible et à la fois assez coûteuse à moins qu'une grande quantité (plusieurs milliers) de sondes identiques ne soient fabriquées.

TABLE XIII COMPARAISON ENTRE LES PRINCIPALES CONCEPTIONS DE SONDES 2D DÉTERMINISTES DANS LA LITTÉRATURE

Caractéristiques / Travaux	Régulières / Non-régulières	Simulations large bande	Sensible à la forme des éléments	BP en TX / BP en TX et RX	Multi-profondeur	Nombre d'élément actifs connus a priori	Symétrie libre / constraintes fabrication	éléments TX = éléments RX	Aucune apodisation	optimisation	caclul du BP à chaud (non pré-calculé)	Aucun a priori sur le SLL
Smith, 1991	✓ / ×	×	✓	× / ✓	×	✓	× / ✓	×	×	×		
Lockwood, 1996	✓ / ×	✓	✓	× / ✓	×	✓	× / ✓	×	×	×		
Brunke, 1997	✓ / ×	×	✓	× / ✓	×	×	× / ✓	×	×	×		
Schwartz, 1998	✓ / ×	✓	×	✓ / ✓	✓	✓	× / ×	×	×	×		
Austeng, 2002	✓ / ×	×	×	× / ✓	×	×	× / ×	×	✓	×		
Karaman, 2009	✓ / ×	✓	×	× / ✓	✓	✓	× / ✓	×	✓	×		
Martínez-Graullera, 2010	× / ✓	✓	×	× / ✓	×	✓	× / ✓	×	✓	×		
Tekes, 2011	× / ✓	✓	×	× / ✓	×	✓	× / ✓	×	✓	✓	×	✓
Ramadas, 2014	× / ✓	×	×	✓ / ×	✓	✓	× / ×	✓	✓	×		
Ramalli, 2015	× / ✓	✓	✓	✓ / ×	✓	✓	× / ✓	✓	✓	×		

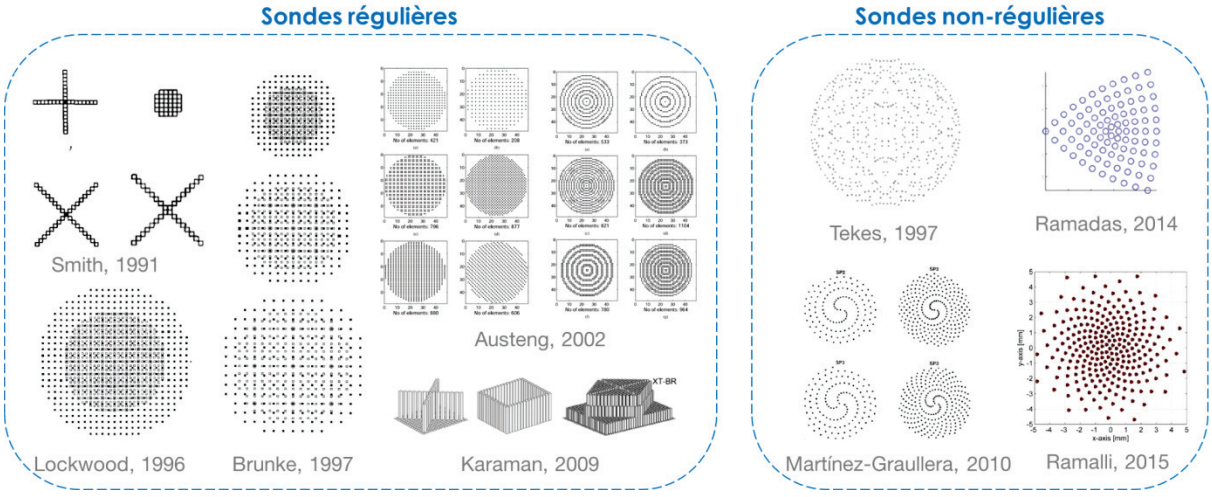


Figure 63 Conceptions de sondes déterministes 2D proposés dans la littérature, à gauche les configurations régulières (les éléments sont disposés sur une grille régulière) et à droite les configurations non-régulières (dispositions arbitraires des éléments).

Les sondes déterministes sont définies très rapidement, avec très peu de calculs, et peuvent être immédiatement testées avec des simulations car la géométrie de la configuration est connue à l'avance. En revanche, la conception des sondes déterministes manque de flexibilité et leurs performances, en termes de SLL/GLL, dépend essentiellement de l'utilisation d'un groupe d'éléments pour émettre différent de celui utilisé pour recevoir. Dans le cas où le multiplexage n'est pas souhaitable (par exemple pour avoir les éléments continuellement connectés à l'échographe), le nombre d'éléments qui peuvent être utilisés dans chacun des groupes (TX et RX) est limité par le nombre de canaux de l'échographe alors que l'utilisation de l'ensemble des canaux de l'échographe à la fois en TX et en RX maximise la surface active de l'ouverture. C'est le cas par exemple dans des propositions récentes de configurations de sondes en spirales (Ramalli et al. 2015; Martínez-Graullera et al. 2010) qui montrent des résultats prometteurs.

TABLE XIV COMPARAISON ENTRE LES PRINCIPALES CONCEPTIONS DE SONDES 2D STOCHASTIQUES DANS LA LITTÉRATURE

Caractéristiques / Travaux	Régulières / Non-régulières	Simulations large bande	Sensible à la forme des éléments	BP en TX / BP en TX et RX	Multi-profondeur	Nombre d'élément actifs connus a priori	Symétrie libre / constraintes fabrication	éléments TX = éléments RX	Aucune apodisation	optimisation	caclul du BP à chaud (non pré-calculé)	Aucun a priori sur le SLL
Turnbull and Foster, 1991	✓ / ×	✓	✓	× / ✓	✓	✓	× / ✓	✓	×	×		
Boni, 1994	× / ✓	×	×	✓ / ×	×	×	× / ×	✓	×	✓	✓	✓
Weber, 1994	✓ / ×	×	×	✓ / ×	×	×	✓ / ✓	✓	✓	✓	✓	×
Davidsen, 1994	✓ / ×	✓	✓	× / ✓	✓	✓	✓ / ✓	×	✓	×		
Holm, 1997	✓ / ×	×	×	✓ / ×	×	×	× / ×	✓	×	✓	✓	×
Austeng, 1997	✓ / ×	×	×	× / ✓	×	✓	✓ / ✓	×	✓	✓	✓	✓
Trucco, 1999	✓ / ×	×	×	✓ / ×	×	×	× / ✓	✓	×	✓	✓	×
Austeng, 2002	✓ / ×	×	×	× / ✓	×	×	× / ×	×	✓	×		
Chen, 2010	✓ / ×	×	×	✓ / ×	×	×	✓ / ✓	✓	×	✓	✓	×
Choe, 2010	✓ / ×	✓	✓	× / ✓	✓	✓	× / ✓	×	✓	✓	×	✓
Diarra, 2013	✓ / ✓	×	×	× / ✓	×	×	✓ / ✓	✓	×	✓	✓	×
Sciallero, 2015	✓ / ✓	✓	✓	× / ✓	×	✓	× / ✓	×	×	✓	✓	×
Roux, 2016	✓ / ✓	✓	✓	✓ / ×	✓	✓	✓ / ✓	✓	✓	✓	✓	✓

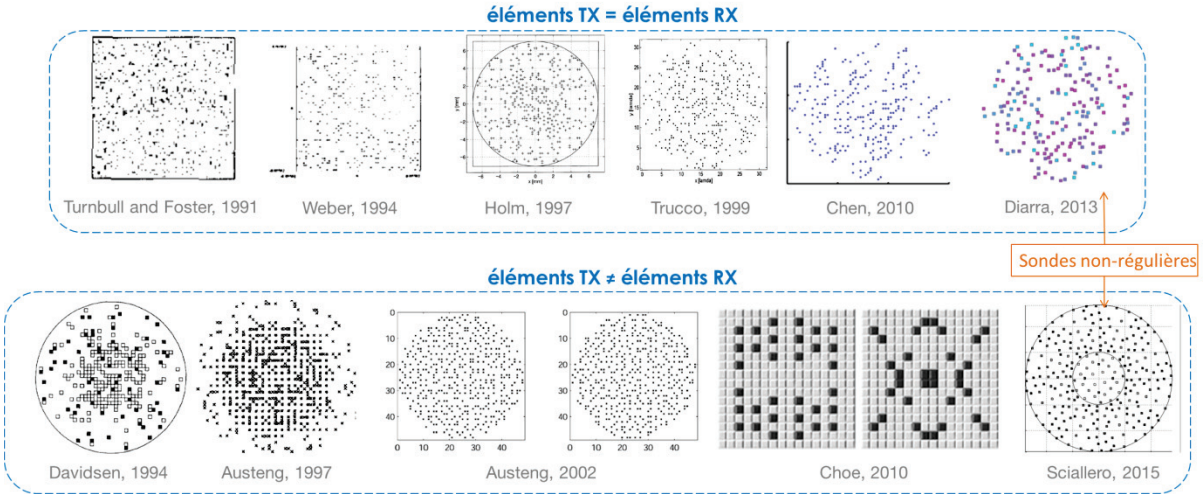


Figure 64 Conceptions de sondes stochastiques 2D proposés en la littérature. en haut, les configurations où les même éléments sont utilisés à la fois en transmission (TX) et en réception (RX) ; en bas, les configurations ou deux groupes d'éléments différents sont utilisés en TX et RX.

Dans le cas des sondes parcimonieuses aléatoires des configurations sont tirées aléatoirement à partir d'une sonde 2D pleinement peuplée définie initialement. Parmi elles la configuration qui présente les meilleures performances (par exemple en termes de SLL ou GLL) est sélectionnée. Avec cette approche le nombre de solutions explorées est restreint (Davidsen, Jensen, and Smith 1994; Austeng and Holm 2002; Turnbull and Foster 1991) et il n'est pas possible de garantir que les meilleures performances qui peuvent potentiellement être obtenues sont effectivement atteintes. Ce manque de robustesse tient au fait que chaque nouvelle solution est générée sans tenir compte des solutions testées précédemment. Au contraire, les approches d'optimisation stochastique bénéficient des essais précédents pour itérativement proposer une configuration optimale. Puisque la recherche d'une solution optimale parmi toutes les configurations de sondes parcimonieuses est un problème d'optimisation combinatoire de grande taille, le recuit simulé (Sciallero and Trucco 2015; Diarra et al. 2013; Tekes, Karaman, and Degertekin 2011; P. Chen et al. 2010; Choe, Oralkan, and Khuri-Yakub 2010; Holm et al. 2001; Trucco 1999; Holm and Elgetun 1995) convient mieux que

l'algorithme génétique (Holm et al. 2001; Austeng et al. 1997; Weber et al. 1994; Haupt 1994). En effet, la principale difficulté qui se pose lors de la résolution d'un problème combinatoire de grande taille avec un algorithme génétique est la gestion d'une très grande population de solutions candidates, car cette opération est très coûteuse à la fois en temps et en mémoire de stockage. Par ailleurs, les algorithmes génétiques ont souvent le défaut de converger prématurément et ils présentent une plus faible capacité à sortir des minimums locaux que le recuit simulé: voir par exemple (Hwang and He 2006; Adler 1993).

Afin d'atteindre les meilleures capacités d'imagerie en 3D, la fonction d'énergie à optimiser avec l'approche stochastique doit être basée sur les caractéristiques du diagramme de rayonnement acoustique (BP) des solutions testées. En pratique, calculer le BP de manière réaliste à chaque itération est souvent impossible car l'étape de simulation peut s'avérer très longue. De façon à réduire cette charge de calcul, la majorité des travaux portant sur l'optimisation stochastique des sondes 2D parcimonieuses (Diarra et al. 2013; Tekes, Karaman, and Degertekin 2011; P. Chen et al. 2010; Holm et al. 2001; Trucco 1999; Austeng et al. 1997; Holm and Elgetun 1995; Weber et al. 1994; Haupt 1994) font l'approximation d'un BP monochromatique en champ lointain. L'approximation en champ lointain implique que chaque élément actif est réduit à une source ponctuelle située au centre de l'élément physique (la taille de l'élément ne peut pas être prise en compte). L'approximation monochromatique signifie que la forme d'onde transmise est une onde monochromatique oscillant à la fréquence centrale de la sonde (pas de considération réaliste du signal d'excitation ni de la réponse impulsionnelle des éléments actifs). D'après les publications examinées les seuls exceptions sont les travaux de (Sciallero and Trucco 2015; Choe, Oralkan, and Khuri-Yakub 2010) où l'optimisation stochastique est réalisée avec une fonction d'énergie utilisant le BP (aller-retour) dans des conditions de simulations large bande. Enfin, des contraintes de symétrie sont souvent imposées ce qui permet de réduire encore la charge de calcul en réduisant le nombre de solutions possibles (Sciallero and Trucco 2015; Choe, Oralkan, and Khuri-Yakub 2010).

Sur la base de cet état de l'art, les chapitres suivants sont organisés comme suit de manière à introduire les contributions de ce travail de thèse :

- Le chapitre II présente les techniques d'accélération permettant l'intégration de simulation acoustiques réalistes et l'utilisation de fonctions d'énergie large bande et sensibles à la forme des éléments actifs dans un cadre général d'optimisation des sondes 2D parcimonieuses.
- Le chapitre III présente une application du schéma général d'optimisation des sondes 2D parcimonieuses (introduit au chapitre II) au cas des sondes 2D non-régulières. De nouvelles fonctions d'énergie multi-profondeur sont introduites et leur impact est mis en avant via l'analyse des sondes 2D non-régulières optimales obtenues.
- Le chapitre IV présente les lignes directrices pour introduire des contraintes de fabrication dans le schéma d'optimisation et les résultats sont obtenus en cherchant la meilleure sélection d'un nombre fixé d'éléments à activer parmi ceux d'une sonde matricielle 2D régulière.

IIChapitre II Simulations acoustiques réalistes dans un cadre général d'optimisation des sondes 2D parcimonieuses

Les avantages de l'intégration de simulations acoustiques réalistes dans un cadre général d'optimisation des sondes 2D parcimonieuses sont les suivants : une meilleure capacité à distinguer des sondes jusqu'alors considérées comme identiques (Figure 23), l'accès à de nouveaux degrés de liberté (taille, forme, orientation et signal d'excitation des éléments), et la possibilité de tester au cours de l'optimisation des sondes qui se comportent de façon similaire à si elles étaient physiquement construites. La plus grosse limitation réside dans la charge imposée par le calcul du champ de pression large bande (Trucco 1999). Pour résoudre cette problématique deux techniques ont été implémentées pour accélérer les simulations acoustiques du champ de pression généré par la sonde. La première technique est une gestion ergonomique des données déjà simulées permettant une mise à jour rapide du champ de pression sans avoir à recalculer les contributions de tous les éléments actifs de la sonde. La deuxième technique consiste en une stratégie d'échantillonnage de l'espace entourant la sonde selon une spirale 3D ce qui permet de réduire le nombre de points de mesure de pression (PMP).

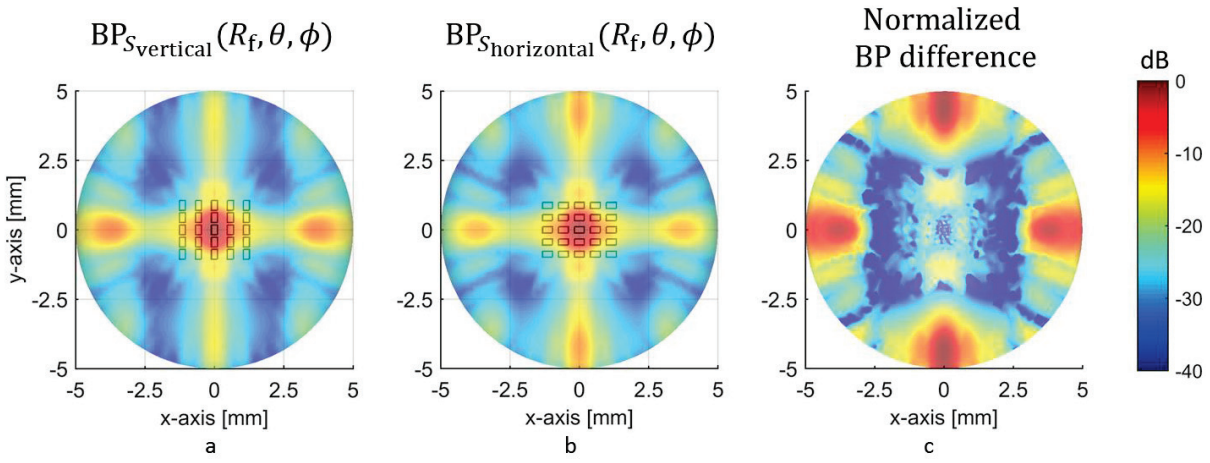


Figure 65 Deux sondes 5x5 avec les éléments actifs dont les centres sont positionnés aux mêmes endroits et dont les dimensions sont identiques à une rotation de 90 ° près. (a) La configuration verticale sur laquelle est superposée son rayonnement acoustique $\mathrm{BP}_{S_{\mathrm{vertical}}}(R_{\mathrm{f}},\theta,\phi)$; (b) la configuration horizontale sur laquelle est superposée son rayonnement acoustique $\mathrm{BP}_{S_{\mathrm{horizontal}}}(R_{\mathrm{f}},\theta,\phi)$; (c) la différence normalisée entre $\mathrm{BP}_{S_{\mathrm{vertical}}}(R_{\mathrm{f}},\theta,\phi)$ et $\mathrm{BP}_{S_{\mathrm{horizontal}}}(R_{\mathrm{f}},\theta,\phi)$. Les deux sondes seraient considérées comme identiques avec un modèle de source ponctuelle pour les éléments actifs.

II.A Accélération des simulations acoustiques réalistes

La réduction du nombre N_{PMP} de PMP s'effectue sans perte de précision dans l'évaluation du champ de pression. La stratégie de placement des éléments utilisée dans (Viganó et al. 2009) a été transposée en 3D en disposant les PMP sur un hémisphère centré sur la sonde et le long du bras d'une spirale 3D de manière à ce qu'aucune périodicité ne soit introduite (ou cachée) par la mesure (Figure 18 et Figure 21). Cette stratégie d'échantillonnage du champ de pression est très flexible

(Figure 19) et grâce à l'enroulement des points sur le bras d'une spirale 3D, le nombre de dimensions nécessaires pour représenter profil de rayonnement est réduit (Figure 22).

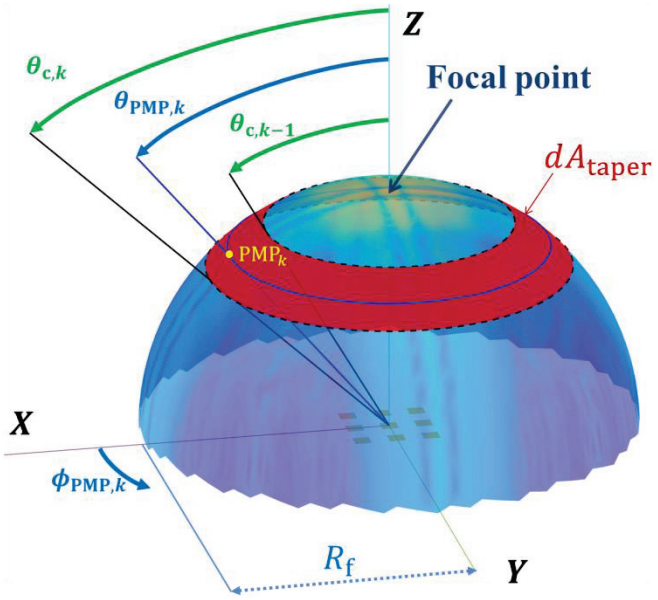


Figure 66 Cercles délimitant les bandes de surface dA_{taper} utilisées pour le placement des points de mesure de pression (PMP). Le premier PMP est placé sur l'axe z à la profondeur focale R_{f}, puis chaque k-ième PMP est placé à l'angle $\theta_{\text{PMP},k}$ séparant en deux la bande de surface dA_{taper} qui est délimitée par les deux angles $\theta_{\text{c},k-1}$ et $\theta_{\text{c},k}$.

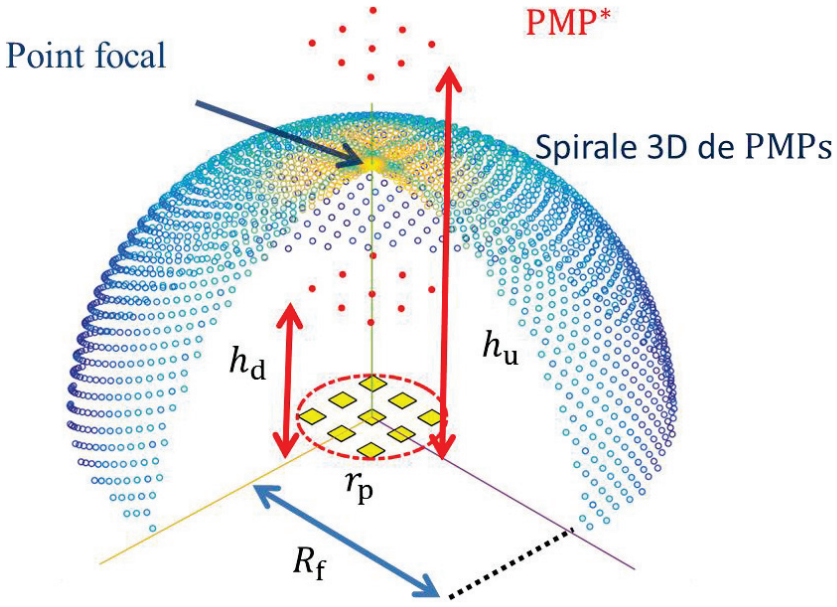


Figure 67 Illustration des PMP disposés le long d'une spirale 3D reposant sur un hémisphère de rayon R_{f} centré sur la sonde. Les deux PMP* situés au-dessus de chaque élément actif sont également représentés. Le rayon de l'ouverture est r_{p} (cercle rouge en pointillés).

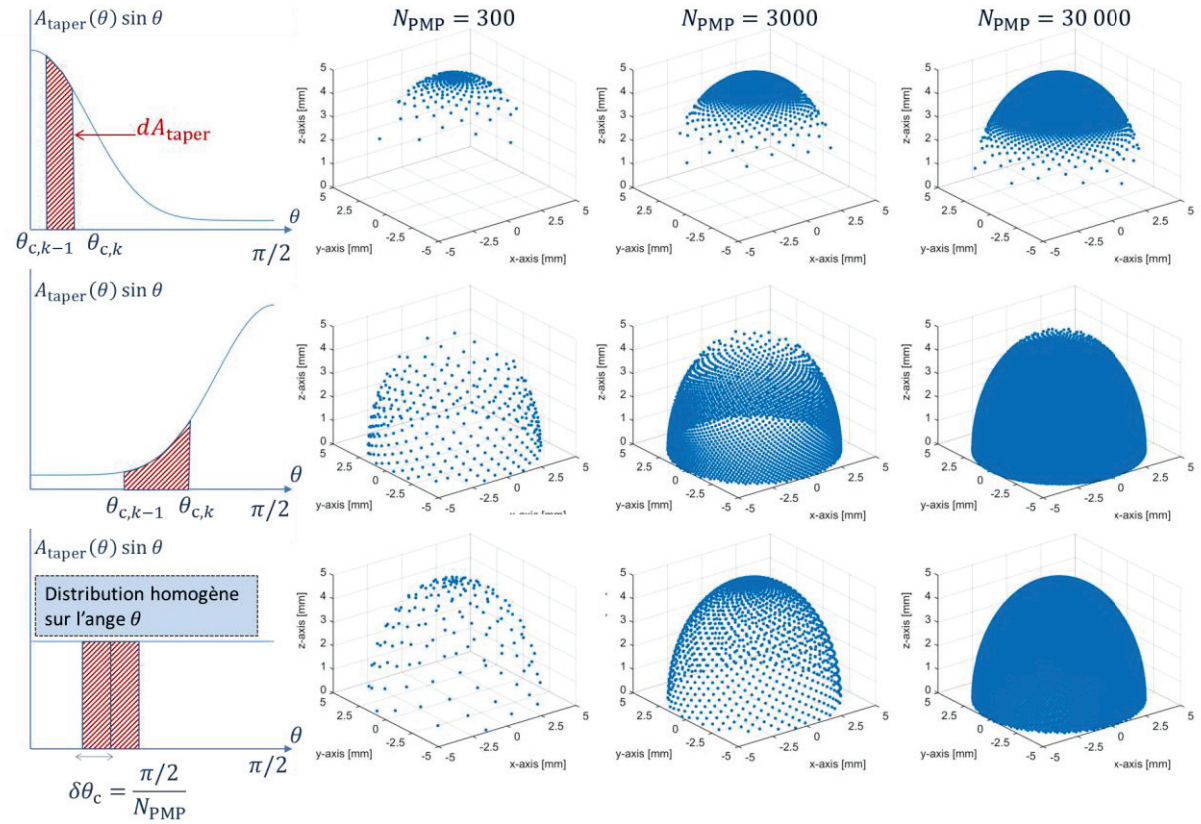


Figure 68 Illustration de la densité ajustable de la distribution des points de mesure de pression (PMP) en utilisant différentes lois de densité $A_{\text{taper}}(\theta)$: un nouveau cercle est délimité chaque fois qu'une bande de surface élémentaire dA_{taper} est intégrée sous la courbe $A_{\text{taper}}(\theta)\sin\theta$. Il en résulte que les PMP s'enroulent le long d'une spirale 3D disposée sur la surface de l'hémisphère de rayon R_f. Trois lois de densité (une par lignes) sont illustrées pour trois valeurs différentes du nombre de PMP (sur les colonnes) $N_{\text{PMP}} = \{300, 3000, 30\,000\}$.

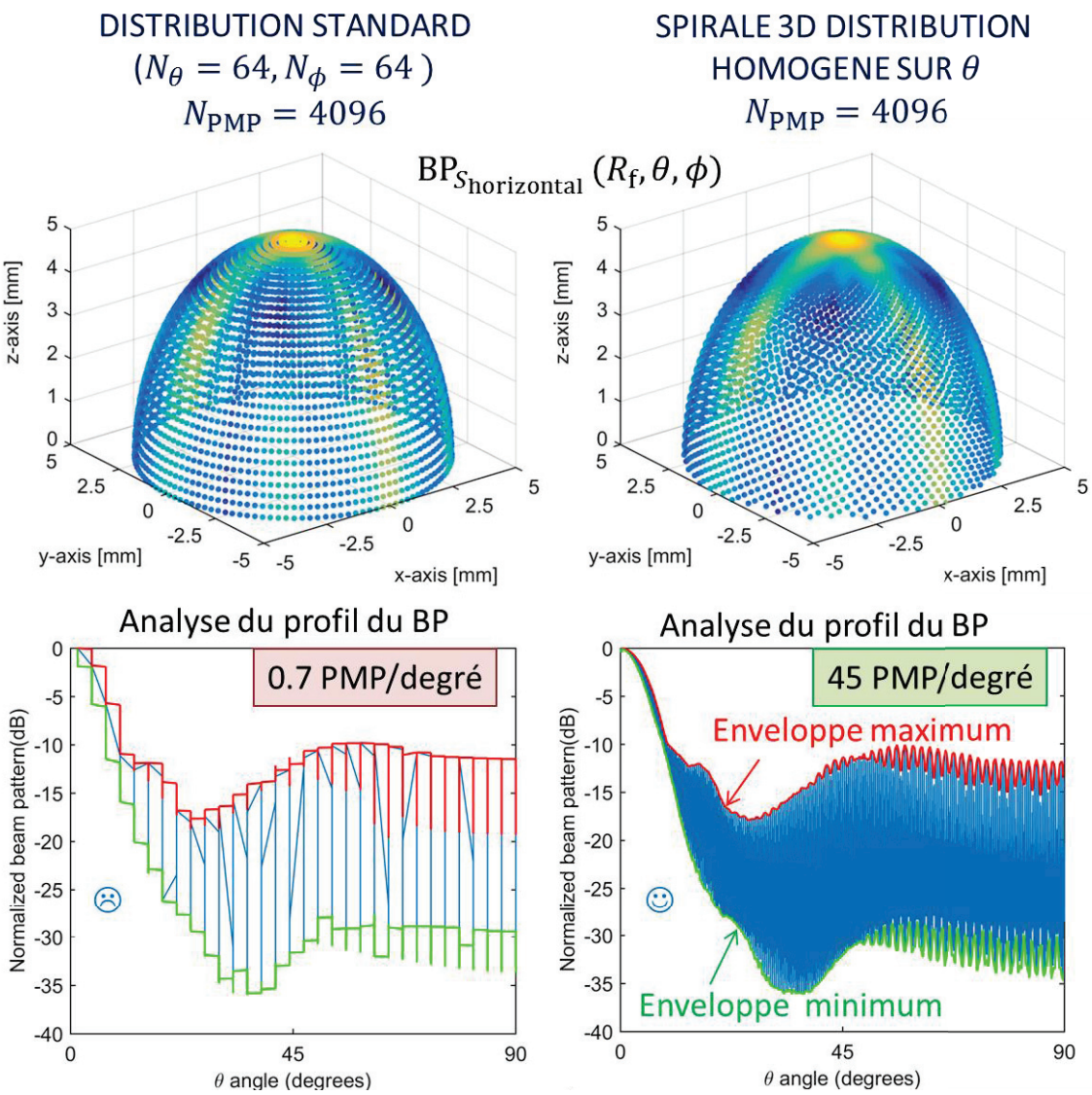


Figure 69 Comparaison de la méthode standard de distribution des PMP (64 échantillons sur θ et 64 échantillons sur ϕ) avec la technique de réduction proposée (4096 PMP distribués de manière homogène selon l'angle θ). Les analyses (en bas) des profils du diagramme de rayonnement (beam pattern -BP) illustrent l'intérêt de la réduction du nombre de dimension nécessaire pour représenter le BP en 2D. L'enveloppe supérieure (pire cas) et l'enveloppe inférieure (meilleur cas) sont tracées sur les profils de BP en lignes pleines rouge et verte respectivement.

En se plaçant dans des conditions de propagation linéaire des ondes, le champ de pression peut être évalué comme la superposition des contributions individuelles des éléments actifs. La Figure 20 illustre comment le nouveau champ de pression $\mathrm{PF}_{S_{n+1}}$ est mis à jour à partir du champ de pression actuel PF_{S_n} suite à la translation d'un élément $\mathbf{e}_n$ en $\mathbf{e}_{n+1}$. Le champ de pression initial PF_{S_0} est calculé une unique fois au début de l'optimisation puis il est mis à jour selon (39).

$$\mathrm{PF}_{S_{n+1}} = \mathrm{PF}_{S_n} - \mathrm{PF}_{\mathbf{e}_n} + \mathrm{PF}_{\mathbf{e}_{n+1}} \tag{83}$$

En particulier, seule la nouvelle contribution $\mathrm{PF}_{\mathbf{e}_{n+1}}$ de l'élément perturbé $\mathbf{e}_{n+1}$ doit être calculée. Dans (39) et sur la Figure 20 l'index n désigne le numéro de l'itération.

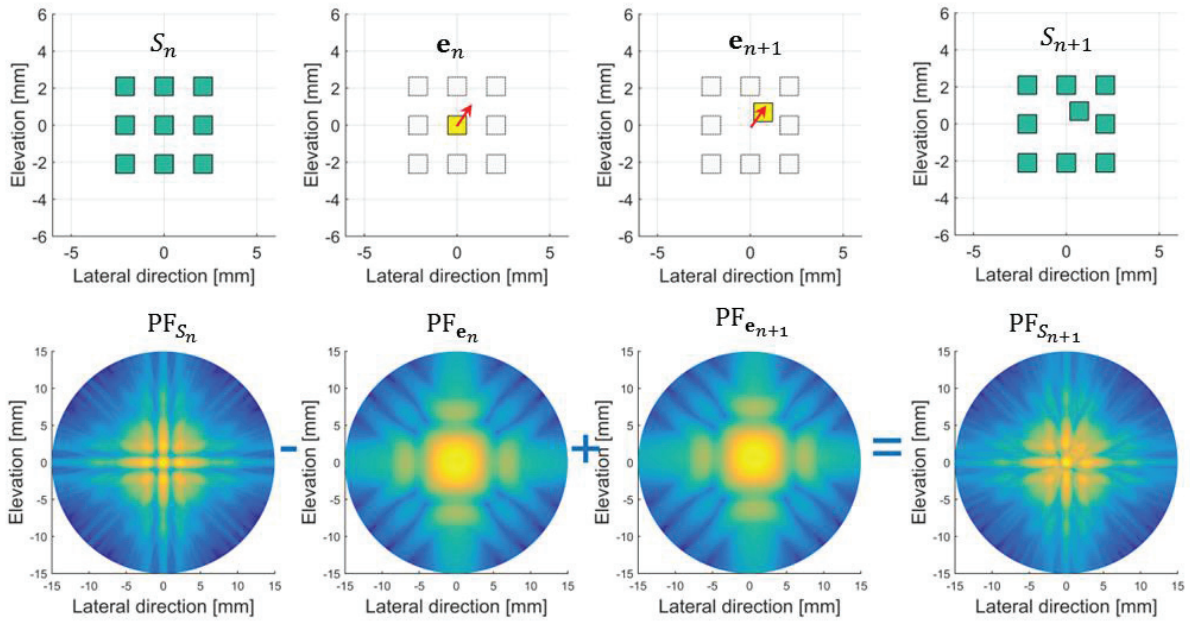


Figure 70 Détails des étapes de la mise à jour rapide du champ de pression suite à la translation d'un élément $\mathbf{e_n} \rightarrow \mathbf{e_{n+1}}$ de la sonde S_n évoluant vers une nouvelle solution S_{n+1}. La configuration initiale S_n, l'élément $\mathbf{e_n}$ avant translation, l'élément $\mathbf{e_{n+1}}$ après translation et la nouvelle solution S_{n+1} sont représentés de gauche à droite en haut. Les champs de pression associés (PF_{S_n}, $\mathrm{PF}_{\mathbf{e}_n}$, $\mathrm{PF}_{\mathbf{e}_{n+1}}$, $\mathrm{PF}_{S_{n+1}}$) sont respectivement représentés de gauche à droite en bas.

L'accélération qui résulte de l'implémentation des deux techniques (10 000 PMP sur un hémisphère de rayon R_f = 25 mm) décrites précédemment est d'environ un facteur 75 pour l'optimisation d'une ouverture de rayon r_p = 6 mm ≈ 30 λ où sont répartis 256 éléments fonctionnant à 7 MHz de fréquence centrale et focalisant à 25 mm sur l'axe z.

II.B Cadre général d'optimisation des sondes 2D parcimonieuses.

La recherche d'une solution optimale S_opti s'effectue en minimisant une fonction d'énergie U (qui fixe les objectifs en termes de performances acoustiques) sur un espace d'état Ω (l'ensemble discret des solutions possibles). L'optimisation est réalisée à l'aide d'un algorithme de recuit simulé en explorant Ω à l'aide d'un mécanisme de communication Θ qui précise quelles sont les transitions possibles entre une solution S et une nouvelle proposition $\tilde{S}$. Une des propriétés de l'algorithme utilisé est d'accepter des transitions où la variation de la fonction d'énergie $\Delta U = U(\tilde{S}) - U(S)$ est positive (ce qui correspond à une dégradation des performances). La probabilité d'accepter une telle transition est toutefois réduite au fur et à mesure de la progression de l'optimisation avec l'aide d'une séquence de refroidissement $(\beta_n)_{n\in\mathbb{N}}$. L'espace d'état et le mécanisme de communication sont définit de manière suffisamment générale pour pouvoir être appliqué aux cas des sondes régulières (éléments disposés selon une grille) et des sondes non-régulières (positionnement arbitraire des éléments sur la surface de l'ouverture). La fonction d'énergie est définie à partir du diagramme de rayonnement large bande $\mathrm{BP}_{S_n}(R,\theta,\phi)$ de la sonde S_n. Son objectif est de limiter la largeur du lobe principal et de réduire au maximum les lobes latéraux afin d'obtenir une bonne qualité d'image en termes de résolution et de contraste respectivement. L'organigramme du déroulement de l'optimisation est présenté sur la Figure 24.

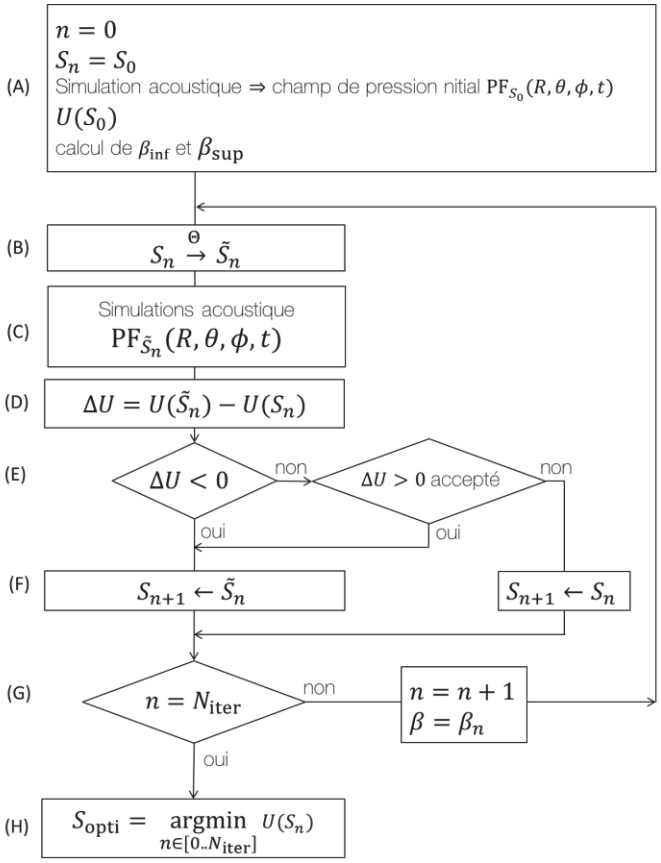


Figure 71 Diagramme du cadre général d'optimisation des sondes 2D parcimonieuses par recuit simulé.

L'hypothèse de propagation linéaire des ondes, sur laquelle repose la mise à jour rapide du champ de pression, est une limitation. En cas de simulation non-linéaire (Varray et al. 2011) le calcul de l'ensemble des contributions doit se faire systématiquement.

Il a été montré deux techniques permettant d'intégrer les simulations large bande du diagramme de rayonnement des sondes 2D parcimonieuses au sein d'un algorithme d'optimisation de recuit simulé. Les avantages de cette intégration de simulations réaliste dans un processus d'optimisation sont illustrés à travers une étude montrant une meilleure distinction de configuration de sondes, mais aussi à travers les nouveaux degrés de liberté (taille, forme, orientation, signal d'excitation, réponse impulsionnelle) qui peuvent être pris en compte dans un cadre général d'optimisation des sondes 2D parcimonieuses qui a été mis en place dans un second temps. Le processus d'optimisation peut explorer des solutions qui dont le comportent se rapproche de celui qu'auraient des sondes testées physiquement.

III Chapitre III Optimisation multi-profondeurs du rayonnement acoustique de sondes 2D non-régulières parcimonieuses.

Dans ce chapitre il est question d'optimiser la définition de sondes 2D non-régulières parcimonieuses grâce au libre déplacement des éléments sur la surface de l'ouverture. Une nouvelle contribution réside dans la prise en compte du rayonnement acoustique à plusieurs profondeurs permettant de définir des fonctions d'énergies multi-profondeurs. Les propriétés de stratégie d'optimisation proposée sont illustrées sur la Figure 25.

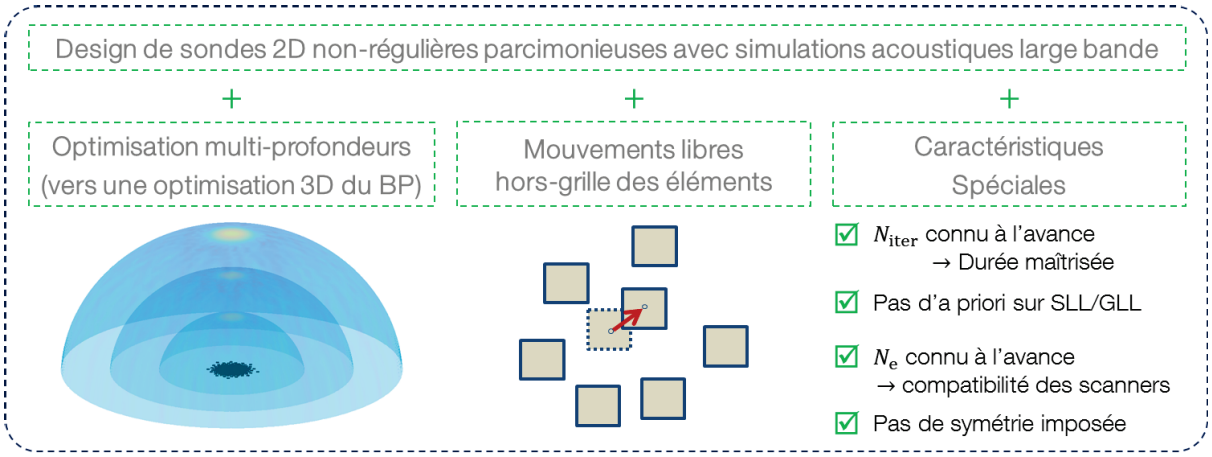
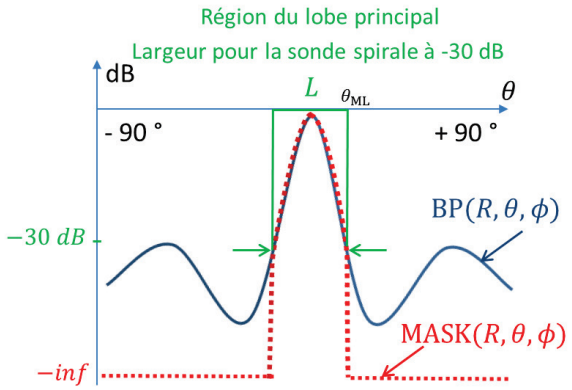


Figure 72 Stratégie proposée pour l'optimisation des sondes 2D non-régulière parcimonieuses: simulations acoustiques large bande, fonction d'énergie multi-profondeur et mouvements libres hors-grille des éléments. Le nombre d'itérations et le nombre d'éléments actifs sont connus à l'avance ce qui permet de maîtriser la durée de l'optimisation et d'assurer la compatibilité avec les échographes. Enfin aucune symétrie n'est imposée et le niveau des lobes latéraux n'a pas besoin d'être prédit (l'objectif est le niveau le plus bas atteignable).

III.A Paramétrage de l'optimisation et définition des fonctions d'énergie multi-profondeur

Dans cette étude l'espace d'état est l'ensemble des sondes 2D non-régulière parcimonieuses dont les N_e = 256 éléments ne se chevauchent pas à l'intérieur d'un disque de rayon r_p centré en (0,0,0). Le mécanisme de communication est défini de telle sorte que les transitions $S \to \tilde{S}$ correspondent à une translation d'un unique élément. Trois fonctions d'énergie $U_{1,R}(S_n)$, $U_{2,R}(S_n)$ et $U_{3,R}(S_n)$ sont définies (Figure 73) à partir de la mesure du rayonnement acoustique d'une sonde spirale prise comme référence (Ramalli et al. 2015). Pour chacune de ces trois fonctions d'énergie deux configurations sont calculées : une première configuration en ne considérant que le rayonnement acoustique à la profondeur focale de 40 mm (1HS) et une deuxième configuration où le rayonnement acoustique est considéré aux trois profondeurs (3HS) de 15 mm, 25 mm et 35 mm (Figure 74). Dans le deuxième cas (multi-profondeurs) les valeurs de fonction d'énergie obtenues à chaque profondeur sont sommées. Les paramètres suivants sont communs à toutes les optimisations étudiées ici: le nombre d'éléments actifs N_e = 256, la fréquence centrale f_c = 7 MHz (bande passante 72 %), le rayon maximal d'ouverture $r_p = 6\,\text{mm} \sim 30\lambda$, la taille des éléments

(carrés) 200 µm ~ λ (comme la sonde spirale de référence). Le poids de chaque élément est fixé à 1 (pas d'apodisation) pour maximiser la sensibilité des sondes.



$$U_{1,R} = \left(\max_{(\theta,\phi)\notin L}\left(\mathrm{BP}(R,\theta,\phi)\right)\right)^2$$

$$U_{2,R} = U_{1,R}\left(\frac{\iint_{(\theta,\phi)\notin L}\mathrm{BP}(R,\theta,\phi)}{\iint_{(\theta,\phi)\in L}\mathrm{BP}(R,\theta,\phi)}\right)^2$$

$$U_{3,R} = \left(M_+(R)\left(\frac{\iint_{(\theta,\phi)\notin L}\mathrm{BP}(R,\theta,\phi)}{\iint_{(\theta,\phi)\in L}\mathrm{BP}(R,\theta,\phi)}\right)\right)^2$$

with $M_+ = \max(\mathrm{BP} > \mathrm{MASK})$

Figure 73 Les trois fonctions d'énergie proposées $U_{1,R}$, $U_{2,R}$ et $U_{3,R}$ sont toutes définies à partir du rayonnement acoustique $\mathrm{BP}(R,\theta,\phi)$ et en considérant la largeur à - 30 dB du faisceau de la sonde spirale (référence) comme la région du lobe principal L. En particulier $U_{3,R}$ forme le lobe principal en utilisant un masque sculptant (MASK).

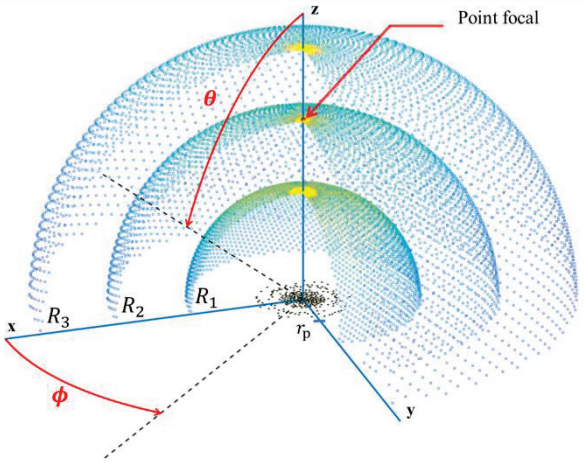


Figure 74 Système de coordonnées pour les trois hémisphères de rayon R_1, R_2 et R_3, sur chacun desquels sont disposés N_{PMP} points de mesure de pression (PMP). Les hémisphère sont centrés sur la sonde 2D parcimonieuse de rayon d'ouverture r_p.
Le point focal est sur l'axe z à la profondeur z =R_2.

III.B Sondes non-régulières optimisées et comparaison avec une sonde spirale

Les configurations obtenues[40] avec les trois fonctions d'énergie $U_{1,R}(S_n)$, $U_{2,R}(S_n)$ et $U_{3,R}(S_n)$ dans chacun des cas 1HS et 3HS sont représentées sur la Figure 75. Le profil de leur rayonnement acoustique aux trois profondeurs de 15 mm, 25 mm et 35 mm est tracé sur la Figure 76 (cas sans dépointage en haut, cas avec dépointage de 30 ° en bas). L'étude complète compare les résultats de seize optimisations pour identifier l'impact du nombre d'itération, du nombre de points de mesure de pression, du nombre d'hémisphères et de la définition de la fonction d'énergie. Les critères de comparaison sont basés sur des simulations de champ de pression 3D et ils sont évalués pour 81 angles de dépointage du faisceau allant de - 32 ° à + 32 ° (Figure 31).

[40] Les vidéos du déroulement des optimisations sont disponibles en ligne sur https://www.creatis.insa-lyon.fr/site7/en/roux.

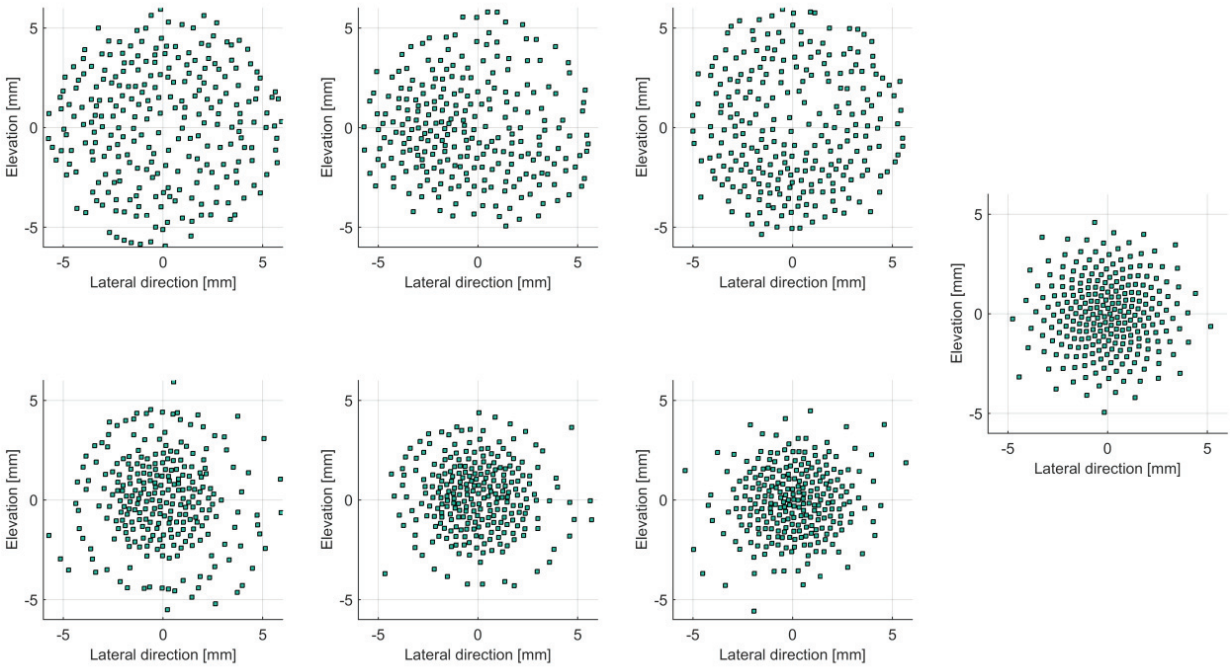


Figure 75 Configuration des sondes optimales obtenues en utilisant un seul hémisphère (en haut, de gauche à droite: U_1 1HS U_2 1HS, U_3 1HS) et en utilisant trois hémisphères (en bas, de gauche à droite: U_1 3HS, U_2 3HS, U_3 3HS). La configuration de la sonde spirale de référence est représentée à droite.

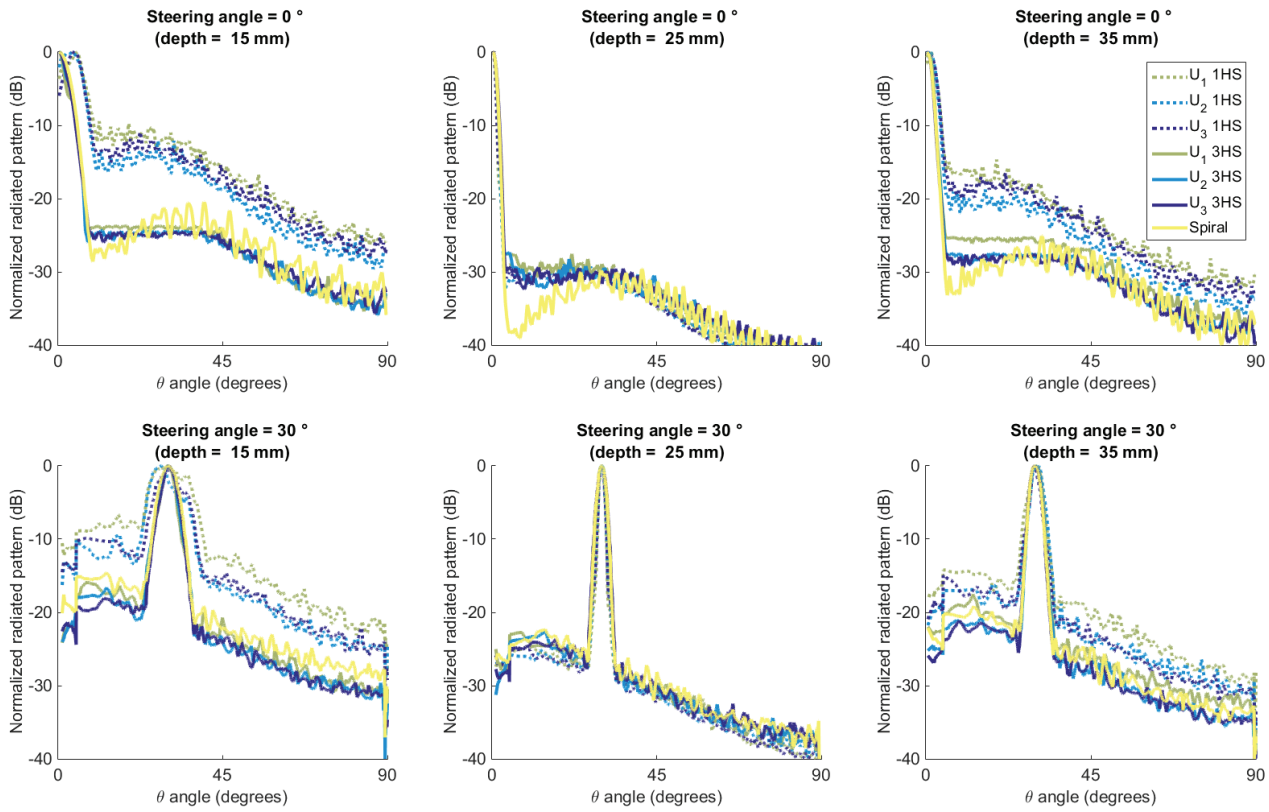


Figure 76 Profils de rayonnement acoustique des sondes optimisées et de la sonde spirale de référence évalués aux profondeurs 15 mm (gauche), 25 mm (centre) et 35 mm (droite). L'angle de dépointage du faisceau est de 0° en haut et de 30 ° en bas.

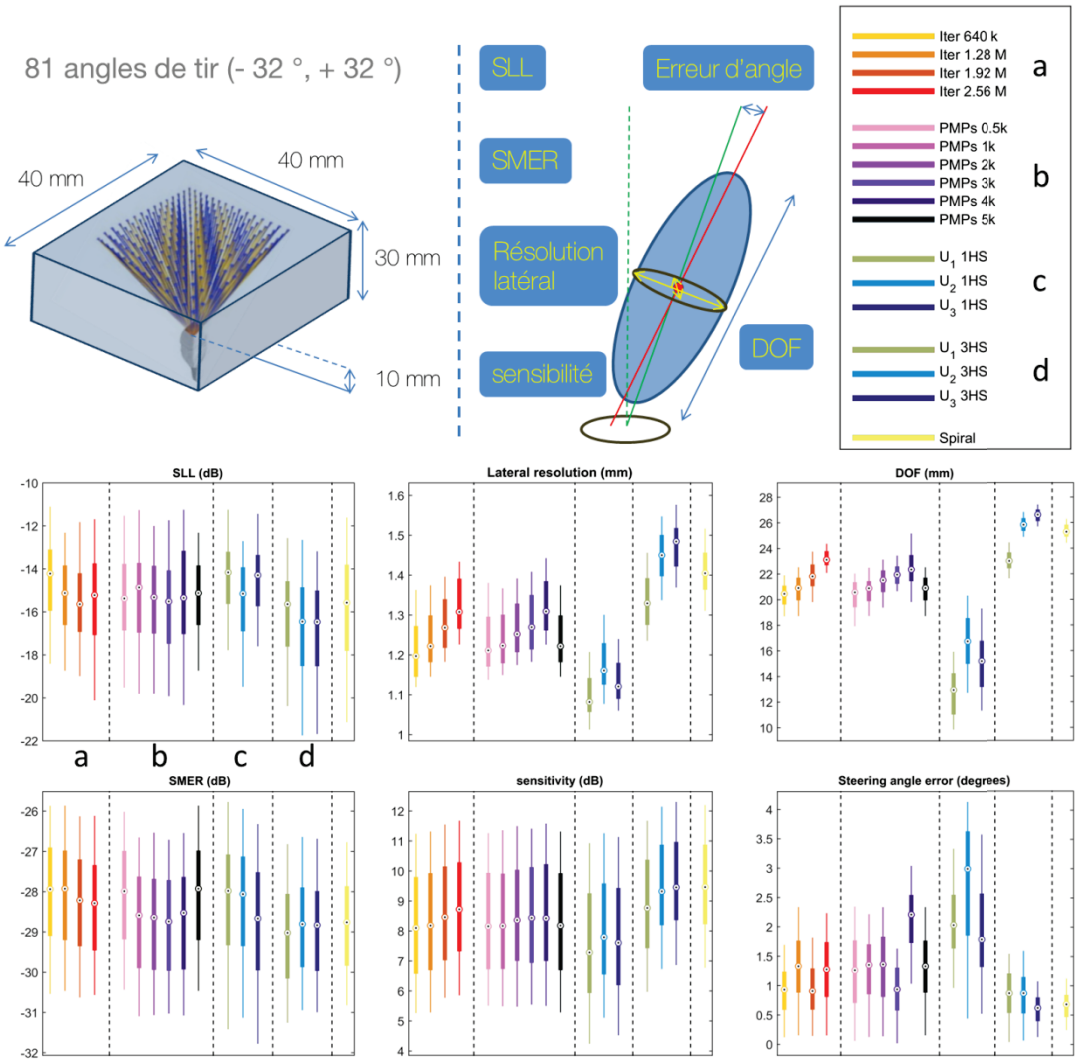


Figure 77 Analyses des performances acoustiques à partir des simulations de champ de pression 3D réalisées pour 81 angles de dépointage pour chaque configuration de sonde. La taille du volume simulé est de 40x40x30 mm^3 et il démarre à z = 10 mm au-dessus de la sonde.

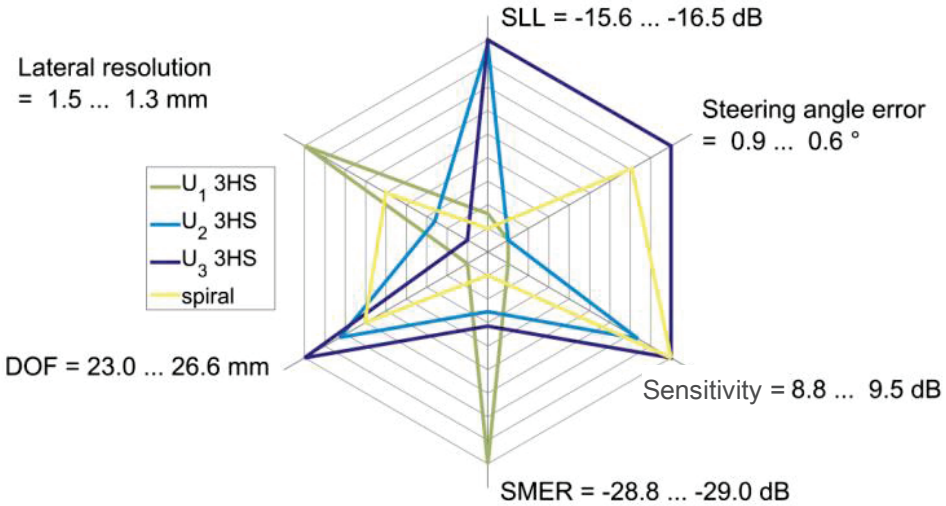


Figure 78 Diagramme de comparaison entre U_1 3HS, U_2 3HS, U_3 3HS et la sonde spirale de référence. Pour chaque critère, la meilleure performance se situe à la périphérie du diagramme.

La configuration optimale obtenue avec la fonction d'énergie $U_{3,R}(S_n)$ aux trois profondeurs (U_3 3HS) est légèrement plus performante que la sonde spirale (Figure 28). Il est montré que le masque utilisé pour sculpter le faisceau principal à plusieurs profondeurs donne lieu à des configurations à symétrie circulaire sans imposer de contraintes géométriques autre que le rayon de l'ouverture et la non superposition des éléments entre eux. Les performances de U_3 3HS sont représentées sur la Figure 32.

La problématique de la définition des sondes 2D parcimonieuses non-régulières a été adressée en introduisant de nouvelles fonctions d'énergie multi-profondeur au sein d'un algorithme d'optimisation de recuit simulé. A chaque itération un élément de la configuration testée peut être translaté sur la surface de l'ouverture et le nouveau diagramme de rayonnement associé est calculé immédiatement. Les résultats montrent un meilleur contrôle du comportement du champ de pression lorsque le rayonnement acoustique est considéré à plusieurs profondeurs pendant l'optimisation. Des performances similaires à celles de la sonde spirale de référence ont également été atteintes.

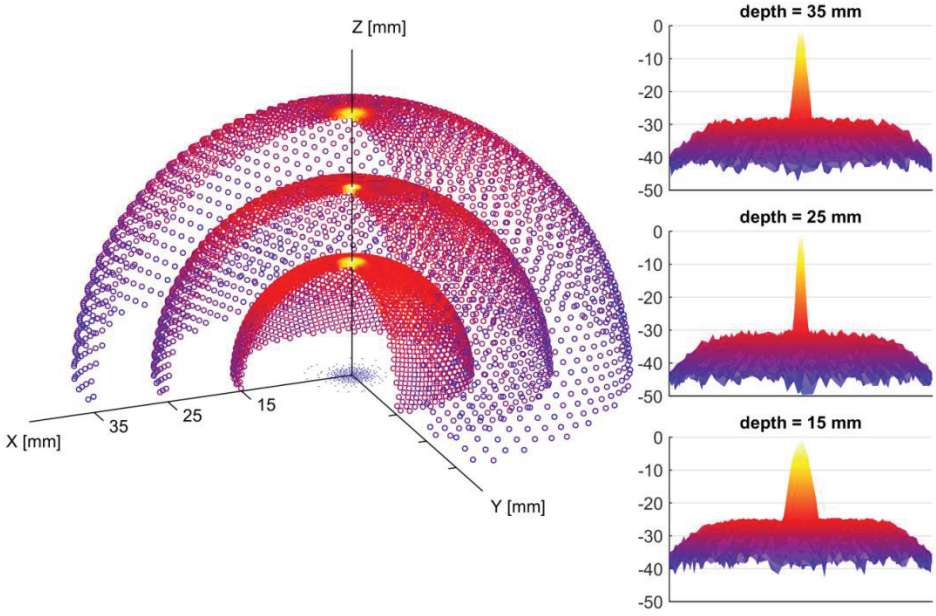


Figure 79 Illustration des performances de la sonde non régulière U_3 3HS obtenue en optimisation le rayonnement acoustique aux trois profondeurs de 15 mm, 25 mm et 35 mm (focalisation à F = 25 mm) et en sculptant le lobe principal avec un masque.

IV Chapitre IV Optimisation large bande de la définition de sondes 2D régulières parcimonieuses avec contraintes de fabrication

IV.A Paramétrage de l'optimisation et de la fonction d'énergie multi-profondeur (avec interface graphique)

Dans ce chapitre, il est question de l'optimisation des sondes 2D régulières parcimonieuses par un algorithme de recuit simulé intégrant des simulations acoustiques large bande. De plus, les configurations de sondes parcimonieuses optimales tiennent compte de contraintes de fabrication sur l'agencement des éléments. L'approche proposée est illustrée par un exemple d'optimisation où le but est de trouver la meilleure sélection de 128, 192 et 256 éléments (désignées par opti128, opti192 et opti256 respectivement) à activer parmi les 1024 éléments d'une sonde régulière 32x32 fonctionnant à 3 MHz (Figure 80).

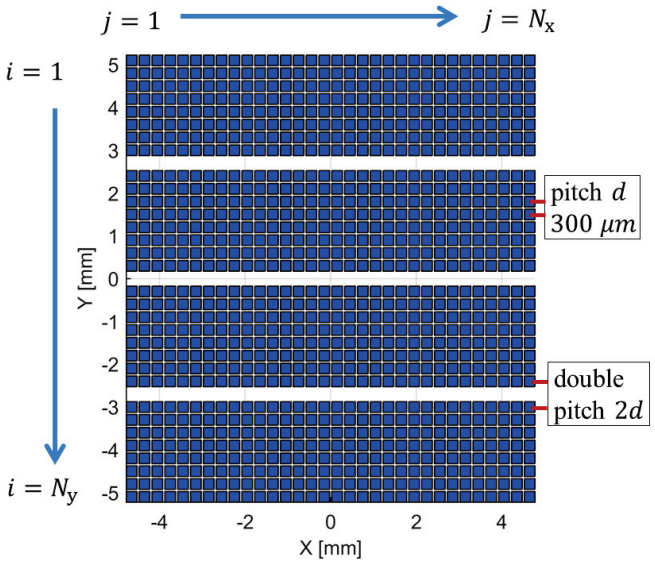


Figure 80 Agencement des éléments de la sonde régulière 2D de 32×32 éléments (ref1024) avec double pitch entre les lignes 8-9, 16-17 et 24-25 pour faciliter les connections électroniques (Jean Provost et al. 2014).

Dans la sonde de 1024 éléments (ref1024) le pitch (distance inter éléments) est doublé entre les lignes 8-9, 16-17 et 24-25 pour faciliter les connections électriques comme décrit dans (Jean Provost et al. 2014). La sonde ref1024 ainsi qu'une sonde de 716 éléments (ref716), obtenue par simple désactivation des coins de ref1024, sont considérées comme références dans cette étude. Les sondes optimales sont également comparées avec la meilleure configuration « aléatoire » (rand256) obtenue en maintenant la température du recuit simulé à l'infini tout au long de l'exploration. L'optimisation se déroule en tenant compte du rayonnement acoustique à trois profondeurs : 30 mm, 40 mm (profondeur focale) et 50 mm. Une nouvelle fonction d'énergie multi-profondeur est présentée ainsi qu'une interface graphique dédiée qui aide à la définition du masque sculptant dans la fonction d'énergie (Figure 81).

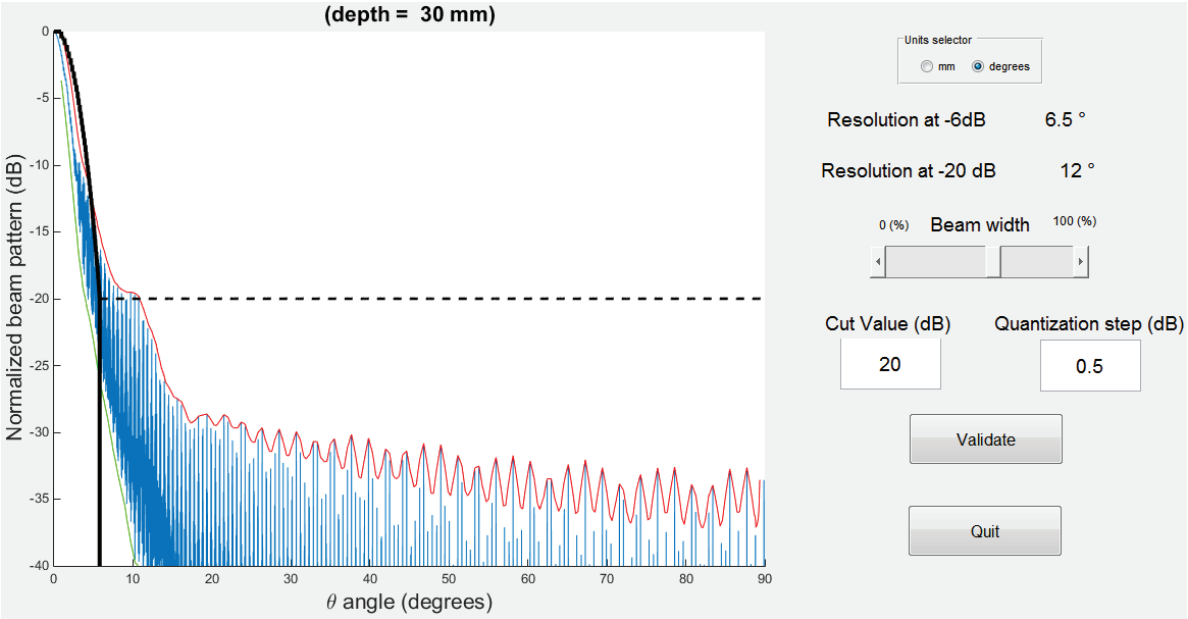


Figure 81 Impression d'écran de l'interface graphique utilisateur dédiée à la définition du masque sculptant dans la fonction d'énergie. Le profil du rayonnement acoustique (BP) le la sonde ref1024 est tracé en bleu (rouge enveloppe du maximum de pression, vert minimum de pression). La contrainte de largeur du lobe principal, la valeur de coupure $C(R)$ (tirets noirs) et le pas de quantification q_{mask} sont ajustables de manière interactive pour définir la forme du masque sculptant (trait plein noir) et ce à chaque profondeur où le rayonnement acoustique est pris en compte dans l'optimisation.

IV.B Performances des sondes optimisées

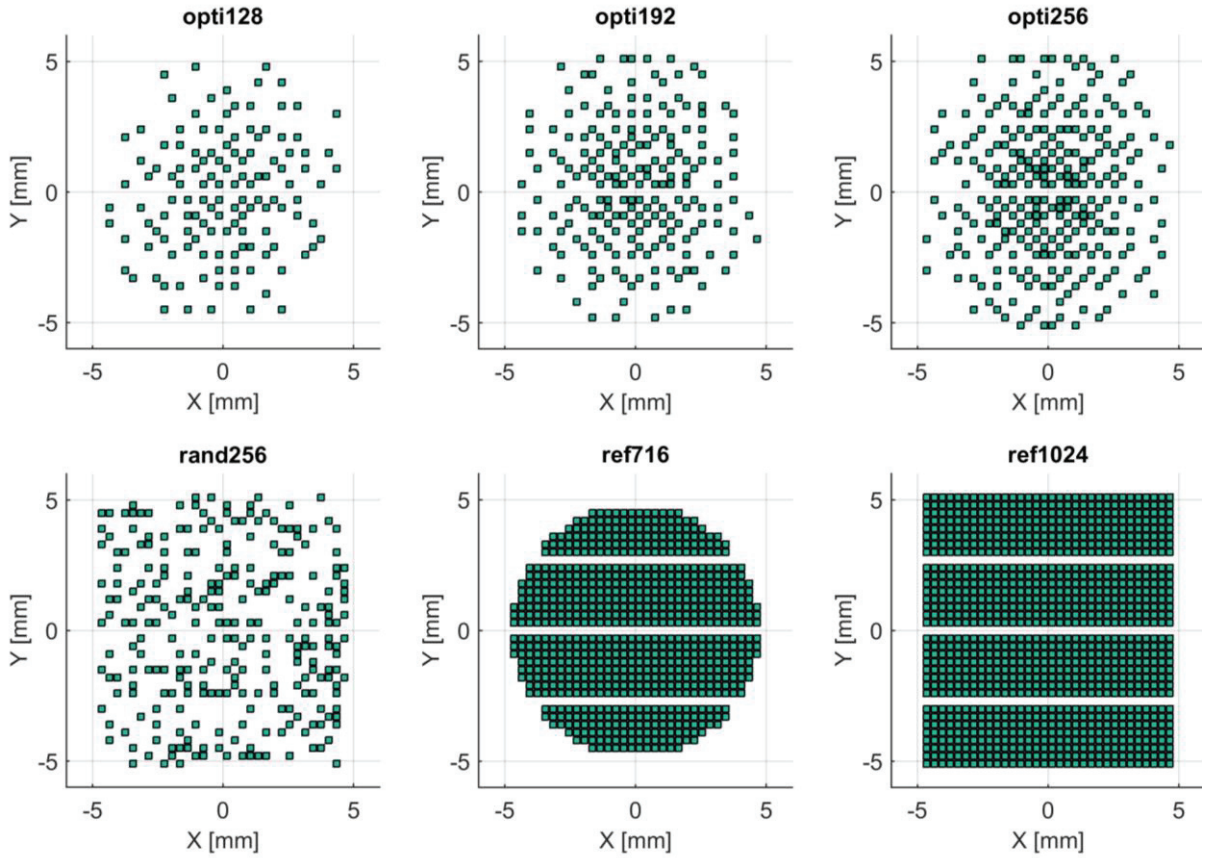


Figure 82 Configuration des sondes optimales opti128, opti192, opti256, de la « meilleure » sonde aléatoire rand256 et des deux références ref716 et ref1024. La suppression des éléments des coins de opti128, opti192 et opti256 est spontanée alors qu'elle est imposée pour ref716.

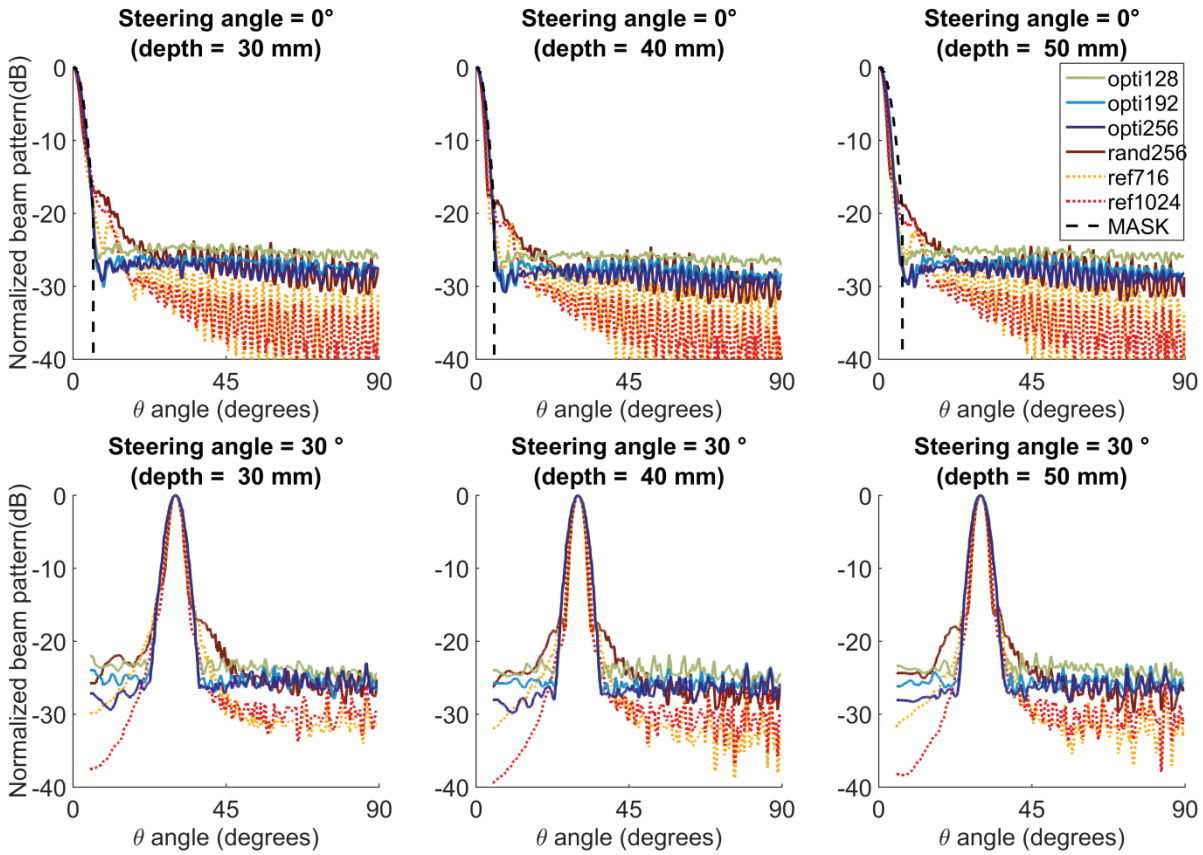


Figure 83 Profils de rayonnement (enveloppe supérieure) aux profondeurs de 30 mm (gauche), 40 mm (centre) et 50 mm (droite) des sondes optimisées, de la sonde aléatoire rand256 et des sondes de références ref716 et ref1024. Le masque de contraintes (MASK) est tracé en tirets noirs. L'angle de dépointage du faisceau est de 0 ° en haut du graphique et de 30 ° en bas du graphique.

Les configurations obtenues sont représentées sur la Figure 82. Elles sont comparées en termes de niveau de lobes latéraux et de résolution à partir de leur profil de rayonnement acoustique aux profondeurs de 30 mm, 40 mm et 50 mm (Figure 83). De plus des simulations de champ de pression en 3D permettent d'évaluer si les performances acoustiques sont homogènes lorsque l'angle de tir (dépointage du faisceau) varie de – 32 ° à + 32 ° (Figure 86). Les images 3D en coupes XZ et YZ d'un fantôme de résolution et d'un fantôme de contraste ont été simulées pour caractériser la capacité des sondes optimisées à produire des images ultrasonores 3D (Figure 87 et Figure 88). La robustesse des résultats a été testée en comparant 10 résultats « clones » obtenus à partir de la même expérimentation mais en partant d'une sonde initiale différente à chaque fois (Figure 89 et Figure 90).

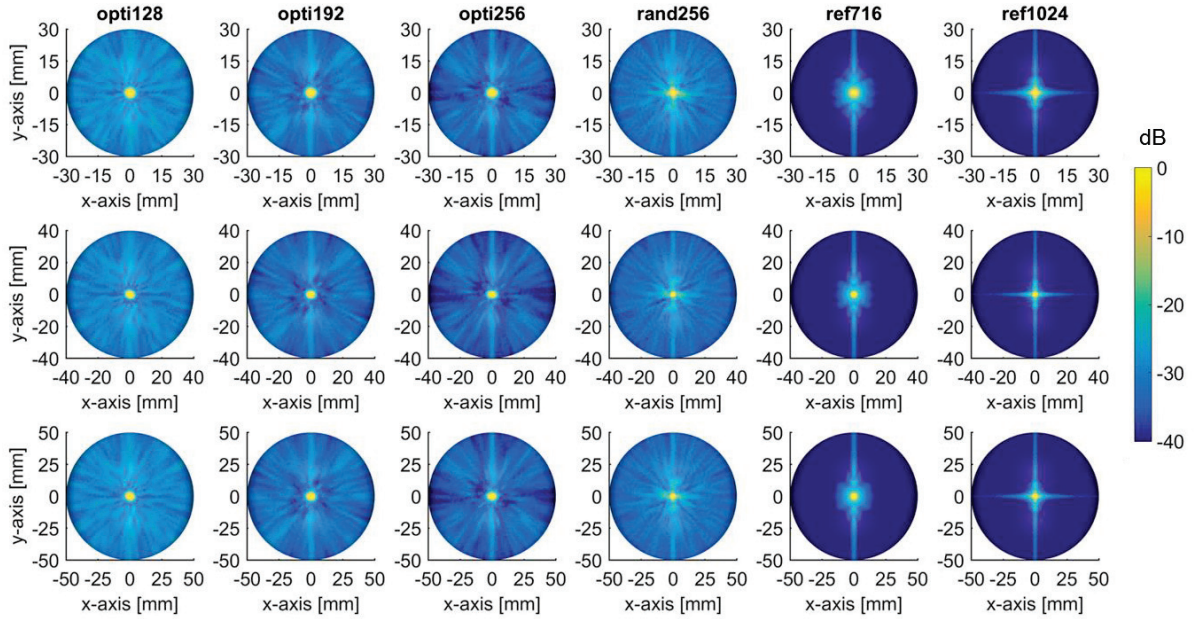


Figure 84 Rayonnement acoustique BP des sondes optimisées, de la sonde aléatoire rand256 et des sondes de référence. Les BP sont évalués au niveau de trois hémisphères situés à 30 mm, 40 mm et 50 mm de profondeur (dépointage de 0 °).

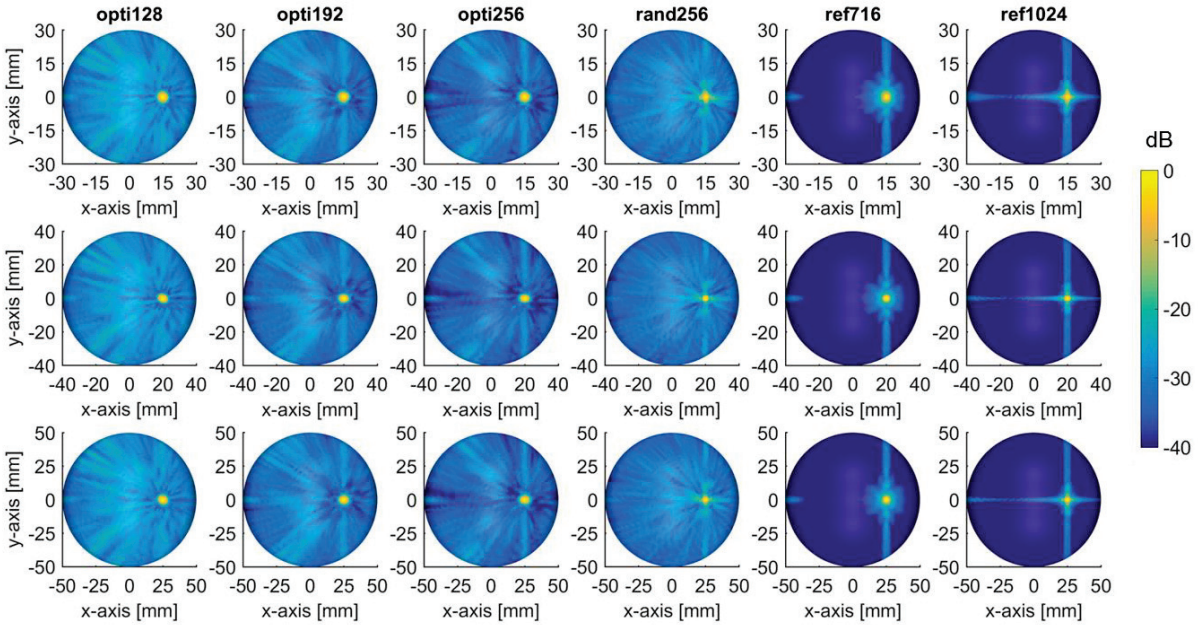


Figure 85 Rayonnement acoustique BP des sondes optimisées, de la sonde aléatoire rand256 et des sondes de référence. Les BP sont évalués au niveau de trois hémisphères situés à 30 mm, 40 mm et 50 mm de profondeur (dépointage de 30 °).

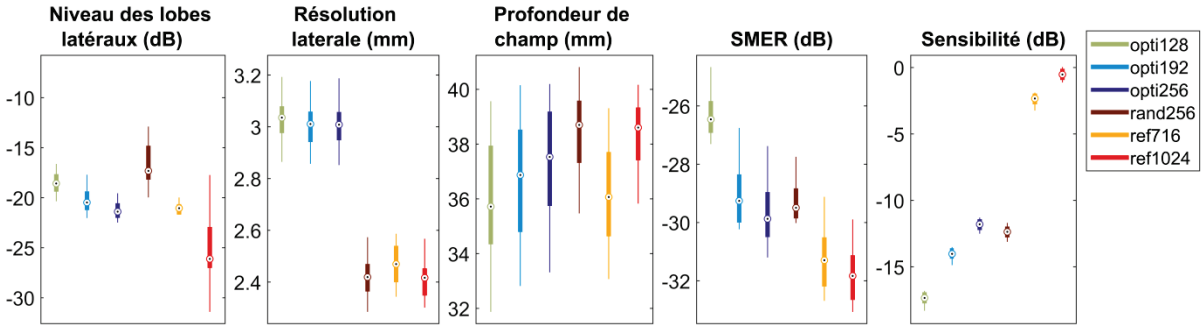


Figure 86 Analyse des BP 3D (statistiques sur 81 angles de dépointage). Les moustaches des boites s'étende jusqu'aux valeurs adjacentes qui sont les valeurs extrêmes non aberrantes.
Les valeurs considérées comme aberrantes sont celles au-delà d'une couverture à 99.3 % (distribution normale).

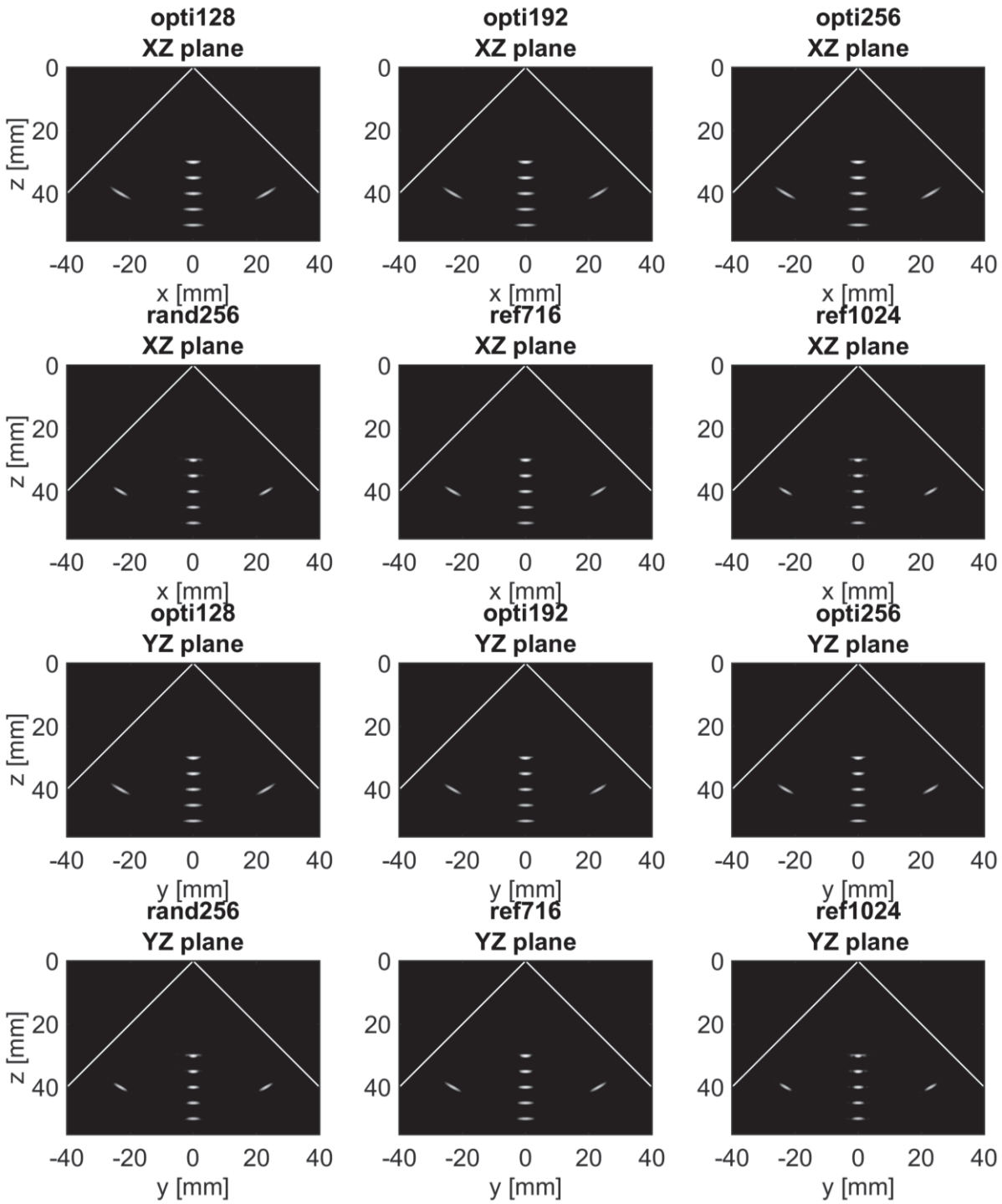


Figure 87 Images 3D de résolution (plan XZ sur les deux premières lignes et plan YZ sur les deux dernières lignes) d'un fantôme contenant 9 diffuseurs: 5 diffuseurs équidistants le long de l'axe z entre 30 mm à 50 mm de profondeur et 2 diffuseurs sur les côtés de chacun des plans XZ et YZ. La dimension latérale des diffuseurs (mesurée at – 6dB) est une conséquence de la largeur du lobe principal dans le BP. Les artefacts autour des zones centrales plus lumineuses de chaque point sont les conséquences des lobes latéraux du BP (particulièrement visible pour rand256 et ref1024). La dynamique des images est de 40 dB.

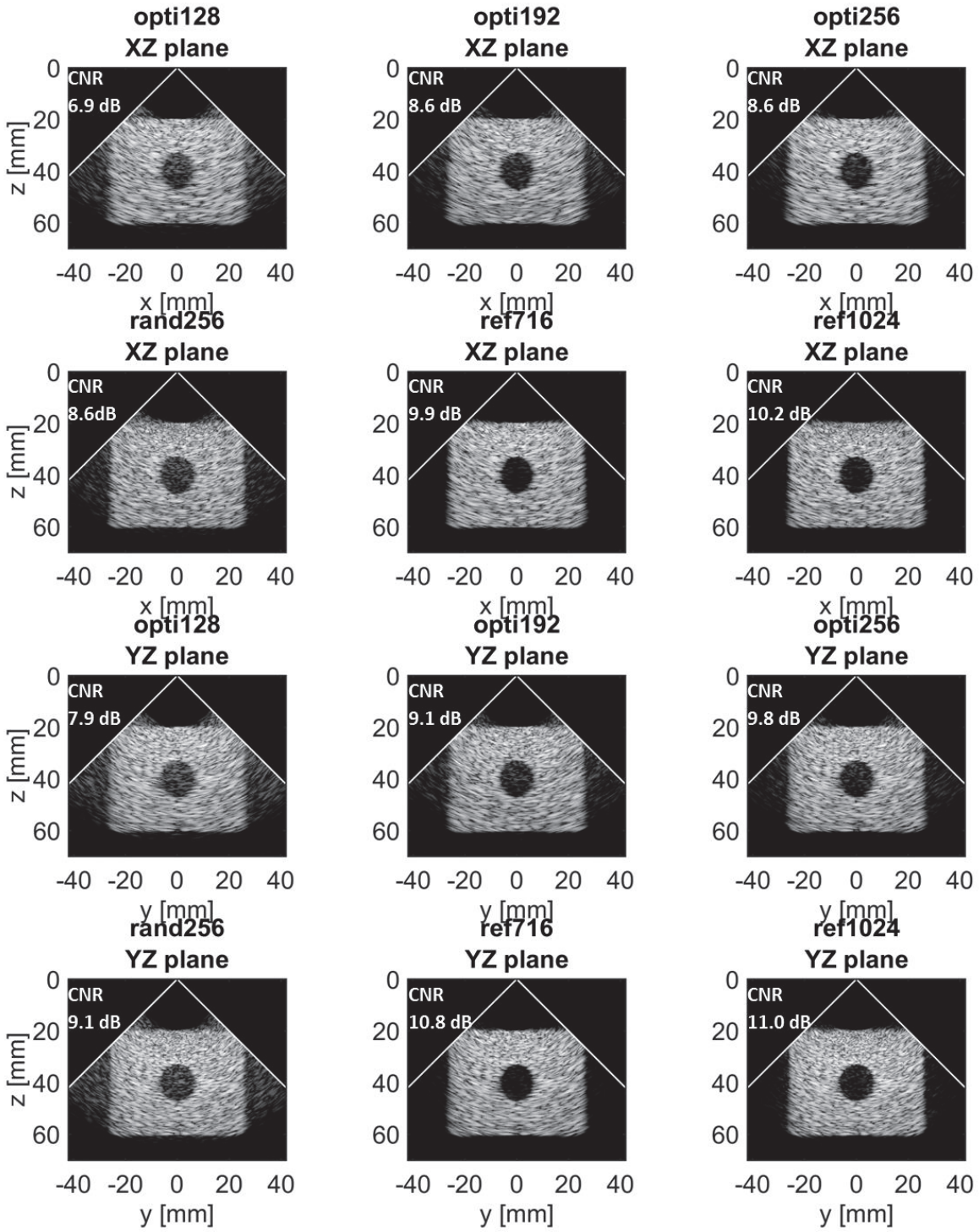


Figure 88 Images 3D de contraste (plan XZ sur les deux premières lignes et plan YZ sur les deux dernières lignes) d'un fantôme de kyste de rayon 7.5 mm localisé à 40 mm de profondeur. La dynamique des images est de 40 dB.

TABLE XV RÉSOLUTION LATÉRALE À - 6 DB ET RAPPORT DE CONTRASTE (CNR) DES IMAGES 3D (SIMULATIONS) POUR CHAQUE SONDE OPTIMALE ET LES RÉFÉRENCES. LES MEILLEURES PERFORMANCES DANS CHAQUE COLONNE SONT MISES EN ÉVIDENCE EN VERT.

	Résolution à - 6 dB (mm) (moyenne sur les 5 diffuseurs)		CNR (dB) Kyste (z = 40 mm, r = 7,5 mm)	
	XZ	YZ	XZ	YZ
opti128	2.3	2.3	6.9	7.9
opti192	2.4	2.1	8.6	9.1
opti256	2.5	1.9	8.6	9.8
rand256	1.8	1.8	8.6	9.1
ref716	2.3	2.3	9.9	10.8
ref1024	1.7	1.4	10.2	11.0

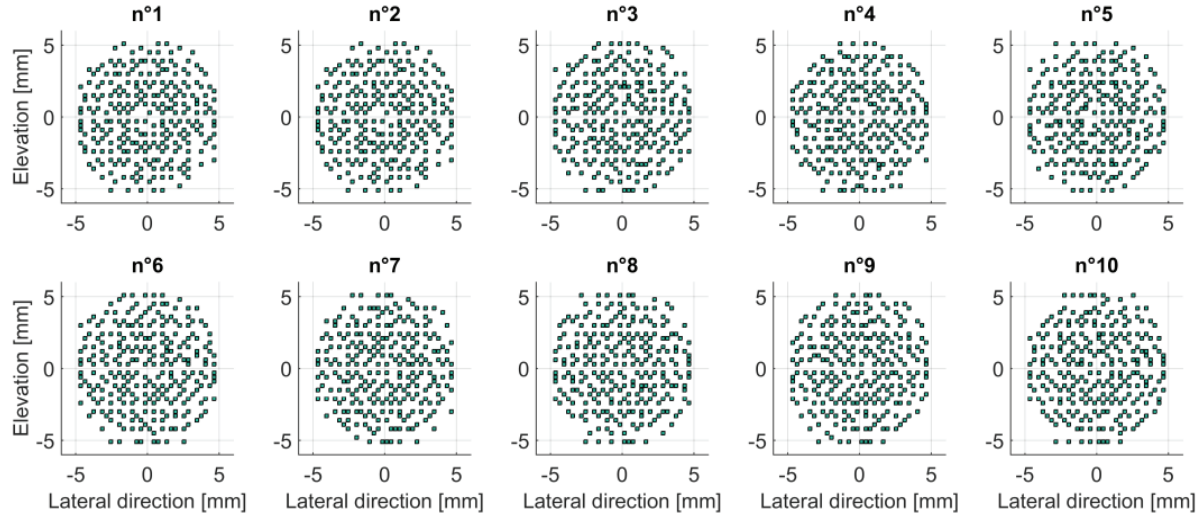


Figure 89 Configurations finales des dix optimisations « clones » obtenues avec la même configuration d'optimisation mais à partir de sondes initiales différentes.

TABLE XVI VALEURS DE LA FONCTION D'ÉNERGIE ASSOCIÉES AUX DIX SONDES « CLONES » OBTENUES AVEC LA MÊME CONFIGURATION D'OPTIMISATION MAIS À PARTIR DE SONDES INITIALES DIFFÉRENTES.

Clone	n°1	n°2	n°3	n°4	n°5	n°6	n°7	n°8	n°9	n°10
U ($\times 10^6$)	111.5	111.5	108.2	113.7	113.9	110.3	109.5	111.1	108.3	111.4

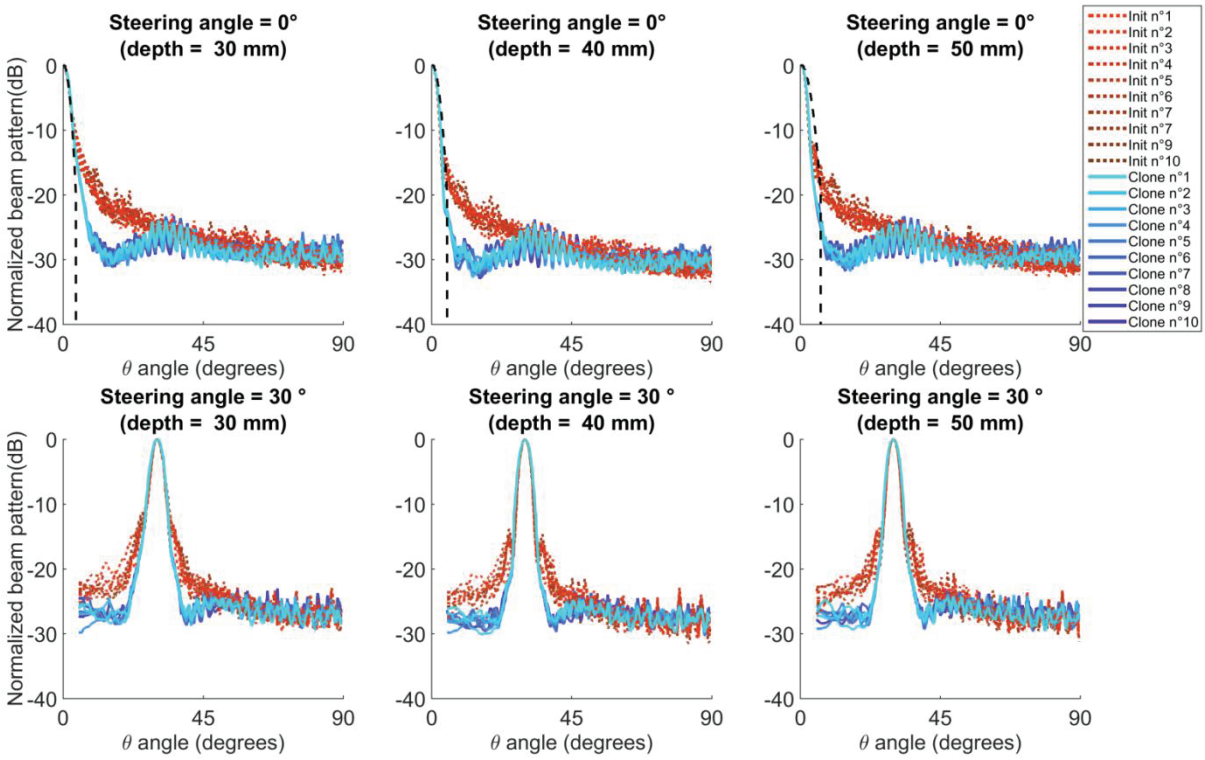


Figure 90 Profils de rayonnement (enveloppe supérieure) aux profondeurs de 30 mm (gauche), 40 mm (centre) et 50 mm (droite) des dix optimisations « clones ». Le masque de contraintes (MASK) est tracé en tirets noirs. L'angle de dépointage du faisceau est de 0 ° en haut du graphique et de 30 ° en bas du graphique.

L'agencement des éléments des sondes optimisées (opti128, opti192 et opti256) ne respectent pas de motif périodique mais une symétrie circulaire semble apparaître (Figure 82). Le confinement des éléments à l'intérieur d'une forme circulaire n'a pas été forcé puisque les éléments des coins se sont désactivés spontanément au cours de l'optimisation. A partir de la Figure 76 il est possible d'analyser la qualité des diagrammes de rayonnement (BP) et de comparer les sondes optimisées avec la sonde aléatoire rand256 et les références ref716 et ref1024. Tout d'abord, les BP de toutes les sondes optimisées respectent les contraintes du masque sculptant. Le lobe principal de leurs BP est suivi d'un plateau (sans lobes de réseau) à niveau relativement constant et ce aux trois profondeurs de 30 mm, 40 mm et 50 mm. Les BP de rand256, ref716 et ref1024 présentent de hauts lobes latéraux par rapport aux sondes optimisées (environ 10 dB au-dessus). En revanche au-delà de θ = 20 ° le niveau moyen du BP décroit plus fortement pour les sondes de référence. Cette comparaison est également valable lorsqu'un angle de dépointage du faisceau de 30 ° est appliqué (Figure 83, bas). Une représentation des BP « vus de dessus » (sans dépointage du faisceau sur la Figure 84 et avec dépointage du faisceau sur la Figure 85) donne une meilleure idée de la répartition des lobes latéraux pour chacune des sondes comparées.

Au niveau des performances évaluées sur les champs de pression 3D (Figure 86), la tendance générale est que plus le nombre d'éléments actifs est grand et meilleure sont les performances. En termes de SLL la meilleure performance est atteinte par la référence ref1024 suivit par la sonde optimisée opti256 qui est légèrement meilleure que la ref716. En revanche la résolution latérale des sondes optimisées est en moyenne 0.6 mm plus grossière que celle des sondes de références et de la sonde aléatoire rand256. La finesse en résolution est directement liée à la dimension de la surface active de l'ouverture qui est plus grande pour rand256, ref716 et ref1024. La profondeur de champ la plus longue est obtenue avec opti256. L'analyse du SMER montre que la configuration opti192 est également très performante et l'analyse de la sensibilité est en accord avec le fait qu'elle augmente d'environ 6 dB lorsque la surface active double.

Au niveau des simulations d'images 3D, les performances en résolution (Figure 87) des sondes optimisées sont très similaires avec une résolution moyenne de 2.4 mm. Quant aux images de contraste (Figure 88) on voit que les performances des sondes optimisées s'améliorent avec le nombre d'éléments actifs. Les meilleures performances sont obtenues avec la sonde de référence ref1024 à la fois en résolution et en contraste.

La comparaison de l'agencement des éléments des dix configurations « clones » (Figure 89), ainsi que la comparaison de leurs BP par rapport aux BP des dix sondes initiales différentes (Figure 90), montrent la robustesse des résultats obtenus et la reproductibilité des expériences d'optimisation.

Enfin l'étude de la sonde rand256 obtenue avec l'expérience de recherche aléatoire (température infinie) met en évidence l'importance de la séquence de refroidissement pour garantir que les configurations explorées convergent vers une solution qui satisfasse au mieux les contraintes imposées par la fonction d'énergie. Enfin la possibilité d'intégrer des contraintes de fabrications dans le processus d'optimisation des sondes offre un nouvel outil aux fabricants de sondes pour les guider parmi plusieurs choix technologiques.

V Discussion générale: limites et perspectives

V.A Le manque d'images expérimentales 3D et de prototype de sonde optimale.

Une des limitations les plus critiques de ce travail est le manque d'acquisition et de reconstruction d'images expérimentales 3D satisfaisantes. En outre, il n'a pas été réalisé de prototype de sondes à partir des configurations optimales obtenues. Toutefois, quelques expérimentations d'acquisition d'images 3D ont été faites avec l'aide de Lorena Petrusca (Post-Doc à CREATIS). en utilisant la sonde 32x32 (ref1024) décrite dans le chapitre IV. Seulement un quart de la sonde pouvait être contrôlée en utilisant les 256 canaux d'un échographe Verasonics mais il était prévu de synchroniser quatre systèmes Verasonics pour piloter indépendamment l'ensemble des 1024 éléments. Malheureusement, les expérimentations n'ont pas abouti à des acquisitions d'images 3D satisfaisantes dans le temps imparti.

V.B L'espace d'état et les simulations acoustiques

L'espace d'état des solutions qui sont explorées pendant l'optimisation est intrinsèquement lié au paramètres qui peuvent être pris en compte dans le simulateur acoustique. Par exemple, une limitation de FIELD II, qui est utilisé dans ce travail, est que la propagation des ondes est supposée linéaire. L'extension à un modèle plus complexe qui tiendrait compte des interfaces électromécaniques (par exemple en considérant les matériaux impliqués dans la transduction), serait possible en utilisant un simulateur multi-physique mais cela demanderait sans doute une implémentation spécifique pour faire face à la puissance de calcul nécessaire. Une façon de faire mieux correspondre l'approche proposée avec la réalité physique serait par exemple de mesurer la réponse impulsionnelle de tous les éléments de la sonde ref1024 et de les intégrer dans les simulations effectuées pendant l'optimisation. Ceci permettrait de pénaliser les éléments ayant une mauvaise réponse impulsionnelle (éléments défectueux) afin qu'ils ne soient pas connectés dans la sonde optimale. En suivant cette même idée, il serait même possible d'enlever directement ces éléments des candidats potentiels. La prise en compte de la réponse impulsionnelle physiquement mesurée garantie une meilleure adéquation entre les simulations calculée pendant l'optimisation et la mesure qui sera effectuée après application du schéma de connexion optimal.

V.C La fonction d'énergie

Il est possible d'attribuer un poids différent à chaque hémisphère où le BP est calculé, autrement dit la fonction d'énergie pourrait favoriser les solutions atteignant prioritairement les objectifs fixés à une certaine profondeur (par exemple la profondeur focale). Il est également envisageable d'ajouter plusieurs hémisphère ou même directement de baser la fonction d'énergie sur la simulation d'un BP 3D. Mais la sculpture d'un champ de pression 3D requière le positionnement de points de mesure dans l'intégralité du volume à imager et non plus seulement sur les hémisphères. L'implémentation d'une fonction d'énergie basée sur le BP 3D peut donc s'avérer très lourde en puissance de calcul nécessaire, exigeant une implémentation GPU.

V.D Le temps de calcul

Trois années de calcul ont été réduites à deux semaines. C'est l'exact facteur d'accélération qui a été atteint pour obtenir les sondes optimales présentées au chapitre III. De manière plus générale l'ensemble des optimisations ont pu être obtenue grâce à l'utilisation du cluster de calcul du laboratoire CREATIS[41]. L'intervalle des temps de calculs nécessaires s'étend de deux jours à cinq semaines selon le paramétrage de l'optimisation (particulièrement le nombre et position des PMP, le nombre d'éléments actifs, et le nombre d'itérations) et de la capacité des machines disponibles sur le cluster. Ce sont des durées acceptables qui peuvent s'intégrer dans le planning de conception complet d'une sonde échographique d'autant plus que l'interface graphique dédiée qui a été développée réduit de manière significative le temps nécessaire à adapter les contraintes acoustiques en fonction de l'application visée.

Mais pourquoi est-il nécessaire de réduire le temps de calcul des simulations acoustiques ? Est-ce simplement pour obtenir les résultats plus rapidement ? Un intérêt plus raffiné est celui d'augmenter la probabilité d'obtenir une solution correspondant au minimum global de la fonction d'énergie. En effet, dans un même intervalle de temps, plus le nombre d'itération est grand et plus la température peut décroitre lentement ce qui augmente la probabilité de rejoindre une solution globalement optimale. Par ailleurs, il a été mis en place une méthode systématique permettant de contrôler l'état d'avancement d'une optimisation à chaque instant. Cette méthode est décrite en annexe I. De plus, en cas de coupure d'électricité ou de mise à jour inattendue, le cluster pouvait être amené à redémarrer sans pour autant relancer les calculs en cours au moment de l'interruption. L'implémentation d'une suite de scripts dédiés à gérer cette situation « d'après interruption » a permis de relancer les calculs à partir de la dernière itération sauvegardée (l'intervalle des sauvegardes régulières est réglable).

V.E Continuation stochastique et modulation continue

Dans ce travail, l'algorithme de recuit simulé était « fixé » au sens que ni la fonction d'énergie et ni le mécanisme de communication n'évoluait au cours de l'optimisation. Malgré cette définition « statique » de l'algorithme, les vidéos présentant le déroulement des optimisations permettent d'illustrer que la définition d'une sonde peut être vu comme un processus dynamique[42] plutôt qu'une solution absolue donnée par un motif prédéterminé. Une description détaillée du contenu affiché sur les vidéos[43] est présentée en annexe II. Plus que les résultats obtenus, l'aspect vraiment

[41] En 2015 le cluster de calcul du laboratoire CREATIS (qui a été utilisé dans ce travail)a été mis à jour avec un parc de 24 machines hétérogènes regroupant ensemble un total de 274 CPU et 942 GB RAM sur un réseau gigabit où 14 TB de données peuvent être partagées. Toutes les machines sont exploitées par Fedora 20 (64 bits). Plus d'information sur la soumission des *jobs* et le *batch manager* sont données en annexe I.

[42] « On pourrait sans aucun doute affirmer que la transduction ne saurait être présentée comme procédé logique ayant valeur de preuve ; aussi bien, nous ne voulons pas dire que la transduction est un procédé logique au sens courant du terme ; elle est un procédé mental, et plus encore qu'un procédé une démarche de l'esprit qui découvre. Cette démarche consiste à *suivre l'être dans sa genèse*, à accomplir la genèse de la pensée en même temps que s'accomplit la genèse de l'objet. », (Simondon 2005), p. 34.

[43] Comme précisé dans la note de bas de page 40 (p. 24), les vidéos du déroulement des optimisations sont disponibles en ligne en document complémentaires sur https://www.creatis.insa-lyon.fr/site7/en/roux.

important ici est la démarche/l'opération qui y mène. La citation écrite par Deleuze et Guattari dans (Deleuze and Guattari 1987) extraite par Andrew Iliadis dans (Iliadis 2013) est particulièrement appropriée: "*En résumé, Simondon critique le modèle hylémorphique parce qu'il prend la forme et la matière comme deux termes définis séparément, […], [et leur interaction] comme une simple relation de modelage derrière laquelle il y a une modulation continue, perpétuellement variable, qu'il n'est plus possible d'appréhender.*" (Traduction personnelle). Le fait que dans notre travail l'algorithme de recuit simulé n'est pas modifié au cours de l'optimisation peut être rapproché dans la précédente citation de cette idée d'une simple opération de modelage dans laquelle il manque la modulation continue de la fonction d'énergie. Pour faire le lien avec l'optimisation du diagramme de rayonnement, cela pourrait être vu comme la nécessité de « moduler continuellement » le masque sculptant. Ce qui veut dire que, non seulement le masque de contraintes devrait évoluer avec la décroissance progressive de la température, mais aussi que les solutions explorées au cours du processus d'optimisation devraient elles-aussi avoir un impact sur la forme du masque de contrainte.

Il est possible d'adapter facilement le travail proposé pour qu'une opération progressive fasse évoluer le processus d'optimisation avec la température. La continuation stochastique (SC) désigne une classe d'algorithmes qui s'obtient par la généralisation d'un recuit simulé température-dépendent nécessitant des conditions suffisantes de convergence globale étonnamment simple (Robini and Reissman 2013): *"La première idée est de relaxer le processus du recuit en révélant graduellement la complexité du problème d'optimisation. La deuxième idée est de faciliter l'exploration de l'espace d'état en adaptant le mécanisme de communication au régime de température."* Ces deux idées soulevées par la continuation stochastique sont complémentaires de ce qui se passe en intégrant les simulations acoustiques dans le processus d'optimisation. Les simulations donnent plus de flexibilité à la définition de l'espace d'état grâce aux nouveaux degrés de liberté disponibles et la continuation stochastique donne plus de flexibilité dans la définition de la fonction d'énergie et du mécanisme de communication. La combinaison du présent travail avec la continuation stochastique représente une source riche d'investigation en reliant ensemble la flexibilité des définitions de l'espace d'état, de la fonction d'énergie et du mécanisme de communication.

V.F Ordres d'individuation multiples des sondes ultrasonores 2D parcimonieuses

La définition des sondes ultrasonores 2D parcimonieuses, vue comme une opération dynamique et non comme une solution déterministe absolue, prend la forme d'un processus de résolution de tension vers un but fixé par l'application (à travers la définition de la fonction d'énergie). L'évolution s'opère tout en maintenant un équilibre métastable. Cet équilibre métastable est le cœur de la définition de la sonde et paradoxalement il n'existe que grâce à l'évolution subtile et délicate du taux de tolérance de déséquilibres (le taux d'acceptation des variations positives de la fonction d'énergie décroit progressivement). Dans sa propre thèse *Différence et répétition* écrit en 1968 (Deleuze 1994) : *"Gilbert Simondon a montré récemment que l'individuation présuppose un état métastable préalable" (1994, p. 246).* Ce qui rejoint l'idée de processus transductif (note de bas de page 34) opérant à travers trois échelles de processus qui interagissent. La conception de la sonde est l'échelle centrale entourée par deux autres échelles: une échelle intérieure associée avec la cristallisation (recuit) qui produit le matériau piézoélectrique et une échelle extérieure associée avec

l'algorithme d'optimisation (la continuation stochastique permet une modulation continue de la fonction d'énergie et du mécanisme de communication). Un processus de conception multi-échelle/multi-ordre de grandeurs peut alors être individué, agent de l'opération d'individuation qu'il forme pour résoudre une problématique de tensions crée par la minimisation de la fonction d'énergie[44].

V.G Autres champs d'application

Le présent travail pourrait potentiellement être appliqué dans d'autres domaines scientifiques et techniques. Par exemple les fonctions de coût multi-profondeur pourraient être adaptées pour des applications en ultrasons focalisés de haute intensité (HIFU) ou pour les sondes *dual mode* (HIFU and B-mode). Le secteur de l'acoustique sous-marine (P. Chen, Tian, and Chen 2010; Trucco, Palmese, and Repetto 2008) représente un autre champ d'applications où, des systèmes de sonar pourrait profiter des schémas d'optimisation proposés.

Actuellement l'industrie du divertissement développe d'innovants systèmes d'images 3D (lunettes 3D au cinéma, Samsung Gear VR[45] développées par Oculus VR[46]) pour créer l'illusion d'une réalité virtuelle 3D. Qu'en est-il des systèmes de son 3D pour la réalité virtuelle et le multimédia (Begault and Trejo 2000) ? Aujourd'hui il est relativement facile de produire de l'audio multi phoniques[47] où les différentes pistes peuvent être diffusées sur un ensemble (orchestre) de haut-parleurs. Dans le résumé[48] du projet européen EDISON 3D (Project ID ANR-13-CORD-0008), le coordinateur Etienne Corteel de Sonic Emotion Labs[49] écrit: « *Les initiatives actuelles des entités de standardisation (MPEG, ITU) et des principaux acteurs de l'industrie du cinéma (Dolby, Barco, etc.) laissent entendre que des productions de contenus audio 3D vont émerger dans les prochaines années pour des applications de consommation audio et audiovisuelles. Cependant il n'existe pas de consensus sur les outils de création de ces contenus, les formats ou les méthodes de distribution du son 3D ».* Contrairement à l'écoute binaural où chaque auditeur individuel a besoin d'un casque audio et un traitement personnalisé du son tenant compte de sa propre fonction de transfert relative à la tête (HRTF) pour apprécier l'illusion d'un son spatialisé en 3D, une approche plus intéressante consiste à diffuser un champ sonore réel (holophonie) (holophonic sound) avec des techniques comme la synthèse de champ d'ondes (*Wave Field Synthesis* -WFS) (Berry, Dia, and Robin 2012; Berkhout, Vries, and Vogel 1993), *high-order* Ambisonics (Daniel, Moreau, and Nicol 2003) ou les harmoniques sphériques (Poletti 2005). La réduction de bruit représente également une application potentielle avec la création de panneaux acoustiques optimaux ou le control actif du bruit (S. M. Kuo and Morgan 1999; Sen M. Kuo and Morgan 1995) afin de préserver la chance de pouvoir écouter le silence[50].

---

[44] « En même temps qu'une énergie (condition d'ordre de grandeur *supérieur*) s'actualise, une matière s'ordonne et se répartit (condition d'ordre de grandeur *inférieur*) en individus structurés à un ordre de grandeur *moyen*, se développant par un processus médiat d'amplification. », (Simondon 2005), p. 27.

[45] http://www.samsung.com/global/galaxy/gear-vr/ (visité en Août 2016)

[46] https://www.oculus.com/ (visité en Août 2016)

[47] http://multiphonie.free.fr/ (en Français; visité en Août 2016)

[48] http://www.agence-nationale-recherche.fr/?Project=ANR-13-CORD-0008 (visité en Août 2016)

[49] http://www2.sonicemotion.com/ (visité en Août 2016)

[50] http://soundtracker.com/ site internet de Gordon Hempton, auteur de *One Square Inch of Silence, 2010*

Conclusion générale

Le contexte de l'imagerie ultrasonore 3D a été présenté, en commençant par les principes physiques sur lesquels l'imagerie ultrasonore est basée, et jusqu'aux solutions techniques actuelles (et leurs limites) proposées par les laboratoires de recherche académique les plus actifs et les solutions déjà commercialisées proposant des échographes 3D temps-réel.

Une première section est dédiée à l'explication de comment les ondes acoustiques sont générées à partir de la matière grâce à la capacité de transduction électroacoustique des matériaux piézoélectriques. Il a ensuite été décrit comment les ondes ultrasonores sont utilisées dans le cadre médical en se concentrant sur les stratégies d'émission et le principe de reconstruction des images à partir des échos reçu du milieu observé. Il a été détaillé comment un groupe de transducteur produit un champ de pression auquel peut être associé un diagramme de rayonnement acoustique (BP). La relation entre la qualité des images reconstruites et la forme du BP a été illustrée en présentant les bases de la reconstruction d'images échographiques. Les difficultés rencontrées pour réaliser des images 3D temps-réel ont été exposées. Les sondes ultrasonores matricielles 2D existantes utilisant le principe de balayage électronique ont été examinées. La définition des sondes 2D parcimonieuses, en réduisant considérablement le nombre d'éléments actifs, a été présentée comme une solution pour réaliser de l'imagerie ultrasonore 3D en conservant la pleine flexibilité d'une configuration où un élément actif de la sonde est relié en continu à un canal de l'échographe. Le besoin d'intégration des simulations acoustiques large bande, dans le cadre de la définition des sondes 2D parcimonieuses, a été mis en évidence à partir de l'étude de la littérature.

La première contribution de cette thèse est l'intégration de simulations acoustiques large bande dans un cadre général d'optimisation des sondes 2D parcimonieuses. Deux techniques d'accélération ont été implémentées pour atteindre une vitesse de calcul suffisante du champ de pression pour pouvoir être intégré dans un processus d'optimisation dont la durée soit raisonnable (entre quelques jours et quelques semaines). La première technique consiste à réduire le nombre de point de mesure du champ de pression nécessaires pour évaluer le diagramme de rayonnement de la sonde. La deuxième technique consiste en une mise à jour ergonomique des valeurs du champ de pression lorsqu'un seul élément de la sonde est perturbé. Les avantages suivants qui en résultent ont été étudiés : le facteur d'accélération de l'implémentation, la réduction du nombre de dimensions nécessaires à la représentation du diagramme de rayonnement acoustique, les nouveaux degrés de liberté (taille, forme, orientation, signal d'excitation, réponse impulsionnelle) disponibles et une meilleure capacité de distinction des sondes. Un autre avantage de l'intégration de simulations large bande est qu'au cours de l'optimisation les configurations se comportent comme si elles étaient physiquement testées. Un cadre général d'optimisation des sondes 2D parcimonieuses a été introduit sur la base de l'algorithme de recuit simulé dont les composantes (espace d'état, fonction d'énergie, mécanisme de communication) sont décrites dans le contexte de la définition de sondes ultrasonores. Les limitations et les possibles améliorations de la présente implémentation ont été discutées.

La deuxième contribution de cette thèse est l'introduction de fonction d'énergie multi-profondeur, qui représente une étape vers l'optimisation du champ de pression en 3D dans le cadre de l'optimisation de sondes parcimonieuses non-régulières. Dans cette deuxième étude, les rayonnements acoustiques (BP) de seize sondes parcimonieuses de 256 éléments ont été optimisés. L'exploration des solutions s'est déroulée en déplaçant les éléments de façon arbitraire pour optimiser leur position au sens des trois fonctions d'énergie proposées. Une des fonctions d'énergies forme le lobe principal du BP en le « sculptant » avec un masque de contraintes. En particulier, les fonctions d'énergie vérifient la qualité du diagramme de rayonnement en plusieurs profondeurs de manière à mieux contrôler le comportement du champ de pression avant et après la profondeur focale. Dans cette étude le BP était évalué à 15 mm, 25 mm (profondeur focale) et 35 mm et le processus d'optimisation avait pour objectif d'obtenir la même largeur de lobe principal et d'abaisser les lobes latéraux comme dans le cas d'une sonde spirale prise comme référence. Les performances des configurations obtenues ont été évaluées sur leurs rayonnements acoustiques 3D. Une des configurations optimisées a fourni des performances légèrement meilleures que celles de la sonde spirale qui est prise comme référence. L'utilisation d'un masque sculptant le lobe principal du BP (de manière identique selon tous les angles ϕ) à plusieurs profondeurs semblent générer des solutions à symétrie circulaire même si aucune contrainte de symétrie n'est imposée. L'apparition de cette symétrie circulaire a été discutée ainsi que la possibilité d'intégrer de nouveaux degrés de liberté et de nouvelles contraintes.

La troisième contribution de cette thèse est l'étude de l'optimisation de sonde 2D parcimonieuses régulière où sont exposées les lignes directrices pour intégrer des contraintes de fabrication dans la cadre général d'une optimisation du diagramme de rayonnement (BP) large bande. La problématique traitée est celle de trouver la meilleure configuration d'un nombre d'élément fixé à activer parmi ceux d'une sonde matricielle 2D. Cette question a été traitée dans les cas où 128, 192 et 256 éléments étaient choisis parmi une sonde de 32x32 éléments. Dans cette étude également la fonction d'énergie avait pour objectif de sculpter la forme du BP à plusieurs profondeurs. De plus, une interface utilisateur a été développée pour aider à la définition du masque sculptant utilisé dans la fonction d'énergie. Les résultats obtenus ont été comparés en termes de largeur du lobe principal à – 6dB et à – 20 dB, en termes de niveau de lobes latéraux (SLL) et de niveau moyen de ces lobes ($\mathrm{SLL_{ave}}$) calculés sur les BP multi-profondeur. Tout comme dans le chapitre précédent, une analyse des performances a été réalisée sur les BP 3D. Pour évaluer la capacité des sondes obtenues à produire des images ultrasonores de qualité, des images 3D (coupe XZ et YZ) d'un fantôme de résolution et d'un fantôme de contraste ont été simulées. La robustesse des optimisations par rapport à l'état initial a été validée avec la comparaison des résultats de dix expériences identiques démarrant avec une sonde initiale différente à chaque fois. Une sonde aléatoire a également été obtenue. Sa comparaison avec les sondes optimales a permis de mettre en évidence le rôle précieux que joue l'évolution de la température dans l'optimisation. Enfin l'intégration de contraintes de fabrication dans le processus d'optimisation enrichie la conception théorique des sondes ultrasonores : pour une application donnée, cela constitue un nouvel outil disponible pour les fabricants de sondes pour choisir parmi plusieurs solutions technologiques.

Une discussion générale a permis d'aborder les limites du schéma d'optimisation général proposé et ses exigences en termes de calcul. Mais ce fut aussi une opportunité pour suggérer les extensions potentielles de cette thèse. Enfin cette discussion contient une tentative de replacer l'état du travail *présent*-é dans une perspective fascinante d'une étude dynamique avec l'espoir de ne pas être

restreinte à la conception des sondes ultrasonores 2D parcimonieuses. L'imagerie médicale, et l'imagerie ultrasonore en particulier, ont changé la manière de pratiquer la médecine depuis 50-60 ans. En retour, les médecins ont influencé quelles informations devaient être extraites et la façon de les présenter (ce qui qui est également vrai pour l'échographie 3D). Malheureusement, les interactions entre les médecins et les ingénieurs sont typiquement trop peu fréquentes et constructives comme elles devraient l'être. Cependant, lorsqu'une heureuse rencontre se produit, il est fort probable qu'émerge à la fois des innovations technologiques de pointes et des pratiques de santé efficaces. Il semble que pour la transdisciplinarité (Nicolescu 2016; Nicolescu 2008), un état métastable soit nécessaire, caractérisé par l'acceptation d'une « perturbation » partielle (variation positive d'énergie, effort ?) de la part des deux disciplines. De formidables progrès peuvent arriver d'un processus transductif *two-way.* En l'absence d'une *zone obscure centrale* (Simondon 2005) incluse au milieu, ils ne pourraient pas être inventés car chaque environnement resterait fermé sur lui-même et stable. Quelques rares personnes peuvent incarner ce « tiers inclus » quand ils ont courageusement réalisé à la fois des études d'ingénierie et de médecine.

Publications personnelles

Articles de journaux

Roux, E., A. Ramalli, P. Tortoli, C. Cachard, M. Robini, and H. Liebgott. 2016. "2D Ultrasound Sparse Arrays Multi-Depth Radiation Optimization Using Simulated Annealing and Spiral-Array Inspired Energy Functions." *IEEE Transactions on Ultrasonics, Ferroelectrics, and Frequency Control,* Dec. 2016, vol. 63, no. 12, pp. 2138–2149. doi:10.1109/TUFFC.2016.2602242

Roux, E., A. Ramalli, H. Liebgott, C. Cachard, M. Robini, and P. Tortoli. 2016. "Wideband 2D Array Design Optimization with Fabrication Constraints for 3D US Imaging." *IEEE Transactions on Ultrasonics, Ferroelectrics, and Frequency Control,* Jan. 2017, vol. 64, no. 1, pp. (published Oct. 2016, 3rd on IEEE Explore - printed release in Jan. 2017). doi:10.1109/TUFFC.2016.2614776

Images de couverture de journaux

Ramalli, A., E. Boni, E. Roux, and P. Tortoli. 2015. "Density-Tapered Sunflower: A Deterministic Sparse Array Solution." *IEEE Transactions on Ultrasonics, Ferroelectrics, and Frequency Control [Cover]* 62 (8): c1–2. doi:10.1109/TUFFC.2015.620801

Conférences internationales

Diarra, B., **E. Roux**, H. Liebgott, S. Ravi, M. Robini, P. Tortoli, and C. Cachard, "Comparison of different optimized irregular sparse 2D ultrasound arrays," in Ultrasonics Symposium (IUS), 2016 IEEE International, 2016, pp. 1-4 doi:10.1109/ULTSYM.2016.7728414

Diarra, B., M. Robini, **E. Roux**, H. Liebgott, C. Cachard, and P. Tortoli. 2014. "Optimization of Free-Moving Elements in 2D Ultrasound Sparse Arrays." In Ultrasonics Symposium (IUS), 2014 IEEE International, pp. 2189–92. doi:10.1109/ULTSYM.2014.0545

Roux, E., B. Diarra, M. Robini, C. Cachard, P. Tortoli, and H. Liebgott. 2014. "Realistic Acoustic Simulation of 2-D Probe Elements in Simulated Annealing Sparse Array Optimization." In Ultrasonics Symposium (IUS), 2014 IEEE International, pp. 2125–28. doi:10.1109/ULTSYM.2014.0529

Roux, E., A. Ramalli, M. Robini, H. Liebgott, C. Cachard, and P. Tortoli. 2015. "Spiral Array Inspired Multi-Depth Cost Function for 2D Sparse Array Optimization." In Ultrasonics Symposium (IUS), 2015 IEEE International, pp. 1–4. doi:10.1109/ULTSYM.2015.0096

Roux, E., A. Ramalli, P. Tortoli, C. Cachard, M. Robini, and H. Liebgott. 2015. "Speed-up of Acoustic Simulation Techniques for 2D Sparse Array Optimization by Simulated Annealing." In Ultrasonics Symposium (IUS), 2015 IEEE International, pp. 1–4. doi:10.1109/ULTSYM.2015.0431

Conférences nationales

Roux, Emmanuel, Marc C. Robini, Alessandro Ramalli, Piero Tortoli, Christian Cachard, and Hervé Liebgott. 2015. "Modélisation et Simulation Acoustique Pour L'optimisation de Sondes Échographiques 2D Par Recuit Simulé." In XXVème Colloque GRETSI. Lyon, France. https://hal.archives-ouvertes.fr/hal-01286079.

Roux, Emmanuel, Alessandro Ramalli, Piero Tortoli, Marc Robini, Hervé Liebgott, and Christian Cachard. 2015. "Optimisation du rayonnement acoustique de sondes parcimonieuses pour l'échographie 3D temps-réel." 22ème Congrès Français de Mécanique, 24 au 28 août 2015, Lyon, France (FR). http://documents.irevues.inist.fr/handle/2042/57698.

Autres

« Ma thèse en 180 secondes »



Figure 91 Présentation “ma thèse en 180 secondes”
(lien Youtube https://www.youtube.com/watch?v=iIxG-7y3pV4)

En Avril 2016 j’ai participé à la finale locale de l’Université de Lyon du concours "Ma thèse en 180 secondes". La vidéo de la présentation de mes travaux dans ce format de vulgarisation scientifique est disponible sur Youtube (lien https://www.youtube.com/watch?v=iIxG-7y3pV4).

Image de l’année 2013 du laboratoire CREATIS

Chaque année un concours interne au laboratoire CREATIS permet d’élire « l’image de l’année » qui sera ensuite imprimée sur les cartes de vœux du laboratoire. J’ai réalisé l’image qui a été sélectionnée en 2013 sur la base des résultats d’optimisation obtenus par Bakary Diarra. L’image était accompagnée de la légende suivante : *« Simulation of a 3D ultrasound optimized sparse array by random positioning of 256 active elements and apodization »*. B. Diarra, **E. Roux**, M. Robini, C. Cachard, H. Liebgott. Collaboration : P. Tortoli, MSD-Lab, Université de Florence, Italie

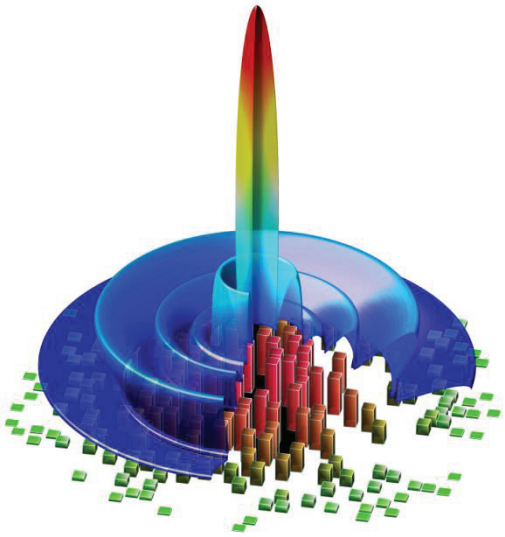


Figure 92 Image de l’année 2013 à CREATIS: *Simulation of a 3D ultrasound optimized sparse array by random positioning of 256 active elements and apodization.* B. Diarra, **E. Roux**, M. Robini, C. Cachard, H. Liebgott. Collaboration : P. Tortoli, MSD-Lab, Université de Florence, Italie

Références

Adler, D. 1993. “Genetic Algorithms and Simulated Annealing: A Marriage Proposal.” In *, IEEE International Conference on Neural Networks, 1993*, 1104–9 vol.2. doi:10.1109/ICNN.1993.298712.

Austeng, A, and S. Holm. 2002. “Sparse 2-D Arrays for 3-D Phased Array Imaging - Design Methods.” *IEEE Transactions on Ultrasonics, Ferroelectrics, and Frequency Control* 49 (8): 1073–86. doi:10.1109/TUFFC.2002.1026019.

Austeng, A., S. Holm, P.K. Weber, N. Aakvaag, and K. Iranpour. 1997. “1D and 2D Algorithmically Optimized Sparse Arrays.” In *, 1997 IEEE Ultrasonics Symposium, 1997. Proceedings*, 2:1683–86 vol.2. doi:10.1109/ULTSYM.1997.663319.

Barnes, Stephen, Mirsaid Bolorforosh, and Robert Phelps. 2005. System and method for 2D partial beamforming arrays with configurable sub-array elements. US20050228277 A1, filed April 5, 2004, and issued October 13, 2005. http://www.google.com/patents/US20050228277.

Begault, Durand R., and Leonard J. Trejo. 2000. “3-D Sound for Virtual Reality and Multimedia.” http://ntrs.nasa.gov/search.jsp?R=20010044352.

Berkhout, A. J., D. de Vries, and P. Vogel. 1993. “Acoustic Control by Wave Field Synthesis.” *The Journal of the Acoustical Society of America* 93 (5): 2764–78. doi:10.1121/1.405852.

Berry, Alain, Rokhiya Dia, and Olivier Robin. 2012. “A Wave Field Synthesis Approach to Reproduction of Spatially Correlated Sound Fields.” *The Journal of the Acoustical Society of America* 131 (2): 1226–39. doi:10.1121/1.3675942.

Boni, C., M. Richard, and S. Barbarossa. 1994. “Optimal Configuration and Weighting of Nonuniform Arrays according to a Maximum ISLR Criterion.” In *, 1994 IEEE International Conference on Acoustics, Speech, and Signal Processing, 1994. ICASSP-94*, v:V/157-V/160 vol.5. doi:10.1109/ICASSP.1994.389424.

Brunke, S.S., and G.R. Lockwood. 1997. “Broad-Bandwidth Radiation Patterns of Sparse Two-Dimensional Vernier Arrays.” *IEEE Transactions on Ultrasonics, Ferroelectrics, and Frequency Control* 44 (5): 1101–9. doi:10.1109/58.655635.

Caliano, G., R. Carotenuto, E. Cianci, Vittorio Foglietti, A. Caronti, A. Iula, and M. Pappalardo. 2005. “Design, Fabrication and Characterization of a Capacitive Micromachined Ultrasonic Probe for Medical Imaging.” *IEEE Transactions on Ultrasonics, Ferroelectrics, and Frequency Control* 52 (12): 2259–69. doi:10.1109/TUFFC.2005.1563268.

Caronti, Alessandro, G. Caliano, R. Carotenuto, A. Savoia, M. Pappalardo, E. Cianci, and V. Foglietti. 2006. “Capacitive Micromachined Ultrasonic Transducer (CMUT) Arrays for Medical Imaging.” *Microelectronics Journal* 37 (8): 770–77. doi:10.1016/j.mejo.2005.10.012.

Chen, Kailiang. 2014. “A Column-Row-Parallel ASIC Architecture for 3D Wearable / Portable Medical Ultrasonic Imaging.” Thesis, Massachusetts Institute of Technology. http://dspace.mit.edu/handle/1721.1/87916.

Chen, Peng, Bin-jian Shen, Li-sheng Zhou, and Yao-wu Chen. 2010. “Optimized Simulated Annealing Algorithm for Thinning and Weighting Large Planar Arrays.” *Journal of Zhejiang University SCIENCE C* 11 (4): 261–69. doi:10.1631/jzus.C0910037.

Chen, Peng, Xiang Tian, and Yaowu Chen. 2010. “Optimization of the Digital Near-Field Beamforming for Underwater 3-D Sonar Imaging System.” *IEEE Transactions on Instrumentation and Measurement* 59 (2): 415–24. doi:10.1109/TIM.2009.2024368.

Choe, Jung Woo, O. Oralkan, and P.T. Khuri-Yakub. 2010. “Design Optimization for a 2-D Sparse Transducer Array for 3-D Ultrasound Imaging.” In *2010 IEEE Ultrasonics Symposium (IUS)*, 1928–31. doi:10.1109/ULTSYM.2010.5935854.

Christiansen, T.L., M.F. Rasmussen, J.P. Bagge, L. Nordahl Moesner, J.A. Jensen, and E.V. Thomsen. 2015. “3-D Imaging Using Row-Column-Addressed Arrays with Integrated Apodization - Part Ii: Transducer Fabrication and Experimental Results.” *IEEE Transactions on Ultrasonics, Ferroelectrics, and Frequency Control* 62 (5): 959–71. doi:10.1109/TUFFC.2014.006819.

Curie, Jacques, and Pierre Curie. 1880. “Développement, Par Pression, de L’électricité Polaire Dans Les Cristaux Hémièdres À Faces Inclinées.” Comptes rendus hebdomadaires des séances de l’Académie des sciences / publiés... par MM. les secrétaires perpétuels -- 1880-07 -- periodiques. http://gallica.bnf.fr/ark:/12148/bpt6k30485.

———. 1881. “Contractions et Dilatations Produites Par Des Tensions Électriques Dans Les Cristaux Hémièdres À Faces Inclinées.” Comptes rendus hebdomadaires des séances de l’Académie des sciences / publiés... par MM. les secrétaires perpétuels -- 1881-07 -- periodiques. http://gallica.bnf.fr/ark:/12148/bpt6k3049g.

Daniel, Jerome, Sebastien Moreau, and Rozenn Nicol. 2003. “Further Investigations of High-Order Ambisonics and Wavefield Synthesis for Holophonic Sound Imaging.” In *Audio Engineering Society Convention 114*. http://www.aes.org/e-lib/browse.cfm?elib=12567.

Davidsen, R. E., J. A. Jensen, and S. W. Smith. 1994. “Two-Dimensional Random Arrays for Real Time Volumetric Imaging.” *Ultrasonic Imaging* 16 (3): 143–63. doi:10.1006/uimg.1994.1009.

Deffieux, T., J.-L. Gennisson, M. Tanter, and M. Fink. 2008. “Assessment of the Mechanical Properties of the Musculoskeletal System Using 2-D and 3-D Very High Frame Rate Ultrasound.” *IEEE Transactions on Ultrasonics, Ferroelectrics, and Frequency Control* 55 (10): 2177–90. doi:10.1109/TUFFC.917.

Deleuze, Gilles. 1994. *Difference and Repetition*. New York: Columbia University Press.

Deleuze, Gilles, and Félix Guattari. 1987. *A Thousand Plateaus: Capitalism and Schizophrenia*. Minneapolis: University of Minnesota Press.

Deprez, Jean-François, Elisabeth Brusseau, Cédric Schmitt, Guy Cloutier, and Olivier Basset. 2009. “3D Estimation of Soft Biological Tissue Deformation from Radio-Frequency Ultrasound Volume Acquisitions.” *Medical Image Analysis*, Includes Special Section on Medical Image Analysis on the 2006 Workshop Microscopic Image Analysis with Applications in Biology, 13 (1): 116–27. doi:10.1016/j.media.2008.07.003.

Diarra, B., M. Robini, E. Roux, H. Liebgott, C. Cachard, and P. Tortoli. 2014. “Optimization of Free-Moving Elements in 2D Ultrasound Sparse Arrays.” In *Ultrasonics Symposium (IUS), 2014 IEEE International*, 2189–92. doi:10.1109/ULTSYM.2014.0545.

Diarra, B., M. Robini, P. Tortoli, C. Cachard, and H. Liebgott. 2013. “Design of Optimal 2-D Nongrid Sparse Arrays for Medical Ultrasound.” *IEEE Transactions on Biomedical Engineering* 60 (11): 3093–3102. doi:10.1109/TBME.2013.2267742.

Fenster, Aaron, Dónal B. Downey, and H. Neale Cardinal. 2001. “Three-Dimensional Ultrasound Imaging.” *Physics in Medicine and Biology* 46 (5): R67. doi:10.1088/0031-9155/46/5/201.

Fernandez, A. T., K. L. Gammelmark, J. J. Dahl, C. G. Keen, R. C. Gauss, and G. E. Trahey. 2003. “Synthetic Elevation Beamforming and Image Acquisition Capabilities Using an 8 /spl Times/ 128 1.75D Array.” *IEEE Transactions on Ultrasonics, Ferroelectrics, and Frequency Control* 50 (1): 40–57. doi:10.1109/TUFFC.2003.1176524.

Fisher, R, K Thomenius, R Wodnicki, R Thomas, S Cogan, C Hazard, W Lee, et al. 2005. “Reconfigurable Arrays for Portable Ultrasound.” In *Proc. IEEE Ultrason. Symp*, 1:495–499.

Gazdag, J., and P. Sguazzero. 1984. “Migration of Seismic Data.” *Proceedings of the IEEE* 72 (10): 1302–15. doi:10.1109/PROC.1984.13019.

Hasegawa, Hideyuki, and Hiroshi Kanai. 2011. “High-Frame-Rate Echocardiography Using Diverging Transmit Beams and Parallel Receive Beamforming.” *Journal of Medical Ultrasonics* 38 (3): 129–40. doi:10.1007/s10396-011-0304-0.

Haupt, Randy L. 1994. “Thinned Arrays Using Genetic Algorithms.” *IEEE Transactions on Antennas and Propagation* 42 (7): 993–99. doi:10.1109/8.299602.

Holm, S., A. Austeng, K. Iranpour, and J.-F. Hopperstad. 2001. “Sparse Sampling in Array Processing.” In *Nonuniform Sampling*, edited by Farokh Marvasti, 787–833. Information Technology: Transmission, Processing, and Storage. Springer US. http://link.springer.com/chapter/10.1007/978-1-4615-1229-5_19.

Holm, S., and B. Elgetun. 1995. “Optimization of the Beampattern of 2D Sparse Arrays by Weighting.” In *, 1995 IEEE Ultrasonics Symposium, 1995. Proceedings*, 2:1345–48 vol.2. doi:10.1109/ULTSYM.1995.495805.

Holm, S., B. Elgetun, and G. Dahl. 1997. “Properties of the Beampattern of Weight- and Layout-Optimized Sparse Arrays.” *IEEE Transactions on Ultrasonics, Ferroelectrics, and Frequency Control* 44 (5): 983–91. doi:10.1109/58.655623.

Hwang, Shun-Fa, and Rong-Song He. 2006. “Improving Real-Parameter Genetic Algorithm with Simulated Annealing for Engineering Problems.” *Advances in Engineering Software* 37 (6): 406–18. doi:10.1016/j.advengsoft.2005.08.002.

Iliadis, Andrew. 2013. “A New Individuation: Deleuze’s Simondon Connection.” *MediaTropes* 4 (1): 83–100.

Jensen, J.A. 1996. “FIELD: A Program for Simulating Ultrasound Systems.” In *10th NordicBaltic Conference on Biomedical Imaging, Vol. 4, Supplement 1, Part 1:351–353*, 351–353.

Jensen, J. A., M. F. Holten-Lund, R. T. Nilsson, M. Hansen, U. D. Larsen, R. P. Domsten, B. G. Tomov, et al. 2013. “SARUS: A Synthetic Aperture Real-Time Ultrasound System.” *IEEE Transactions on Ultrasonics, Ferroelectrics, and Frequency Control* 60 (9): 1838–52. doi:10.1109/TUFFC.2013.2770.

Jensen, J.A., and N.B. Svendsen. 1992. “Calculation of Pressure Fields from Arbitrarily Shaped, Apodized, and Excited Ultrasound Transducers.” *IEEE Transactions on Ultrasonics, Ferroelectrics, and Frequency Control* 39 (2): 262–67. doi:10.1109/58.139123.

Jespersen, Søren K., Jens E. Wilhjelm, and Henrik Sillesen. 1998. “Multi-Angle Compound Imaging.” *Ultrasonic Imaging* 20 (2): 81–102. doi:10.1177/016173469802000201.

Karaman, Mustafa, I.O. Wygant, O. Oralkan, and B.T. Khuri-Yakub. 2009. “Minimally Redundant 2-D Array Designs for 3-D Medical Ultrasound Imaging.” *IEEE Transactions on Medical Imaging* 28 (7): 1051–61. doi:10.1109/TMI.2008.2010936.

Kortbek, Jacob, Jørgen Arendt Jensen, and Kim Løkke Gammelmark. 2013. “Sequential Beamforming for Synthetic Aperture Imaging.” *Ultrasonics* 53 (1): 1–16. doi:10.1016/j.ultras.2012.06.006.

Kruizinga, P., F. Mastik, N. de Jong, A.F.W. van der Steen, and G. van Soest. 2012. “Plane-Wave Ultrasound Beamforming Using a Nonuniform Fast Fourier Transform.” *IEEE Transactions on Ultrasonics, Ferroelectrics, and Frequency Control* 59 (12). doi:10.1109/TUFFC.2012.2509.

Kuo, S. M., and D. R. Morgan. 1999. “Active Noise Control: A Tutorial Review.” *Proceedings of the IEEE* 87 (6): 943–73. doi:10.1109/5.763310.

Kuo, Sen M., and Dennis Morgan. 1995. *Active Noise Control Systems: Algorithms and DSP Implementations*. 1st ed. New York, NY, USA: John Wiley & Sons, Inc.

Light, Edward D, Salim F Idriss, Patrick D Wolf, and Stephen W Smith. 2001. “Real-Time Three-Dimensional Intracardiac Echocardiography.” *Ultrasound in Medicine & Biology* 27 (9): 1177–83. doi:10.1016/S0301-5629(01)00421-5.

Lindseth, Frank, Thomas Langø, Tormod Selbekk, Rune Hansen, Ingerid Reinertsen, Christian Askeland, Ole Solheim, Geirmund Unsgård, Ronald Mårvik, and Toril A Nagelhus Hernes. 2013. “Ultrasound-Based Guidance and Therapy.” *Advancements and Breakthroughs in Ultrasound Imaging*, 28–82.

Lockwood, G.R., and F.S. Foster. 1996. “Optimizing the Radiation Pattern of Sparse Periodic Two-Dimensional Arrays.” *IEEE Transactions on Ultrasonics, Ferroelectrics, and Frequency Control* 43 (1): 15–19. doi:10.1109/58.484458.

Logan, A.S., L.L.P. Wong, A.I.H. Chen, and J.T.W. Yeow. 2011. “A 32 X 32 Element Row-Column Addressed Capacitive Micromachined Ultrasonic Transducer.” *IEEE Transactions on Ultrasonics, Ferroelectrics, and Frequency Control* 58 (6): 1266–71. doi:10.1109/TUFFC.2011.1937.

Martínez-Graullera, Oscar, Carlos J. Martín, Gregorio Godoy, and Luis G. Ullate. 2010. “2D Array Design Based on Fermat Spiral for Ultrasound Imaging.” *Ultrasonics*, Selected Papers from ICU 2009, 50 (2): 280–89. doi:10.1016/j.ultras.2009.09.010.

Matrone, G., A.S. Savoia, M. Terenzi, G. Caliano, F. Quaglia, and G. Magenes. 2014. “A Volumetric CMUT-Based Ultrasound Imaging System Simulator with Integrated Reception and μ-Beamforming Electronics Models.” *IEEE Transactions on Ultrasonics, Ferroelectrics, and Frequency Control* 61 (5): 792–804. doi:10.1109/TUFFC.2014.2971.

Montaldo, G., M. Tanter, J. Bercoff, N. Benech, and M. Fink. 2009. “Coherent Plane-Wave Compounding for Very High Frame Rate Ultrasonography and Transient Elastography.” *IEEE Transactions on Ultrasonics, Ferroelectrics, and Frequency Control* 56 (3): 489–506. doi:10.1109/TUFFC.2009.1067.

Nadeau, C., Hongliang Ren, A. Krupa, and P. Dupont. 2015. “Intensity-Based Visual Servoing for Instrument and Tissue Tracking in 3D Ultrasound Volumes.” *IEEE Transactions on Automation Science and Engineering* 12 (1): 367–71. doi:10.1109/TASE.2014.2343652.

Nelson, Thomas R., and Dolores H. Pretorius. 1998. “Three-Dimensional Ultrasound Imaging.” *Ultrasound in Medicine & Biology* 24 (9): 1243–70. doi:10.1016/S0301-5629(98)00043-X.

Nicolescu, Basarab. 2008. *Transdisciplinarity: Theory and Practice*. Cresskill, NJ: Hampton Press.

———. 2016. *Le Tiers caché dans les domaines de la connaissance*. L’Isle-sur-la-Sorgue: Le Bois d’Orion.

Ningning, Song. 2014. “Quantitative Photoacoustic Tomography for Breast Cancer Screening.” Theses, Centrale Marseille. https://hal.archives-ouvertes.fr/tel-01280134.

Oralkan, O., A. S. Ergun, J. A. Johnson, M. Karaman, U. Demirci, K. Kaviani, T. H. Lee, and B. T. Khuri-Yakub. 2002. “Capacitive Micromachined Ultrasonic Transducers: Next-Generation Arrays for Acoustic Imaging?” *IEEE Transactions on Ultrasonics, Ferroelectrics, and Frequency Control* 49 (11): 1596–1610. doi:10.1109/TUFFC.2002.1049742.

Papadacci, C., M. Pernot, M. Couade, M. Fink, and M. Tanter. 2014. “High-Contrast Ultrafast Imaging of the Heart.” *IEEE Transactions on Ultrasonics, Ferroelectrics, and Frequency Control* 61 (2): 288–301. doi:10.1109/TUFFC.2014.6722614.

Piwakowski, B., and K. Sbai. 1999. “A New Approach to Calculate the Field Radiated from Arbitrarily Structured Transducer Arrays.” *IEEE Transactions on Ultrasonics, Ferroelectrics, and Frequency Control* 46 (2): 422–40. doi:10.1109/58.753032.

Poletti, Mark A. 2005. “Three-Dimensional Surround Sound Systems Based on Spherical Harmonics.” *J. Audio Eng. Soc* 53 (11): 1004–1025.

Prager, R. W., U. Z. Ijaz, A. H. Gee, and G. M. Treece. 2010. “Three-Dimensional Ultrasound Imaging.” *Proceedings of the Institution of Mechanical Engineers, Part H: Journal of Engineering in Medicine* 224 (2): 193–223. doi:10.1243/09544119JEIM586.

Provost, J., C. Papadacci, C. Demene, J. L. Gennisson, M. Tanter, and M. Pernot. 2015. “3-D Ultrafast Doppler Imaging Applied to the Noninvasive Mapping of Blood Vessels in Vivo.” *IEEE Transactions on Ultrasonics, Ferroelectrics, and Frequency Control* 62 (8): 1467–72. doi:10.1109/TUFFC.2015.007032.

Provost, Jean, Clement Papadacci, Juan Esteban Arango, Marion Imbault, Mathias Fink, Jean-Luc Gennisson, Mickael Tanter, and Mathieu Pernot. 2014. “3D Ultrafast Ultrasound Imaging in Vivo.” *Physics in Medicine and Biology* 59 (19): L1. doi:10.1088/0031-9155/59/19/L1.

Ramadas, S., J. Jackson, J. Dziewierz, R. O’Leary, and A. Gachagan. 2014. “Application of Conformal Map Theory for Design of 2-D Ultrasonic Array Structure for Ndt Imaging Application: A Feasibility Study.” *IEEE Transactions on Ultrasonics, Ferroelectrics, and Frequency Control* 61 (3): 496–504. doi:10.1109/TUFFC.2014.2933.

Ramalli, A., E. Boni, A.S. Savoia, and P. Tortoli. 2015. “Density-Tapered Spiral Arrays for Ultrasound 3-D Imaging.” *IEEE Transactions on Ultrasonics, Ferroelectrics, and Frequency Control* 62 (8): 1580–88. doi:10.1109/TUFFC.2015.007035.

Ramalli, A., and P. Tortoli. 2014. “256-Element Density-Tapered Spiral Matrices for Ultrasound Phased Imaging.” In *Ultrasonics Symposium (IUS), 2014 IEEE International*, 2087–90. doi:10.1109/ULTSYM.2014.0520.

Rasmussen, M.F., T.L. Christiansen, E.V. Thomsen, and J.A. Jensen. 2015. “3-D Imaging Using Row-Column-Addressed Arrays with Integrated Apodization - Part I: Apodization Design and Line Element Beamforming.” *IEEE Transactions on Ultrasonics, Ferroelectrics, and Frequency Control* 62 (5): 947–58. doi:10.1109/TUFFC.2014.006531.

Robini, Marc C., and Pierre-Jean Reissman. 2013. “From Simulated Annealing to Stochastic Continuation: A New Trend in Combinatorial Optimization.” *Journal of Global Optimization* 56 (1): 185–215. doi:10.1007/s10898-012-9860-0.

Robinson, Andrew L., David N. Roundhill, Brent Stephen Robinson, and Paul Detmer. 2003. 2D ultrasonic transducer array for two dimensional and three dimensional imaging. US6582367 B1, filed September 15, 2000, and issued June 24, 2003. http://www.google.com/patents/US6582367.

Roux, E., B. Diarra, M. Robini, C. Cachard, P. Tortoli, and H. Liebgott. 2014. “Realistic Acoustic Simulation of 2-D Probe Elements in Simulated Annealing Sparse Array Optimization.” In *Ultrasonics Symposium (IUS), 2014 IEEE International*, 2125–28. doi:10.1109/ULTSYM.2014.0529.

Roux, E., A. Ramalli, M. Robini, H. Liebgott, C. Cachard, and P. Tortoli. 2015. “Spiral Array Inspired Multi-Depth Cost Function for 2D Sparse Array Optimization.” In *Ultrasonics Symposium (IUS), 2015 IEEE International*, 1–4. doi:10.1109/ULTSYM.2015.0096.

Roux, E., A. Ramalli, P. Tortoli, C. Cachard, M. Robini, and H. Liebgott. 2015. “Speed-up of Acoustic Simulation Techniques for 2D Sparse Array Optimization by Simulated Annealing.” In *Ultrasonics Symposium (IUS), 2015 IEEE International*, 1–4. doi:10.1109/ULTSYM.2015.0431.

Savoia, A. S., G. Caliano, and M. Pappalardo. 2012. “A CMUT Probe for Medical Ultrasonography: From Microfabrication to System Integration.” *IEEE Transactions on Ultrasonics, Ferroelectrics, and Frequency Control* 59 (6): 1127–38. doi:10.1109/TUFFC.2012.2303.

Savord, B., and R. Solomon. 2003. “Fully Sampled Matrix Transducer for Real Time 3D Ultrasonic Imaging.” In *2003 IEEE Symposium on Ultrasonics*, 1:945–953 Vol.1. doi:10.1109/ULTSYM.2003.1293556.

Savord, Bernard J. 2012. System and method for amplifying transmit waveforms generated by an ultrasonic system. US8257260 B2, filed June 27, 2005, and issued September 4, 2012. http://www.google.fr/patents/US8257260.

Savord, Bernard J., and Karl E. Thiele. 1999. Phased array acoustic systems with intra-group processors. US5997479 A, filed May 28, 1998, and issued December 7, 1999. http://www.google.com/patents/US5997479.

Schwartz, J. L., and B. D. Steinberg. 1998. “Ultrasparse, Ultrawideband Arrays.” *IEEE Transactions on Ultrasonics, Ferroelectrics, and Frequency Control* 45 (2): 376–93. doi:10.1109/58.660149.

Sciallero, Claudia, and Andrea Trucco. 2015. “Design of a Sparse Planar Array for Optimized 3D Medical Ultrasound Imaging.” In . Nice, FRANCE.

Simondon, Gilbert. 2005. *L’individuation à la lumière des notions de forme et d’information*. Editions Jérôme Millon.

Smith, S.W., Jr. Pavy H.G., and O.T. von Ramm. 1991. “High-Speed Ultrasound Volumetric Imaging System. I. Transducer Design and Beam Steering.” *IEEE Transactions on Ultrasonics, Ferroelectrics, and Frequency Control* 38 (2): 100–108. doi:10.1109/58.68466.

Stepanishen, Peter R. 1971. “Transient Radiation from Pistons in an Infinite Planar Baffle.” *The Journal of the Acoustical Society of America* 49 (5B): 1629–38. doi:10.1121/1.1912541.

Stetten, GEORGE D, TAKAHIRO Ota, CHIKAI J Ohazama, CRAIG Fleishman, JOHN Castellucci, JOHN Oxaal, THOMAS Ryan, J Kisslo, and OT von Ramm. 1998. “Real-Time 3D Ultrasound: A New Look at the Heart.” *Journal of Cardiovascular Diagnosis and Procedures* 15 (2): 73–84.

Sugeng, Lissa, Victor Mor-Avi, Lynn Weinert, Johannes Niel, Christian Ebner, Regina Steringer-Mascherbauer, Frank Schmidt, et al. 2006. “Quantitative Assessment of Left Ventricular Size and Function Side-by-Side Comparison of Real-Time Three-Dimensional Echocardiography and Computed Tomography With Magnetic Resonance Reference.” *Circulation* 114 (7): 654–61. doi:10.1161/CIRCULATIONAHA.106.626143.

Tanter, M., J. Bercoff, L. Sandrin, and M. Fink. 2002. “Ultrafast Compound Imaging for 2-D Motion Vector Estimation: Application to Transient Elastography.” *IEEE Transactions on Ultrasonics, Ferroelectrics, and Frequency Control* 49 (10): 1363–74. doi:10.1109/TUFFC.2002.1041078.

Tekes, C., M. Karaman, and F.L. Degertekin. 2011. “Optimizing Circular Ring Arrays for Forward- Looking IVUS Imaging.” *IEEE Transactions on Ultrasonics, Ferroelectrics, and Frequency Control* 58 (12): 2596–2607. doi:10.1109/TUFFC.2011.2123.

Thomenius, Kai E., Robert Gideon Wodnicki, and Ye-Ming Li. 2010. Transmit and receive interface array for highly integrated ultrasound scanner. US7775979 B2, issued August 17, 2010. http://www.google.com/patents/US7775979.

Trucco, A. 1999. “Thinning and Weighting of Large Planar Arrays by Simulated Annealing.” *IEEE Transactions on Ultrasonics, Ferroelectrics, and Frequency Control* 46 (2): 347–55. doi:10.1109/58.753023.

Trucco, A., M. Palmese, and S. Repetto. 2008. “Devising an Affordable Sonar System for Underwater 3-D Vision.” *IEEE Transactions on Instrumentation and Measurement* 57 (10): 2348–54. doi:10.1109/TIM.2008.922111.

Turnbull, D.H., and F.S. Foster. 1991. “Beam Steering with Pulsed Two-Dimensional Transducer Arrays.” *IEEE Transactions on Ultrasonics, Ferroelectrics, and Frequency Control* 38 (4): 320–33. doi:10.1109/58.84270.

Unsgaard, G., O. M. Rygh, T. Selbekk, T. B. Müller, F. Kolstad, F. Lindseth, and T. A. Nagelhus Hernes. 2005. “Intra-Operative 3D Ultrasound in Neurosurgery.” *Acta Neurochirurgica* 148 (3): 235–53. doi:10.1007/s00701-005-0688-y.

Varray, F., A. Ramalli, C. Cachard, P. Tortoli, and O. Basset. 2011. “Fundamental and Second-Harmonic Ultrasound Field Computation of Inhomogeneous Nonlinear Medium with a Generalized Angular Spectrum Method.” *IEEE Transactions on Ultrasonics, Ferroelectrics, and Frequency Control* 58 (7): 1366–76. doi:10.1109/TUFFC.2011.1956.

Viganó, Maria Carolina, Giovanni Toso, Gerard Caille, Cyril Mangenot, and Ioan E. Lager. 2009. “Sunflower Array Antenna with Adjustable Density Taper.” *International Journal of Antennas and Propagation* 2009 (April): e624035. doi:10.1155/2009/624035.

Weber, P.K., R.M. Schmitt, B.D. Tylkowski, and J. Steck. 1994. “Optimization of Random Sparse 2-D Transducer Arrays for 3-D Electronic Beam Steering and Focusing.” In *, 1994 IEEE Ultrasonics Symposium, 1994. Proceedings*, 3:1503–6 vol.3. doi:10.1109/ULTSYM.1994.401875.

Wildes, D. G., R. Y. Chiao, C. M. W. Daft, K. W. Rigby, L. S. Smith, and K. E. Thomenius. 1997. “Elevation Performance of 1.25D and 1.5D Transducer Arrays.” *IEEE Transactions on Ultrasonics, Ferroelectrics, and Frequency Control* 44 (5): 1027–37. doi:10.1109/58.655628.

Wygant, I.O., N. Jamal, H. Lee, A. Nikoozadeh, O. Oralkan, Mustafa Karaman, and B. Khuri-yakub. 2009. “An Integrated Circuit with Transmit Beamforming Flip-Chip Bonded to a 2-D CMUT Array for 3-D Ultrasound Imaging.” *IEEE Transactions on Ultrasonics, Ferroelectrics, and Frequency Control* 56 (10): 2145–56. doi:10.1109/TUFFC.2009.1297.

Yiu, Billy Y. S., Simon S. M. Lai, and Alfred C. H. Yu. 2014. “Vector Projectile Imaging: Time-Resolved Dynamic Visualization of Complex Flow Patterns.” *Ultrasound in Medicine & Biology* 40 (9): 2295–2309. doi:10.1016/j.ultrasmedbio.2014.03.014.

Zhao, Yue, Adeline Bernard, Christian Cachard, and Hervé Liebgott. 2014. “Biopsy Needle Localization and Tracking Using ROI-RK Method.” *Abstract and Applied Analysis* 2014 (October): 973147. doi:10.1155/2014/973147.

ANNEXES

I. Pipeline d’optimisation et d’analyse

II. Description des vidéos en ligne

III. Activités de dissémination

ANNEXE I: Pipeline d'optimisation et d'analyse

Le pipeline mis en place pour réaliser les optimisations présentées dans ce manuscrit (Figure 48) a été présenté au "Club des Développeurs "[51] qui se tenait au laboratoire CREATIS le 15 Janvier 2016.

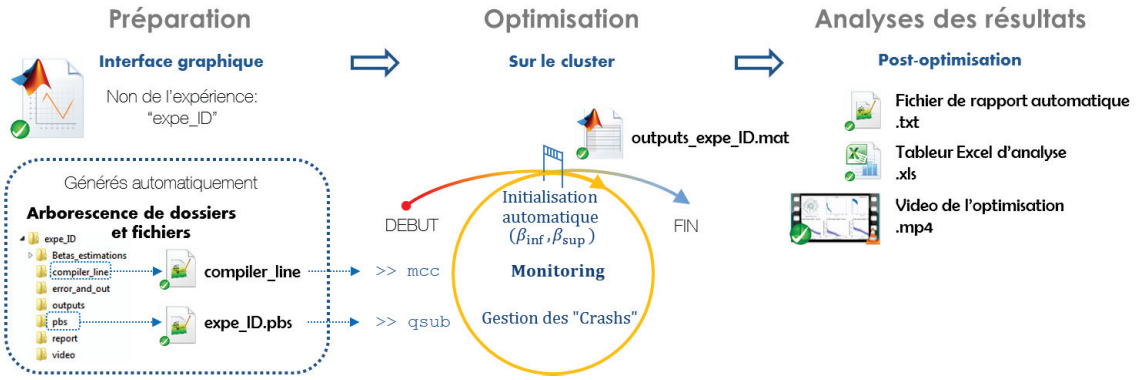


Figure 93 Illustration du pipeline d'optimisation et d'analyse

La description du pipeline démarre avec la description des fichiers et dossiers structurant l'implémentation du cadre général d'optimisation des sondes 2D parcimonieuses proposé (nommé optibox) avant de détailler les trois principales étapes de son fonctionnement (préparation des expérimentations, déroulement des optimisations et production des résultats) (Figure 48).

Optibox: Structure des fichiers et dossiers

Comme le représente la Figure 49, l'implémentation du cadre général d'optimisation des sondes 2D parcimonieuses proposé (optibox) est basée sur deux principaux dossiers: *data* (région colorée en vert sur la Figure 49) et *src* (région colorée en bleu sur la Figure 49). Par exemple, en considérant "expe_ID" l'identifiant d'une nouvelle expérimentation.

- Le dossier principal *data* contient des informations spécifiques pour la nouvelle experimentation "expe_ID", dans un sous-dossier nommé *data/experiments/expe_ID*. Mais *data* contient aussi, dans le sous-dossier *data/notouch* subfolder, des informations qui peuvent être partagées par toutes les expérimentations.
- Le dossier principal *src* contient le logiciel de simulation ultrasonore FIELD II (note de bas de page 36 p. 13) dans *src/FIELDII*, l'interface graphique utilisateur (GUI) (région colorée en marron sur la Figure 49) dans *src/GUI*, et l'implémentation du processus de recuit simulé (SA) dans *src/SA_box.* Il contient aussi les fichiers suivants:
  - *init_inf_fun.m* et *init_sup_fun.m*: pour estimer les paramètres initiaux β_{inf} et β_{sup}.
  - *monitoring.m* (ex *check_it_out.m)*: pour traiter les résultats intermédiaires et suivre le déroulement de l'optimisation (monitoring). Ce même fichier est exécuté une fois l'optimisation terminée pour produire une analyse post-optimisation.
  - *optimize.m*: to start the optimization process. It calls the two initializing scripts *init_inf_fun.m* and *init_sup_fun.m* automatically.

[51] Le concept de programmation orientée objet (OOP) a été présenté par Emmanuel Roux et Eduardo Davila pendant la séance du « club des développeurs » qui se tenait à CREATIS le 29 Mai 2016. L'exemple de code MATLAB OOP qui y était présenté est disponible sur https://www.creatis.insa-lyon.fr/site7/en/roux

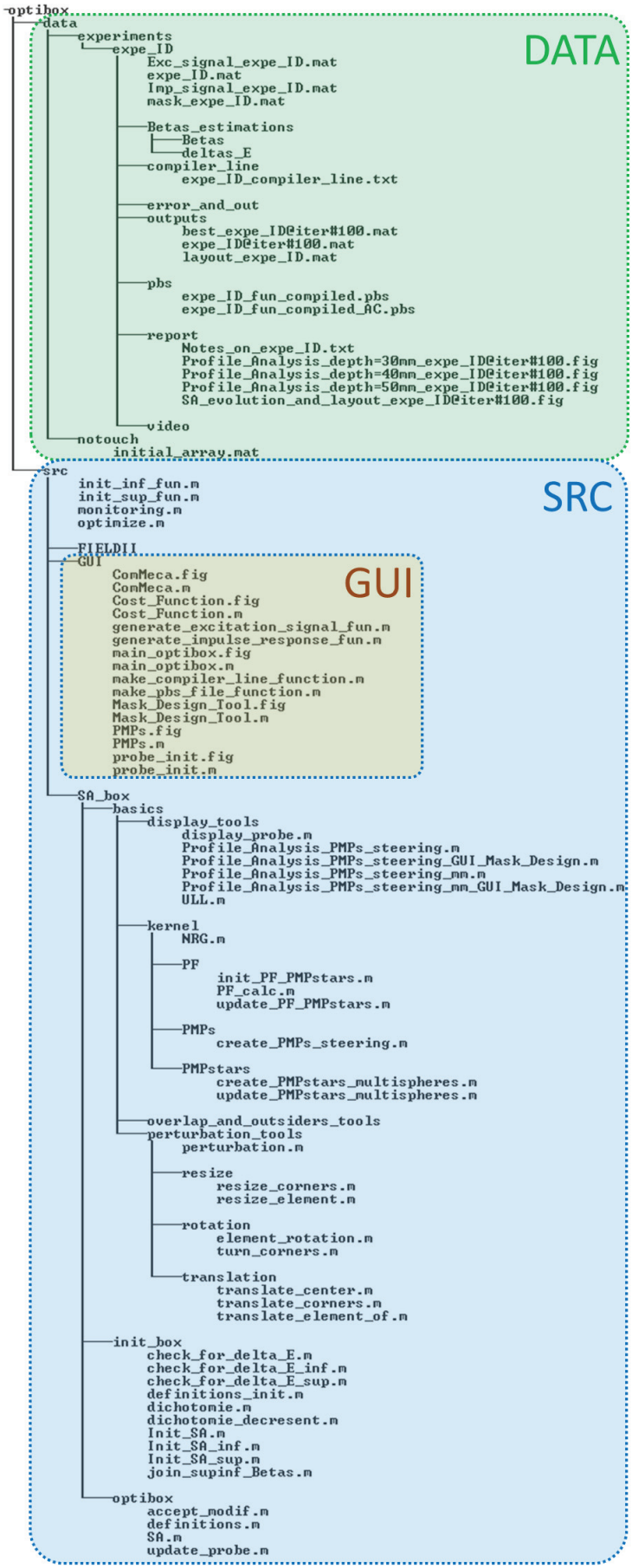


Figure 94 Structure des dossiers et fichiers du cadre d'optimisation des sonde 2D parcimonieuses proposé (optibox)

Préparation des expérimentations

L'interface graphique utilisateur (GUI) est utilisée pour paramétrer l'optimisation. Cinq des six entités qui compose l'interface GUI sont visible sur la Figure 50. La sixième entité a déjà été présentée sur la Figure 81 and elle apparaît automatiquement lorsque la troisième fonction d'énergie U_3 est sélectionnée dans l'entité *Cost_Function*.

Les entrées de chacune des cinq entités présentées sur la Figure 50 sont les suivantes:

- *main_optibox*:
  - La fréquence d'échantillonnage F_s en Hz
  - La valeur de σ pour fixer le nombre d'itérations
  - Les coordonnées du point focal (x_f, y_f, z_f) en mm
  - L'identifiant de l'expérimentation (par exemple "expe_ID")
- *probe_init*:
  - Le fichier de la sonde initiale (générée en dehors de l'optibox)
  - Le rayon maximal de l'ouverture r_p (si nécessaire) en mm
  - La fréquence centrale f_c en Hz
  - La vitesse du son c en m/s
  - La marge de non-superposition (l'inverse de la valeur entrée est multipliée par λ)
- *PMP*:
  - Les rayons des hémisphères (R_1, R_2 et R_3) où le champ de pression est calculé en mm. Par exemple pour définir trois hémisphères aux profondeurs 15 mm, 25 mm et 35 mm ce champ doit contenir "15,25,35".
  - Le nombre de PMP à placer sur chaque hémisphère
- *Cost_Function*:
  - Le sélecteur permet de choisir la définition de la fonction d'énergie (ici nommée *cost function*) entre U_1 (bouton du haut), U_2 (bouton du milieu) et U_3 (bouton du bas).
  - Quand U_1 ou U_2 sont sélectionnées il est nécessaire d'entrer en mm la résolution desirée (largeur de la région du lobe principal θ_ML) au niveau entrée en dB pour la limite du masque (équivalent à la valeur de coupure C). Il faut entre une valeur par hémisphère et séparer ces valeurs par une virgule.
  - Quand U_3 est sélectionnée, la résolution et les limites du masque ne sont pas à renseigner car elles sont calculées par l'entité *MASK_Design_Tool* (Figure 81) qui s'ouvre automatiquement lorsque l'on clique sur le bouton "Run" après que toutes les autres entités soient correctement renseignées.
- *ComMeca*:
  - Le type de perturbation à activer (pour l'instant il est possible de choisir parmi la translation, la rotation et la variation de taille des éléments actifs).
  - Quand la translation est activée, son amplitude maximale doit être entrée en $\mu\mathrm{m}$.

Quand toutes les entités sont correctement renseignées, les dossiers et les fichiers spécifiques à l'expérience *expe_ID* sont créés dans le sous-dossier *data/experiments/expe_ID* en cliquant sur le bouton "Run" de l'entitée *main_optibox*. L'entité *MASK_Design_Tool* (Figure 81) s'ouvre avant la création des fichiers spécifiques si la fonction d'énergie U_3 a été sélectionnée.

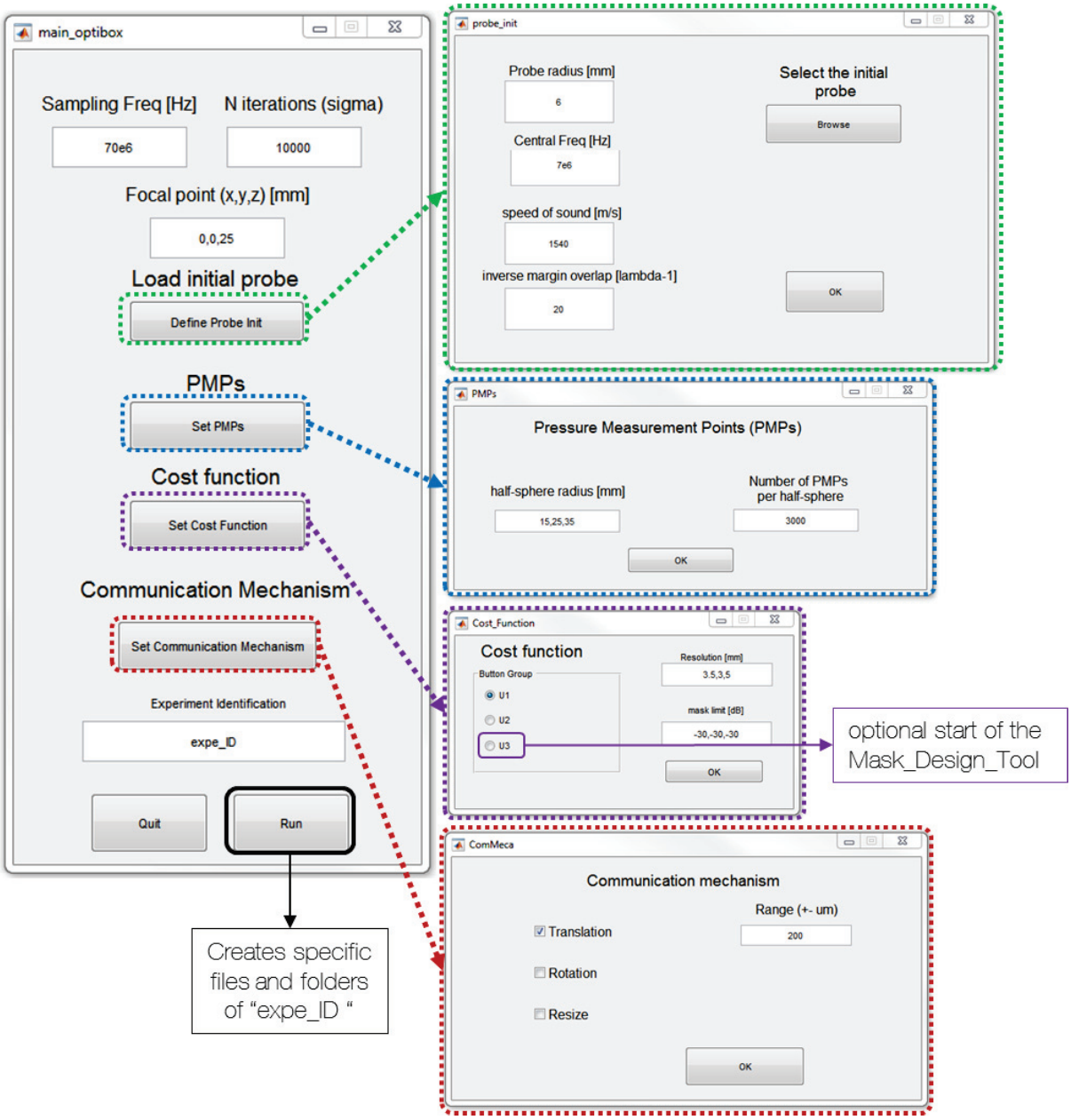


Figure 95 Détails des entités de l'interface graphique utilisateur (GUI) implémentée pour paramétrer les expérimentations d'optimisation.

Les dossiers spécifiques qui sont générés automatiquement et leur contenu sont les suivants:

- *Betas_estimations*: pour sauvegarder les paramètres initiaux β_{inf} and β_{sup} et les vecteurs ΔU^{+} qui contiennent les variations d'énergie utilisées pour calculer β_{inf} et β_{sup}.
- *compiler_line*: une ligne de commande est générée automatiquement et sauvegardée dans un fichier texte pour n'avoir qu'à la copier/coller pour compiler le code sur le cluster.
- *error_and_out*: en cas d'interruption, ce dossier contiendra (dans des fichiers texte) les messages d'erreur et les sorties générés par les machines du cluster.
- *outputs*: pour sauvegarder le résultat final et les résultats intermédiaires (pour le suivi).
- *pbs*: pour sauvegarder les fichiers pbs qui servent à soumettre une tâche sur le cluster.
- *report*: pour sauvegarder les graphiques des résulats (profils de rayonnement, évolution de l'optimisation) et le fichier de rapport automatique (*Notes_on_expe_ID.txt).*
- *video*: pour sauvegarder la vidéo du déroulement de l'optimisation une fois terminée.

Les fichiers spécifiques qui sont créés automatiquement par l'interface GUI sont les suivants:

- *expe_ID.mat*: ce fichier contient tous les paramètres de l'expérimentation.
- *Exc_signal_expe_ID.mat*: ce fichier contient le signal d'excitation (forme d'onde).
- *Imp_signal_expe_ID.mat*: ce fichier contient la réponse impulsionnelle du transducteur.
- *mask_expe_ID.mat* (optional): la masque sculptant généré par le *MASK_Design_Tool*.
- *expe_ID_compiler_line.txt*: la ligne de commande pour compiler les codes sur le cluster.
- *expe_ID_fun_compiled.pbs*: le fichier pbs normal pour soumettre au cluster la tâche d'optimisation (en conditions normales).
- *expe_ID_fun_compiled_AC.pbs*: le fichier pbs normal pour soumettre au cluster la tâche d'optimisation (après une interruption). Utile pour continuer une optimisation à partir du dernier résultat intermédiaire sauvegardé.

Déroulement des optimisations

Pour démarrer l'optimisation, l'intégralité du dossier optibox doit d'abord être uploaded, or même mieux, synchronisé sur le cluster. Pour ne pas utiliser trop de licences MATLAB la compilation du code est nécessaire si plusieurs expérimentations doivent être faites en parallèle (rien ne garantit que le *batch manager* lance la tâche sur la même machine). Le code est compilé sur le cluster[52] en exécutant la ligne de commande suivante :

```
>>mcc -R -nodisplay -R -singleCompThread -m optimize_expe_ID.m -a
.././data/ -a .././src/FIELDII -a .././src/SA_box
```

Une fois la compilation terminée, la soumission de la tâche d'optimisation peut être faite via le *batch manager* avec la commande qsub et le fichier pbs comme argument:

```
>>qsub expe_ID_fun_compiled.pbs
```

A partir de cette étape (et sans doute après avoir attendu quelques temps en file d'attente), l'optimisation démarre (l'initialisation est incluse). Il est possible de vérifier l'évolution de l'optimisation en exécutant le fichier *monitoring.m* (sur n'importe quel ordinateur personnel –ayant MATLAB et l'optibox-, mais pas sur le cluster). Cela lance une analyse du profil de rayonnementdu résulat intermédiaire et met à jour le fichier de rapport automaique dans le sous-dossier *data/experiments/expe_ID/report*. Il est important de préciser que si le dossier *optibox* n'est pas synchronisé, il est nécessaire de télécharger les résultats intermédiaires depuis le dossier *data/experiments/expe_ID/outputs* avant d'exécuter le fichier *monitoring.m.*

De plus, le déroulement de l'optimisation peut être interrompu de manière inopinée (coupure d'électricité, maintenance…). Pour gérer cette situation, un fichier pbs dédié (dans le sous-dossier *data/experiments/expe_ID/pbs*) peut être soumis afin de continuer l'optimisation à partir du dernier résultat intermédiaire sauvegardé (`>>qsub expe_ID_fun_compiled_AC.pbs`).

A la fin du processus d'optimisation, un fichier de sortie *outputs_expe_ID.mat* est généré dans le sous-dossier *data/experiments/expe_ID/outputs*. Ce fichier contient toute les informations nécessaires pour l'analyse post-optimisation.

---

[52] Dans cette étape il est nécessaire de se connecter en mode interactif au cluster (`>>qsub -I`) ensuite il faut ouvrir MATLAB et définir *optibox/src* folder comme répertoire de travail.

Production des résultats

L'analyse post-optimisation consiste à exécuter le fichier *monitoring.m* une fois que l'optimisation est terminée (le fichier *outputs_expe_ID.mat* doit avoir été généré). Ce fichier réalise l'analyse du profil de rayonnement (niveau de lobes latéraux et résolution latérale) de la meilleure configuration rencontrée au cours de l'optimisation. Il met également à jour le fichier de rapport automatique sans écraser ce qu'il contient déjà mais en ajoutant la dernière évaluant à la fin du rapport. Enfin, ce fichier produit une vidéo du déroulement de l'optimisation et la sauvegarde dans le sous-dossier dédié *data/experiments/expe_ID/video*.

Tous les résultats des optimisations sont ensuite listés et analysés dans une feuille de calcul Excel. Par exemple, la feuille de calcul qui a été utilisée pour produire les résultats présentés au chapitre III.B est affichée sur la Figure 51. Cliquer dans la sixième colonne permet d'ouvrir le dossier contenant le fichier de rapport de l'expérimentation sélectionnée et cliquer dans la dernière colonne lance la vidéo du déroulement de l'optimisation. La description du contenu affiché sur les vidéos du déroulement des optimisations est détaillée dans l'annexe II.

						SLL (dB)			Resolution @6dB (in degrees)			ID array	video
Experiment name	#iterations	#HS	#PMPs/HS	U	Report files location	R = 15 mm	R = 25 mm	R = 35 mm	R = 15 mm	R = 25 mm	R = 35 mm		
nts spiral (Blackman Density	-	-	-	-	l_256_Blackman_tapered\re	-20.2	-29.3	-25.2	7.8	2.6	3.8	spiral	
#Iterations study													
3PMPspheres_equitheta_NR	2500	3	5000	U1	MPspheres_equitheta_NRG_	-20.1	-24.4	-19.8	3.0	1.9	4.2	Iter 640 k	video
3PMPspheres_equitheta_NR	5000	3	5000	U1	MPspheres_equitheta_NRG_	-20.0	-24.8	-22.6	3.9	2.1	2.4	Iter 1.28 M	video
3PMPspheres_equitheta_NR	7500	3	5000	U1	MPspheres_equitheta_NRG_	-21.1	-26.0	-23.5	4.0	2.1	3.9	Iter 1.92 M	video
pti256_3PMPspheres_equit	10000	3	5000	U1	256_3PMPspheres_equitheta	-21.4	-24.9	-24.1	6.7	2.2	3.9	Iter 2.56 M	video
#PMPs study													
0612_256e_3HS_500p_ma	5000	3	500	U1	12_256e_3HS_500p_max_	-17.4	-23.5	-17.5	5.1	2.0	4.3	PMPs 0.5k	video
612_256e_3HS_1000p_m	5000	3	1000	U1	2_256e_3HS_1000p_max_	-19.5	-26.3	-19.8	3.0	2.1	4.5	PMPs 1k	video
612_256e_3HS_2000p_m	5000	3	2000	U1	2_256e_3HS_2000p_max_	-20.3	-25.1	-22.9	7.5	2.1	4.2	PMPs 2k	video
612_256e_3HS_3000p_m	5000	3	3000	U1	2_256e_3HS_3000p_max_	-22.3	-26.4	-24.4	5.4	2.0	4.0	PMPs 3k	video
612_256e_3HS_4000p_m	5000	3	4000	U1	2_256e_3HS_4000p_max_	-19.5	-24.6	-24.1	4.2	2.1	3.4	PMPs 4k	video
3PMPspheres_equitheta_NR	5000	3	5000	U1	MPspheres_equitheta_NRG_	-20.0	-24.8	-22.6	3.9	2.1	2.4	PMPs 5k	video
1HS (U1, U2, U3)													
609_256e_1HS_3000p_ma	10000	1	3000	U1	0_256e_1HS_3000p_max_	-9.4	-28.9	-14.7	14.1	1.6	6.1	U1 1HS	video
_256e_1HS_3000p_max_x	10000	1	3000	U2	56e_1HS_3000p_max_x_ra	-12.1	-29.3	-18.8	8.3	1.9	6.0	U2 1HS	video
e_1HS_3000p_q_sculpt_m	10000	1	3000	U3	1HS_3000p_q_sculpt_max	-10.9	-29.3	-16.5	12.2	1.6	6.6	U3 1HS	video
3HS (U1, U2, U3)													
610_256e_3HS_3000p_ma	10000	3	3000	U1	0_256e_3HS_3000p_max_	-23.7	-27.5	-25.3	4.6	2.2	3.8	U1 3HS	video
ti256_3HS_3000PMPs_ma	10000	3	3000	U2	56_3HS_3000PMPs_max_x	-24.4	-27.3	-27.5	5.3	2.7	3.7	U2 3HS	video
_3HS_3000PMPs_q_sculpt	10000	3	3000	U3	HS_3000PMPs_q_sculpt_m	-24.5	-29.7	-27.6	6.1	2.6	3.4	U3 3HS	video

Figure 96 Impression d'écran de la feuille de travail Excel utilisée pour l'analyse préalable des résultats présentés au chapitre III.

ANNEXE II: Description des vidéos en ligne

Les vidéos du déroulement des optimisations des résultats suivants sont disponibles en ligne sur https://www.creatis.insa-lyon.fr/site7/en/roux

Chapitre III

Mono-profondeur

- U_1 1HS
- U_2 1HS
- U_3 1HS

Multi-profondeur

- U_1 3HS
- U_2 3HS
- U_3 3HS

Chapitre IV

- opti128
- opti192
- opti256

Le contenu affiché sur chacune des vidéos est le suivant:

- En haut à gauche: l'évolution de la distribution des éléments actifs
- En haut au centre: l'évolution des valeurs de la fonction d'énergie.
- En haut à droite: l'évolution des valeurs du taux d'acceptation.
- En bas: l'évolution du profil de rayonnement aux profondeurs considérées pendant l'optimisation.

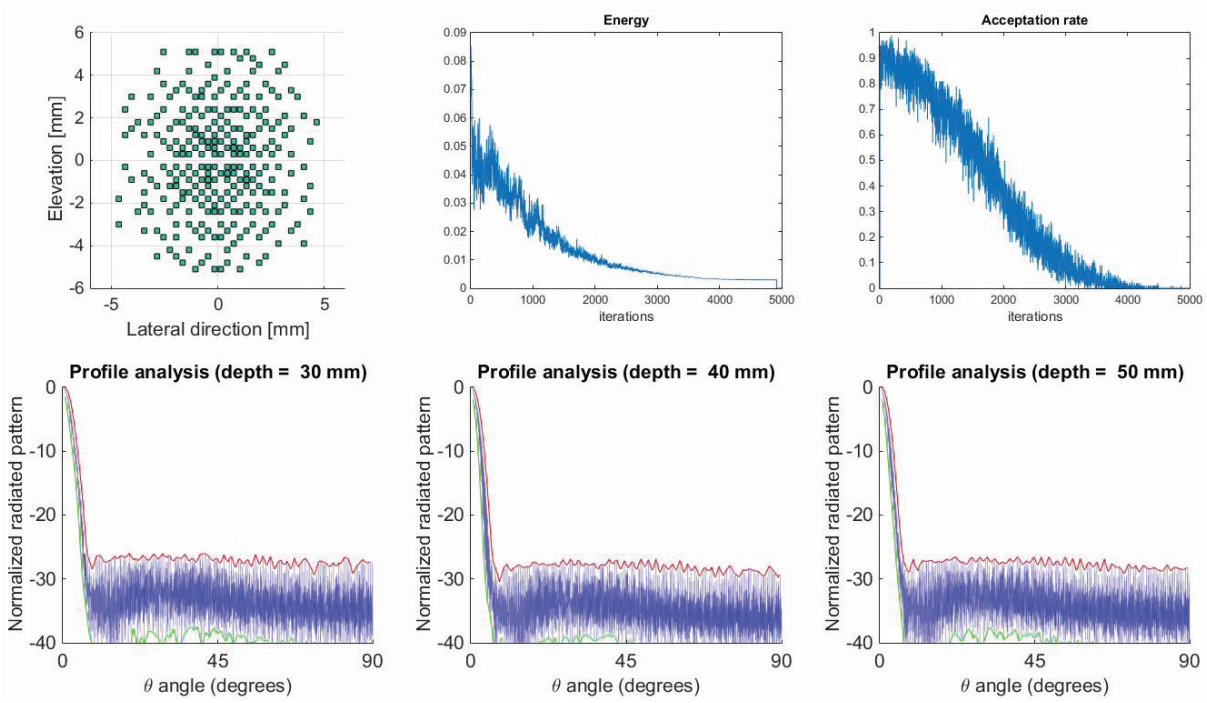


Figure 97 Impression d'écran de la vidéo du déroulement de l'optimisation de opti256 (chapter IV). Cet écran présente (haut-gauche) l'évolution de la disposition des éléments actifs, (haut-centre) ; le tracé de l'évolution des valeurs de la fonction d'énergie, (haut-droite) ; le tracé de l'évolution des valeurs du taux d'acceptation et (bas de gauche à droite) les profils de rayonnement à 15 mm, 25 mm, et 35 mm.

ANNEXE III: Activités de dissémination

Thèses's Art



Figure 98 La photo de Thèse's Art prise par Eric Le Roux.
Cette photographie a été imprimée en grand format (1.80m x 2.50m) et exposée dans le centre de la ville de Lyon en Octobre 2015.
(p. 48 de la brochure disponible sur http://www.univ-lyon1.fr/medias/fichier/cataloguethesesart_1465548618561-pdf).

Eric Le Roux a réalisé cette photographie au 7ème étage du bâtiment du laboratoire (désormais fermé…) dans le cadre du projet *Thèse's Art* (Université Claude Bernard Lyon 1): les photographies capturent l'esprit de quelques doctorants de l'Université et les représentent en grand format (1.80m x 2.50m). Une exposition a eu lieu dans le centre de la ville de Lyon le 3 Octobre 2015. L'intégralité des photographies réalisées dans le cadre de ce projet ainsi que son introduction par Cédric Villani (p.3) sont disponibles sur (visité en Août 2016):

http://www.univ-lyon1.fr/medias/fichier/cataloguethesesart_1465548618561-pdf